CYRIC

ANNUAL REPORT

1994

(January 1994- December 1994)

CYCLOTRON AND RADIOISOTOPE CENTER
TOHOKU UNIVERSITY

PREFACE

In this fifteenth issue of the CYRIC Annual Report, we summarize the activities for research and development and results of training for radioisotope safe-treatment at Cyclotron and Radioisotope Center, Tohoku University during the calendar year 1994.

In 1994 research programs in various fields such as nuclear physics, nuclear chemistry, solid state physics and element analyses by PIXE and activation were carried out, and radioisotopes were produced for use in engineering, biology and medicine. At the same time several facility improvements have been carried out. A total of 3300 hours of the cyclotron beam was delivered for the scheduled researches, while 50 hours for research and development for the accelerator and related facilities. It should be noted here that a two weeks long unscheduled shut-down occurred in this year due to the break down of the RF power supply device, while unscheduled shut-down so far experienced by the last year was limited to a few percents of the total beam time used. In almost 50% of the beam time, protons were accelerated for nuclear physics and short-lived radioisotopes for medical and other studies, in 15% deuteron beams for the same purposes, while in 16% ^{4}He beams for material and solid state physics. Heavier ions such as ^{13}C and ^{15}N have been accelerated as well for some limited works.

During 1994, 477 of staff members and students of Tohoku University were trained at this Center in the beginner's course of safe handling of radiation and radioisotopes, while 219 staff members and students in the "x-ray course". In addition, a new course of safe handling of radiation from a SOR (Synchrotron Orbital Radiation) has been opened.

In this year, a system of the high-resolution positron-emission tomograph SET 2400W-S fabricated by Shimazu Co. Ltd. has been installed. This PET machine is capable of producing quantitative cross-sectional images of isotope distribution in e. g. a tissue, being optimized for 2D and 3D data acquisition with 32 detector rings involving 21,504 BGO crystals and 1,792 PMTs. Superior resolution (4.0 mm FWHM) and high sensitivity (40 kcps/Bq/cc) have been achieved. For reconstruction of three dimensional images with a tremendous quantity of data, a powerful SX-3/44 super computer system of the Computer Center, Tohoku University, is utilized. Data are transferred by an ultra high speed campus network (Super TAINS). As such, this full dressed PET machine is expected to yield further activities in the research fields of medicine and biology.

As mentioned in the last issue, the present Model 680 AVF cyclotron with K= 50 MeV is becomming less powerful both qualitatively and quantitatively from the view points of progress of science and activities of Tohoku University. Some people may require more

energetic and/or high-intense beams including those of heavy nuclide or even of unstable nuclei. Others expect that polarized and unpolarized intense neutron beams may promise further fruitful researches for physics and technology.

Application of the ion beam for scientific and industrial purposes is one of the national projects. Based on the results of the 18 years-long multi-purpose use of Cyclotron and Radioisotopes, we have drawn up a master plan facilitating the education and researches in this field at Tohoku University. The basic idea of this plan is to extend the multi-purpose uses of a cyclotron to those of an ensemble of accelerators. We regard an accelerator as a micro- and new-materials processing machinery as well as the tool for inducting nuclear reactions . For these purposes, an accelerator complex consisting of cyclotrons, tandem type electrostatic generator, etc. are needed.

On the other hand, deterioration of the present AVF cyclotron is evident, an example for which is the break down of the RF power supply as mentioned above. It is of crucial importance to replace the cyclotron by a new one with higher specifications to maintain the present activities in CYRIC.

We are very grateful to Tohoku University and to the Ministry of Education, Science and Culture for their continuous support.

January 1995

Hikonojo ORIHARA

Director
Cyclotron and Radioisotope Center
Tohoku University

EDITORS:

Hikonojo ORIHARA
Manabu FUJIOKA
Tatsuo IDO
Takashi NAKAMURA
Masatoshi ITOH

WORD PROCESSED BY

Yu-ko YAMASHITA

CONTENTS

I. PHYSICS AND TECHNOLOGY

II. CHEMISTRY

III. BIOLOGY AND MEDICINE(BASIC)

IV. MEDICINE (CLINICAL)

V. RADIATION PROTECTION AND TRAINING OF SAFEHANDLING

VI. PUBLICATIONS

VII. MEMBERSW OF COMMITTEES

VIII. PERSONNEL

I. PHYSICS AND TECHNOLOGY

I. 1. Study of Two-Proton States of the ^{20}Ne Nucleus by (^{3}He, n) Reaction

*Fujii Y., Tohei T., Nakagawa T., Narita A.*****, Hino T., Orihara H.*, Ishii K.*, Terakawa A.*, Hosaka M.******, Guan Z.*, Ito K., Teramoto Y., Yamamoto A.*, Abe K.**, Suehiro T.***, and Ohnuma H.*****

Department of Physics, Tohoku University
*Cyclotron and Radioisotope Center, Tohoku University **
*Department of Nuclear Engineering, Tohoku University ***
*Tohoku Institute of Technology ****
*Department of Physics, Tokyo Institute of Technology *****
*Faculty of Science, Hirosaki University ******
*Institute for Nuclear Study, University of Tokyo *******

Two-nucleon transfer reactions by light ions are expected to excite states of two particle configuration selectively, if they proceed with a direct reaction process. There are many measurements for two-neutron or proton-neutron transfer reactions at present, but relatively little information is available for a two-proton transfer reaction like (^{3}He,n), which has been mainly accomplished at low incident energies.

Two-proton states of the ^{20}Ne nucleus have been studied through the ^{18}O(^{3}He,n) reaction at 18MeV[1]. However, this energy is not enough high to proceed mainly through a direct reaction and observed angular distributions of the cross section have not been distinguished clearly for transitions with large transfer momenta. Therefore, the incident energy of 30MeV was selected to make the direct reaction more dominant.

The experiment was carried out using a 30MeV ^{3}He beam from the AVF cyclotron at the Cyclotron and Radioisotope Center, Tohoku University. Neutron energies were measured by a time-of-flight (TOF) technique[2]. Twelve neutron detectors of 5cm thickness filled with liquid scintillator NE213 were located at 35m from the target, where the effective detection solid angle was 0.37msr. Angular distributions of emitted neutrons were measured at laboratory angles between 0 ° to 45 ° using a beam-swinger system. ^{18}O gas isotopically enriched to 98.0% was used as a target. The gas was contained in two types of gas cells, disk typed and cylindrical ones. Target thickness was ranged from 1.9 to 3.2mg/cm^{2}.

The excitation energy range up to 23MeV were covered in the present measurements and angular distributions of the differential cross sections were obtained for 27 peaks. Typical overall time resolution was 2.0ns, which corresponded to the energy resolution of 600keV for the ground state transition. In Table 1, excitation energies and spin-parities for

observed peaks are shown together with the results of Evers et al.[1] and the compilation by Ajzenberg-Selove[3] for states which the correspondence is well established (except for the state at 18.37MeV).

Finite-range distorted-wave Born-approximation (DWBA) calculations for the differential cross section have been accomplished with the code DWUCK5[4]. The potential parameters for the entrance and exit channels were taken from systematic ones of Becchetti & Greenlees[5] and Watson et al.[6], respectively. Spectroscopic amplitudes employed in the DWBA calculations were obtained from a shell-model calculation with the code OXBASH[7], using full sd-shell effective interactions of Wildenthal[8]. Negative parity states have been calculated with a pure $(1f_{7/2}, 1d_{5/2})$ configuration.

In Figure 1, typical experimental angular distributions are shown together with DWBA predictions. The theoretical curves have been normalized to the data. The DWBA calculations well reproduce the experimental angular distributions for the seven states with well-known spin-parities, but one for 5.68MeV 1^- state fails to reproduce the data. From the comparison of the DWBA predictions with the data, new spin-parities are tentatively proposed for four peaks at 8.52, 9.08, 10.67 and 18.37MeV, and two spin-parity candidates for other seven peaks as shown in Table 1. For the peaks at 8.52 and 9.08MeV, corresponding states have not been reported yet. Though the DWBA calculation for the peak at 18.37MeV cannot exclude 3^-, we would be able tentatively to identify the peak as the 18.43MeV first T=2, 2^+ state, because this peak is strongly excited and only the angular distribution shape of this peak shows one for low spin state around this excitation energy in the present measurement.

In Table 2, obtained enhancement factors are listed with these for ^{16}O, $^{40,42,44}Ca(^3He,n)$ reactions obtained by our group[9,10]. In the table a tendency is seen that enhancement factors for the 0^+ states are greater than these for the 2^+ and 4^+ states. From our results, one can guess that typical enhancement factors for the DWBA analysis using DWUCK5 are about 8 for the 0^+_1 states and 3 for the 2^+_1, 4^+_1 states.

Analyses taking account a sequential transfer ^{3}He-d-n process have been also carried out within the framework of the second order DWBA calculation with the code TWOFNR[11]. The potential parameters for intermediate channels were taken from systematic ones of Daehnick et al.[12] Spectroscopic amplitudes for the (^{3}He,d) and (d,n) steps were also obtained from the above described shell model calculation, and 11 states of ^{19}F were employed as the intermediate channels. In Figure 2, the direct (^{3}He,n) term (dotted), sequential ^{3}He-d-n term(broken) and coherent sum of them (solid) are displayed without any normalization to the data. The present results of the calculations indicate that contributions from sequential transfer process are important for the two nucleon transfer reaction cross section and the fits of the angular shape to the data become rather worse by the inclusion of the present sequential transfer process. However, there are some remaining problems in the present work. Especially the used optical potential parameters were selected to reproduce

experimental angular distributions by one step term only. So the parameters may include the effect of the sequential transfer term, already. Other problems may be on the three body wave function used in the present analyses and on the neglected non-orthogonal term of the sequential transfer process. Further discussions for these problems are in progress.

References

1) Evers D. et al., Nucl. Phys. **A275** (1977) 363.
2) Orihara H. et al., Nucl. Instr. and Meth. **A257** (1987) 189.
3) Ajzenberg-selove F., Nucl. Phys. **A475** (1984) 1.
4) Kunz P. D., DWBA code DWUCK5, unpublished.
5) Becchetti F. D., Jr. and Greenlees W., Polarization Phenomena in Nuclear Reactions. The University of Wisconsin Press, Madison, Wis (1971).
6) Watson B. A., Singh P. P. and Segel R. E. Phys. Rev. **182** (1969) 977.
7) Etchegoyen A., Rae W. D. M. and Godwin N. S., Shell Model Code OXBASH, unpublished.
8) Wildenthal B. H., Prog. Part. Nucl. Phys. **11** (1984) 5.
9) Hosomi K. et al., CYRIC Annual Report (1991) 5.
10) Narita A. et al., CYRIC Annual Report (1993) 16.
11) Igarashi M., DWBA code TWOFNR, unpublished.
12) Daehnick W. W., Childs J. D. and Vrcelj Z., Phys. Rev. **C21** (1980) 2253.

Table 1. Excitation energies and spin-parities for the present observed peaks.

Present		Ajzenberg-selove [3]		Evers et.al. [1]	
E_x(MeV)	J^π	E_x(MeV)	J^π	E_x(MeV)	J^π
0.00	0^+	0.0	0^+	0.0	0^+
1.61	2^+	1.6337	2^+	1.65	2^+
4.24	4^+	4.2477	4^+	4.21	4^+
5.68	1^-	5.6214	1^-	5.71	1^-
		6.725	0^+	6.72	0^+
7.17	3^-	7.1563	3^-	7.15	3^-
8.52	4^+				
				(8.74)	
9.08	1^-				
10.14	$2^+;1$	10.274	$2^+;1$	10.24	$2^+;1$
10.67	4^+			10.83	
11.17					
				11.48	(0^+)
12.23	$2^+;1$	12.221	$2^+;1$	12.21	$2^+;1$
12.86	$(2^+,4^+)$				
13.59	$(2^+,4^+)$			13.57	(2^+)
14.01	$(3^-,4^+)$			13.93	(2^+)
14.57					
15.00				(15.1)	
15.58	$(3^-,4^+)$			15.52	$(2^+;1)$
16.09	$(2^+,3^-)$			16.01	$(2^+;1)$
16.76	$0^+;2$	16.732	$0^+;2$	16.73	$0^+;2$
17.69				17.55	$(2^+;1)$
				17.91	(0^+)
18.37	$2^+;2$	18.430	$2^+;2$		
19.33				19.33	
19.88	$(2^+,3^-)$				
20.75					
21.60					
22.36	$(2^+,3^-)$				
22.95					

Table 2. Enhancement factors for well known states near the ground states obtained with DWBA analyses using DWUCK5 together with the results of the other works.

	^{20}Ne 30MeV*	^{18}Ne [9] 30MeV*	^{18}Ne [9] 45MeV*	^{42}Ti [10] 50MeV*	^{44}Ti [10] 50MeV*	^{46}Ti [10] 50MeV*
0_1^+	8.6	3.3	2.8	6.0	11	14
2_1^+	3.1	1.9	1.9	2.9	2.6	3.6
4_1^+	4.0	2.1	1.8	2.8	2.6	3.1
6_1^+	-	-	-	3.5	5.9	7.4
$2_1^+;1$	6.6					
$2_2^+;1$	4.1					
$0_1^+;2$	15.5					
$2_1^+;2$	6.3					

* Incident energy

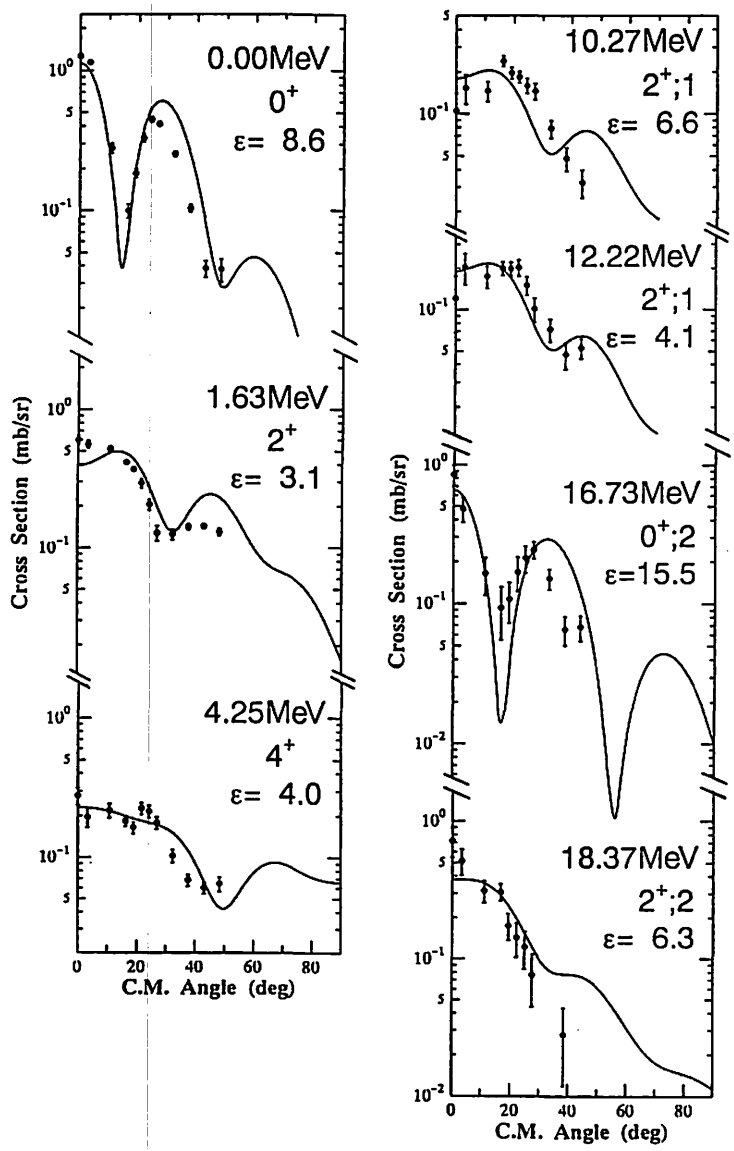

Fig. 1. Typical angular distributions obtained in the ^{18}O(^{3}He,n)^{20}Ne reaction at 30MeV. Curves represent the DWBA predictions by DWUCK5. The theoretical curves have been normalized to the data.

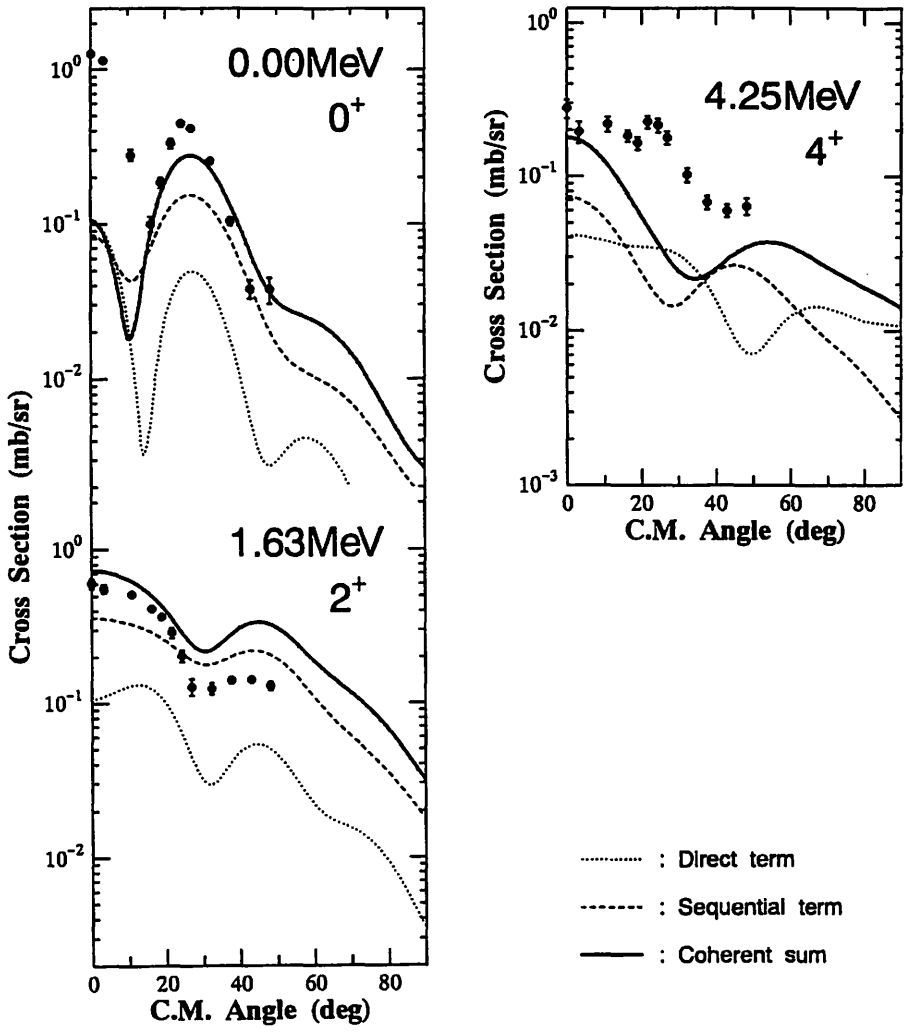

Fig. 2. Angular distributions and DWBA predictions by TWOFNR for the 0^+_1, 2^+_1 and 4^+_1 states. Dotted and broken curves represent the direct term and sequential term, respectively, and solid curves represent the coherent sum of them. The curves are displayed without any normalization.

I. 2. Forward Nuclear Glory in $^{13}C+^{28}Si$ Scattering

Yamaya T, Ishiyama H, Yamazaki A, Kotajima H*, Suzuki K*, Tanaka M*, Fujioka. M**, and Shinozuka.T***

Depertment of Physics,Tohoku University
*Depertment of Nuclear Enginerring,Tohoku University**
*Cycrotoron and Radioisotope Center, Tohoku University***

The optical glory is a well known phenomenon, which is due to the scattering of visible light from water droplets. Like the rainbow, the forward glory scattering produces an intensity enhancement in the forward direction because of the axial focusing effect. This scattering phenomenon has been predicted and observed in molecular and atomic collisions[1,2]. In nuclear collisions, its exitence has been predicted by many theorists[3,4]. Recently, a proof of the forward nuclear glory was experimentally suggested for $^{12}C+^{12}C$ scattering system in a energy region of $E_{c.m.}$=6.4-11.5 MeV[5]. Furthermore, using the forward nuclear glory phenomenon at higher incident energies of E/A~4~5 MeV, the total reaction cross sections have been measured for the scattering systems, ^{12}C, ^{15}N $^{16}O+^{28}Si$[6].

In the present work, the elastic differential cross sections at smaller angles than that in previous experiment[6]were measured in the $^{13}C+^{28}Si$ scattering system at E_{Lab}=60 MeV. The result of the experiment showed undoubted oscillations and undulating envelope shapes in the sum-of-differences cross sections.

The elastic differential cross sections were obtained for the scatterings of ^{13}C by ^{28}Si using $^{13}C^{4+}$ beam of E=60 MeV provided from the Tohoku University model 680-cyclotron. For the determination of the seattering amplitude $|f_N(0)|$ by means of the generalized optical theorem(GOT), it is necessary to measure the elastic differential cross sections in the very forward angular range. The most crucial point is how far forward angles the measurement can be performed. It comes to a problem how small errors the absolute scattering angles can be determined.

For the measurements at extremely forward angles (0.6°-4.0°), a trapezoidal scattering chamber was designed and installed at the down stream of a large scattering chamber as shown in Figure 1. A distance between a target and a defined slit of the detector system was 1599 mm. The detector system consists of two 25 μm totally depleted silicon detectors and a 240 μm position-sensitive silicon detector, i.e, this system had two telescopes. Each telescope was mounted by a thin tantalum plate with three slit apertures of $0.4\times2mm^2$ in front of the ΔE detectors. Three slit apertures defined the solid angles of 3.1×10^{-7}sr, and the

differential angles of $\Delta\theta$=0.014° assuming a point beam spot on the target. The accuracy of angle setting was 5×10^{-4} degree.

Four solid-state detectors to monitor relative beam deflection were symmetrically situated with respect to the beam axis. This monitor system was movable on the scattering plane and an accuracy of absolute scattering angles was 0.02°. The target was a self-supporting natural Si metal of 180 $\mu g/cm^2$ thickness. The beam was doubly collimated to a spot diameter less than 0.4 mm on the target.

The differential cross sections were measured for angles of 0.6°-1.2° with step of 0.05°, for 1.2°-8.5° with step of 0.1°, and for 8.5°-60° with step of 1.0° in the laboratory system. The statistical error was smaller than 0.3% at angles smaller than 8.5°.

For the determination of the exact scattering angles with the incident beam axis, a primary problem is an unstability of the beam position on the target during taking data. The present collimeter system for the incident beam has the maximum dispersive beam angle of ±0.11°. However, the present measurement requires a precision of the order of ±0.001° in the scattering angles to achive the observation of the nuclear glory phenomenon up to 0.5°. If the incident beam is very unstable, the uncertainty of the scattering angle concerning the definite slit aperture of the detector is ±0.014° in an maximum value, where the beam spot on the target is equal to 0.4 mmϕ

In order to monitor the deflection of the beam intensity distribution in the beam spot, the four monitor detectors were symmetrically placed on a circle with a small corn angle of 1.1° with the incident beam axis. Figure 2 shows the relative shift of the scattering angle by the beam deflection for each data run, where $\Delta\phi$ is the shift of vertical component for the scattering plane, and $\Delta\theta$ is the shift of horizontal component. Each shift was determinded in the accuracy of ±0.003° for each data run.

The secondary problem is an angle dependency of the effective area for a solid angle in a region of very small angles because of the small corn angle. Figure 3 shows deviations of the Rutherford cross sections for the practical solid angles from those assuming a constant solid angle for scattering angles. These deviations increase with $\Delta\phi$.

As the physical effects for the elastic scattering data at such very small angles, the effects of multiple sacttering, the electron screening and vacuum polarization, should be considerd. The effects of the first and second terms were negligible for the data at angles larger than 0.2° at least. However, the effect of the third term was taken into account for the data. In addition, the contribution from the target contaminations should be taken into account in order to keep the resulting error small. We found a contaminant material of about 3.7×10^{-3}% in ^{28}Si target which was estimated as a mass number of near A=180, it might be Au, from the elastically scattered energy spectra at the large angles.

The determination of the absolute scattering angles was achived by measuring the symmetry of the Ruthford scattering yields with the beam axis. Elastic scattering yields at

symmetrical angle points with the beam axis were measured. The ratios of elastic scattering yields to Rutherford cross sections should show the symmtrical structures with the beam axis. These results are shown in Figure 4. A difference between yields at symmtrical points can correspond to the deviation of $\Delta\phi$=0.003° in the absolute scattering angles. Therefore, in the present work, absolute scattering angles could be determinded with an accurancy of ±0.003°.

The experimental angular distribution in $^{13}C+^{28}Si$ scattering system is shown in Figure 5, together with the result of the optical model potential (OMP) analysis[10]. The angular distribution at θ_{Lab}=0.6°~4.0° is expanded in Figure 6. The sum-of-differences cross sections were calculated from the measured elastic cross sections. The data of elastic cross sections have been renormalized as the median of upper and lower envelopes of $\sigma_{SOD}(\theta_0)$ should become a horizontal line. This final normarization could reduce systematic errors from each data of the measured elastic cross sections. Figure 7 shows the obtained sum-of-differences cross sections. It exhibits exactly those features which were predicted in Refs.3 and 4, i.e, rapid oscillations at very forward angles with constant amplitude and being nearly vanished at an angle called glory minimum. These features are proofs of an exitence of the forward nuclear glory.

The quantities ,which are nuclear scattering amplitude $|f_N(0)|$, reaction cross section σ_R, and glory angular momentum l_{gl}, should be determinded from the SOD analysis. As mentioned in Ref.9, The result of the analysis has a small deviation from the measured $\sigma_{SOD}(\theta_O)$ in the angular range near the glory minimum. It may be caused because the phase of nuclear scattering amplitude $\phi_N(\theta_0)$ is approximately represented by the $\phi_N(0)$ and the $C'(\theta_0)$ has a finite value. An exact glory minimum could be estimated for the θ_0=4.0°~5.5° from the SOD analysis. The values of l_{gl} and $|f_N(0)|$ were 30 ± 5 and 21 ± 4fm, respectively. The obtained reaction cross section was 2090 ± 80mb. The result of χ^2-fit for the SOD is shown in Figure 8 by a solid curve together with a value of σ_R.

The nuclear scattering amplitude $|f_N(\theta)|$ derived from the present data exhibited rapid oscillation at forward angle and nonvanishing at $\theta\rightarrow 0°$. It was suggested that a forward nuclear glory in the $^{13}C+^{28}Si$ system existed at E_{Lab}=60MeV.

References

1) Bernstein.R. B., J. Chem. Phys. **34** (1961) 361.
2) Bernstein. R. B, Adv. Chem. Phys. vol.X (Wiley, NewYork,1966) 75.
3) Hussein. M. S., et al., Phys. Lett. **B114** (1982) 1.
4) Barrette. J and Alamanos. N., Phys. Lett. **B115** (1985) 208.
5) Ostorski. A. N et al., Phys. Rev. **C44** (1991) 2082.
6) Yamaya. T. et al., Proc. Int. Symp. on 3rd. IN2P3-RIKEN. , Saitama, 1994.
7) Holdman. J. T and Thaler. R. M., Phys. Rev. **B139** (1965) 186.
8) Marty. C, Z. Phys. **A309** (1983) 261.
9) Barrette. J. and Alamanos. N., Nucl. Phys. **A441** (1985) 733.
10) Yamaya. T, et al., Phys. Rev. **C37** (1988) 2585.

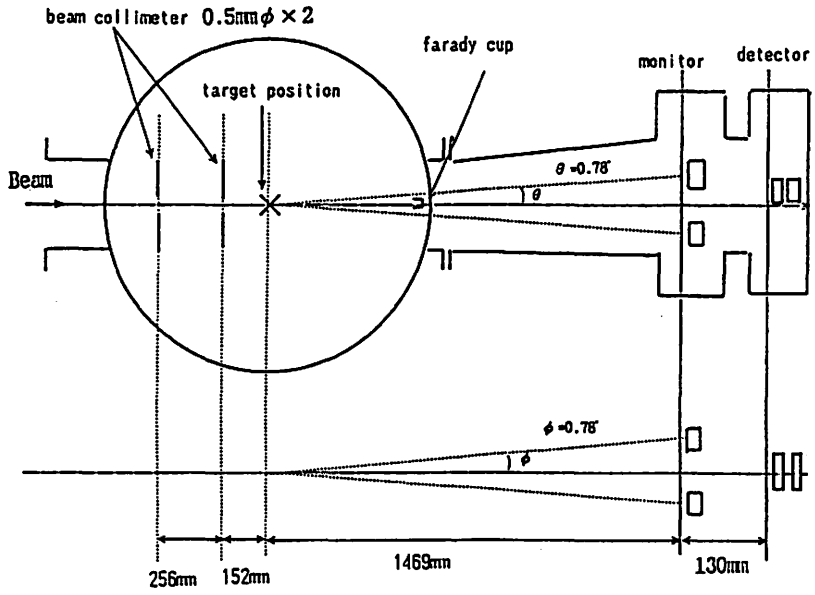

Fig. 1. Schematic layout for the measurement of forward elastic scattering.

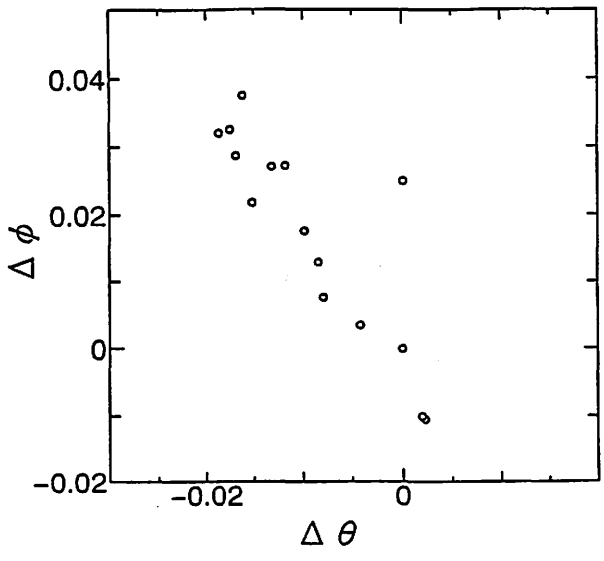

Fig. 2. The shift of beam deflection angle for each data run.

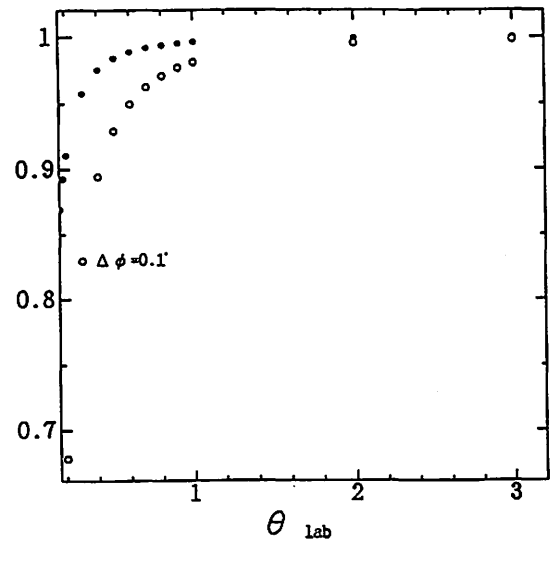

Fig. 3. The deviations of Rutherford cross sections for practical solid angles from those for a constatnt solid angle. The practical solid angles depend on the scattering angles near 0 degree. Solid and open circles indicate the deviations at $\Delta\phi=0°$ and $\Delta\phi=+0.1°$, $\Delta\phi=+0.1°$,$\Delta\phi=+0.1°$,respectively.respectively.

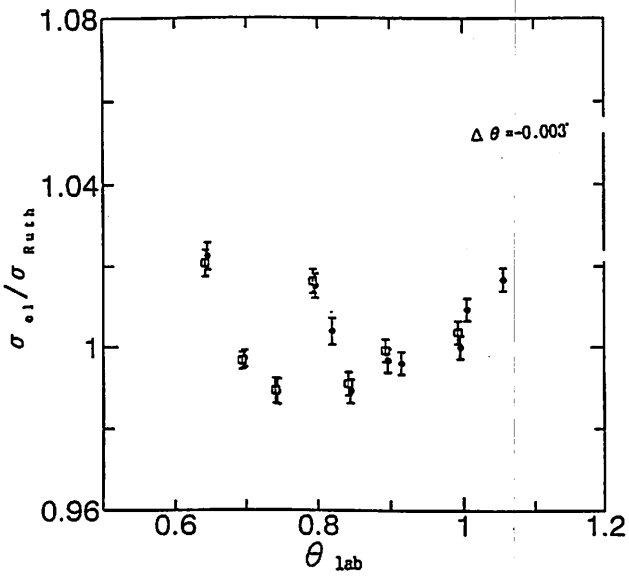

Fig. 4. Ratios of elastic scattering to the Rutherford scattering cross sections at symmetry angles with beam axis. The open squares and solid circles indicate data points at the left-side and right-side angles with the direction of beam current, respectively. A correction of scattering angles with beam axis is only 0.003° to right side.

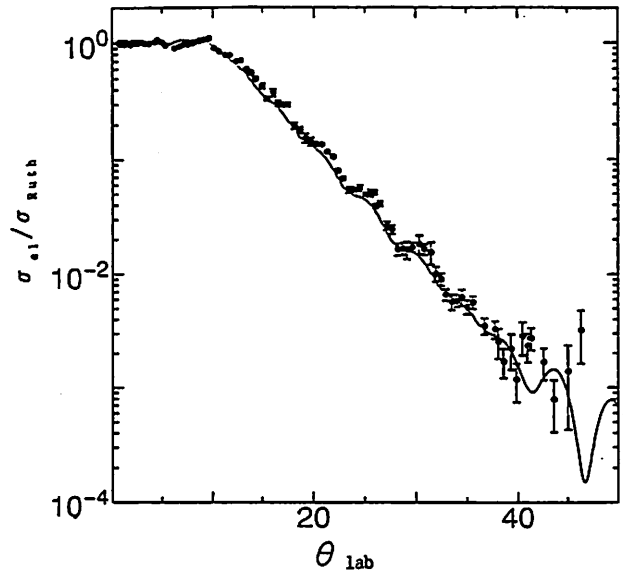

Fig. 5. Comparison between the measured cross sections and the OMP curve.

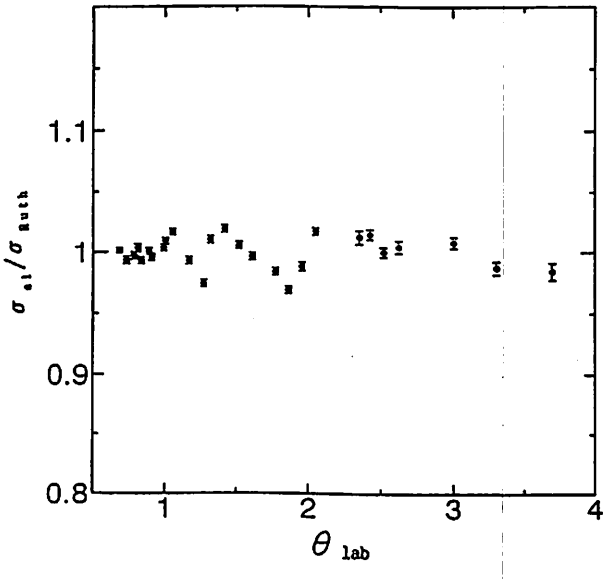

Fig. 6. The expanded angular distribution at θ_{Lab}= 0.6°~4.0°.

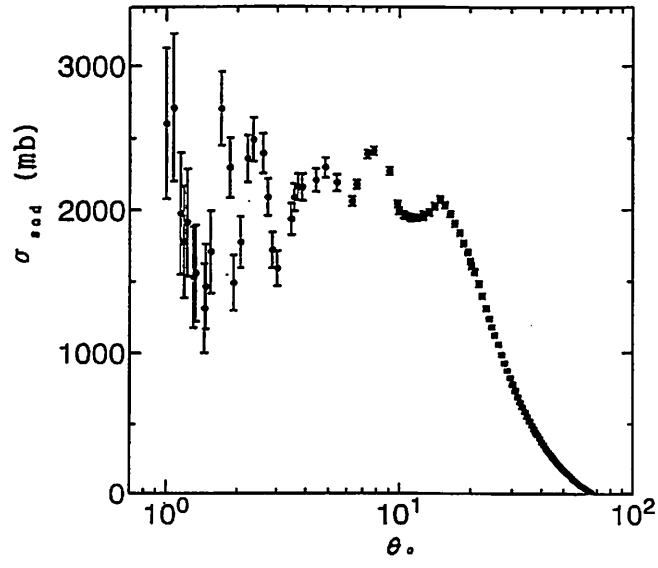

Fig. 7. The $\sigma_{SOD}(\theta_0)$ distribution as a function of θ_0.

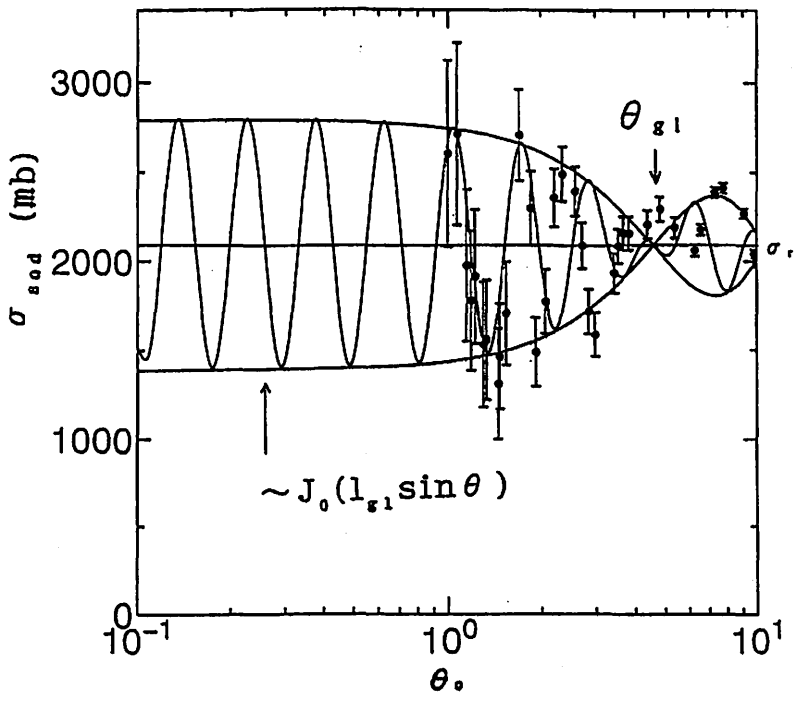

Fig. 8. The χ^2 fit of the GOT calculation for the SOD cross sections.

I. 3. Comparative Study of the (p,n) Reactions on ^{40}Ca and ^{40}Ar for the 1.6 MeV-State in the A=40 Isobar Triplet

Orihara H., Itoh K., Teramoto Y., Yamamoto A., Zhong G., Hosaka M., Terakawa A., Ishii K., Fujii Y., Nakagawa T.*, Miura K.**, and Ohnuma H.****

Cyclotron and Radioisotope Center, Tohoku University
*Department of Physics, Tohoku University**
*Tohoku Institute of Technology, Sendai 982, Japan***
*Department of Physics, Tokyo Institute of Technology, Tokyo 152, Japan** **

Charge independence of the nuclear force provide us corresponding information between mirror nuclei and that among isobar multiplets, while a number of discussions about charge symmetry breaking have been reported for details of the nuclear phenomena. The nuclei ^{40}K, ^{40}Ca(T=1) and ^{40}Sc form a family of the isobar triplet. In deed, the spin-parity of their ground state is 4^-, though except that no spin-parity assignments have been made for ^{40}Sc. Discussions for nuclear structure of ^{40}Sc have so far been based on that of well known ^{40}K or ^{40}Ca.

Supposing a double closed shell for ^{40}Ca, the (p,n) reaction on ^{40}Ca excites selectively $1\hbar\omega$ jump negative parity states, while that on ^{40}Ar primarily yields positive parity states. Thus, a comparative study of the (p,n) reaction on ^{40}Ar and ^{40}Ca may give us a complete set of nuclear structure of A=40 isobar triplets. The (p,n) reaction has provided us with information about spin-isospin, as well as isospin excitation modes in nuclei. One can selectively excite the spin-flip components in the (p,n) reaction at intermediate energies through the relatively strong spin-isospin effective interaction ($V_{\sigma\tau}$). Low energy (p,n) reactions, due to the strong spin non-flip isovector effective interaction (V_τ), give us equivalent information on both excitation modes. Moreover, it gives us a sufficient energy resolution to discuss (p,n) strength for individual nuclear levels[1,2], although exchange contributions are important at low energies. Various problems associated with the distorted-wave (DW) analysis of low-energy (p,n) data were discussed in detail by Ohnuma et al.[3]. It has been found possible to obtain basically the same information as that at intermediate energies if careful analysis including exchange terms is carried out.

In this report, we discuss mainly about the second excited state located around 1.6 MeV in A=40 nuclei[4], the spin-parity for which is assigned as 0^+ in ^{40}K, then this state should be weakly populated in the (p,n) reaction on ^{40}Ca, if this assignment is valid for ^{40}Sc too.

The experiment was carried out using a 35 MeV proton beam from the AVF cyclotron and the time-of-flight facilities[5,6] at the Cyclotron and Radioisotope Center at Tohoku University. A beam swinger system was used to measure angular distributions of emitted neutrons between 0° and 140° (lab).

The Ar target was argon gas enriched to 99 % in ^{40}Ar. The gas was contained in two types of gas cell. A drum-shaped cell having a longitudinal length of 2 cm was used for small-angle measurements ($\theta_{lab} \leq 30°$). The target for large-angle measurements ($\theta_{lab} \geq 30°$) was 20 cm long cylindrical cell to allow us to shield the neutron detectors against neutrons emitted from the window foils. The effective target thicknesses were of the order of 1 mg/cm^2, and overlap region of detection angles was used for relative normalization. The window material was metallic calcium foil for the drum-shaped cell, while it was Havar foil for the cylindrical cell, their thicknesses being ~10 mg/cm^2. Backgrounds due to the window materials did not give any serious problems because of the large Q-value difference. These backgrounds were measured in separate "empty runs", and subtracted from the data. The Ca target was a metallic foil of enriched ^{40}Ca prepared by vacuum evaporation. The thickness and enrichment of the target were, respectively, 2.0 mg/cm^2 and 99.9%.

Neutrons were detected by an array of twelve detectors, which were located at 44.3 m from the target and contained a total of 23.2 liters of NE213 scintillator. The detector efficiencies were obtained from Monte Carlo calculations for monoenergetic neutrons with $E_n \leq 34$ MeV. Absolute detector efficiencies were also measured by counting neutrons from the ^{7}Li(p,n)^{7}Be reaction and comparing its yield with the absolute neutron fluence determined by activation. They were in good agreement with the Monte Carlo calculations. Overall time resolution was typically 1.3 ns corresponding to 175, and 90 keV for the most energetic neutrons to ^{40}K and ^{40}Sc, respectively. Main contributions to the former resolution were attributed to the small Q-value in negative, and the energy loss and straggling of incident protons in the entrance-window of the target gas cell. Errors in the absolute scale of the cross sections were estimated to be less than 15%.

In Fig. 1, neutron excitation energy spectra are compared for the (p,n) reactions on ^{40}Ar and ^{40}Ca. Remarkable deferences are clearly seen; i. e. neutron spectrum begins at 1.6 MeV in the former, while it starts at the ground state in the latter as predicted by theoretical calculation by the shell-model and DW theories, which will be discussed later on. Figures 2 and 3 show experimental and theoretical cross sections for the transitions leading to the 1.6-MeV states in ^{40}K and ^{40}Sc, respectively. These for the transition to the IAS is also illustrated in Fig. 2 for comparison.

The cross-section data were compared with the DW results calculated by the computer code DWBA-74[7], which includes knock-on exchange effects in an exact manner. Optical potential parameters of Becchetti and Greenlees[8] were used for the entrance channel. Those for the exit channel were self-consistent potential parameters derived by Carlson et al.[9]. The effective nucleon-nucleon interactions used in the present DW analysis were those by Bertsch

et al. (M3Y)[10]. Spectroscopic amplitudes for the transition to the 0^+ state in ^{40}K were obtained from the *sdpf* shell-model calculations with the SDPFMW interaction[11] in the code OXBASH[12], assuming the configurations of $[\pi(f_{7/2}p)^{2,4}(f_{5/2}p)^{0,2}, \nu(sd_{5/2})^{16,16}(d_{3/2})^{2,4}]$ for both the initial and final states. That for the transition to the 1.6-MeV state in ^{40}Sc were obtained, assuming $\Delta J=1^-$ with $[\pi(fp)^{0,2}, \nu(sd)^{24,22}]$ and $[\pi(fp)^1, \nu(sd)^{-1}]$ for the initial and final states, respectively. Single-particle radial wave functions used in DW calculations were generated in a Woods-Saxon potential with r_0 = 1.25 fm, a = 0.6 fm, V_{LS} = 6 MeV and the depth adjusted to reproduce the binding energy of a valence nucleon.

Firstly, we discuss about the 1.64 MeV transition in the ^{40}Ar(p,n)^{40}K reaction, the angular distribution for which is shown in Fig. 2 together with theoretical predictions obtained by the DWBA calculation with transition amplitudes listed in Table 1. Also tabulated are those for the IAS transition leading to the 4.38-MeV state in ^{40}K. The latter indicates that the 1.64-MeV 0^+ state is the anti-analog state being orthogonal to the IAS. Cross section magnitudes and angular distribution shapes are well reproduced as shown in Fig. 2.

As for the ^{40}Ca(p,n)^{40}Sc reaction, we have identified the 1.69-MeV state to be due to a $\Delta J^\pi=1^-$ transition based on the shell-model and DW calculations. As shown in Figs. 3, the experimental cross section magnitudes, their angular distribution shape and its excitation energy are quite reasonably explained by the theoretical comparison. With a reasonable ground state correlation for ^{40}Ca mentioned above we have obtained transition amplitudes listed in Table 1. The cross sections thus obtained for the $\Delta J^\pi=0^+$ transition are two orders of magnitude smaller than those for $\Delta J^\pi=1^-$ as shown in Fig. 3. As such, we have assigned this transition to be $\Delta J^\pi=1^-$. The present result dose not reject the possibility of the existence of $J^\pi=0^+$ state in ^{40}Sc at $E_x\approx$2MeV, except that we will emphasize the existence of $J^\pi=1^-$ state.

In conclusion, by means of the comparative study of the (p,n) reactions on ^{40}Ar and ^{40}Ca, we have separately made clear the positive and negative parity states in A=40 asobar multiplets. Especially, we have located a $J^\pi=1^-$ state at E_x = 1.64 MeV in ^{40}Sc, and have observed the 0^+ anti-analog state by a charge-exchange reaction at E_x = 1.69 MeV in ^{40}K.

References

1) Orihara H. et al., NUCLEAR WEAK PROCESS AND NUCLEAR STRUCTURE, edited by Morita M. et al., (World Scientific Pub. Co. Pte. Ltd. and Yamada Science Foundation, 1989) p.336.
2) Kiang G. C. et al., Nucl. Phys. **A499** (1989) 339.
3) Ohnuma H. et al., Nucl. Phys. **A467** (1987) 61.
4) Endt P. M. Nucl. Phys. **A521** (1990)1.
5) Orihara H. and Murakami T., Nucl. Instrum. Methods **181** (1981) 15.
6) Orihara H. et al., Nucl. Instrum. Methods **A257** (198 7) 189.
7) Schaeffer R. and Raynal J., unpublished.
8) Becchetti F. D. and Greenlees G. W., Phys. Rev. **182** (1969) 1190.
9) Carlson J. D.,Zafiratos C. D. and Lind D. A., Nucl. Phys. **A249** (1975) 29.
10) Bertsch G., Borysowics J., McManus H. and Love W. G., Nucl. Phys. **A284** (1977) 399.
11) Wildenthal B. H., Phys. Rev. **C41** (1990) 1147.
12) The shell model code OXBASH, Echegoyen A. E., National Superconducting Cyclotron Laboratory Report No. 524 (1984).

Table 1. One body transition densities (OBTD).

Particle-Hole	$^{40}Ar(p,n)^{40}K$ reaction		$^{40}Ca(p,n)^{40}Sc$ reaction
	T=2, 0^+, #1 (4.384MeV, IAS)	T=1, 0^+, #1 (1.644MeV)	T=1, 0^+, #1
$\pi d_{5/2}, \nu d_{5/2}^{-1}$	-	-	-0.00287
$\pi s_{1/2}, \nu s_{1/2}^{-1}$	-	-	0.00171
$\pi d_{3/2}, \nu d_{3/2}^{-1}$	0.49140	-0.48943	0.08224
$\pi f_{7/2}, \nu f_{7/2}^{-1}$	0.35782	0.34697	-0.05505
$\pi f_{5/2}, \nu f_{5/2}^{-1}$	0.00106	-0.00060	0.00165
$\pi p_{3/2}, \nu p_{3/2}^{-1}$	0.00111	-0.00052	-0.00301
$\pi p_{1/2}, \nu p_{1/2}^{-1}$	0.00022	-0.00001	-0.00155

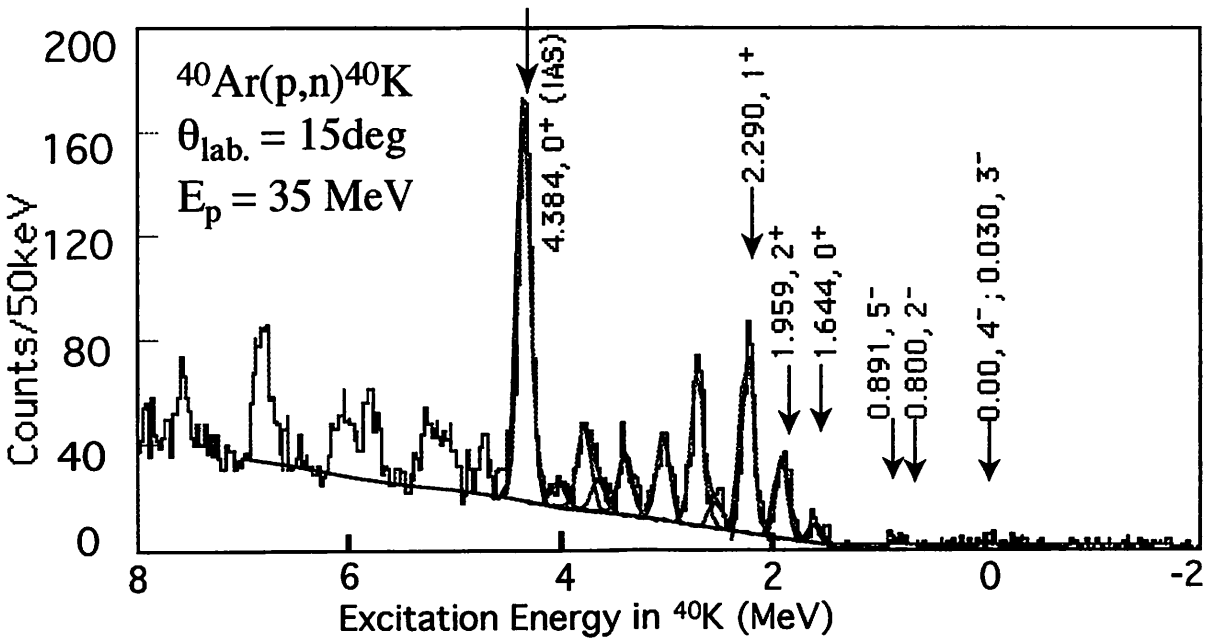

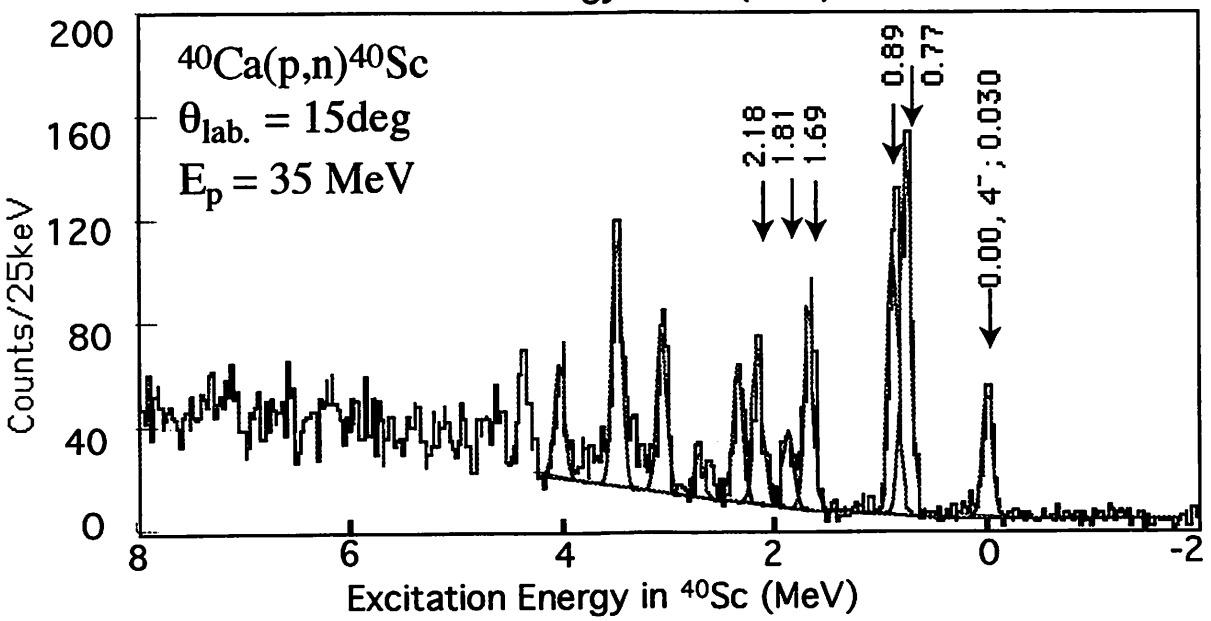

Fig. 1. Excitation energy neutron spectra for the (p,n) reactions on ^{40}Ar and ^{40}Ca.

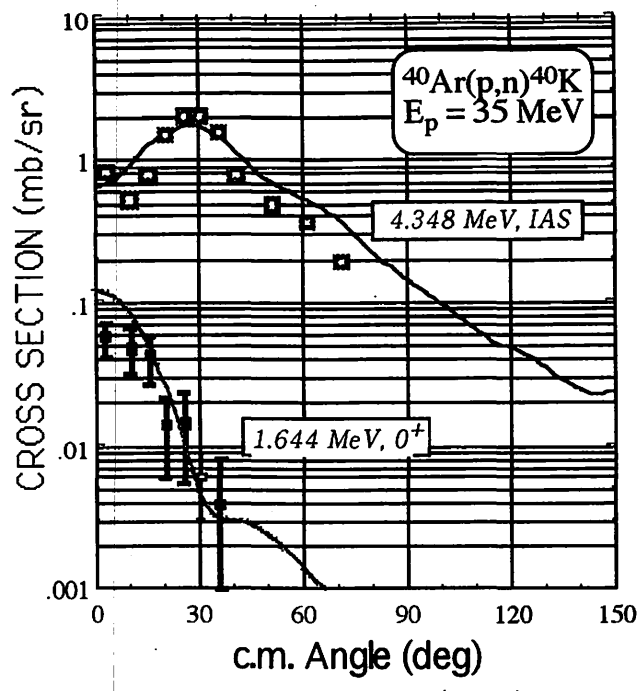

Fig. 2. Experimental and theoretical cross sections for the $0^+ \rightarrow 0^+$ transitions to IAS and to the 1.644-MeV state in ^{40}K.

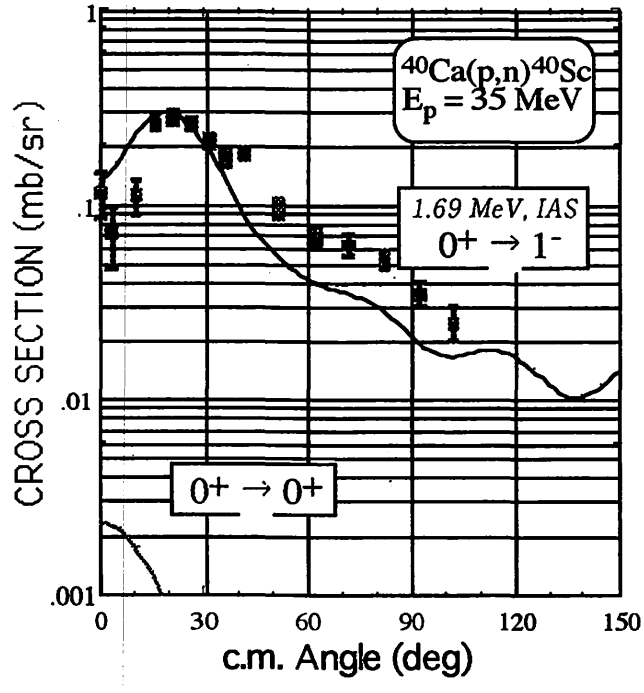

Fig. 2. Experimental and theoretical cross sections for the $0^+ \rightarrow 1^-$ transitions to the 1.69-MeV state in ^{40}Sc. The theoretical prediction for the $0^+ \rightarrow 0^+$ transition is also plotted for comparison.

I. 4. Negative Parity States in ^{40}Sc Observed in the (p,n) Reaction on ^{40}Ca

Itoh K., Orihara H., Teramoto Y., Yamamoto A., Zhong G., Terakawa A., Ishii K., Fujii Y., Nakagawa T.*, and Ohnuma H.***

Cyclotron and Radioisotope Center, Tohoku University
*Department of Physics, Tohoku University**
*Department of Physics, Tokyo Institute of Technology, Tokyo 152, Japan***

The (p,n) reaction has provided us with information about spin-isospin, as well as isospin excitation modes in nuclei. One can selectively excite the spin-flip components in the (p,n) reaction at intermediate energies through the relatively strong spin-isospin effective interaction ($V_{\sigma\tau}$). Low energy (p,n) reactions, due to the strong spin non-flip isovector effective interaction (V_{τ}), give us equivalent information on both excitation modes. Moreover, it gives us a sufficient energy resolution to discuss (p,n) strength for individual nuclear levels[1,2], although exchange contributions are important at low energies. Various problems associated with the distorted-wave (DW) analysis of low-energy (p,n) data were discussed in detail by Ohnuma et al.[3] It has been found possible to obtain basically the same information as that at intermediate energies if careful analysis including exchange terms is carried out.

Like the cases of ^{16}F, ^{20}Na, ^{28}P, ^{32}Cl and ^{36}K, the nuclear structure of ^{40}Sc is not well known . Spectroscopic study for these nuclei have so far been carried out mainly by limited measurements for β-decay. As for ^{40}Sc, several excited states have been reported, but the spin-parities for them are not known except for the case of the ground state. The (p,n) reaction on N=Z nuclei, especially that with 35-MeV protons, gives us a good place for probing the structure of these nuclei[2].

Since the target nucleus of ^{40}Ca is one of the double closed shell nuclei, the present prominent excitations are $1\hbar\omega$ jump negative parity transitions. In this report, a number of negative parity states are proposed together with their spectroscopic nature based on the microscopic DW analysis with the shell-model transition densities.

The experiment was carried out using a 35 MeV proton beam from the AVF cyclotron and the time-of-flight facilities[4] at the Cyclotron and Radioisotope Center at Tohoku University. A beam swinger system was used to measure angular distributions of emitted neutrons between 0° and 110° (lab). The target was a metallic foil of enriched ^{40}Ca prepared by vacuum evaporation. The thickness and enrichment of the target were, respectively, 2.0 mg/cm^2 and 99.9%.

Neutrons were detected by an array of twelve detectors, which were located at 44.3 m from the target and contained a total of 23.2 liters of NE213 scintillator. The detector efficiencies were obtained from Monte Carlo calculations for monoenergetic neutrons with $E_n \leq 34$ MeV. Absolute detector efficiencies were also measured by counting neutrons from the $^7Li(p,n)^7Be$ reaction and comparing its yield with the absolute neutron fluence determined by activation. They were in good agreement with the Monte Carlo calculations. Overall time resolution was typically 1.3 ns corresponding to 90 keV for the most energetic neutrons. Errors in the absolute scale of the cross sections were estimated to be less than 15%, and those for the excitation energy were ±15keV. Further experimental details have been given in a previous report[5].

Typical neutron spectra measured for the $^{40}Ca(p,n)^{40}Sc$ reaction at a laboratory angle 40° are shown in Fig. 1 together with peak-fitting results. In the figure, the levels corresponding to the peaks at 2.18, 3.05 and 4.04 MeV are newly observed. In Fig. 2, the angular distributions of emitted neutrons leading to the 2.18, 2.38 and 3.05-MeV states, spin-parities for which have been newly assigned to be, respectively, 0^-, 4^- and 3^-. Curves in the figure are theoretical comparisons described later on.

The cross-section data were compared with the DW results calculated by the computer code DWBA-74[6], which includes knock-on exchange effects in an exact manner. Optical potential parameters of Becchetti and Greenlees[7] were used for the entrance channel. Those for the exit channel were self-consistent potential parameters derived by Carlson et al.[8] The effective nucleon-nucleon interactions used in the present DW analysis were those by Bertsch et al. (M3Y)[9]. Spectroscopic amplitudes for the negative parity transition to ^{40}Sc were obtained from the *sdpf* shell-model calculations with the SDPFMW interaction[10] in the code OXBASH[11], assuming the configurations of $[\pi(fp)^{0,2}, \nu(sd)^{24,22}]$ and $[\pi(fp)^1, \nu(sd)^{-1}]$ for the initial and final states, respectively. Single-particle radial wave functions used in DW calculations were generated in a Woods-Saxon potential with $r_0 = 1.25$ fm, $a = 0.6$ fm, $V_{LS} = 6$ MeV and the depth adjusted to reproduce the binding energy of a valence nucleon.

In Fig. 3, the present results are compared, for the excitation energies, with the recent compilation by Endt[12] and with shell-model calculation. One of the striking features is the assignment for the 1.69-MeV state. We have identified this prominent transition to be $\Delta J^\pi = 1^-$ state based on the shell-model and DW calculations as discussed separately in Ref. 13 in this issue.

The transition leading to the 2.18-MeV state may be $\Delta J^\pi = 0^-$, then it carries the intrinsic pionic quantum number, and is highly sensitive to the effective isovector tensor interaction. Cross sections are absolutely fitted by the theoretical prediction as shown in Fig. 2. Orihara et al. have reported for observation of the $\Delta J^\pi = 0^-$ transitions in the (p,n) reactions on ^{16}O[14], and on ^{13}C and $^{14,15}N$[15]. In the angular distribution in Fig. 2, the shoulder at ~50° gives a measure for the tensor force contribution. Comparison with those for p-shell

nuclei, the tensor interaction is less important like the case of the $1/2^- \rightarrow 1/2^+$ transition in the $^{13}C(p,n)^{13}N$ reaction.

The second 4^- state, the first being the ground state, has been located at 2.38 MeV. Magnitudes of the cross section together with their shape are in excellent agreement with the calculations as illustrated in Fig. 2. The theoretical predictions locate a prominent 3^- transition around 3.5MeV, an candidate for which is that to the 3.09-MeV state. Though we need a rather small normalization factor of 0.4 to fit the data, the cross sections are well reproduced in their angular distribution shape.

Figure 3 summarize the present results. In conclusion, a number of isovector spin and spin non-flip transitions have been observed in the high-resolution measurement for the $^{40}Ca(p,n)^{40}Sc$ reaction at 35 MeV. Almost all prominent transitions, predicted by the DWBA using transition densities calculated with the recent shell model, have experimentally observed.

Acknowledgment

The authors thank Mr. M. Katoh for his help in the preparation of ^{40}Ca target.

References

1) Orihara H. et al., NUCLEAR WEAK PROCESS AND NUCLEAR STRUCTURE, edited by Morita M. et al., (World Scientific Pub. Co. Pte. Ltd. and Yamada Science Foundation, 1989) p.336.
2) Kiang G. C. et al., Nucl. Phys. **A499** (1989) 339.
3) Ohnuma H. et al., Nucl. Phys. **A467** (1987) 61.
4) Orihara H. and Murakami T., Nucl. Instrum. Methods **181** (1981) 15.
5) Orihara H. et al., Nucl. Instrum. Methods **A257** (198 7) 189.
6) Schaeffer R. and Raynal J., unpublished.
7) Becchetti F. D. and Greenlees G. W., Phys. Rev. **182** (1969) 1190.
8) Carlson J. D.,Zafiratos C. D. and Lind D. A., Nucl. Phys. **A249** (1975) 29.
9) Bertsch G., Borysowics J., McManus H. and Love W. G., Nucl. Phys. **A284** (1977) 399.
10) Wildenthal B. H., Phys. Rev. **C41** (1990) 1147.
11) The shell model code OXBASH, Echegoyen A. E., National Superconducting Cyclotron Laboratory Report No. 524 (1984).
12) Endt P. M. Nucl. Phys. **A521** (1990)1.
14) Orihara H. et al., CYRIC Annual Report 1994, in this issue.
13) Orihara H. et al., Phys. Rev. Lett. **49** (1982) 1318.
14) Orihara H. et al., Phys. Lett. **187** (1987) 240.

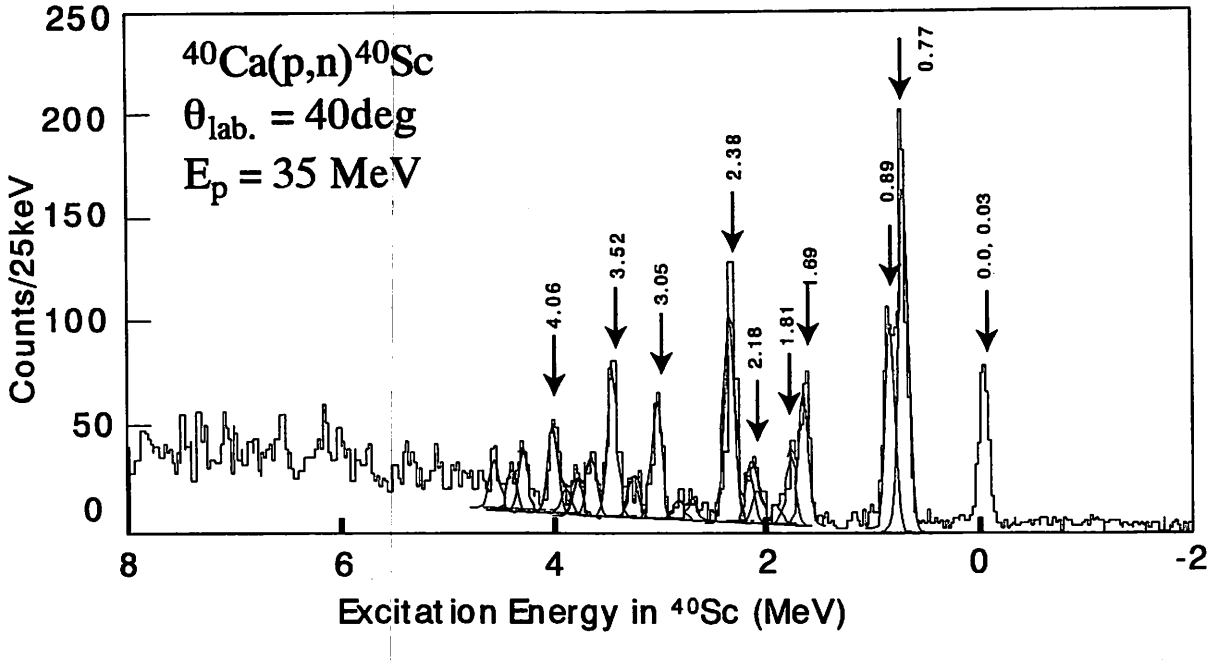

Fig.1. A sample energy spectrum for the ^{40}Ca(p,n)^{40}Sc reaction taken at 40^{o} with a flight path of 44.3 m. Energy per bin is 25 keV.

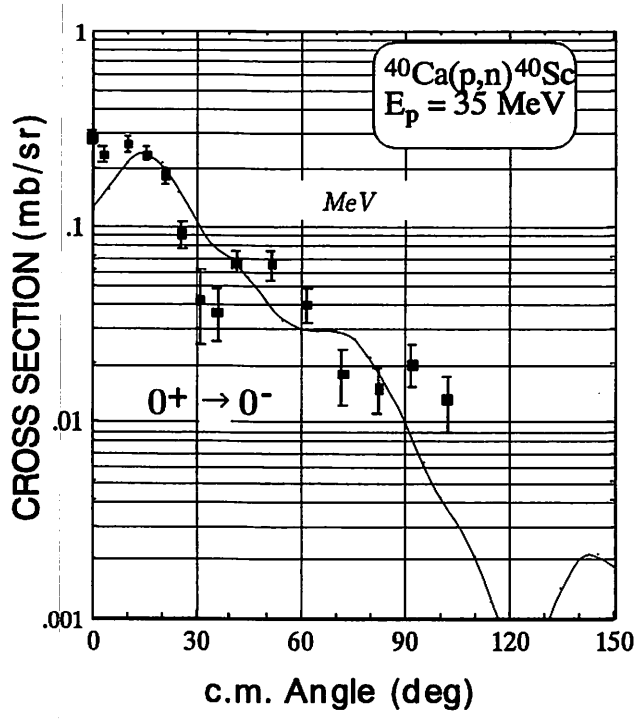

Fig. 2. Experimental and theoretical cross sections for the $0^+ \rightarrow 0^-$ transitions to the 2.18-MeV state in ^{40}Sc.

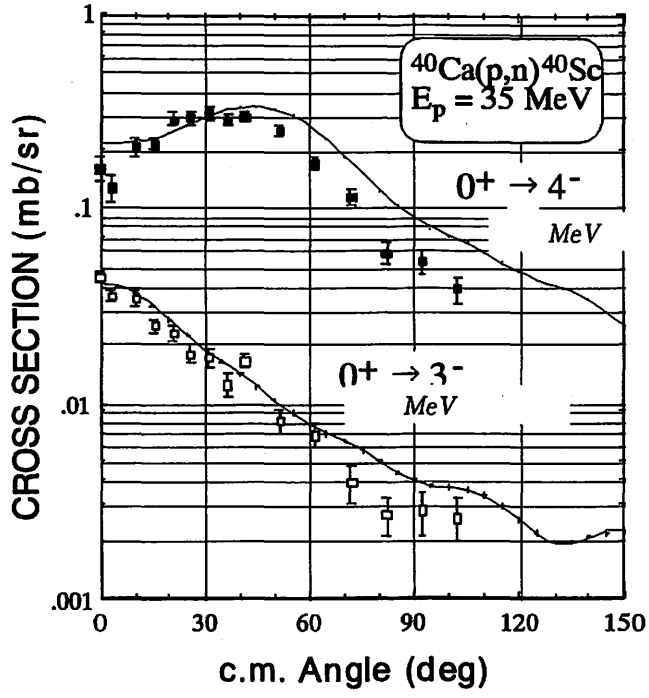

Fig. 2. Experimental and theoretical cross sections for the $0^+ \rightarrow 4^-$ transitions to 2.38-MeV, and for the $0^+ \rightarrow 3^-$ transitions to 3.05-MeV states in ^{40}Sc.

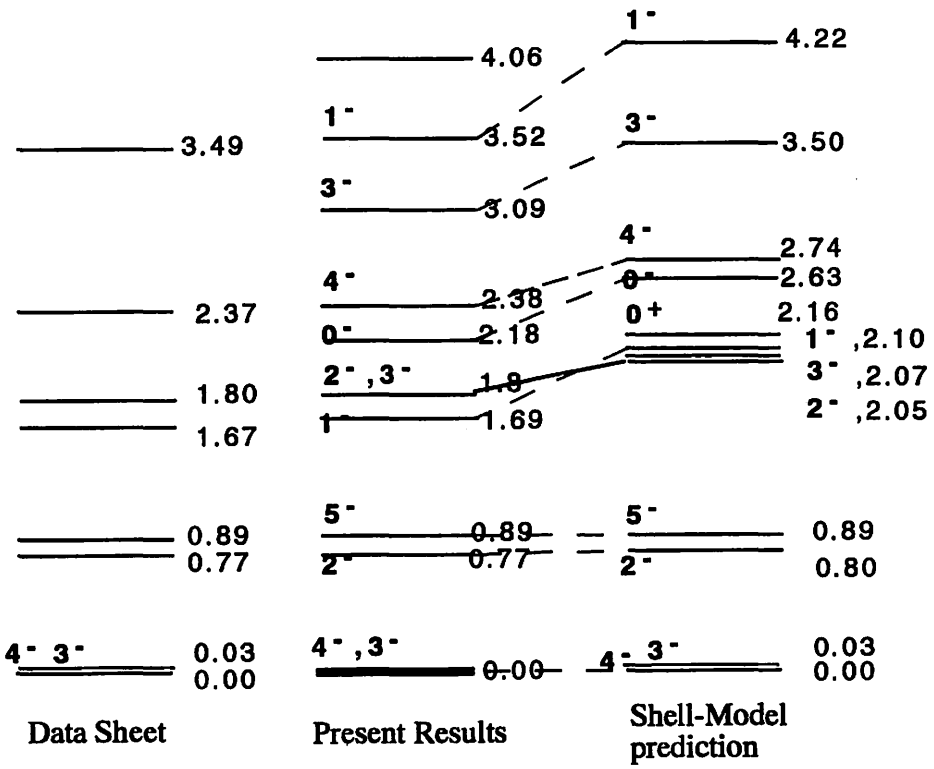

Fig. 3. Experimental and theoretical level diagram for ^{40}Sc. That from the compilation is also shown in the left side of the figure for comparison.

I. 5. Nuclear g-Factor of the 1579 keV 3⁻ Isomer in ^{146}Gd and the Paramagnetic Correction Factor of the Gd Ions in Samarium Oxide

Kawamura N. , Kimura Y.**, Watanabe A.***, Fujita M.***, Shinozuka T.****, and Fujioka M.****

Faculty of Engineering, Aomori University,*
*Department of Physics, Faculty of Science, Tohoku University***
*Cyclotron and Radioisotope Center, Tohoku University****

The first 3⁻ excited states for doubly even N=82 nuclei with 54≤Z≤64 are considered as octupole excitations between orbits $2d_{5/2}$ and $1h_{11/2}$[1]. The wave functions obtained from a calculation of the particle-core coupling[2] also show a nearly pure $\pi[(2d_{5/2})^{-1}(1h_{11/2})^{1}]_{3^-}$ character. On the other hand the half-life of the 3⁻ level in ^{146}Gd found to be 1.06(12) ns[3] corresponds to an E3 strength of 37 Weisskopf units for the transition from the 3⁻ isomer to the 0⁺ ground state. This indicates a feature of the collective motion rather than the single particle.

The nuclear g-factor may provide useful information to study the excitation mechanism of the 3⁻ states. However there are no experimental data, only the g-factor of the 3⁻ isomer in ^{146}Gd is known to be 0.7(3)[4], and it is difficult to draw a conclusion from the value due to the relatively large error. We therefore have been remeasured the nuclear g-factor of the 1549 keV 3⁻ isomer in ^{146}Gd using the ^{144}Sm(α,2n)^{146}Gd reaction and the time-integral perturbed angular distribution (TIPAD) method for in-beam γ-rays. The ^{146}Gd nuclei were populated by the ^{144}Sm(α,2n)^{146}Gd reaction using an α-beam of 23.5 MeV from the CYRIC cyclotron. The beam energy was determined by excitation-function measurements so as not to disturb the TIPAD of the 3⁻ isomer by the excitation of levels lying above 1579 keV. An enriched $^{144}Sm_2O_3$ target of 11 mg/cm^2 thickness was placed in an external magnetic field of ±1.81(1) T applied perpendicularly to the beam-detector plane.

The time-integral perturbed angular distributions(TIPAD) of the 1579 keV in-beam γ-rays emitted from the 3⁻ isomer were measured with a 230 cm^3 HPGe detector at seven angles between 64 and 130 degrees.

The TIPAD data were fitted to an expression:

$$W(\theta \pm B_{eff}) = A_0 + \sum_n A_n P_n \cos\left[n(\theta \mp \theta_n)\right]; \quad (n = 2 \text{ and } 4),$$

where $\Delta\theta_n$ is the angular shift due to the Larmor precession, and given by the Larmor angular velocity ω and mean life τ as

$$\Delta\theta_n = (1/n)\tan^{-1}(n\,\omega\,\tau); \quad (n=2 \text{ and } 4).$$

The results of the least-squares fits are shown in table 1.

The nuclear g-factor is deduced from the Larmor angular velocity ω as

$$g=\hbar\omega/\mu_N B_{eff},$$

where μ_N is the nuclear magneton and B_{eff} is the effective magnetic field at the site of Gd nuclei in the target.

The effective magnetic fields for rare-earth ions are quite different from the external field B_{ext} by the large paramagnetic effect[5]. The B_{eff} is written as

$$B_{eff} = \beta\, B_{ext},$$

where β is the paramagnetic correction factor.

In order to deduce the g-factor from the experimental $\Delta\theta_n$ of the TIPAD, another experiment was carried out to obtain the β for Gd nuclei in the Sm_2O_3 target. We took the 2982 keV 7^- isomer with the half-life of 6.7(2) ns[3] in ^{146}Gd of which the g-factor was known[4,6,7]. TIPADs similar to those for 1579 keV γ-ray were measured at $B_{ext}=\pm1.21(1)$ T for the 324 keV γ-ray from the transition between the 2982 keV 7^- and the 2658 keV 5^- levels.

The least-squares results of the TIPAD of the 324 keV γ-ray are also listed in table 1. A strong attenuation of the A_2 coefficient for the 324 keV γ-ray is observed. It may be due to a rapid relaxation of the alignment and is responsible for errors of the $\omega\tau$ and consequently of the β.

Using a weighted-mean g-factor, $g(7^-)=1.251(23)$, of refs. 4, 6 and 7, we have deduced the paramagnetic correction factor to be

$$\beta = 0.59\ (11)$$

from the $\omega\tau$ in the table 1 and $B_{ext}=1.21(1)$T From a comparison between the present β and theoretical values[5] it is suggested that the Gd ions populated in Sm_2O_3 by nuclear reactions are in a mixed ion state with valence values of 3 and 4.

Using the present β the g-factor of the 3^- isomer is obtained to be

$g(3^-$ in ^{146}Gd) = 1.00(22).

The major part of the error is caused by that of the β.

Possible configurations for a low-lying 3^- state in ^{146}Gd are listed in table 2 together with expected g-factors which were calculated using experimental g-factors for single-particle(or hole) components[8]. The present result is in good agreement with the expected g-

factor for $\pi[(2d_{5/2})^{-1}(1h_{11/2})^{1}]_{3^-}$ configuration, which indicates that the 3^- isomer in ^{146}Gd has this configuration as a main component. However, the enhancement of the E3 transition from the isomer to ground state suggests also a possibility of a coherent mixture of many one particle one hole excitations due to the existence of the ground state correlations[9]. These correlations may be responsible for the enhancement of the electromagnetic transition rates.

References

1) Bohr A. and Mottelson B. R., Nuclear Structure Vol II, Benjamin, (1975).
2) Enghardt W., Kaubler L., Prade H., Keller H.- J. and Stary F., Nucl. Phys. **A449** (1986) 417).
3) Kleinheinz P., Ogawa M., Broda R., Daly P. J., Haenni D., Beuscher H. and Kleinrahm A., Z. Phys. **A286** (1978) 27.
4) Keitel R., Bertschat H.H., Butt R., Grawe H., Haas H., Dahm D., Klaumunzer S., Menningen M., Sielemann R. and Zeit W.-D, Z. Phys. **A290** (1979) 229.
5) Gunther C. and Lindgren I., Perturbed Angular Correlations, ed. Karlsson E., Mattias E. and Siegbahn K. (North-Holland, Amsterdam, 1964) p.356.
6) Hausser 0., Taras P., Trautmann W., Ward D., Alexander T.K., Andrews H. R., Haas B. and Horn D., Phys. Rev. Lett. **42** (1979) 1451.
7) Faestermann T., Bohn H., Feilitzsch F.v. and Sunyar A.W., Phys. Lett. **80B** (1979) 190.
8) Raghavan P., Atomic Data and Nuclear Data tables **42** (1989),189.
9) Rowe D. J., Nuclear Collective Motion, Methuen, (1970).

Table 1. Experimental results of TIPADs.

Isomer[keV, J^{π}, τ (ns)]	A2	A4	$\omega\tau$ (rad)
[1579, 3^-, 1.06(12)]	0.43(3)	0.046(29)	-0.0824(58)
[2982, 7^-, 6.7(2)]	0.087(32)	0.035(30)	-0.413(79)

No corrections were made for A2 and A4 coefficients.

Table 2. Expected g-factors for possible configurations.

configuration	g(expected)	g(s.p/s.h)
$\pi(2d_{5/2}{}^{1}h_{11/2})_{3^-}$	1.167(5)	$g(\pi d_{5/2})$=1.481(1)[a]
		$g(\pi h_{11/2})$=1.288(3)[a]
$\pi(2g_{7/2}{}^{1}h_{11/2})_{3^-}$	1.437(11)	$g(\pi g_{7/2})$=0.80(1)[b]
		$g(\nu f_{7/2})$=-0.304[c]
$\nu(3s_{1/2}{}^{2}f_{7/2})_{3^-}$	-0.304(2)	$g(\nu s_{1/2})$=-1.54[d]

a) taken from $g(5/2^+)$ and $g(11/2^-)$ of $^{145,147,149}Eu$[8]
b) $g(7/2^+)$ of ^{141}Pr[8]
c) $g(7/2^-)$ of ^{143}Nd[8]
d) $g(1/2^+)$ of ^{133}Ba[8]

I. 6. Half-Life Measurement of the 105.9 keV 2+ State of Neutron Deficient $^{178}_{74}W_{104}$ Isotope

Fujita M., Shinozuka T., Watanabe A., Kimura Y., Kanai Y.**, Fujioka M.*, and Sugai I.****

Department of Physics, Tohoku University
*CYRIC, Tohoku University**
*Department of Nuclear Engineering, Tohoku University***
Institute for Nuclear Study, University of Tokyo

In the deformation region, the nuclear intrinsic E2 moments show larger values than the theoretical estimations calculated from the spherical shell model. This is the result of collective motion of nuclei, and it can be understood by applying the Nilsson model which considers the shape of a nucleus to be deformed. The deformed nuclei are expected to have rotational bands, and fast electric quadropole radiation (E2 transition) should be observed.

In the case of $2^+ \rightarrow 0^+$ transition, the relation between the reduced transition probability B (E2; $2^+ \rightarrow 0^+$) (e^2fm^4) and the intrinsic E2 moment Q' (fm^2) is

$$B(E2;2^+ \rightarrow 0^+) = \frac{1}{16\pi} e^2 Q'^2 .$$

We define δ as the deformation parameter, and its definition is

$$\delta \equiv \frac{R_z - R_x}{R_0} = \frac{5}{4ZR_0^2} Q' .$$

The R_z', and R_x' are the radius along the symmetrical axis of deformation and the radius along the axis perpendicular to the symmetrical axis, respectively. The R_0 is the radius when the nucleus is spherical, and we use $R_0 = 1.2\, A^{1/3}$ (fm).

Then the deformation parameter δ can be written by using the mean life-time τ (ns) of the 2^+ state as

$$\delta = \frac{5}{4ZR_0^2}\left(\frac{16\pi}{1.22E_\gamma^5 \tau(1+\alpha)} \times 10^{-9}\right),$$

where Z and α denote the atomic number and the internal conversion coefficient, respectively. The units of E_γ and R_o are MeV and fm. We can deduce the deformation parameter from experimental half-life of the first 2^+ state using this equation.

The ^{178}W is in the nuclear deformation region and its neutron number N is 104. The number 104 means the neutron mid-shell between the 82 and 126 magic numbers. So far, the experimental data from ^{186}W to ^{180}W have shown the tendency that the deformation becomes larger towards the neutron mid-shell (see table 1). Therefore, the life-time measurement of the $2^+ \rightarrow 0^+$ transition at $^{178}W^{104}$ is impotant to discuss the deformation in this region.

The half-life measurement of the first 2^+ state of ^{178}W has different and difficult situations from those of heavier tungsten nuclei, ^{180}W, ^{182}W and so on. The measurements for the heavier tungstens could utilize population to the excited 2^+ states from the β^--decay of Ta isotopes having long half-lives (several hrs). On the other hand, the 2^+ state of ^{178}W can only be fed from the β^+-decay of ^{178}Re having a short half-life (13.4 min). Therefore, the on-line mass separation is crucial to prepare purified samples under low back-ground conditions. It has been, however, hardly possible for the conventional on-line mass separation techniques to obtain the refractory Re radioisotopes with any type of ion sources.

The Ion Guide method is one of the breakthrough techniques to mass-separate on-line the refractory elements Re, W, and Hf etc. . With the CYRIC-IGISOL, we could obtain the mass-separated ^{178}Re of intensity of 3,000 atoms/sec by the $^{180}W(p, 3n)^{178}Re$ reaction with an enriched ^{180}W (93.1 %) target.

The measurement of the life-time for of 2^+ state of ^{178}W has been done by a γ-γ coincidence method and a γ-conversion electron coincidence method for the $4^+ \rightarrow 2^+$ transition and the $2^+ \rightarrow 0^+$ transition of ^{178}W.

Two BaF_2 scintilators have been used in the γ - γ coincidence and a BaF_2 and a plastic scintillator have been used in the γ-conversion electron coincidence. The time spectrum of the γ-γ coincidence measurement is shown in Fig.1. From these measurements, the fitted half-lives of the first 2^+ state of ^{178}W are 0.900 ± 0.014 ns and 0.947 ± 0.055 ns, respectively. We have thus deduced the half-life of the first 2^+ state of ^{178}W as 0.903 ± 0.014 ns as the weighted average of γ - γ and γ-conversion electron coincidence experiments.

The deformation parameter obtained from this experiment is δ=0.285 ± 0.002. It shows that the deformation of ^{178}W is larger than those of the hevier W isotopes. It is interesting to examine whether more neutron deficient tungsten isotopes beyond the neutron mid-shell have larger deformations or not.

Reference

1) Lederer C. M. and Shirly V. S., Table of Isotopes 7th edition, Wiley- interscience.

Table 1 : deformation parameters and related values of W isotopes. The data of ^{180,182,184,186}W are taken from Ref. 1.

A	E_γ	α	$t_{1/2}$ (ns)	$B(\mathrm{E2})$ $(e^2\mathrm{fm}^4)$	Q' (fm^2)	δ
178	0.1059	3.03	0.903(14)	11728(181)	767.8(6.0)	0.285(2)
180	0.10365	3.29	1.17(3)	9463(242)	689.7(8.8)	0.254(3)
			1.19(4)	9304(323)	683.9(11.5)	0.252(4)
			1.22(3)	9075(223)	675.4(8.3)	0.249(3)
			1.33(5)	8324(313)	646.9(12.2)	0.238(4)
			1.37(3)	8082(177)	637.4(7.0)	0.235(3)
182	0.1001	3.77	1.26(4)	9398(298)	687.3(10.9)	0.251(3)
			1.32(3)	8971(204)	671.5(7.6)	0.245(3)
			1.38(2)	8581(124)	656.7(4.8)	0.240(2)
184	0.1112	2.50	1.252(14)	7617(85)	618.8(3.5)	0.224(1)
			1.24(4)	7691(248)	621.8(10.0)	0.225(4)
186	0.1225	1.73	1.01(4)	7463(296)	612.5(12.1)	0.220(4)
			1.04(1)	7275(70)	604.7(2.9)	0.218(1)
			1.12(2)	6730(120)	581.6(5.2)	0.209(2)

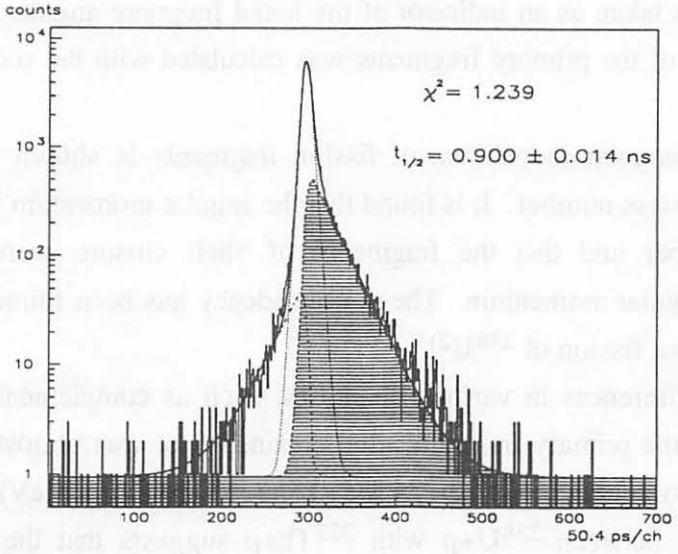

Fig.1. Time spectrum measured by the γ - γ coincidence method.

I. 7. Angular Momentum of Fission Products in ^{232}Th+p System (II)

Kudo H., Saito D., Yasuda K., Fujioka M., Shinozuka T.*, and Fujita M.**

Faculty of Science, Niigata University, Niigata Japan
*Cyclotron and Radioisotope Center, Tohoku University **

The angular momentum of the fission fragment is important to understand fission process, because it provides information on the scission point configuration and on the mechanism of angular momentum transfer from fissioning nucleus to fission fragments. Several methods have been applied to the determination of angular momenta of fission fragments. In the present work, the isomeric yield ratios of fission products were measured for the evaluation of angular momenta of primary fission fragments.

Isomeric yield ratio of 24 fission products in the system of 24 MeV proton-induced fission of ^{232}Th were measured by the use of IGISOL. The yields of fission products were determined by a gamma-ray spectrometry. The obtained isomeric yield ratios were converted to the angular momenta of primary fission fragments by assuming a statistical spin distribution,

$$P(J)=P_0(2J+1)\exp(-J(J+1)/\langle J^2\rangle),$$

The $J_{rms}=\langle J^2\rangle^{1/2}$ was taken as an indicator of the initial fragment angular momentum. The de-excitation process of the primary fragments was calculated with the modified GROGI-II code[1].

The obtained angular momentum of fission fragments is shown in Figure 1 as a function of fragment mass number. It is found that the angular momentum increased with the fragment mass number and that the fragments of shell closure were found to have considerably small angular momentum. The same tendency has been found in the system of 24 MeV proton-induced fission of ^{238}U[2].

Despite the differences in various quantities, such as complementary fragment and available energies of the primary fragments, the obtained J_{rms} was almost the same for the same nuclide in both systems of ^{238}U+p (24 MeV) and ^{232}Th+p (24 MeV) as seen in Figure 2. This comparison between ^{238}U+p with ^{232}Th+p suggests that the fragment angular momentum is not affected by the fission system but by the nature of individual fragment or by the mode of fission[3].

References

1) Grover J. R. and Gilat J., Phys. Rev. **157**, (1967) 802.
2) Tanikawa M., et al., Z. Phys. **A 347**, (1993) 53.
3) Kudo H. et al., Radiochim. Acta, in print.

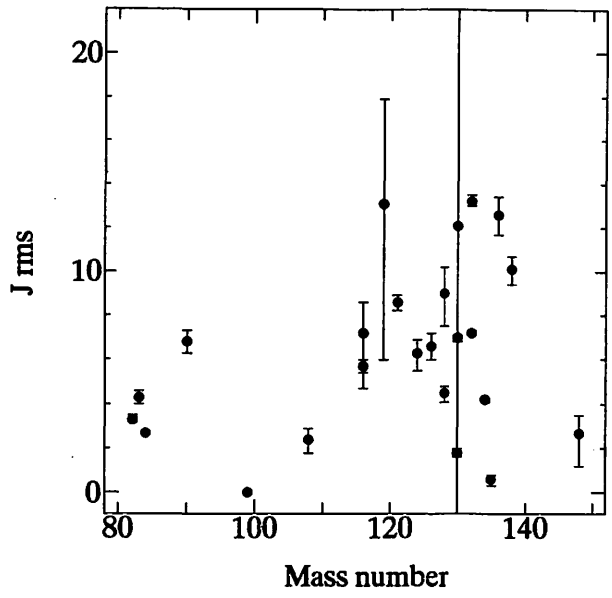

Fig. 1. Deduced J_{rms} of fission products produced in 24 MeV protons on ^{232}Th.

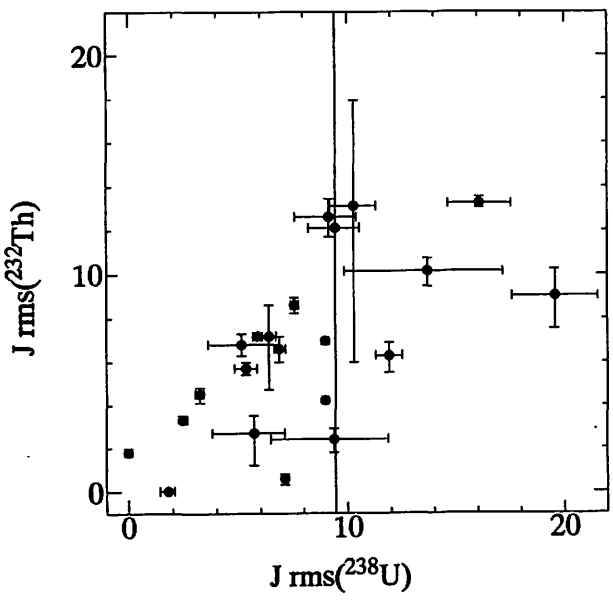

Fig. 2. Comparison of J_{rms} between ^{238}U+p (24 MeV) and ^{232}Th+p(24 MeV) systems.

I. 8. An $^{56}Fe(d, p)^{57}Fe$ Mössbauer Measurement

*Nasu S. and Hanada R.**

Department of Material Physics, Faculty of Engineering Science, Osaka University
*Institute for Material Research, Tohoku University**

Introduction

It is well recognized that the Mössbauer spectroscopy is one of the powerful technique to study physical and chemical properties of solids through the hyperfine interactions of probe nuclei embedded in solids. Especially the ^{57}Fe Mössbauer spectroscopy has been applied to many research fields, because iron is an important element in material research and the resonant gamma-ray photon of ^{57}Fe has a quite narrow line width. Narrow line width of the resonant gamma-ray of ^{57}Fe is identical to an extremely high energy resolution in the range of nano eV and make it possible to detect the ultra-small energy-shifts like a gravitational red-shift of photon. Generally for the ^{57}Fe Mössbauer measurements, gamma-ray from ^{57}Co in Rh matrix which is relatively long-lived radioactive isotope and a mother nucleus of ^{57}Fe has been used as a photon source. To perform the Mössbauer spectroscopy the rather large facilities are not necessary in general and many researchs in material science have been performed in rather small size laboratories.

However, recent development and progress in the synchrotron radiation facility and its use for research in natural science show clearly the possibility to perform nuclear excitation experiments with synchrotron radiation. In fact, the new research field has been opened and started for the nuclear excitation experiments with synchrotron radiation. Nuclear excitation with synchrotron radiation should be performed in-beam condition, in which the coherent excitation and the subsequent de-excitation of the resonant nucleus have been detected simultaneously. In-beam Mössbauer spectroscopy using a short-lived radioactive isotope produced by a nuclear reaction in accelerator is also a technique to perform the simultaneous excitation and the detection of de-excitation photon from resonant nucleus. In-beam Mössbauer spectroscopy has many advantages for material research, since the method is principally source experiment in which nuclear excitation and de-excitation occurred simultaneously. These methods make it possible to perform some experiments which have not been possible in a conventional Mössbauer spectroscopy using a long-lived radioactive isotope.

In this letter, we present a brief description what kinds of in-beam Mössbauer spectroscopy are available now and preliminary results obtained by an $^{56}Fe(d, p)^{57}Fe$ reaction at CYRIC of Tohoku University.

In-Beam Mössbauer Spectroscopy

It is well known that the Mössbauer spectroscopy is related to the recoilless nuclear resonant absorption and emission of gamma-rays and its experiment has been performed using a combination of gamma-ray source and absorber or scatterer. In a conventional Mössbauer spectroscopy long-lived radioactive isotope embedded in standard material like Rh has been used as a gamma-ray source and a probe nucleus in the specimen is used as an absorber and/or scatterer. Such long-lived radioactive isotope was originally produced by the nuclear reaction using accelerators and/or nuclear reactor. Since the long lifetime of the isotope it is possible to use the gamma-ray source as off-line source from accelerator for the Mössbauer measurements. When the lifetime of the gamma-ray source is quite short, it is always necessary to perform the on-line measurements in which the creation of the source by the nuclear reaction and the detection of the resonance should be performed simultaneously.

One can define the in-beam Mössbauer spectroscopy as an Mössbauer spectroscopy by simultaneous creation of Mössbauer levels and detection of the resonant absorption or scattering using accelerator beams. Nuclear excitation of the Mössbauer levels with synchrotron radiation from the electron or positron storage-ring may be one of the in-beam Mössbauer spectroscopy because of its on-line measurement. From the above discussion, there are two distinguishable methods for the in-beam Mössbauer spectroscopy. One is an in-beam Mössbauer spectroscopy with synchrotron radiation and the other is the spectroscopy using accelerator like cyclotron. Following reactions have been reported for the in-beam Mössbauer spectroscopy using accelerators.

(1) $^{54}Cr(\alpha, p; \alpha, p\gamma)^{57}Mn \rightarrow {}^{57}Fe$
(2) $^{56}Fe(n, \gamma)^{57}Fe$
(3) $^{56}Fe(d, p)^{57}Fe$
(4) Coulomb excitation

Especially the coulomb excitation method (4) using a high energy heavy ion beam is very important for the material research, because this method can create ^{57}Fe Mössbauer levels by Coulomb excitation and simultaneously recoil-implant the ^{57}Fe atoms into any kinds of materials even if the solid solubility of Fe is practically null.

In the reactions (2) and (3), ^{57}Fe Mössbauer levels have been created in the specimen by the bombardments of neutron or deuteron to the target of ^{56}Fe nuclei whose natural abundance is 91.8%. Mössbauer measurements have been performed using the gamma-ray followed by de-excitation of the nuclear levels and it is possible to perform a time dependent

Mössbauer measurement as a function of period from just after the nuclear reaction. Since the deuteron energy to accomplish the reaction (3) is much larger than the energy of neutron beam for (2) from nuclear reactor, the recoil energy of atoms and the radiation damage given by the reaction (3) are larger and heavier than those in the case of (2).

^{56}Fe(d, p)^{57}Fe Mössbauer Spectroscopy

Details of the reaction ^{56}Fe(d, p)^{57}Fe have been reported previously[1] during the course of the nuclear structural study of ^{57}Fe nuclei and the cross section of the reaction is relatively large.

Although the first Mössbauer measurement followed by this reaction was performed by the group in John-Hopkins University using a Van de Graaff accelerator[2] and followed by the group in Hahn-Meitner Institute[3-6], a detailed study for the material research has not yet been reported as one of the applications of the in-beam Mössbauer spectroscopy. We are interested in ^{56}Fe(d, p)^{57}Fe Mössbauer spectroscopy to apply the material research, because from this method it is possible to examine the detailed behavior of resonant Fe atoms in iron based intermetallic compounds just after nuclear reaction. For instance, one can ask and discuss from this method where is and how many final landing positions of Fe in such compounds just after reaction and how are their temperature dependencies. Present study aimed to perform the first step for such kinds of material research using simple combination of target material and detection system.

There is a sever technical problem for the in-beam Mössbauer spectroscopy, which is a high counting rate of the background noise superimposed on the Mössbauer resonant gamma-rays. Mössbauer gamma-ray has a relative low energy and the background noise is mainly due to the X-rays emitted after photoelectric effect induced in the target material. By a conventional detection system used in Mössbauer spectroscopy the signal to noise ration (S/N ratio) is too low to construct a good Mössbauer resonance pattern. In order to get a good Mössbauer resonance pattern, it is essential to extract the Mössbauer gamma-rays from the high intense X-rays induced by the deuteron bombardment to the target in accelerator. For ^{57}Fe in-beam Mössbauer spectroscopy, some methods have been proposed and performed to extract the Mössbauer gamma-ray from the intense background noise in order to increase the S/N ratio. One method is to use the coincidence technique between 14.4 keV Mössbauer gamma-rays and 122 keV gamma-rays emitted beforehand. Other methods are to use a delayed coincidence technique between the pulses for the operation of the accelerator beam and the detection signals from the target in order to avoid the high intense prompt signals. In present investigation, we have used another method to extract 14.4 keV Mössbauer gamma-rays from high intense background noise, that is to use the resonant conversion electron detector which contains a resonance material enriched by ^{57}Fe and is nearly insensitive to the X-ray photons. This method is the similar one to extract the photons to excite the nucleus from the broad band synchrotron radiation using a nuclear resonance filter.

Experimental conditions in present study are as follows:

(1) Accelerator : AVF cyclotron of CYRIC at Tohoku University.

(2) Energy of deuteron beam : 6 MeV.

(3) Current of deuteron beam : 600 nA.

(4) Target : 310 stainless steel foil whose thickness is 25 μm.

(5) Detector : Resonant conversion electron detector containing a 310 stainless steel foil enriched to ^{57}Fe 1mg/cm^2.

Figure 1 shows the top and side views of the resonant conversion electron detector containing an ^{57}Fe enriched 310 stainless steel foil. Using this detector, the S/N ratio during the continuous operation of the cyclotron at the above conditions is high enough to construct the good Mössbauer emission spectrum of 310 stainless steel foil. Figure 3 shows the Mössbauer emission spectrum obtained by 310 stainless steel foil in which ^{56}Fe(d, p)^{57}Fe reaction occurred under the above conditions of the cyclotron. By the relatively short measuring period the quality of the emission spectrum is not excellent but we can see a single resonance line of 310 stainless steel whose full width at half maximum (FWHM) seems to be large compared to the spectrum obtained from usual transmission geometry using a ^{57}Co radioactive source. It is not yet clear that the large FWHM causes by the deuteron bombardments or after effects of the nuclear reaction. It is worthwhile to continue the measurements of ^{56}Fe(d, p)^{57}Fe Mössbauer spectroscopy in order to clarify the effect of recoil and nuclear reaction in target material.

Summary

We performed an ^{56}Fe(d, p)^{57}Fe Mössbauer spectroscopy using AVF cyclotron of CYRIC at Tohoku University. Using a resonant conversion electron detector containing an ^{57}Fe enriched 310 stainless steel foil, an Mössbauer emission spectrum has been successfully obtained from the target of 310 stainless steel foil at 300 K.

References

1) J. A. Thomson: Nucl. Phys., **A227** (1974) 485.
2) D. A. Goldberg, P. W. Keaton, Jr., Y. K. Lee, L. Madansky and J. C. Walker: Phys. Rev. Lett., **15** (1965) 418.
3) J. Christansen, E. Recknagel and G. Weyer: Phys. Lett., **20** (1966) 46.
4) J. Christansen, P. Hindennach, U. Morfeld, E. Recknagel, D. Riegel and G. Weyer: Nucl. Phys., **A99** (1967) 345.
5) J. Christansen, H. E. Mahnke, U. Morfeld, E. Recknagel, D. Riegel and W. Witthuhn: Z. Phys., **261** (1973) 13.
6) E. Vapirev, E. Dafni, H. E. Mahnke, M. H. Rafailovich, P. S. Kamenov and G. D. Sprouse: J. de Phys., **41** (1980) C1-473.

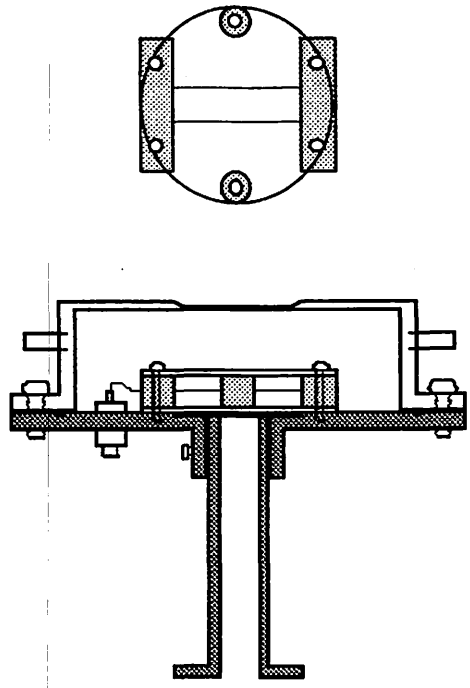

Fig. 1 Schematic drawing of the conversion electron Mössbauer detector containing an ^{57}Fe enriched 310 stainless steel. Top and side views are shown.

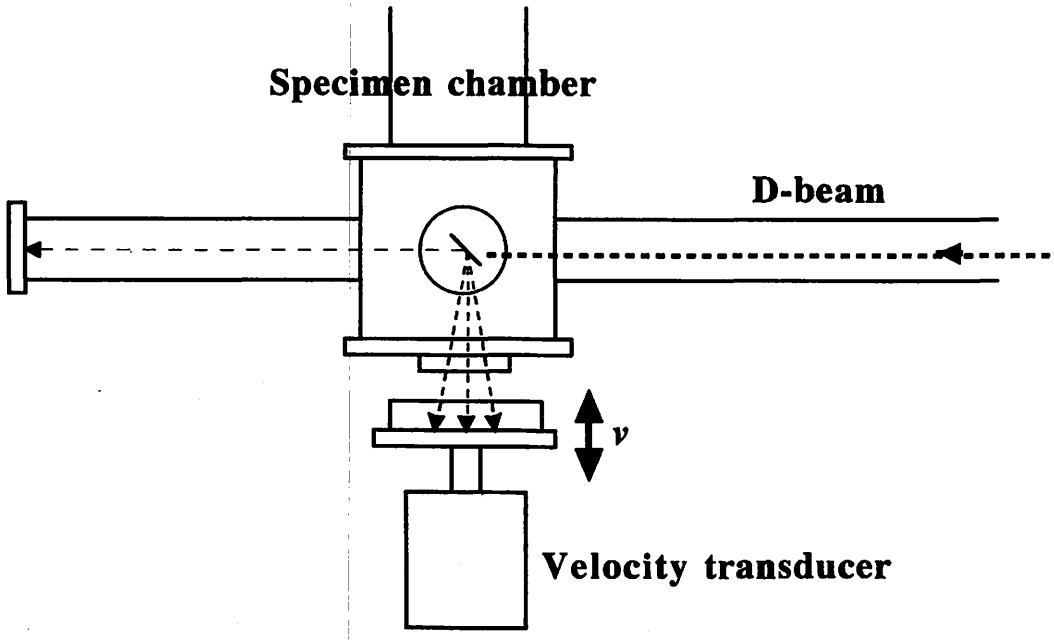

Fig. 2 Experimental arrangement for in-beam $^{56}Fe(d, p)^{57}Fe$ Mössbauer measurements at CYRIC of Tohoku University.

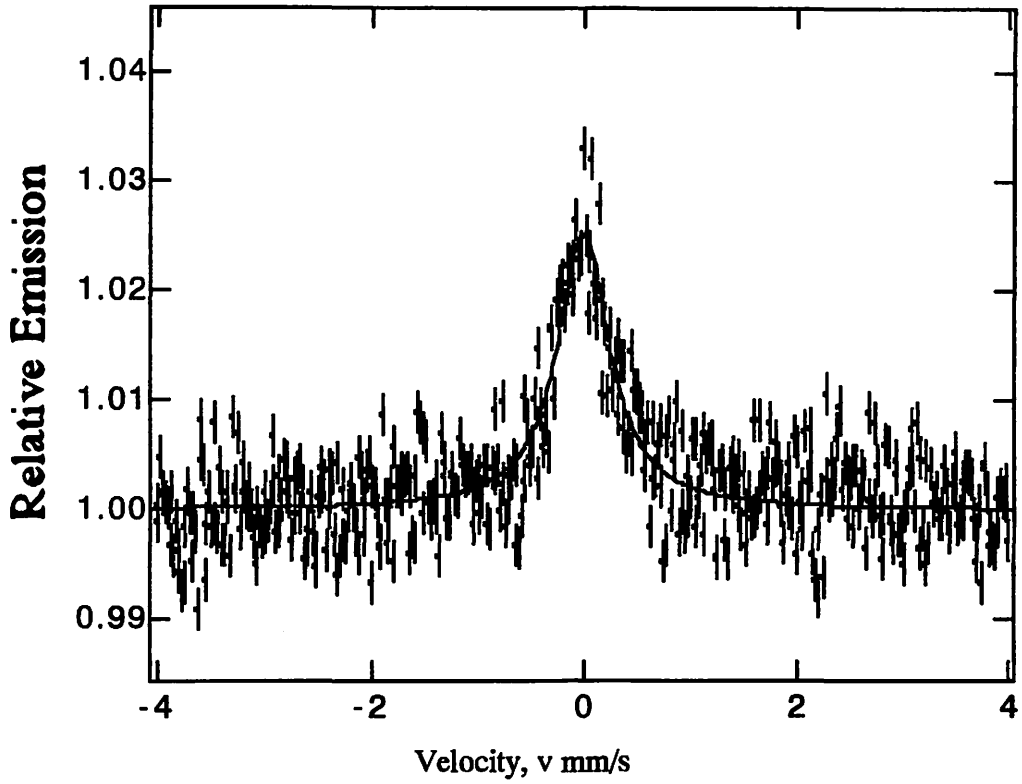

Fig. 3 ^{57}Fe Mössbauer spectrum of 310 stainless steel foil at 300 K resulting from ^{56}Fe(d, p)^{57}Fe reaction by 600 nA, 6 MeV D-beam at CYRIC of Tohoku University. Detection was performed by using a CEMS detector and an experimental setup as shown in Figs. 1 and 2.

I. 9. The Practice of Ion Implantation of ^{111}In and Stable Isotopes Using ISOL at CYRIC.

Hanada R.

Institute for Materials Research, Tohoku University

Introduction

^{111}In is the most popular nuclear probe for PAC spectroscopy because of its proper intermediate state (I=5/2) half decay time(84ns) for solid state studies and of it's convenient half decay time (2.8 days) of ^{111}In to ^{111}Cd in the radioactivity handling. Several attempts by the present author to prepare the source specimens by a diffusion method (800Cx a few hrs in H_2 or in UHV (ultra high vacuum) were successful for some elements but not so for Fe and Si. Since the ISOL (Isotope Separator on Line) at CYRIC (Cyclotron Radioisotope Center, Tohoku University, Sendai) becomes available for ion implantation work, ^{111}In implantation has been attempted for PAC spectroscopy of Si and Fe, of which practical side will be described in the followings.

Ion Implantation by ISOL

^{111}In IMPLANTATION

Several mCi of $^{111}InCl_3$ was charged to the crucible of the 910 type ion source for the ISOL and accelerated to 40 keV for the implantation. A separate experiment for natural Cd which has 8 isotopes with the AMU (atomic mass unit) between 106 and 116 to examine the capability of the isotope separation of the ISOL reveals that 14 mm separation is achieved for the AMU difference $\Delta M=1$ in this AMU range at 40 keV (Figure 1). So two slits were made (Figure 2), one for ^{111}In and one for ^{115}In at the distance of 55 mm and a small electrical current (nA-pA) due to the natural In (^{115}In:95.7%) was monitored to keep it maximum during the implantation. This marker method seemed to work that about 10μ Ci of ^{111}In is always implanted to a specimen after 6 hrs of implantation after employing the double slits system. In the radioactivity implantation some marker method is necessary since the current by the radioactive ion is negligibly small for the monitoring and yet small drifts in the accelerating voltage and the current for the analyzing magnet are always present, which results in the radioactivity beam shift from the specimen position.

STABLE ISOTOPES IMPLANTATION

In order to prepare alloyed specimen or to implant gas impurities ,several stable isotopes are implanted to mostly to Si. Rare gases implantation is rather easy since it is achieved by just substituting the carrier gas for the ion source (Ar) by other rare gases (He,Ne,Kr,Xe) He gives a very small ion current because of the poor ionization in the present ion source. The acceleration energy was limited to 26 keV for Ne since some discharge was observed above it. Other rare gases give 10 μ A ion current for an unit area (1 cm^2) at most and so a high dose implantation can be achieved in a reasonably short time, of which application for TDS (Thermal Desorption Spectroscopy) for Ar in Fe will be described in a separate report in this volume. Carbon and oxygen beams were obtained by using CO as the carrier gas and N beam with N_2 gas as described in the manual of the ISOL.

Elements with the low melting point (Zn,Cd,Ga,In,Pb,As,Sb,Bi,Se,Te,Ca) and a high vapor pressure at about 1000 C (the crucible temperature with the heater on) give several 10 to 100 nA beam. Sn and Cu beams were difficult to obtain because of the low vapor pressure at the temperature though several nA beam was obtained for several hours.

Since the isotope separation capability is excellent in the present ISOL, only one isotope with one AMU can be implanted for elements with many isotopes. Unfortunately at present, this merit of the isotope separation capability is not utilized for solid state studies of implanted materials. One good example of the application of stable isotope has been found in Si solid state studies where the hyperfine interaction of impurities trapped electrons with ^{29}Si nucleus (4.7%) has been utilized to determine the electron distribution around the impurity.

For other elements with the high melting points, a different type of ion source or the chloride method will be necessary. The latter has not been applied because the possible corrosion of ISOL parts by Cl ion was feared. If the former becomes available, the implantation of ^{57}Fe (2.2%) or ^{119}Sn (8.6%) to the dose above $10^{15}/cm^2$ will be useful for Mössbauer spectroscopy of implanted materials.

Acknowledgement

The author is indebted to Professors T. Shinozuka and M. Fujioka for their advice during the ISOL operation. This work is supported by a Grant-in Aid for Scientific Research for Priority Area from the Ministry of Education, Science and Culture of Japan.

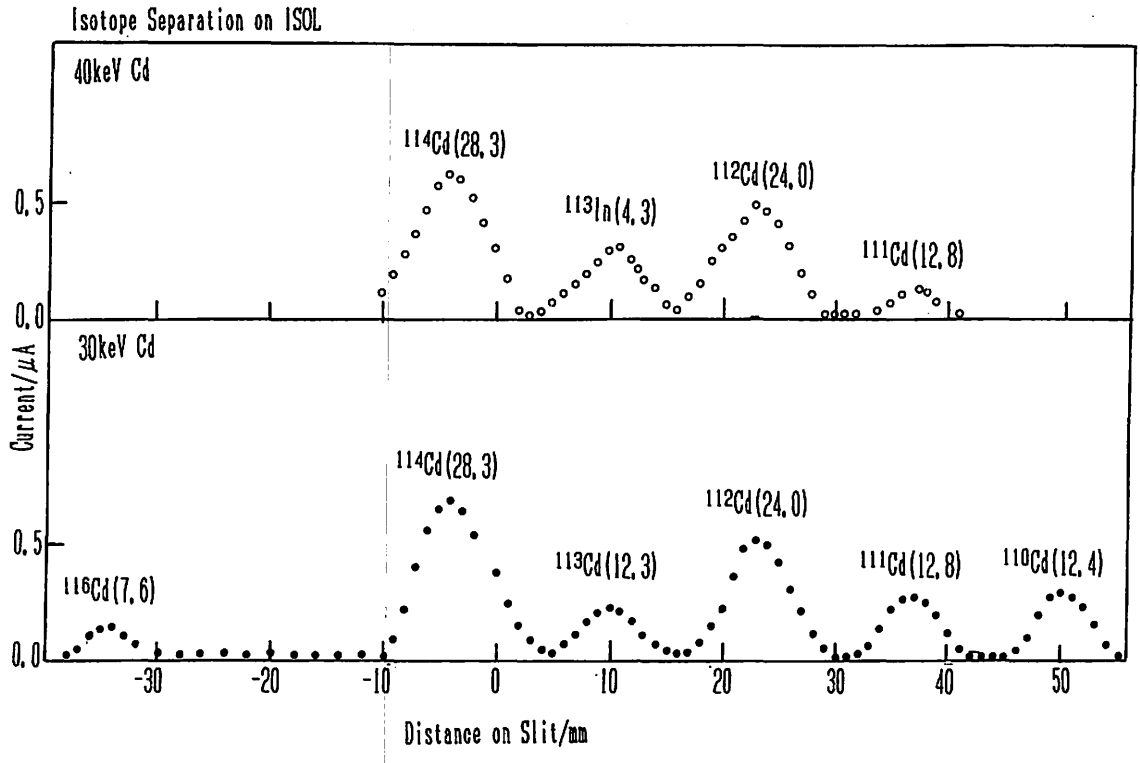

Fig. 1 Isotope separation capability of ISOL. The Cd(8 isotopes)ion current was measured as a function of slit(4mm) position. Acceleration energies 30 and 40keV.

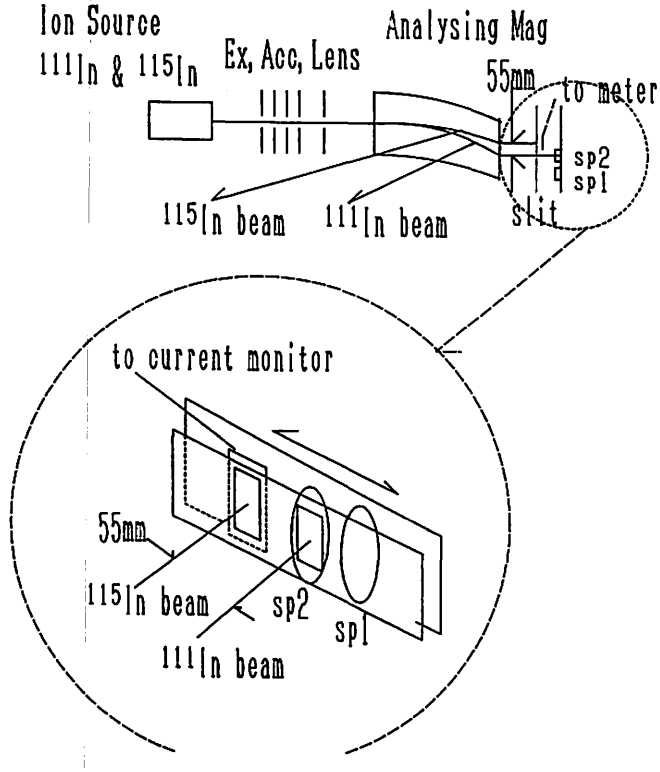

Fig. 2 A schematic diagram for the double slits system. The ^{115}In current was monitored during ^{111}In implantation. Results in Fig.1 are used to determine the distance between the two slits.

I. 10. TRIM Calculation of Distribution of Ions Implanted to Si in the Energy Range of ISOL(10-60keV)

Hanada R.

Institute for Materials Research, Tohoku University

Introduction

The method of ion implantation is one of the most convenient way to introduce radioactive probe nuclei into specimen materials. Recently the ion implantation of ^{111}In, a most convenient PAC (Perturbed Angular Correlation) probe, has been attempted by the present author using the ISOL (Isotope Separator on Line) in CYRIC. The details of the implantation practice and results of PAC spectrum measurement using the probe are described in separate reports in this volume.

In this report, results of a calculation to examine the ion distribution and the radiation damage after implantation of several ions into Si matrix will be described. Here, a simulation program, TRIM[1], has been used for the purposes.

The purposes of the calculation are : (1) to find the optimum implantation energy of several ions to obtain a maximum overlap with the implanted ^{111}In and (2) to know the degree of the radiation damage introduced by the implantation.

The Method of Calculation

Six ions (C, Ne, Ar, As, In and Bi) between the energy 10-60keV in Si were simulated to obtain (1) Ions concentration, (2) Longitudinal straggling (3) Depth and (4) Number of Frenkel pairs produced by the implantation. The results are plotted against the AMU(atomic mass unit) of the implanted ions as the implantation energy as a parameter. The calculation was done by an IBM compatible personal computer with the calculation time of several hours to finish 10^5-1 events. For the radiation damage calculation ,the displacement energy of 20eV,the default value in TRIM, and the Kinchin-Pease model (one alternative in TRIM to estimate the cascade effect) were assumed to estimate the cascade damage. The calculated damage is the total number of Frenkel pair(a pair of a lattice vacancy and an interstitial) produced by one incident ion and no effect of annealing (the annihilation of the pair by the recombination) was taken into account. Usually about 10% of them are left in a form of cluster or isolated point defect (vacancy) because of the annealing after the

implantation at RT (the room temperature) as shown by experimental recovery results of low temperature irradiated metals.

Results and discussion

Figure 1 through Figure 4 show results of the calculation. Namely, Figure 1 for the ion range, Figure 2 for the ion concentration, Figure 3 for the straggling (the full width at half maximum for the ion distribution) and Figure 4 for the number of Frenkel pair (designated as vacancy as TRIM does) produced. The solid lines in the figures are obtained by fitting six calculated points by a smooth curve.

Figure 1 shows 40keV ^{111}In has a maximum concentration at 100A and 400A from the surface for the implantation energy of 10 and 60keV, respectively. If one wishes to obtain a maximum overlap for implanted carbon ions ,as an example, with the 40keV ^{111}In(ion range 300A), Figure 1 tells that the carbon implantation energy should be 10keV to obtain the same magnitude of the range or the maximum overlap.

Figure 2 shows the maximum ion concentration given in (ion/cm^3/ion/cm^2) for the abscissa in the left and the mol fraction (number of ion/number of Si atom) in the right. If one wishes to calculate the maximum local concentration of 40keV ^{111}In of 10μCi (3.7×10^5Bq or 1.3×10^{11} ions) implanted per unit area, Figure 2 tells us it is $4.5\times10^5\times1.3\times10^{11}=5.8\times10^{16}$/cm^3 or ^{111}In/Si=$1.2\times10^{-6}$ (1.2 part per million) that is comparable with the impurities concentration in high purity metals and the those of dopants to make Si as n-or p-type. As shown in a separate report in this volume, several element were intentionally implanted to Si to prepare alloyed specimens. In that case the dose was chosen typically as 2×10^{14}/cm^2, that gives a local impurity concentration of $3.5\times10^5\times2\times10^{14}=7\times10^{19}$/cm^3, as an example for 40keV As (arsenic ion). These examples show the local impurity concentration becomes quite high for a reasonably small implantation dose. This is because the implanted ions distribute in a narrow range of several 100 A for the implantation energy of several 10keV as shown in Figure 3 for the straggling. In Figure 3 one can see the trend that the width of the distribution becomes smaller for heavier elements and for lower implantation energy. Correspondingly in Figure 2, the local concentration becomes higher for heavier element ions and for lower implantation energy.

Figure 4 summarizes the number of Frenkel pair produced (designated as vacancy/ion) as a function of incident ion AMU with the energy as a parameter. The damage increases almost linearly with AMU up to As (AMU=75) and saturates above it. For the case of 40keV ^{111}In, the value is about 500 per one incident ion. So even in the case of RT implantation, considerable amount of damage should be present after the implantation.

Although not shown here, similar results as in Figure 1-Figure 3 for the ion distribution were calculated for the damage distribution. For the case of 40keV ^{111}In in Si, the maximum of the damage distribution is at 170A from the surface and the width (FWHM) is about 250A. So the damage is present in a localized volume near the ion that causes the

damage. The local damage concentration may be estimated as high as 1.2×10^{-3}. The estimation was done by approximating the local damage zone by a sphere of which diameter is 250A and 500 Frenkel pairs are distributed uniformly in the sphere. As a characteristic of the low energy implantation, this high density of the radiation damage is always associated with the implanted ion even when the dose of the ion approaches to null. If the dose of the implanted ion exceeds a certain limit, the local damage zone starts to overlap and in that case only the average defect concentration should have meaning. This limit dose may be estimated as $2\times10^{15}/cm^2$ for the 40keV ^{111}In in Si that is obtained by the projected area of the damaged zone to the surface.

In several years ago a dispute took place that no damage effect should be present when a light probe as B is implanted to Si as usually done in ß-NMR experiment. If one applies the same argument as above for 40keV C in Si using TRIM results for it (vac/ion=200, damage zone diameter of 1500A), the local concentration is estimated as 2.5×10^{-6}, a factor of 5×10^{2} smaller than the ^{111}In case. So the probability of C to meet with point defects that the ion itself creates should be much smaller than the ^{111}In case, though one can never say no damage effect should be present for the light probe atom implantation. Indeed a recent ß-NMR experiment with varying the implantation temperature[2] has shown the magnitude of the substitutional component depends strongly on the temperature suggesting the damages created interact strongly with the probe atoms.

During the course of the calculation described above, several limits have been noticed for the simulation code TRIM. The first is that it does not take into account the effect of accumulated implanted ions on the energy loss for the subsequently incoming ions. When the dose of the implanted ions reaches to the order of $10^{16\text{-}17}/cm^2$, the local ion concentration becomes so high that an alloy phase is formed. The energy loss (electronic and nuclear) in the alloy then should be different from those of the matrix and hence the ion distribution should be a function of the dose.

The second is that it does not take into account the effect of the nuclear transmutation or spallation when the incident energy of ion exceeds several 10^6 eV. No such nuclear reaction takes place in the present energy range of ISOL though several plans are now in progress using high energy accelerator as proton synclotron (600MeV). If one wishes to perform implantation works using such an accelerator, a modified TRIM code taking into account the nuclear reaction and the damage created by these nuclear reaction products will be certainly required.

Acknowledgement

This work is supported by a Grant-in Aid for Scientific Research on Priority Area from the Ministry of Education, Science and Culture of Japan.

References

1) Ziegler J. and Bicrsack J. P.:"The stopping and Range of Ions in Solids (TRIM- 91)" Pergamon Press (1985).
2) Ittermann B.et al., Hyp. Int. 79 (1993) 591.

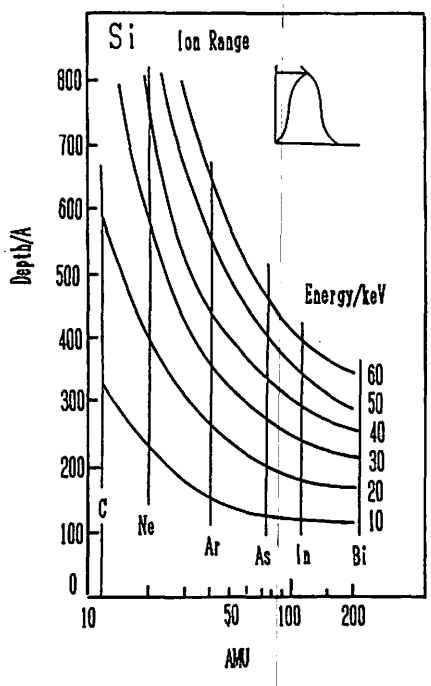

Fig. 1. TRIM result for the ion range(depth from the surface) in Si host.

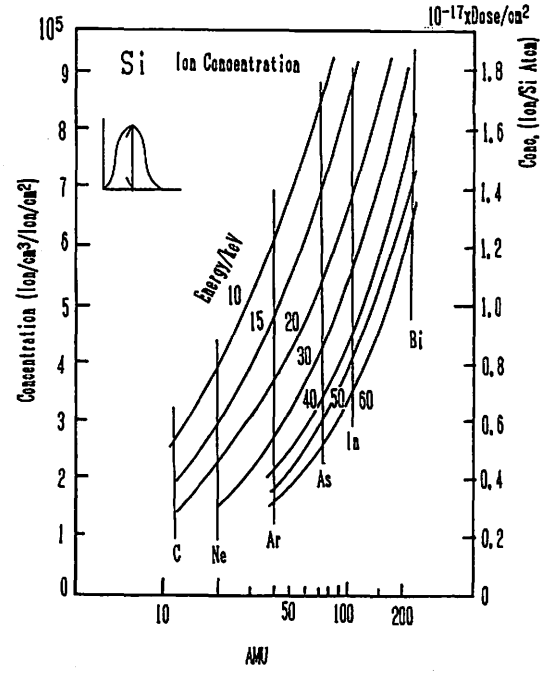

Fig. 2. TRIM result for the implanted ions concentration in Si host. For details see text.

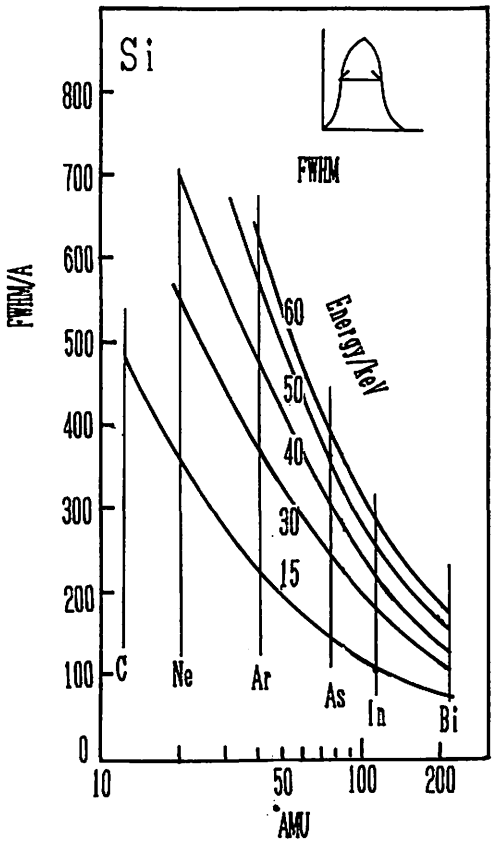

Fig. 3. TRIM result for the distribution width of the implanted ions in Si host.

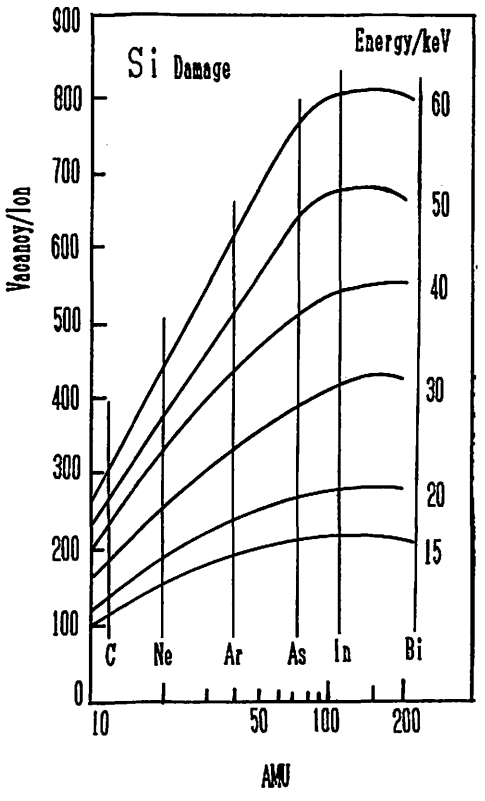

Fig. 4 TRIM result for me radiation damage in Si host.

I. 11. Effects of External Magnetic Field on PAC Spectrum of Ni.

Hanada R.

Institute for Materials Research, Tohoku University,

Introduction

Effects of external magnetic field on PAC spectrum have been worked out theoretically and summarized in Ref.[1]. When the numerical coefficients are evaluated for the PAC spectrum, $R(t)=[N(\pi)-N(\pi/2)]/[(N(\pi)+N(\pi/2)]$ where $N(\pi)$ and $N(\pi/2)$ are the counts for the stop detectors placed at π and $\pi/2$ relative to the start detector respectively, R(t) reads as eq.(1) for the magnetic field applied vertical to the detector plane.

$$R(t)= b_2 \cos(2\omega_L t) \qquad (1)$$

where ω_L is Larmor frequency and given as $-g\mu_N B/\hbar$, where g is the nuclear g factor. μ_N is the nuclear magneton and B is the hyperfine field at the nucleus. The b_2 is calculated to be -0.132 for the case of ^{111}In (^{111}Cd)[2]. This expression agrees with the classical picture of the nuclear precession with the angular frequency of ω_L, which is detected by the γ ray emission that has the π symmetry and hence should give two maxima during one period of the precession.

For the case of the random spin direction, namely, without any external magnetic field, eq.(2) is obtained for R(t) based on the calculation by Matthias et al.[3].

$$R(t)=b_2 [\, 0.2 +0.4 \cos(\omega_L t)+0.4\cos(2\omega_L t) \,] \qquad (2)$$

This expression is different from eq.(1) with the presence of the unperturbed term of 0.2 and the 2nd term with ω_L of which amplitude is the same with the third term of $2\omega_L$. The eq.(2) can be derived from the fundamental formulation for PAC[1]. There, the property of 3j symbol, that gives the transition probability among 2I+1 magnetic sublevels, is used to show only the terms $N=(m_a-m_b)=0, \pm1, \pm2$ survive to give the finite amplitude of $N\omega_L$ frequency. Since this probability is independent of the value of I, we have only one precession frequency with $H\neq0$ and only two with $H=0$ for any I. This is different from the quadrupole interaction where the number of frequency increases with I. (For instance 3 for I=5/2, 6 for I=7/2). So

the magnetic interaction gives a much simpler spectrum than that of the quadrupole interaction and will be quite useful for the PAD experiment where a high spin nuclear probe is utilized.

The purpose of the present work is to verify eq.(1) and (2) for ^{111}In in Ni by measuring PAC spectrum with and without the vertical external magnetic field. Although Matthias et al have experimentally shown that eq.(2) is valid for ^{111}In in Ni, they gave the spectrum without extracting the precession term and also no comparison was made for the case with the vertical magnetic field.

The other purpose of the present work is to find an optimum conditions to prepare a Ni specimen with ^{111}In by a diffusion method. For this purpose, the diffusion treatment was performed at lower temperature than the reported ones[4,5] and subsequently the specimen was annealed at higher temperatures stepwisely to find the temperature to give the maximum amplitude in the PAC spectrum.

Experimental

A high purity polycrystalline Ni (99.995% by Johnson-Matthey Inc.,) specimen ($10\times5\times0.2mm^3$) was annealed in 1 atm hydrogen atmosphere for 12 hrs at 400C with 400 μCi of dried $^{111}InCl_3$ solution to diffuse ^{111}In into the Ni bulk. After measuring the PAC spectrum by a three detector system, the specimen was annealed in an UHV for 1.5hrs from 500C to 980C stepwisely. After the each annealing, the PAC spectrum was measured at RT with and without the vertical magnetic field of 0.25T supplied by a pair of permanent magnet. The spectrum was analyzed by a FFT program to obtain the power spectrum.

Results

Figure 1 shows the PAC time spectrum for Ni with the annealing temperature as a parameter. The spectrum with and without the external magnetic field was measured for the temperatures between 873K and 1250K. Figure 2 shows part of the corresponding Fourier spectra for Figure 1. Figure 3 shows the amplitudes of the two components in Figure 2 as a function of the annealing temperature.

Discussion

EFFECTS OF THE EXTERNAL MAGNETIC FIELD

From Figure 1 nd Figure 2 it is evident that two angular frequencies take place for the case without magnetic field and only one for the case with the magnetic field. This result agrees exactly with the theoretical prediction of eq.(1) and (2).

The close inspection of Figure 2, however, reveals that the value of $2\omega_L$ for the $H\neq0$ case is about 4% lower than that of the H=0 case. This is due to the fact that the hyperfine field at the nucleus is reduced by the external magnetic field. Namely, the external magnetic field H is subtractive from the hyperfine field B or similarly the sign of B is negative. From the measured ω_L for the H=0 case, the hyperfine field B can be determined as-6.34T with

knowing the nuclear g factor of ^{111}In (^{111}Cd)[6]. Indeed the ratio of the external field to the hyperfine field, 0.25/6.34=4%, roughly agrees with the observed shift of 4% in the $2\omega_L$. If one can measure the shift as a function of the magnitude of the external field H, one can determine both g and B at the same time with an appropriate extrapolation method for H=0.

AMPLITUDE OF THE PRECESSION PATTERN

As seen from Figure 1 or Figure 3, the amplitude of the precession is quite low right after the diffusion treatment at 400C. It grows with the annealing temperature and reaches to a maximum at 600-700C and then gradually decays between 700 and 1000C.

The low amplitude at 400C can be interpreted that only part of ^{111}In diffuse into Ni bulk as the substitutional impurity and the other part are still on the surface. Indeed Figure 3 as well as Figure 1 reveal that there exists a very low frequency component (10Mrads-1) at 400C or 500C. The site corresponding to this low frequency is not known at present. Possibilities are:(1) ^{111}In adsorbed at the surface or (2) ^{111}In in the $InCl_3$ solution that has not been reduced by the H_2 annealing.

The maximum amplitude R for the H≠0 case is 0.11 at 700C that is comparable with the theoretical value of $|b_2| = 0.132$. So most of ^{111}In are at the Ni substitutional site at this temperature. The remaining part of 0.132-0.11=0.022 should be in the other sites that do not give unique precession frequencies, of which species are not known at present. Indeed Figure 3 shows the magnitude of the a broad frequency distribution above and below $2\omega_L$ increases with the annealing temperature.

Practically, the above results suggest that 700C is the most appropriate temperature if one wishes to prepare a Ni source specimen by a diffusion method.

The present results show the theoretical prediction of eq.(1) and (2) are quite valid with respect to the effect of the external magnetic field (the vertical magnetization) for the case of Ni.

Acknowledgement

This work is supported by a Grant-in-Aid for Scientic Research on Priority Area from the Ministry of Education, Science and Culture of Japan.

References

1) Frauenfelder H. and Steffen R. M:"Angular Distribution of Nuclear Radiation" in Alpha-, Beta- and Gamma-Ray Spectroscopy vol.2 ed.by Kai Siegbahn ,North-Holland pub.co., (1968) p1113.
2) Hanada R. :CYRIC-Annual Report- (1993) p42.
3) Matthias E. , Rosenblum S. S. , and Shirley D. A.: Phys. Rev. Letters **14** (1965) 46.
4) Cisneros J. I. , Liljegren G. L. , Lindqvist T. and Lopez-Garcia A. :Arikiv. für Fysik. **38** (1968) 363.
5) Hanada R. :CYRIC Annual Report-1988 (1989) 65.
6) Table of Isotopes 7th edition, App-51 ed by Lederer C. M. and Shirley V. S. pub by Wiley-Interscience Pub. (1978).

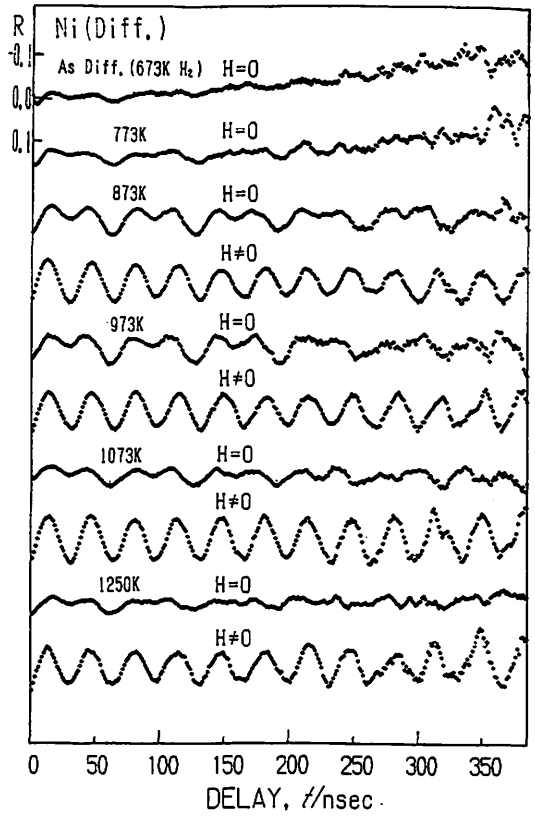

Fig. 1. PAC spectrum by ^{111}In in Ni. The spectra with and without the external magnetic field are shown. RT measurement.

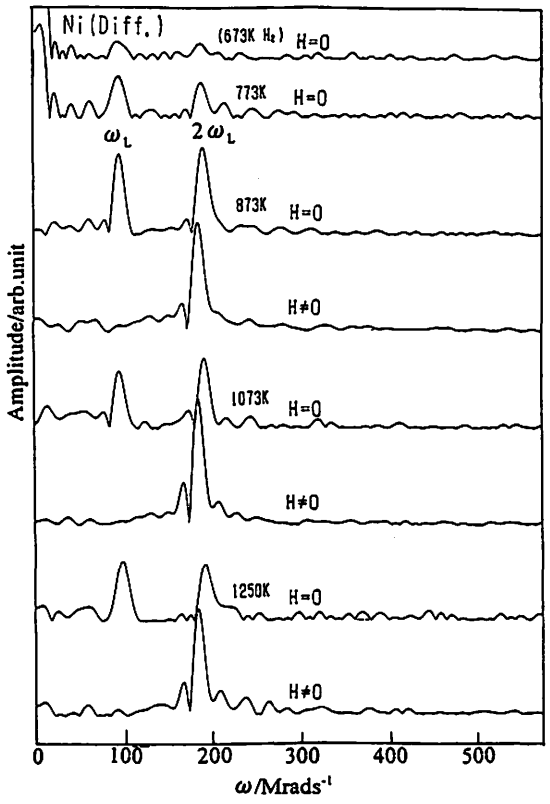

Fig. 2. A Fourier power spectra for Fig. 1. Two frequencies without the external magnetic field and only one with the field.

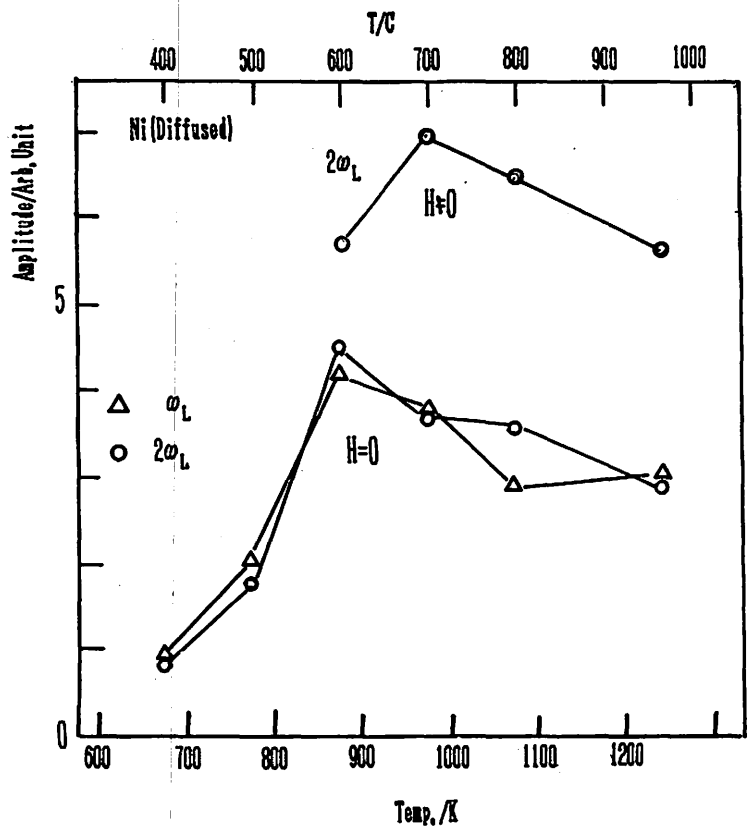

Fig. 3. Amplitudes of the two components as a function of the annealing temperatures after the diffusion treatment at 400C.

I. 12. PAC Spectroscopy of Fe and Fe Alloys by ^{111}In Implanted or Diffused

Hanada R.

Institute for Materials Research, Tohoku University,

Introduction

Although Mössbauer or NMR/ON spectroscopies have been used to investigate solid state of Fe or Fe alloys, the applications of PAC spectroscopy to them have been rather scarce. Since PAC spectroscopy utilizes very dilute radioactive probes, studies of point defects or impurities in Fe will be most suited subject by the method.

Since the technique of the ion implantation of PAC probe,^{111}In, has been established using ISOL at CYRIC, several research subjects by PAC spectroscopy by it are now in progress, among which the part to investigate Fe and Fe alloys will be reported in the followings.

The subjects are classified into 4 categories.

(1) PAC spectroscopy in pure Fe. This experiment is aimed (i) to examine the magnetic hyperfine interactions in Fe host as done in Ni and (ii) to find possible interactions with point defects introduced during the implantation.

(2) PAC spectroscopy in interstitial impurities doped Fe. This is aimed to find possible interactions with interstitial impurities, C, N, O. For this purpose, interstitial impurities, C, N, O were implanted to Fe specimens first and subsequently the PAC probe ^{111}In was implanted for spectroscopy.

(3) PAC spectroscopy in substitutional impurities doped Fe. Fe-V and Fe-Si alloys specimens were chosen for ^{111}In implantation and PAC spectroscopy was performed. The aim is the same with the case (2).

(4) PAC spectroscopy in pure Fe given by a diffusion treatment to prepare ^{111}In PAC specimen. This is (i) to compare the PAC spectrum with those prepared by the implantation method and (ii) to compare with the results by others who have applied diffusion methods to prepare the ^{111}In specimens.

Experimental

Details of the specimens investigated in the present are summarized in Table 1. Some

specimens were given an etching treatment using a chemical solution [HF(20), H_2O_2(400), H_2O(50)] to remove the surface layer until a metallic luster was obtained.

All specimens except Fe(diff) were implanted by 40keV ^{111}In with using ISOL and PAC spectrum was measured at RT without the external magnetic field. Also an isochronal annealing schedule (100K step, 0.5-1hr, 10^{-7} Torr UHV) was given to each specimen and the spectrum was measured after each annealing. The purpose of the annealing is (1) to anneal out the radiation damage due to implantation and (2) to make impurities to diffuse or point defects to form a pair with ^{111}In. In the present runs, no intermediate annealing was given to specimens between the impurities (C, N ,O) implantation and ^{111}In implantation.

The diffusion treatment for Fe(diff.) is exactly the same with that for Ni described in a paper in this volume and also an isochronal annealing was given up to 700C.

Results and discussion

PURE Fe

Figure 1 shows the PAC spectrum for a pure Fe specimen(JM) implanted by 40keV ^{111}In. Although small in magnitude, a modulation pattern, of which period is 11.2nsec, is present at annealing temperatures upto 600C. Since the spectrum measurement was performed without the external magnetic field, there should be two frequencies ω_L and $2\omega_L$ according to theoretical treatments for magnetic hyperfine interactions. Such theoretical results have been proved to be valid by experiments, one of which is reported in a paper in this volume for Ni. A Fourier analysis of Figure 1 however, shows only one frequency of 560Mrads^{-1} which should be ω_L and not $2\omega_L$. As shown by the Ni result, PAC spectrum should show a small $2\omega_L$ rotation component (5.6nsec) between those of the ω_L component (11.2nsec) for the Fe case without magnetic field. Unfortunately this $2\omega_L$ component is not resolved in the present PAC spectrum of Figure 1. This is probably because of the small amplitude of the modulation pattern and also by the rough time scale (80nsec/60channel) used in the present . Indeed such $2\omega_L$ term has been observed in Refs.1 and 2 for the Fe spectrum without the external magnetic field.

The hyperfine field B at ^{111}In nuclei in Fe substitutional site is determined as-39 T by the measured value of ω_L with the relation ω_L=-gμB/h. Here a tabulated value of g=(μ/I) is used[3].

To examine the possible interactions with point defects introduced by the implantation, the spectrum in Figure 1 is Fourier analyzed to look for the defects component. However, a clear component is only that of ^{111}In at the substitutional site (S-site,ω_L=560Mrads^{-1}) and no other clear component was resolved for all annealing temperatures. However, the magnitude of the S component is dependent on the annealing temperature as shown in Figure 2 together with those of other specimens. As shown in Figure 2, the magnitude is highest for pure Fe among all specimens and shows a broad maximum at 200-400C. This shows that part of ^{111}In in the S site without trapping any defects or impurities is highest for pure Fe and also

some recovery to perfect crystal takes place between RT and 400C. Also shown in Figure 2, the S component decays to almost null between 600 and 700C. This shows ^{111}In atoms diffuse a long distance at this temperatures and reach to some sites other than S-site. Although several components are present after the annealing at 700C where the S-component is completely lost, the reproducibility must be examined before going into discussing the nature of them. The diffusion coefficients of S impurities in Fe have been measured to be in the range of 10^{-14}-10^{-15}cm^2 s^{-1} between 600C and 700C. If this value is used for ^{111}In in Fe, the diffusion distance $\sqrt{Dt}$ is about 200A in the present 1hr annealing and hence ^{111}In should reach to the surface, grain boundaries and impurities, which leads to the observed loss of the S-component. Indeed some evaporation of ^{111}In from the specimens was noticed at 600-700C annealing. This leads to a radioactivity loss at these temperatures and results in a low counting rate after the annealing.

INTERSTITIAL IMPURIRITIES IMPLANTED Fe

The PAC spectra in impurities (C, N, O) implanted Fe are almost the same with that of Fe.Namely ,the only clear component is S-component although the magnitude is reduced. Figure 2 also shows the annealing behavior of the S-component in the impurity implanted Fe. The magnitude is almost half of that of pure Fe in specimens implanted by low (2×10^{14}) or intermediate (10^{15}) doses C, N, O. It gradually grows to that of pure Fe up to 300C and decays to null between 600 and 700C as in the case of pure Fe. If the dose becomes high (5×10^{15} for C or O), the S-component is completely lost at all annealing temperatures investigated. Unfortunately no clear component other than the S-component that can be ascribed to ^{111}In-Interstitial impurity pair has been observed so far in the present. This suggests interstitial impurities has no attractive interaction with ^{111}In and no unique hyperfine field is present to give a modulation pattern with different period other than that of the S-component. The gradual recovery to that of pure Fe up to 300C is probably due to the precipitation of implanted impurities since C or N has been known to precipitate around this temperature. The complete loss of the S component in specimens implanted to a high dose shows the presence of interstitial impurities with the local concentration of several at. % completely destroys the unique hyperfine field of the substitutional site.

ALLOYS WITH SUBSTITUTIONAL IMPURITIES

V and Si were chosen for the alloying elements since these elements are soluble to Fe and so a complete solid solution (isolated substitutional impurities) is obtained. The PAC spectra in the alloys, however, more or less are similar with those of the interstitial impurities implanted Fe and only a reduced S-component has been observed. The magnitude of the S-component is also shown in Figure 2. No component corresponding to ^{111}In-V or ^{111}In-Si pair has been observed so far. This is different from Mössbauer spectroscopy results where these alloying elements cause about 10% reduction in ^{57}Fe hyperfine field and gives rise to

clear satellites in the spectrum[4]. The situation is the same for interstitial impurities which cause about 20% reduction and also give rise to clear separated satellites in the Mossbauer spectrum. The very dilute concentration of the PAC probe, and so each of them feels different hyperfine field due to imperfections in Fe lattice, might be responsible for the difference.

DIFFUSED Fe

Figure 3 shows the PAC spectrum for pure Fe where ^{111}In is intended to diffuse into the bulk. Although small in magnitude, a modulation pattern is present up to 600C. The period of 36 nsec is, however, is quite different from that of the S-component (11.2 nsec) in the ^{111}In implanted Fe. So the ^{111}In to give the modulation pattern in Figure 3 should be in different site from the S site in the bulk to give Figure 1. The spectrum was measured without the external magnetic field and a Fourier analysis reveals two components (ω_L and $2\omega_L$) are present in the spectrum. So the hyperfine interaction to give rise to the modulation is magnetic and not quadrupolar. The conceivable sites are (1) ^{111}In on the Fe surface. (2) ^{111}In in the grain boundaries. At present the author prefers to the case(1) since the specimen used is almost a single crystal with small islands and so ^{111}In is adsorbed at a unique site on the surface that have a unique hyperfine field, of which magnitude is about 1/3 of the S-site.

Several experiments to prepare the Fe source specimens by a diffusion method at about 1000C have been reported[1,2] and only the bulk S-component (11.2 nsec) has been observed. The higher annealing temperature (1000C) than the present (700C) seems to be necessary for ^{111}In to diffuse into Fe bulk. Further experiments will be necessary to confirm this.

The angular frequency for Figure 3 and the corresponding hyperfine field are summarized in Table II together with those of pure S-sites in Fe, Ni and Co specimens. Ni results are taken from a separate paper in this volume and Co result is not shown here but obtained by the implantation method by the present author.

Acknowledgement

This work is supported by a Grant-in Aid for Scientific Research for Priority Area from the Ministry of Education, Science and Culture of Japan.

References

1) Cisneros J. I. , Liljegren G., Lindqvist T. and Lopez-Garcia A., Arkiv Für Fysik **38** (1968) 363.
2) Golczwski J. and Maier K. NIM **A244** (1986) 509
3) Table of Isotopes, 7 th edition App-51 ed.by Lederer C. M. and Shirley V. S. pub. by Wiley-Interscience Pub. (1978).
4) Fujita F. E.,"Mössbauer Spectroscopy in Physical Metallurgy in *"Mössbauer Spectroscopy"* ed. by Gonser U. pub. by Springer-Verlag (1975).

Table 1. Summary of Specimens for PAC Spectrum Measurement.

Fe	* MRC ** JM	poly 99.99(RRR=1500) quasi-single 99.995
Fe(diff.)	JM(quasi-single)	400C×12hrs in 1atm H_2 with $InCl_3$
Fe-V	poly	4at.%(Melt)
Fe-Si	single	6at.%(Melt)

	Implantation	***Local Max.Conc.(TRIM)/at.%
Fe-O	2×10^{14}/cm^2, 15keV	0.09
	1×10^{15}/cm^2, 15keV	0.45
	6×10^{15}/cm^2, 15keV	2.7
Fe-C	1×10^{15}/cm^2, 16keV	0.35
	6×10^{15}/cm^2, 16keV	2.1
Fe-N	4×10^{14}/cm^2, 20keV	0.17

*MRC:Materials Reserch Co. **JM:Johnson Matthey Inc.All the specimens were annealed at 800C before the treatments.*** The local max.concentrations are estimated by TRIM code for Fe host.

Table 2. Summary of Hyperfine Field at ^{111}In in Ferromagnetic Hosts.

Host	Prep. Method	Period/ns	ω_L/Mrads^{-1}	B/T
Fe	Implanted	11.2	560	-39
Fe	Diffused	36.5	172	?11.9
Ni	Diffused	66.0	95.2	-6.34
Co	Implanted	15.3	410	?28.3

?: the sign is not determined.

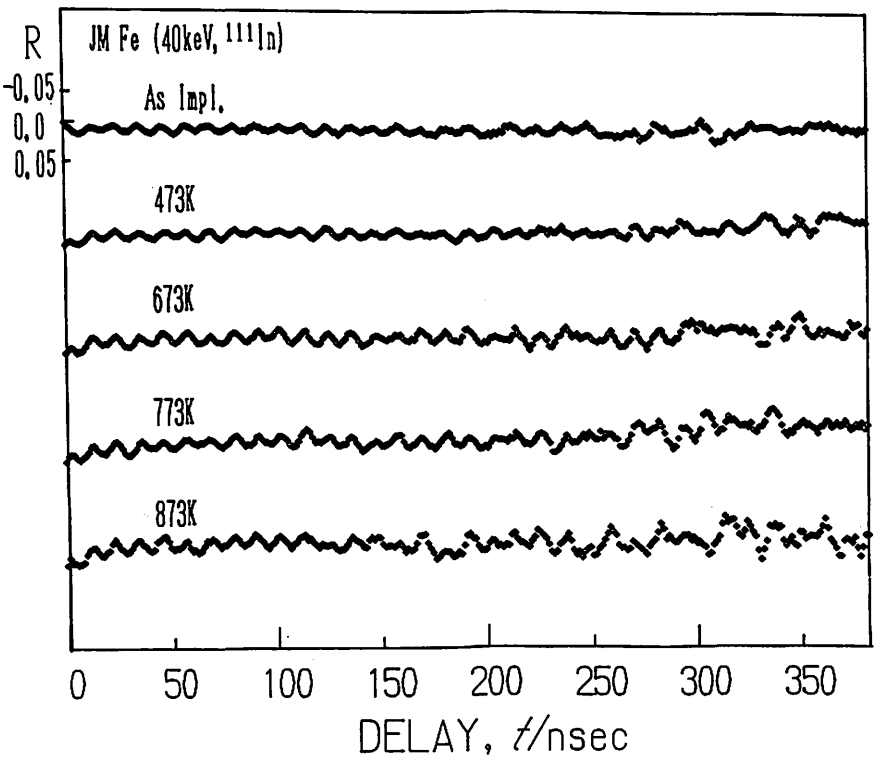

Fig. 1. PAC spectrum by ^{111}In implanted to an Fe(JM) host.

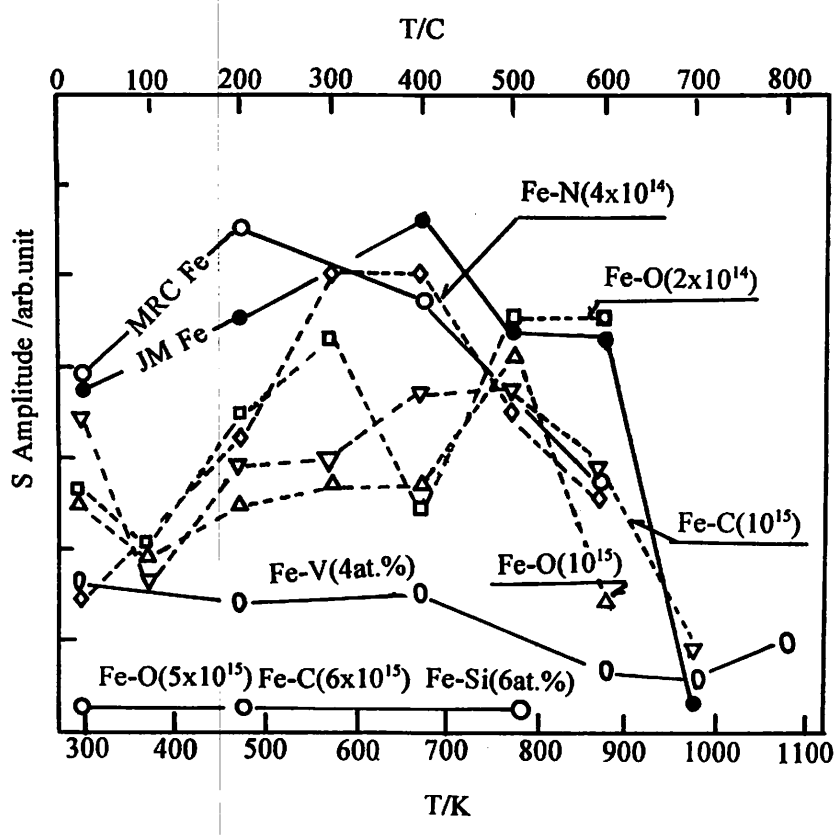

Fig. 2. The amplitude of the substitutional components for pure Fe, impurities implanted Fe and Fe-V, Fe-Si as a function of the annealing temperature.

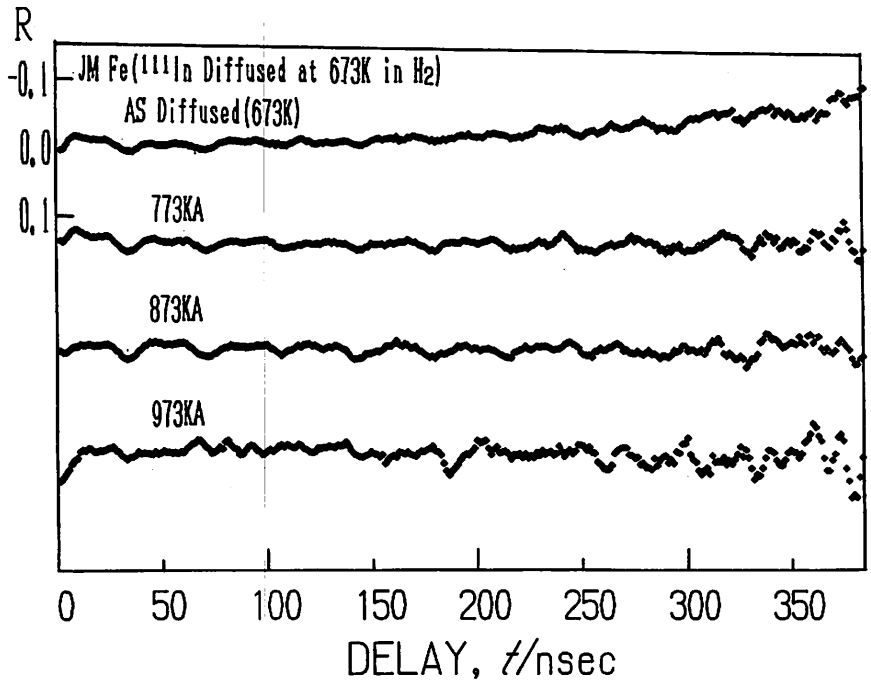

Fig. 3. PAC spectrum by ^{111}In in Fe given a diffusion treatment.

I. 13. Thermal Desorption Spectroscopy (TDS) Study of Rare Gases Implanted to Pure Fe

Hanada R. and Saito S.

Institute for Materials Research, Tohoku University,

Introduction

Rare gases are practically insoluble to Fe and yet can be implanted if accelerated to several 10keV by ISOL. This paper reports the result of TDS study of Ar and Kr implanted to pure Fe with the energy between 20 and 60keV. The purpose of the experiment is to examine the effect of the phase transformation on TDS of rare gases from Fe. Such an example has been reported for Ar from Co. (1)

Fe has three phase transformations. Namely,[1)] Ferromagnetic to paramagnetic transition at 768C(1041K). (2) bcc (body centered cubic) phase (α-phase) to fcc (face centered cubic) phase(γ-phase) at 906C(1179K) and (3) fcc-phase(γ-phase) to bcc phase(δ-phase) at 1401C(1674K). In the present study, TDS was measured between RT and 1000C to examine the effect of the transformations (1) and (2).

Experimental

Fe specimens are high purity (99.995%) polycrystalline foils(10×15×0.3 mm^3) from Johnson Matthey Inc. They were annealed at 800C for 2 days in an UHV for the recrystallization. Because of the long annealing time, the grains grow to 2-5mm in diameter. Ar and Kr were implanted to them at RT using ISOL at CYRIC. The acceleration energies were 20-60keV and the doses were between 10^{16}-$10^{17}/cm^2$. The method of the TDS measurement is exactly the same with those reported in ref. (2).

Result

Figure 1 shows the TDS for Kr implanted to Fe at 40keV with three different doses. One prominent gas release is observed at 1000K for the specimens implanted above $4\times10^{16}/cm^2$ and the other at 1200K for all specimens. Similar results are obtained for Ar implanted Fe and especially the TDS peak at 1200K has been observed all specimens investigated.

These results clearly show a prominent rare gas release takes place at or right after the phase transformation (2), namely, at the α-γ phase transformation.

Discussion

First let us discuss the site of the implanted rare gases in Fe lattice. Since rare gases have much larger atomic sizes(Ne:3.20,Ar:3.82 ,Kr:4.0 and Xe:4.40A)[3] than the interstitial sites of bcc Fe lattice (the o-(octahedral) site:0.19 and the t- (tetrahedral) site:0.36A) or fcc Fe lattice(the o-site :0.28 and the t-site:0.52A)[4], it is very unlikely that they can stay at these sites as interstitial impurities. So even when they happen to land on these interstitial sites after the implantation, they should change the site to the substitutional site either by pushing out the Fe atom or by finding a lattice vacancy and sitting in it. Although the energetics of these processes will be a subject of further considerations, it is usually found in the hyperfine interactions studies that the implanted heavy ions are found at the substitutional site. So let us assume that the implanted Ar or Kr are at the substitutional site.

The first possibility to explain the observed gas release at the phase transition will be the different diffusion coefficients in the different phases. Namely, the diffusion coefficient in the fcc phase (γ-phase) is higher than that of the bcc phase(α-phase) so as the immobile rare gases in the bcc phase start to migrate when the host bcc lattice changes the structure to the fcc structure. However this model does not apply to the substitutional impurities in Fe. Namely, the inspection of the compiled data in Fe reveals that the diffusion coefficients in the fcc phase is 2 order of magnitude smaller than that of the bcc phase for all substitutional impurities investigated[5]. So if this rule applies to the rare gas atoms in Fe, we cannot ascribe the observed gas release upon the phase transition to the difference in the diffusion coefficient.

The second possibility is to ascribe it to a short circuit diffusion (The faster diffusion that takes place in the paths other than the bulk ,for instance, along the grain boundaries or the dislocations)[6]. Namely, it is usually found that a high density of dislocations are formed during the phase transformation, for instance, in the martensitic phase transformations in the alloyed steels. The cause of the dislocation production has been known as to relieve the internal stress caused by the different unit cell volume in the different phase, that can be imagined easily by the Kurdjumov-Sachs relation for bcc to fcc transition[7]. If this applies to the present case, a high density of dislocations is formed at the phase transition temperature and the rare gas atoms diffuse along the dislocation lines (a pipe diffusion, one mechanism of a short circuit diffusion) to be released from the surface. One difficulty of this model is that whether a high density of dislocations is formed during the slow warming up rate (20K/min) as in the present and also if formed they may be annealed out instantaneously because of the high temperature (1200K) where the release takes place.

The other mechanism of the short circuit diffusion is the grain boundary diffusion. If the α-γ phase transition is caused by the nucleation and growth mechanism (the production of the small γ nuclei in α matrix and the subsequent growth that results in the γ bulk), new grain boundaries are formed in the γ phase. So rare gas atoms diffuse along the new grain boundaries. As has been known from the diffusion experiments, grain boundaries as well as

dislocations have been known as a path for a short circuit diffusion. One difficulty of this model is then why no grain boundary diffusion takes place in the α phase up to 1200K.

Several possibilities above are based on the assumption that the implanted rare gases are present in the Fe lattice more or less as an isolated solute. However as has been discussed in ref.[2], the implantation dose is high in the present and the local rare gases atom concentration becomes quite high as to form gas bubbles. Also a channeling study of Kr implanted to Al has revealed that an ordered compound of Kr is formed in the Al lattice[8]. If these are the case for the rare gases in Fe, the interaction of the gas bubble or the compound with the stress or the structure change due to the phase transformation must be examined that is the beyond the scope of the present paper.

Technologically, the sudden gas release from the structure materials at the phase transformation temperature might be hazardous in a fusion or fission reactor operation and the methods of the protection must be found.

Further experimental works are now in progress.

Acknowledgements

The discussion with Prof.Shigeru Suzuki (Institute for Advanced Materials Processing, Tohoku University) is deeply appreciated.

This work is supported by a Grant-in Aid for Scientific Research in a Priority Area from the Ministry of Education, Science and Culture, Japan.

References

1) D. B. Kuzminov:J.Nuclear Materials,**184** (1991) 113.
2) Hanada R. CYRIC Annual report-**1993**, (1994) 33.
3) A. I. P. Handbook pub by McGraw-Hill pub.co.
4) W. C. Leslie: The Physical Metallurgy of Steels, pub by McGraw-Hill pub.co.
5) H. Oikawa:Technology Reports,Tohoku University, **47** (1982) 215.
6) P. G. Shewmon: Diffusion in Solids, McGraw-Hill Co.(1975).
7) C. M. Wayman: "Phase Transformations, Nondiffusive" in Physical Metallurgy II, Third, revised and enlarged edition. ed. by R.W.Cahn and P. Haasen pub by North-Holland Physics Pub.(1983).
8) E. Yagi: "Behavior of Kr Atoms Implanted to Al as Investigated by a Channeling Method" in Fundamental Aspects of Inert Gases in Solids ed by S. E. Donnelly and J. H. Evans pub by Plenum Press (1991).

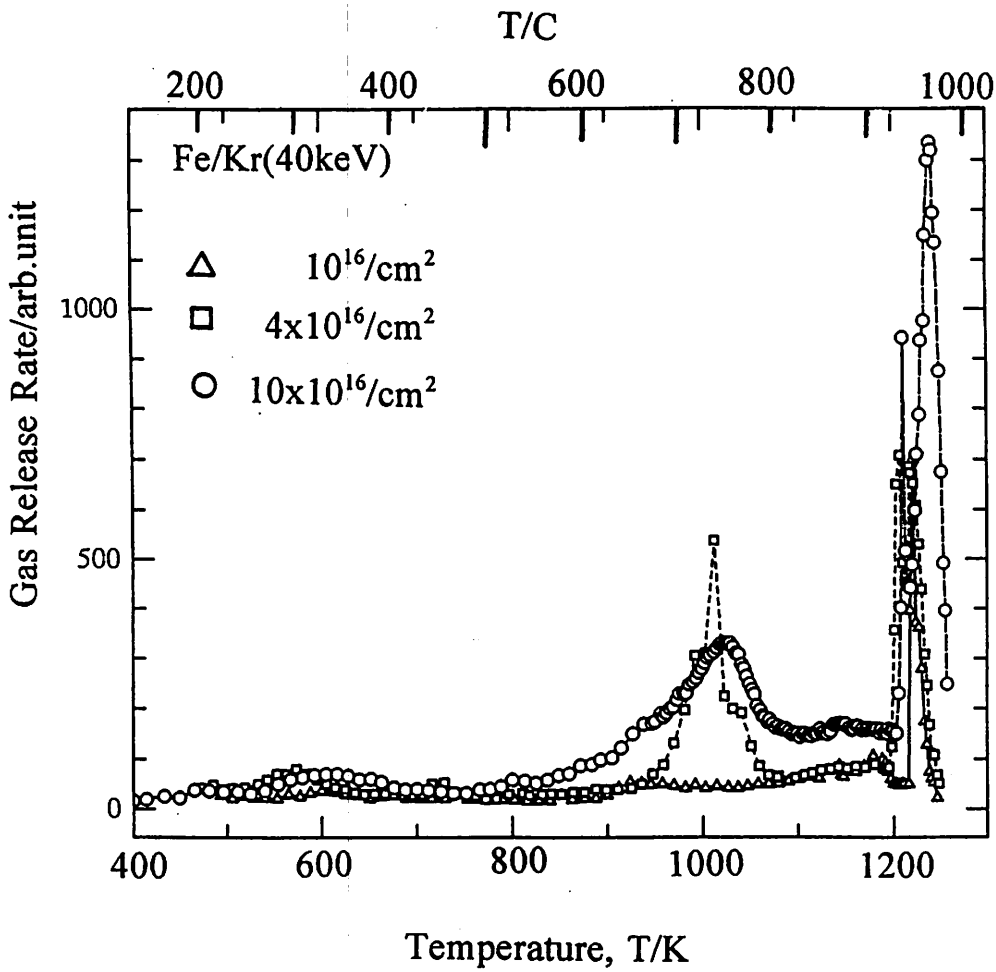

Fig. 1. TDS spectrum for Kr implanted to Fe to various doses Warming up rate 20K/min.

I. 14. Development of an Imaging Plate Radiation Detector

*Takebe M., Abe K., Souda M., Satoh Y., and Kondo Y.**

*Department of Nuclear Engineering, Tohoku University**

The imaging plate is a reusable storage phosphor film, formed with a large area of thin plastic plate coated with photo-stimulable phosphor (e.g. $BaFBr:Eu^{2+}$)[1], which is sensitive to nuclear particle radiations as well as X-rays and energetic electrons and now widely used in various fields.

The latent images caused by irradiation of the imaging plate are usually read out by measuring the Eu^{2+} luminescence at about 390 nm stimulated by 633 nm light of a He-Ne laser scanner, and are reconstructed as two-dimensional dot images on a computer's display.

The imaging plate has many striking performances of radiation detection, such as a simple usage, a high position resolution (25-100 μm), a large detection area, a high detection sensitivity with good signal-to-noise ratio, long time dose accumulation, good dose linearity, extremely wide dynamic range of dose and easy erasing for reuse. In addition to these, we have reported previously that the imaging plate has a feature of good particle discrimination in itself, which is performed using two or more stimulation lights[2].

As to the particle energy measurement with the imaging plate, two techniques have been proposed which are based on the absorber method[3-4]. No feature of energy determination in the imaging plate itself was expected there.

It has been widely conceived that the imaging plate itself can offer no information of incident particle energy, which comes from its character of two-dimensional optoelectronic film, usually formed of thin mono-layer phosphor, and read out by the aid of only superficial scanning with stimulation light. However, while re-examining optical properties of the imaging plate as to establishing particle discrimination for various nuclear particles of various energies, we found that the imaging plate has also a full potential ability to determine the incident particle energies with no additional means, keeping all the high performances of the imaging plate intact. Moreover, the range of the energy covered by the method is wide and the energy resolution is good, the reason of which is not yet clear. This energy determination is quite similar to the particle identification reported previously except that photo-bleaching is not applied in this method[2].

The experimental procedures were as follows: 1] specimen: pieces of imaging plate of 10 mm×20 mm in size were cut out from a BAS3000-UR imaging plate (Fuji Photo Film

Co. Ltd.). The imaging plate was composed of 135 μm thick photo-stimulable phosphor layer of BaFBr:Eu^{2+} on a 230 μm thick supporting substrate and a 10 μm thick polymer film covering the surface of the phosphor layer for protection; 2] measurements of stimulation spectra: A light from a 50-W halogen lamp was dispersed by a grating monochrometer(JASCO CT-50) and was focused on the piece of imaging plate at an incident angle of 60° through a glass filter (Toshiba Y-45), but finally the light was a little diffused to elliptical shape of 4 mm×5 mm in shape at the imaging plate in order to reduce the surface light intensity for the convenience of multiple readout in the present. The photo-stimulated luminescence (PSL) was observed at a right angle with respect to the surface through an interference filter (IF-400, Vacuum Optics Corporation of Japan) which passes light of 390-410 nm full width at half maximum. The intensity of the luminescence was monitored with a Hamamatsu R955 photomultiplier. The output current of the photomultiplier was recorded in an NEC-9801 computer through an 16-bit A/D converter as a function of the wavelength of the stimulating monochromatic light. The intensity of the stimulating light was reduced by ND-filters to the extent that the readout fading of the PSL center was negligible (less than 1% by one scan). One measurement scan over the range of 440-750 nm of stimulation lights took 310 seconds at the rate of 1 sec/ 1 nm. All measurements and irradiations were carried out at room temperature; 3] irradiations: The used proton beam was prepared by a dynamitron of FNL (Fast Neutron Laboratory), the alpha beam by a cyclotron of CYRIC (Cyclotron and Radioisotope Center) and the electron beam by JEM-2000EXII transmission electron microscope of High Voltage Electron Microscope Laboratory, which facilities are all in our university. The proton irradiations were done perpendicularly on the pieces of the imaging plate covered with 8.2 μm thick aluminium foil in a vacuum scattering chamber through Rutherford scattering method that was useful to defocussing and spreading the protons on the imaging plates and to easy beam handling and background rejection. A scatterer of 0.2 μm thick gold foil was set at the center of the chamber at a right angle to the proton beam. The imaging plates were put at 153 mm away from the scatterer with the scattering angle of 5.5° and the number of incident protons was measured through a silicon solid state detector, located 98 mm far from the gold foil, with an angle of 165°. The number of incident protons on the imaging plates were 2.2×10^9 - 2.8×10^9 protons/cm^2 and the irradiation times were 1-17 minutes for proton energies of 3.2-1.5 MeV. The alpha measurement was done in air with the imaging plates covered with 10 μm thick aluminium foil at the course 1 of CYRIC and the electron one in vacuum chamber without wrapping. The imaging plates had been left in dark for initial 18 hours after each irradiation in order to avoid afterglow following the erasing and/or the irradiation, short time thermal fading, possible energy-dependent fading and the effect of difference of the energy-dependent irradiation times.

Figure 1 shows a PSL stimulation spectra made of the proton measurements and preliminary measurements of alpha and electron irradiations, normalized at 500 nm in order to show the clear relative variations around 600 nm. Figure 2 shows the ratios of PSL

intensities of 600 nm to those of 500 nm versus the incident proton energies. A direct relationship between the PSL ratio and the energy is evident. The deviations from the straight line in the figure were within a few percent. The reason why the imaging plate can offer the particle energy determination in itself is not clear, even if the path length of the particle and/or the sharp rise of Bragg curve at the particle ending may be relevant to the evidence. Taking into account that the spatial resolution of the imaging plate is, at most, 50-25 μm and the path length of 3.2 MeV protons is about 80 μm after passing both the wrapping aluminium foil and the surface protection cover, the accuracy of 'a few percent deviation' appears unreasonably good. From the figures the particle energy determination with the imaging plate may be expected to be valid for alphas and electrons as well.

An alpha measurement of a wide range of energy was started by the cooperation with Prof. A. Yamaya and his crew.

The authors are grateful to Prof. M. Fujioka and Prof. D. Shindo for the preliminary alpha and electron irradiations, respectively.

References

1) Sonoda M., Takano M., Miyahara J. and Kato H., Radiology **148** (1983) 833.
2) Takebe M. and Abe K., Nucl. Instr. and Meth. **A345** (1994) 606.
3) Mori C., Matsumura A. and Suzuki T., UTNL-R **0288** (1993) 62; Nuclear Engineering Research Laboratory, University of Tokyo [in Japanese].
4) Nanto H., Extended Abstracts (The 55th Autumn Meeting, 1994); The Japan Society of Applied Physics [in Japanese].

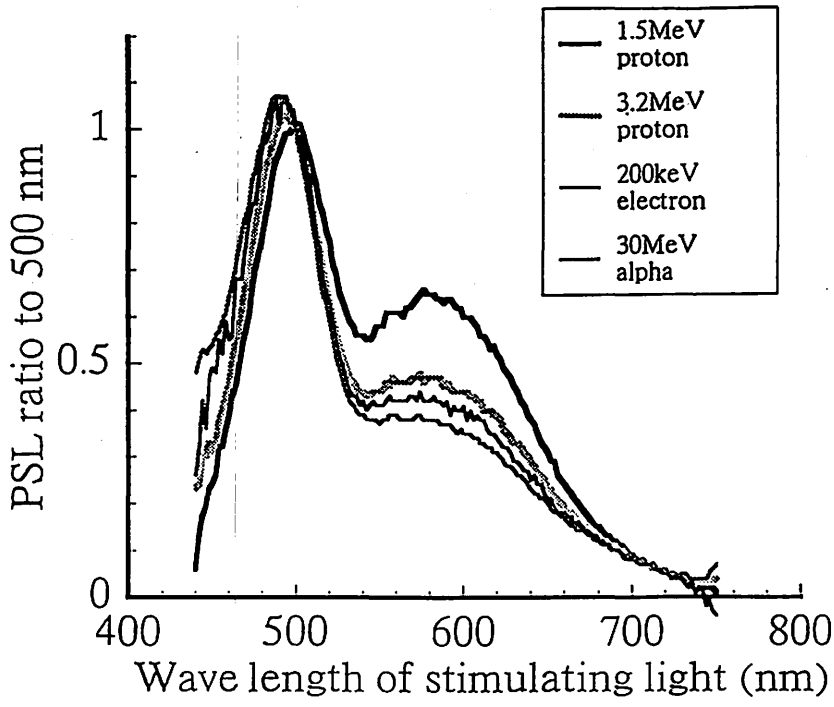

Fig. 1. PSL stimulation spectra for the images of 1.5 and 3.2 MeV protons, 30 MeV alpha particles and 200 keV electrons, normalized at 500 nm.

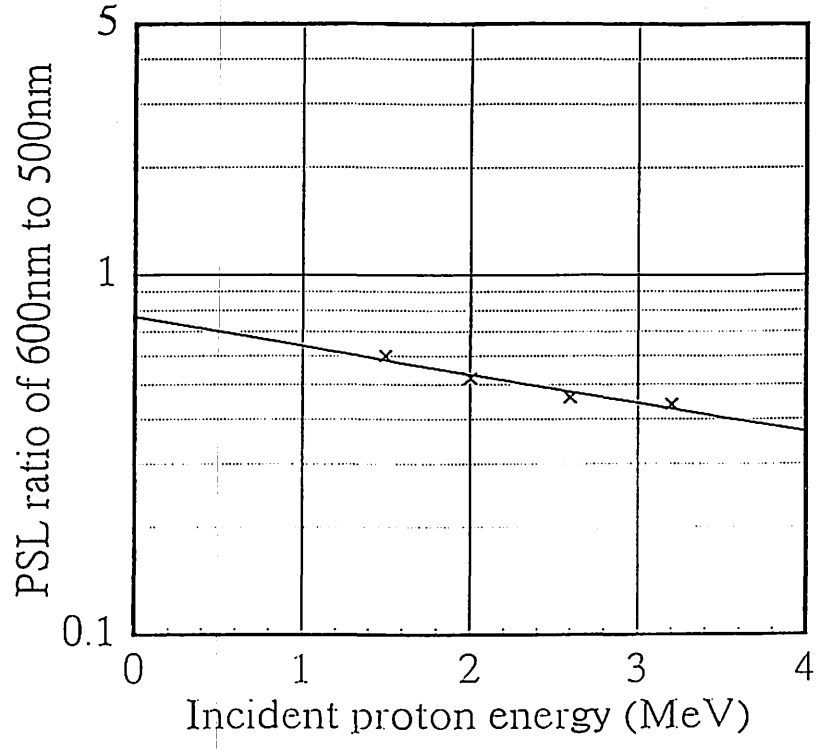

Fig. 2. Energy dependence of PSL ratios of 600 nm to 500 nm for protons.

I. 15. On the Equivalent-Current Method for a Permanent-Magnet Circuit

Fujioka M. and Honma T.

Cyclotron and Radioisotope Center, Tohoku University

In the course of an orbit study of extraction of accelerated negative ions converted into positive ones by a suitably located stripper foil in our CYRIC cyclotron, we were led to a conclusion that a compact steering dipole magnet is required, which from geometrical restrictions must be manufactured using a permanent-magnet circuit (PMD)[1]. A model magnet was actually designed and constructed, and the details of its performance studied[2]. In the numerical part of this study we utilized the equivalent-current method of a permanent magnet having a uniform magnetization M_0. In the following we summarize a derivation of this method for convenience.

For a steady-state magnetics we start from:

$$\mathrm{rot}\,\vec{B} = \mathrm{rot}\,\vec{M} + \mu_0\,\vec{i}_c\ , \tag{1}$$

where $\vec{i}_c$ is the convection-current density and $\vec{M}$ is the magnetization of the component permanent magnets. The vector potential is then obtained as

$$\vec{A}(\vec{r}) = (1/4\pi)\int [(\mathrm{rot}\,\vec{M} + \mu_0\,\vec{i}_c)'/|\vec{r} - \vec{r}'|]dv'\ . \tag{2}$$

Here ' signifies that the relevant quantities are to be evaluated at $\vec{r}'$.

We then consider a permanent magnet having a uniform magnetization $\vec{M} = \vec{M}_0$ in the absence of the convection current. Then from eq.(2) we have

$$\vec{A}(\vec{r}) = (1/4\pi)\int [(\mathrm{rot}\,\vec{M})'/|\vec{r} - \vec{r}'|]dv'\ . \tag{3}$$

Eq.(3) is transformed as

$$\int [\mathrm{rot}'\,\vec{M}'/|\vec{r} - \vec{r}'|]dv' = \int [(\mathrm{rot}'\,(\vec{M}'/|\vec{r} - \vec{r}'|) + \vec{M}' \times \mathrm{grad}\,'(1/|\vec{r} - \vec{r}'|)]dv'\ . \tag{4}$$

We denote the boundary surface of the magnet in question by S, and further consider two surfaces S_1 just inside and S_2 just outside the S, respectively, S_1 and S_2 being apart by ε. Then, eq.(4) can be written as

$$\int_v [\mathrm{rot}'\, \vec{M}' / |\vec{r} - \vec{r}'|]dv' = \int_{v_{12}} [\mathrm{rot}'\, (\vec{M}' / |\vec{r} - \vec{r}'|) + \vec{M}' \times \mathrm{grad}'(1 / |\vec{r} - \vec{r}'|)]dv' \,. \quad (5)$$

Here, the equality holds because inside S_1 $\mathrm{rot}\, \vec{M}' = \mathrm{rot}\, \vec{M}_0 = 0$, and the second part of the right hand side vanishes when $\varepsilon \to 0$: V_{12} is the volume between S_1 and S_2.

Here we are reminded of the "second form" of the Gauss's formula of vector analysis:

$$\int_v \mathrm{rot}\, \vec{f}\, dv = \int_s \vec{n} \times \vec{f}\, d\sigma \,. \quad (6)$$

We apply this to the region V_{12} between S_1 and S_2:

$$\vec{A}(\vec{r}) = (1 / 4\pi) \int_{v_{12}} \mathrm{rot}'\, (\vec{M}' / |\vec{r} - \vec{r}'|)dv' = \int_{s_1 + s_2} \vec{n}' \times \vec{M}' / |\vec{r} - \vec{r}'| d\sigma' \,,$$

Noting that the integral over S_1 vanishes because $\vec{M}' = 0$, and comparing with eq.(2) we get

$$\vec{A}(\vec{r}) = (1 / 4\pi) \int (\mu_0 \vec{i}_{eq}' / |\vec{r} - \vec{r}'|)dv' = -(1 / 4\pi) \int_s \vec{n}' \times \vec{M}_0 / |\vec{r} - \vec{r}'| dv' \,,$$

the minus sign comming from the convention of the outward unit normal vector for $\vec{n}$. Thus we finally obtain the equivalent-current density on the surface of the magnet as

$$\boxed{\vec{i}_{eq} = \mu_0^{-1} \vec{M} \times \vec{n}\, \delta(s)} \quad (7)$$

Because the equivalent current is of a surface density we put a delta function in the direction of $\vec{n}$ at the boundary surface.

We acknowledge Dr. Shinozuka for discussions.

References

1) Honma T., Fujioka M., Shinozuka T. and Matumoto N., Nucler Instrum. and Methods A361(199513.
2) Honma T., PhD thesis, in preparation, Tohoku University, 1995.

I. 16. Measurement of Torque Working on the Permanent-Magnet Dipole

Honma T., Fujioka M., Matsumoto N. and Shinozuka T.*

Cyclotron and Radioisotope Center, Tohoku University
*Tokin Corporation **

Introduction

A proto-type permanent-magnet dipole(PMD)[1] with adjustable field strength and polarity has been designed and constructed.Since the magnetic properties of the PMD were described in the previous reports[1,2], in the present report we deal with the torque working on the PMD.

A set of three permanent-magnet rods is arranged inside the return yoke. The two sets are driven through worm-gear systems; they are rotated in the opposite direction to each other by a single-phase induction motor. Advantages of the worm-gear system employed for the PMD are to give a large gear-ratio even in a small space, and to keep the system rest when the motor is switched off. The total gear-ratio of 400 to rotate the rods by two sets of worm-gear systems having a gear-ratio of 20 was adopted. Main parameters of the worm-gear system are listed in Table 1.

To estimate the total torque T working on the six permanent-magnet rods the total magnetic energy stored in the PMD was calculated for various rotation angle θ of the rods. If we consider a small change of θ the magnitude of the torque T is given by (Note that the differentiation below must be made for θ in radian).

$$T = -\frac{dW(\mathrm{PMD})}{d\theta} , \qquad (1)$$

where W(PMD) is the total magnetic energy as a function of θ .

The code PANDIRA, however, can not calculate this energy for a permanent-magnet problem, so that we calculated the energy using the method of equivalent-cutrrent[3] applied to the code POISSON in the following way[2].

$$(\mathrm{PMD}) = W\,(\mathrm{POI}) + \left[\int_{in} \frac{\mu_0}{2}(\vec{H}_{in})^2\,dV - \int_{in} \frac{1}{2\mu_0}(\vec{B}_{in})^2\,dV\right] (\mathrm{PAN}), \qquad (2)$$

where $\vec{H}_{in}$ (PAN) is the magnetic field in the rod calculated from $\vec{B}_{in}$ (PAN) for various θ using the relation of $\vec{B}_{in} = \mu_0 \vec{H}_{in} + \vec{M}$, and $\int_{in}$ denotes integration within the six magnet rods. In Figure 1 both W(PMD) and W(POI) are plotted together with the torque T calculated by numerical differentiation of the former according to eq. (2). The dependence on θ of both and W(PMD) and W(POI) are seen to be well described by a function $W(\theta)=a+b \cdot \cos 2\theta$. Also, the maximum value of $|T|$ is thus predicted to be T_{cal} (max)=46 N. m at $\theta = \pm 45$ deg.

Measurement of torque

We measured torque working on the drive shaft. When measuring the torque, the drive shaft is released from the coupling. A simple method was applied to measure the torque as follows.

$$F_m = \frac{1}{2}.(F_1 - F_2), \tag{3}$$

where F_1 is the force in a direction of increasing magnetic field and F_2 is the force in the direction opposite to F_1 ; then F_m should be the net amount of force working on the drive shaft due to the magnets. From such measurements of F_1 and F_2 using a spring balance the torque T_{DS} working on the drive shaft is derived as

$$T_{DS} = - F_m \ell, \tag{4}$$

where ℓ (=1 m) is the distance between the axis of the drive shaft and the measuring point of the forces F_1 and F_2. Differences $\Delta F = (F_1 - F_2)$ are plotted in Figure 2 for the various angles θ

In order to compare the measured values of T with those of design calculation (Figure 1) we have to consider the effect of mechanical transmission efficiency η of one set of the worm gear system, which is given[4,5] by

$$\eta = \frac{\tan\gamma.(1+f\tan\gamma.)}{\tan\gamma + f}, \tag{5}$$

where $f \equiv \kappa/\cos\alpha_n$, $\gamma = 3° 35'$ and $\alpha_n = 20°$ are lead angle and pressure angle of the worm-gear system, respectively(see in Table 1), and κ is the coefficient of sliding friction between the worm and the worm wheel. As can be seen in eq.(5) the efficiency is affected remarkably by the value of κ In the case of the worm (made of steel) and the worm wheel (made of AlBC-2; aluminum bronze casting) rubbed together with lubricating oil the coefficient κ is estimated in the range of 0.04 to 0.07[4,5]. Suppose that we have a value of κ=0.055 as the middle value of this range. Then from eq.(5) we have η=52%. Therefore, the maximum (through negative by definition) measured torque due to the six magnets $T_{meas}(max) \equiv T_{meas}(\theta = 45°)$ is derived as follows (Figure 2).

$$T_{meas}(\max) = \frac{1}{2}\ \Delta F(45°) \times \ell \times i^2 \times \eta$$
$$= \frac{1}{2} \times 62.3\ \text{gw} \times 1\text{m} \times 20^2 \times 0.52^2 = 3.4\ \text{kgwm} = 33\ \text{N.m.}$$

Considering the expected scatter of the value of κ, the agreement between experimental and theoretical values of the torque can be said to be good.

References

1) Honma T., et al., CYRIC Ann. Rept.(1993).
2) Honma T, Fujioka M, Shinozuka T. and Matsumoto N, Nucl. Instr. and Meth., (1995) to be published.
3) Fujioka M., et al., CYRIC Ann. Rept.(1980).
4) JGMA Standard, JGMA 405-01., (1978), in Japanese.
5) Handbook of Mechanical Design,7-123, (Kyoritsu Publ.Co., 1976, Tokyo), in Japanese.
6) Catalogue of Gears, KG Stock Gears KG-503, Kyoiku-Haguruma, Co., in Japanese.

Table 1. Parameters of worm and worm wheel[6].

Worm	
Type ;	W1SUR+B and W1SUL1+B
Material ;	SUS304
Module ;	m = 1 mm
Pressure angle ;	$\alpha_n = 20°$
Lead angle ;	$\gamma = 3° 35'$
Pitch diameter ;	$d_1 = 16$ mm
Number of thread ;	$z_w = 1$
Worm wheel	
Type ;	G1A20R1+6 and G1A20L1
Material ;	Aluminum bronze castings
Gear ratio ;	$i = 20$
Number of teeth ;	$z_2 = 20$
Pitch diameter ;	$d_2 = 20$ mm

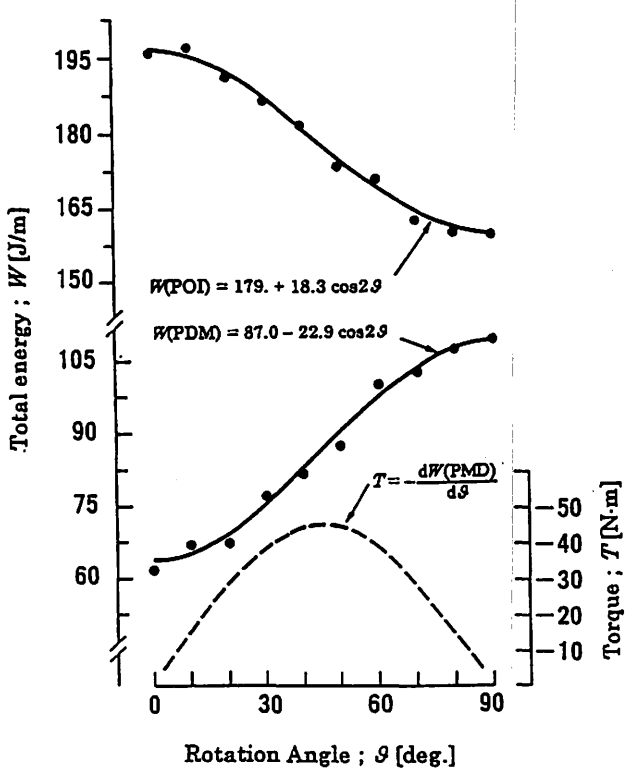

Fig. 1. Calculated total energies W(POI) and W(PMD) as a function of rotation angle θ. These calculated points are fitted by a least-squares method to a function of $a+b$. cos2 θ indicated by solid carves. Calculated torque T using the curvre W(PMD) is also shown by a broken curve. Note that differentiation of T be made with respect to θ in radian.

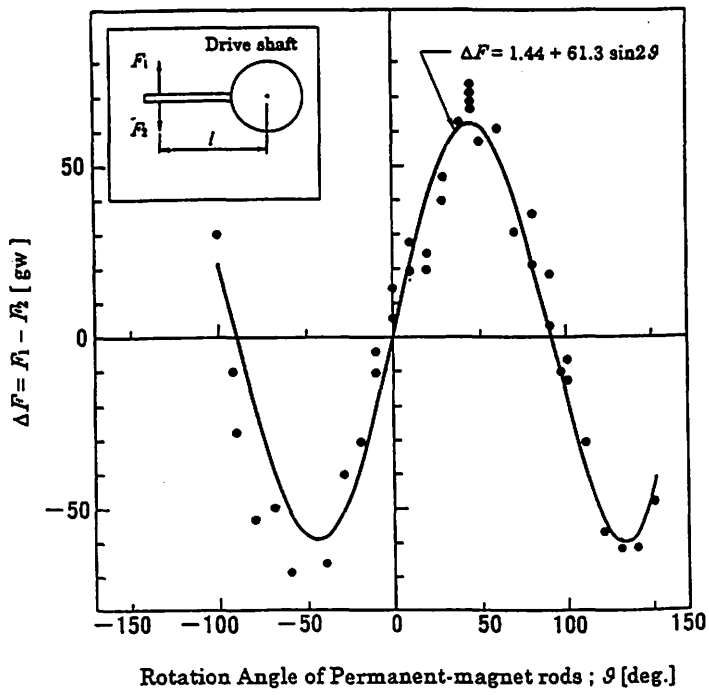

Fig. 2. Diference of the force ΔF(see the text) $\equiv F_1 - F_2$ measured at various rotation angles θ are indicated by solid circles. The curve is a least-squares fit to the data as $\Delta F = a+b.\sin 2\ \theta$.

I. 17. Development of a Negative Ion Source for Unstable Nuclear Beams

Kanai Y., Shinozuka T., Mori Y.**, Fujita M.***, Watanabe A.***, Kohda T.*, Shinto K.****, Takagi A.*****, Yoshii M.*****, Fujioka M.*, and Kotajima K.*

Department of Nuclear Engineering, Tohoku University
*CYRIC, Tohoku University**
*Institute for Nuclear Study, University of Tokyo***
*Department of Physics, Tohoku University****
*Graduate University for Advanced Studies*****
*National Laboratory for High Energy Physics (KEK)******

A negative heavy ion source for unstable nuclear beams is under development on the basis of new concepts to ionize negatively radioactive isotopes. The radioactive nuclei ^{61}Cu(T1/2 = 3.4 hrs) have been ionized negatively with high efficiency and mass-separated by an EMIS (Electro-magnetic Isotope Separator). The negative ionization of the radioactive metal species is the first result in the Isotope Separator On-Line experiments.

There is presently a strong and world-wide interests in the physics which can be studied with radioactive beams. Proposals for RIB(Radioactive Ion Beam) facilities have been put forward in various countries, which are in the various stages of completion. Among the types for RIB facilities the ISOL-type RIB is considered as one of the substantial methods to obtain a highly qualified beam property.

The most crucial part in the R&D (Research and Development) tasks for an ISOL-type RIB facility is on the ion source development. Most works are presently devoted to obtain intense radioactive positive ions. On the other hand, there are few ion sources to obtain the radioactive negative ions, and especially no ion source for negative ionization of radioactive metal species.

We shortly report the ion source development for negative ionization of radioactive species.

The basic design concept for negative ionization is of the plasma sputtering type ion source, which has been developed for high intense negative ion source of stable metal species, copper and gold and so on, at Berkeley, Los Alamos and KEK[1]. This ion source is nicknamed the BLAKE negative ion source. In this ion source, negative ions of stable elements are produced at the metal surface of the converter block which is placed in a Xe plasma confined by a cusp magnetic field generated with Sm-Co permanent magnets. The metal surface is covered with a thin Cs layer (several atomic layers), which is always supplied

with a temperature controlled Cs reservoir. This ion source has proved to give more than 10 mA of Cu- and Au- ion beams. The details of this ion source is described in ref. 1.

The application of the BLAKE ion source to an ISOL was programmed in the following steps.

1. Preparations for negative ion acceleration at CYRIC ISOL (power supplies and a control system).
2. Check of the ionization efficiency by the negatively ionized radioactivities.
3. On-line extraction of negatively ionized radioactive nuclides, which are produced by the cyclotron beam. The radioactivity is:
   - directly produced at the sputtering surface, or,
   - produced at the thick-target oven and transferred to the sputtering surface by evaporation.

All of the power supplies are now equipped for negative ion acceleration, and they are fully computer-controlled by an optical-GPIB system. Interactive operations and monitoring are realized by the software Lab-VIEW[2] on the IBM-PC.

The efficiency of negative ion formation and extraction has been measured by the radioactivity ^{61}Cu($T_{1/2}$ = 3.4 hrs), which was produced in the Ni-converter by the ^{58}Ni(α,p)^{61}Cu reaction. During a sputtering process in the plasma, both stable Ni isotopes and ^{61}Cu radioactive isotope are negatively ionized on the surface of the converter. Two aluminum collection foils are placed just behind the extraction from ion source and behind the magnet for mass-separation, respectively. Four data sets for radioactivity of ^{61}Cu were obtained by a HP(Ge) γ-detector; the two sets are the radioactivities of ^{61}Cu in the converter before and after ion source operation, and the other 2 sets are the radioactivities on the foil behind the extraction and on the foil behind the magnet for mass-separation.

The existence of the radioactivity on the foil after mass-separation shows that the negative ionization has really been realized for Cu radioactivity on the surface of the Ni converter in the ion source. The resulting efficiencies for negative ionization are 2.3 % after extraction and 0.12 % after mass-separation, respectively.

The efficiency for the former is rather competitive in the comparison with the other positive ion sources for metals, but the efficiency for the latter indicates the necessity of improving the ion-optics of our ISOL system. It seems that the space-charge effect has deteriorated the beam transport efficiency, since the stable Ni beam is nearly 1 mA intense just behind the extraction from the ion source. The magnetic quadrupole focusing system are now designed in stead of the einzel lens system for beam transport line behind the extraction region.

The on-line experiment for short half-life radioactivity ^{58}Cu($T_{1/2}$ = 3.2 s) is also presently under progress.

References

1) Mori Y., Rev. Sci . Instr. 63 (1992) 2357-2362.
2) Labview, National Instrument Corporation, (1993).

I. 18. Characteristics of Au-Si Nuclear Detectors Irradiated by 10 MeV α-Rays

Ohba K., Kudoh Y., Mito A., Wakamatsu M., Shoji T., Hiratate Y., Ishii K. and Tohei T.***

Department of Electronics, Tohoku Institute of Technology
*Cyclotron and Radioisotope Center, Tohoku University**
*Department of Physics, Tohoku University***

Introduction

The Au-Si surface barrier nuclear detectors have shown good performance for the charged particle detection. However, radiation damage in the semiconductor detector is serious problems because of the effect of carrier trapping with deep levels[1-4].

The purpose of this report is to investigate the irradiation effects of the detectors bombarded by 10 MeV α-rays. Degradation characteristics are studied by I-V(current-voltage), C-V(capacitance-voltage), radiation counting response and DLTS[5](deep level transient spectroscopy) measurements.

Experimental

The Au-Si surface barrier nuclear detectors used in this study were fabricated from phosphorus doped n-type Si wafer with a resistivity of about 2 kΩ-cm and thickness of 400 μm. After removing the oxidized layer of the one side of the Si specimens(9 mmϕ), in order to make the rear ohmic contact, the aluminum spattering was carried out. The front surface barrier contact was formed by the evaporation of gold.

The detectors were irradiated with α-rays by using the Tohoku University Cyclotron. The irradiations with the 10 MeV α-rays were carried out perpendicularly on the Au surface side of the detector in the vacuum chamber at room temperature. The irradiation doses were up to 5.5×10^{10}n/cm^2.

In order to study the irradiation effects on the detectors, the reverse current, capacitance, counting response to ^{241}Am α-rays(5.48 MeV) and DLTS were measured before and after irradiation. The DLTS is a capacitance transient thermal scanning method at high frequency(1 MHz) and is used to determine the energy levels of deep traps in semiconductors.

Results and Discussion

In the I-V measurements, it was observed that the reverse currents increased after irradiation and with increasing of the α-ray irradiation doses. It is thought that the increasing

of the reverse currents is due to the carrier generation through the irradiation defect-states introduced in the depletion layer of the detector.

Figure 1 shows the C-V characteristics before and after irradiation with the 10 MeV α-rays. As seen in this figure, when the bias voltage is over 10 volts, the C-V characteristics after irradiation does not decrease in proportion as the bias voltage increases. This phenomenon is thought as next. Since the depletion layer width of the detectors for the 10 V bias corresponds to the range(70 μm) of the 10 MeV α-rays in the Si and the induced defect density is condensed in this region as shown by the profile of the Rutherford scattering cross section, the depletion layer does not increase, and consequently, the capacitance does not decrease even if the bias voltage increases.

Counting response of the detector to ^{241}Am α-particles at 20 V bias is shown in Figure 2, before and after irradiation. After irradiation with the α-ray fluxes of $5.5\times10^{10}n/cm^2$, the spectrum is markedly degraded. Small peaks at 5.44 MeV and 5.39 MeV disappear, and the peak position shifts toward the lower channel numbers. The full width at half maximum(FWHM) of the spectrum before irradiation is 26.2 keV, but after irradiation, FWHM becomes 78.4 keV. As this reason, it is thought that the carrier collection efficiency became degraded due to the trapping centers which were introduced by irradiations.

From the DLTS measurements, two energy levels are observed. The energies of two levels are estimated as 0.38 eV and 0.52 eV to the conduction band, respectively. It is thought that the 0.38 eV and 0.52 eV level are the states due to the divacancy and the interaction between divacancy and oxygen, respectively.

Acknowledgment

The authors wish to thank to the staff members of CYRIC for operating the Cyclotron.

References

1) Coleman J. A. et al., IEEE Trans. Nucl. Sci. NS-**15** (1968) 363.
2) Chisaka H., JPN. J. Appl. Phys. **12** (1973) 439.
3) Kraner H. W., IEEE Trans. Nucl. Sci. NS-**29** (1982) 1088.
4) Ohba K. et al., IEEE Trans. Nucl. Sci. NS-**30** (1983) 371.
5) Lang D. V., J. Appl. Phys. **45** (1974) 3023.

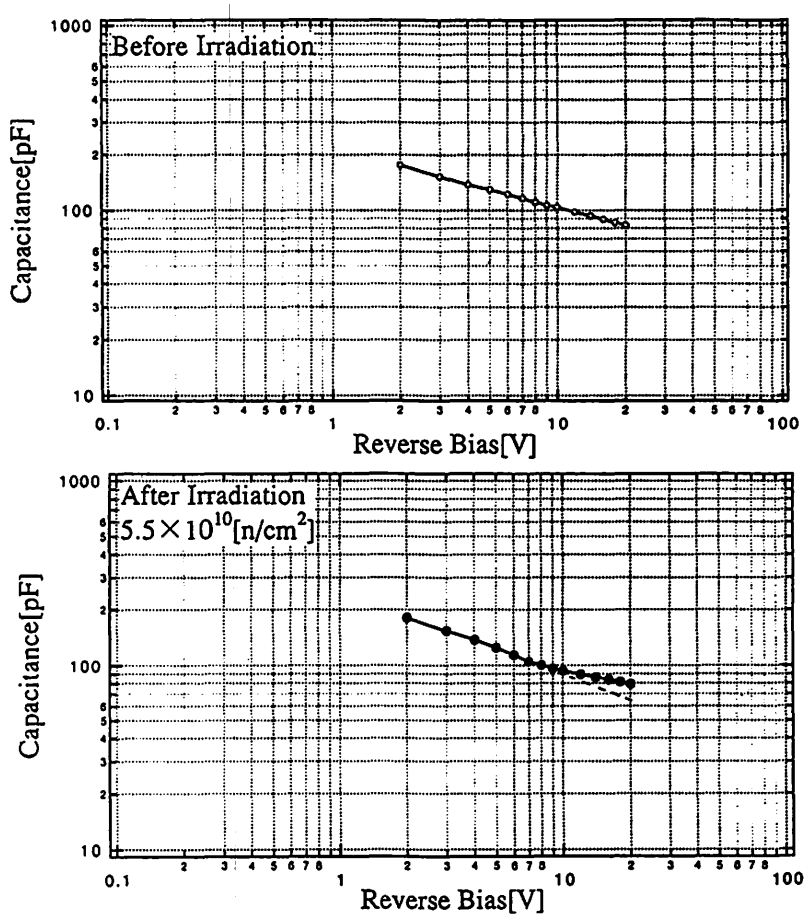

Fig. 1. Capacitance-voltage characteristics before and after irradiation with 10 MeV α-rays.

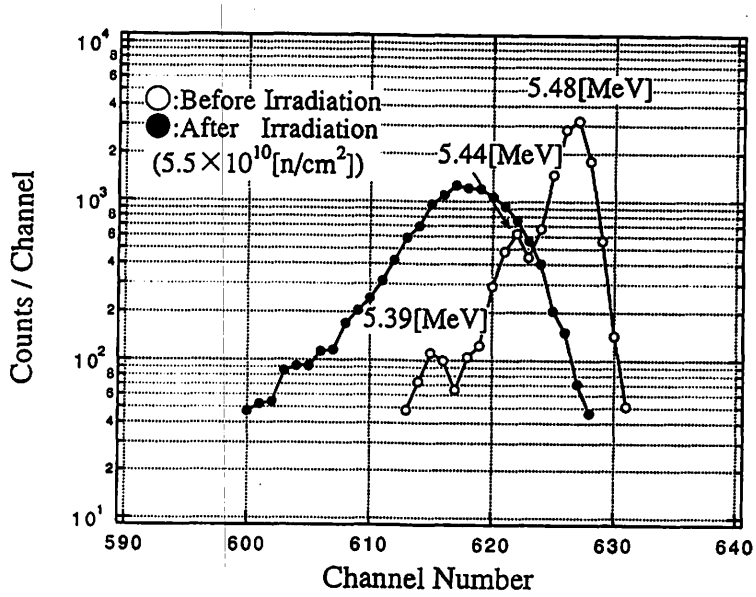

Fig. 2. Counting response to ^{241}Am α-rays(5.48 MeV) before and after irradiation with 10 MeV α-rays.

I. 19. The Influence of Helium on High Temperature Strength of Fe-15Cr-20Ni Austenitic Stainless Steel for Fast Reactor Applications

Hasegawa A., Abe K., Satou M., Kudoh Y., Briyatmoko B., and Masuda N.

Faculty of Engineering, Tohoku University

Introduction

Type 316 austenitic stainless steels have been used for fuel cladding materials of fast breeder reactor such as Monju, a Japanese prototype fast breeder reactor. Maximum irradiation damage of cladding material in Monju will be about 115dpa and maximum temperature is 773K[1]. In a future power reactor, total amount of damage will be higher than 150dpa and helium contents will be higher than about 200appm[2], therefore, further improvement of void swelling resistance, creep strength, high temperature strength and corrosion resistance will be required. The PNC1520, which is a Fe-15Cr-20Ni base alloy, is one of the candidate alloys for the power reactor[1].

The purpose of this work is to study the helium effect on high temperature tensile behavior of Fe-15Cr-20Ni model alloy from the stand point of view of basic study to apply the alloy development by clarifying temperature dependence of tensile behavior of solution annealed specimen.

Experimental

The chemical compositions of Fe-15Cr-20Ni austenitic stainless steel is given in table 1. The Fe-15Cr-20Ni alloy was supplied by PNC (Power Reactor and Nuclear Fuel Development Corporation). The specimens were annealed at 1293K for 120sec in avacuum-shield quartz tube for solution annealed treatment.

Helium implantation was carried out using 36MeV helium ion beam of the cyclotron in CYRIC. A tandem-type energy degrader system was used to obtain uniform helium distribution along the implanted direction. The total amount of helium in a specimen was evaluated to be approximately 100appm for 12h irradiation and the level of displacement damage was 0.04dpa. The He concentrations of 5 and 30appm specimens were also prepared. Maximum specimen temperature during the implantation was kept below 429K.

After implantation, tensile tests were conducted from room temperature to 1123K in a vacuum furnace (1×10^{-4}Pa) with an Instron-type testing machine. Fracture surfaces of

ruptured specimen were examined in a scanning electron microscope(SEM). The detail of the experimental condition has been described elsewhere[3].

Results

Results of 0.2% proof stress (yield stress:σ_y) of unimplanted and helium implanted specimens are shown in figure 1. Yield stress increase by the 100appm helium implantation is observed at room temperature and the σ_y decreased with increasing test temperature but it did not fully recover even at 1123K. Figure 2 shows temperature dependence of total elongation of helium implanted and unimplanted specimens. Reduction of total elongation by helium implantation is observed at all test temperatures, but remarkable decrease of elongation is observed above 723K. Temperature dependence of uniform elongation is almost the same as that of total elongation.

Figure 3-a shows fractograph of the 100appm helium implanted specimen tested at 698K. Fracture mode of figure 3-a is transgranular mode and it shows ductile behavior. Fracture mode of unimplanted specimen was transgranular and had large reduction-of- area at all the test conditions. Figure 3-b shows the fractograph of 100appm helium implanted specimen tested at 923K. Fracture mode of Figure 3-b is intergranular mode. It is a typical fractograph of brittle specimen. Intergranular fracture surface was observed in the implanted specimen tested above 723K. The results show that significant reduction of elongation above 723K is caused by the grain boundary fracture. Therefore, the fraction of grain boundary fracture surface to the total fracture surface can be considered a indication of the extent of helium embrittlement under each testing conditions[3,4].

Figure 4 shows the relationship between fraction of intergranular fracture and helium concentration at various temperatures. It shows the helium embrittlement strongly depends on helium concentration and testing temperature. The results and estimation method of this work will contribute to estimate the effects of alloying elements or heat treatment on suppression of helium embrittlement.

Acknowledgement

The authors would like to thank to the staffs of the CYRIC cyclotron for their cyclotron operation and beam transport.

References

1) Shikakura S. et al., Nihon Genshiryoku Gakkaishi, .36, (1994) .451.
2) Ukai S. et al., Proc. of the 2nd Japan/China Symposium on Materials for Advanced Energy Systems and Fission and Fusion Engineering, June 5-8, 1994, pp.81-86.
3) Hasegawa A. et al., Proc. of the 2nd Japan/China Symposium on Materials for Advanced Energy Systems and Fission and Fusion Engineering, June 5-8 ,1994, pp.359-362.
4) Hasegawa A. et al., Materials Trans. JIM **34** (1993) 1090.

Table 1. Chemical compositions of Fe-15Cr-20Ni (wt%).

Cr	Ni	C	N	O	Si	P
15.02	20.17	0.006	0.0017	0.009	<0.005	0.0009
S	Mn	Al	Co	Cu	Fe	
0.002	<0.001	0.002	0.003	<0.001	bal.	(wt%)

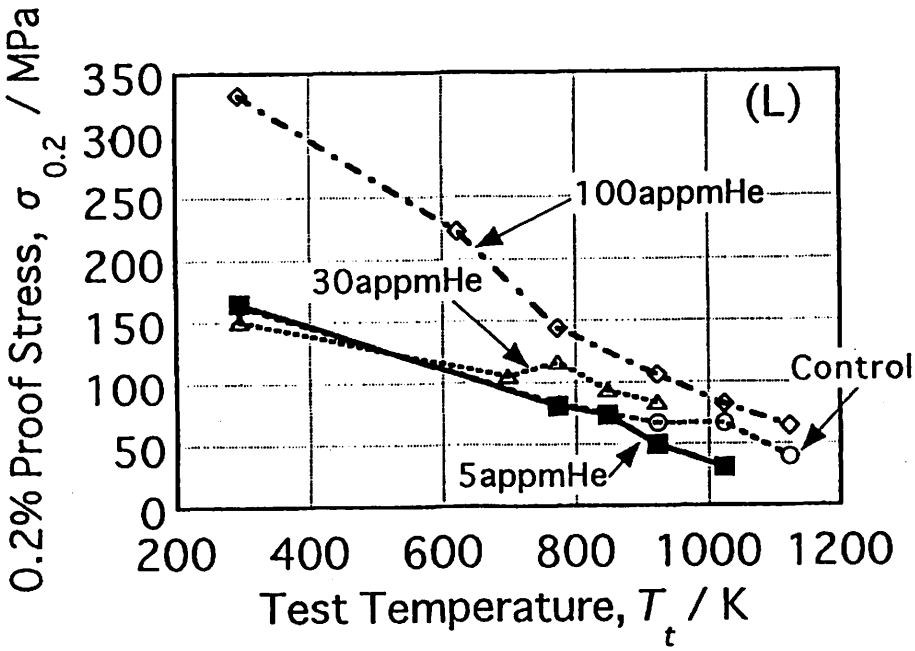

Fig. 1. Helium effects on proof stress.

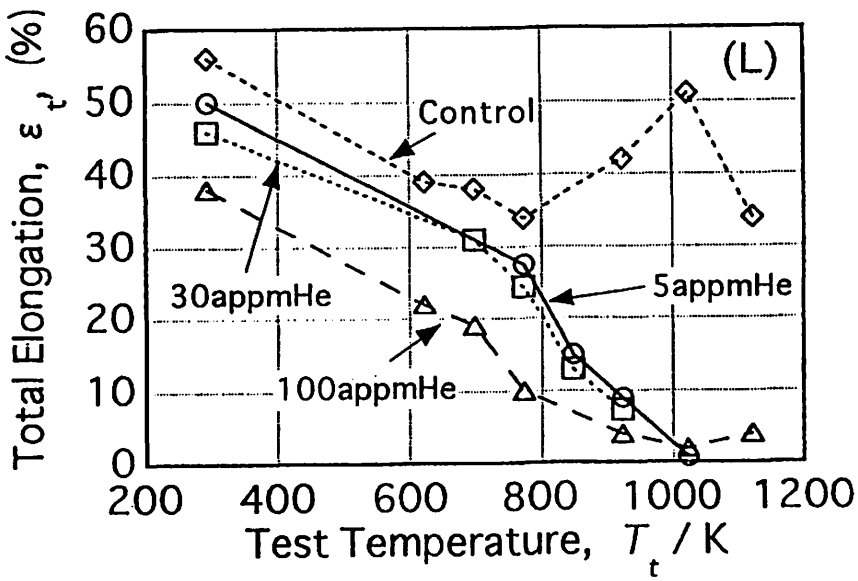

Fig. 2. Helium effects on total elongation.

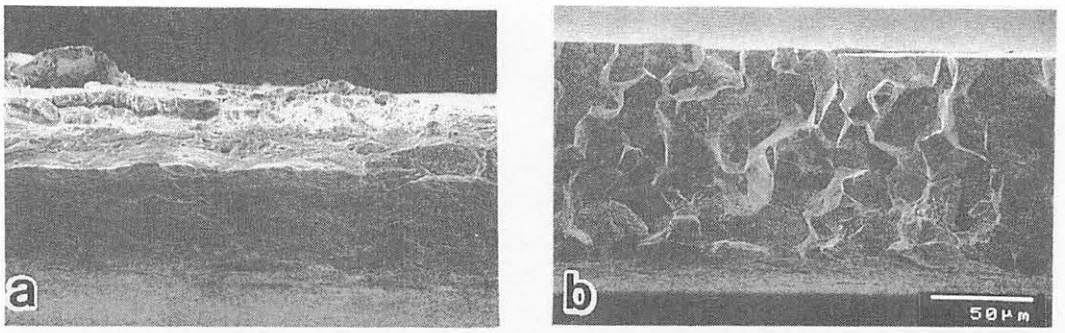

(a) tensile tested at 698K (b) tensile tested at 923K.

Fig. 3. SEM micrographs of 100appm He implanted and tensile tested specimens.

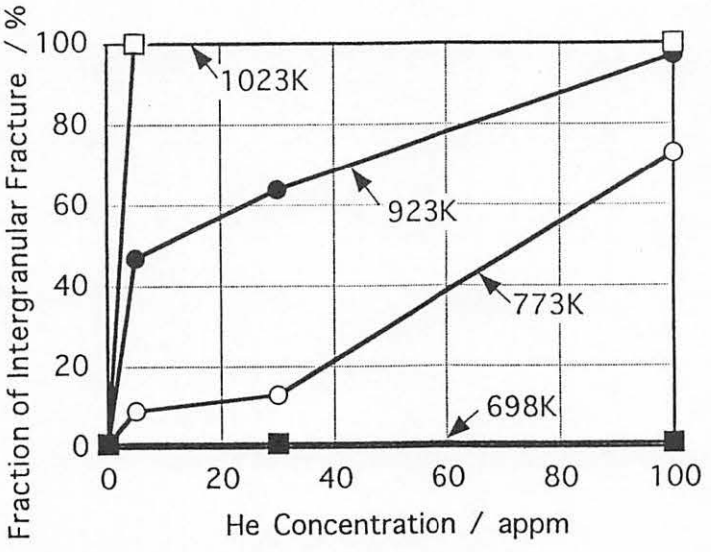

Fig. 4. Relationship between helium concentration and fraction of intergranular fracture at various test temperatures.

(a) Ductile fracture at 77K

(b) Brittle fracture at 673K

Fig. 3. SEM micrographs of 10Cr2Mo steel showing (a) ductile and (b) brittle fracture modes.

Fig. 4. Relationship between helium concentration and fraction of intergranular fracture at various test temperatures.

I. 20. Study on the Compton Scattering for Tohoku 3D PET

Watanuki S., Ishii K., Itoh M., Takahashi S., and Orihara H.*

Cyclotron and Radioisotope Center, Tohoku University
*Shimadzu Corporation**

Introduction

By the use of crystal blocks[1], Positron Emission Tomography (PET) has been much improved[2,3] in the space resolution and the range of axial view. PETs with a wide axial view of 15~20cm have recently been developed for 3 dimensional data acquisition (:volume measurement of positron γ rays).

A new PET system (Shimadzu SET 2400W), which has the axial view of 20cm and 32 slices was recently installed in Cyclotron and Radioisotope Center. In addition to 2 dimensional data acquisition, 3 dimensional data acquisition can be performed with this system(:3D PET). Using the 3 dimensional data, we can obtain a volume image by a technique of 3 dimensional image reconstruction. The sensitivity of this method will be 5~10 times higher than that of a usual method (:2 dimensional deta acquisition)[3]. However, corrections for the Compton scattering, detector efficiency and attenuation lie as troublesome problems on 3D PET. Among them the correction for the Compton scattering is very important for the quantitative analysis in PET study[4]. Up to the present, some methods for this correction were proposed and examined but they were not satifactory. A novel technique for this correction is now in progress at our institute. We studied the effect of the Compton scattering in PET system and examined availability of our new technique.

Experimental

Figure 1 shows a coincidence circuit for the Compton scattering measurement. The lower discri level of SCA(:Single Channel Analyser) was changed in accordance with demmand, but the upper discri level was fixed to be 650 keV during the experiment. The scattered γ rays were detected with two BaF_2 scintilators of 10mm diameter and 50mm length, which can rotate about a central axis. A positron source of ^{22}Na of 100 μCi was placed on the center axis, and, as a γ-ray scatterer, a water phantom of 20cm diameter and 25cm depth was used (see Figure 2 (a)). To measure the contribution of one detector, we shielded one of the detectors with a lead collimator (see Figure 2 (b)). If a lead rod is placed in front of a detector, normal coincidence measurements are prevented and the scattered

coincidence events are mainly detected. This is our idea to measure the scattered coincidence events. We placed a lead rod of 10mm diameter and 20cm length at an edge of the phantom (see Figure 2 (c)) to investigate an effect of this rod on the Compton scattering data.

Results and discussion

Figure 3 (a) shows the angular distributions of the Compton scattering in air and in the phantom under the condition of Figure 2(a), where the lower discri level of SCA was 300keV for each detectors. In this figure, we can see the contribution of the Compton scattering spreading over wide angles and it is approximately 1% of the total coincidence events for a detector pair. However, this effect becomes remarkable because the contributions of the Compton scattering from a whole of hot area are integrated over a LOR. For an example, the hot area of Figure 2(a) is approximated to be 0.125 cm^3 $(=(0.5cm)^3)$ from the detector size, and the contribution of the Compton scattering for the hot area of $8cm^3$ is estimated to be 60% of the total coincidence events. Figure 3 (b) shows the angular distributions as a function of the lower discri level of SCA in a case of the phantom. The dashed line represents a simple calculation for the Compton scattering. The agreement between the theory and the experiment is very good in the region of forward angles and the contributions at large angles (>60°) would be due to the Compton scattering from bound electrons. If photons are scattered mainly at the position of half width of the phantom, the maximum scattering angles are calculated to be 107.6°, 54.1° and 30.4° for the discri levels of 200keV, 300keV, and 400keV, respectively. The dependence on the discri levels in Figure 3 (b) is quite consistent with this prediction. The experimetal result obtained under the condition of Figure 2 (b) is shown in Figure 3 (c). Here, the discri level of SCA was 200keV. The Compton scattered events in the region of scattering angle over 10° are reduced with the lead collimator, however in the region of small angles the coincidence events with the collimator are a little lager than those without the collimator. This increase must be due to the conribution of the Compton scattering in the lead collimator, therefore the Compton scattering in crystal blocks should be corrected in the PET system. Figure 3 (d) shows a result obtained under the condition of Figure 2 (c). The intensity of normal coincidence events is well reduced with the lead rod, whereas that of the scattered coincidence events does not change. This is a very convenient result for the measurement of the Compton scattering with our technique.

Summary

The Compton scattering has been studied on the PET system and it was pointed out that the contribution of this effect is significant in the image of 3D PET. A technique for measurement of the Compton scattering was examined and it is confirmed that this is a useful technique for the correction of Compton scattering.

References

1) Casey M. E., et al., IEEE Trans. NS **33** (1986) 460.
2) Evans A. C., et al., IEEE Trans. ME **10** (1991) 90.
3) Wienhard K., et al., J. Comp. Asst. Tomogr. **16** (1992) 804.
4) Cherry S. R., et al., J. Nucl. Med. **34** (1992) 671.

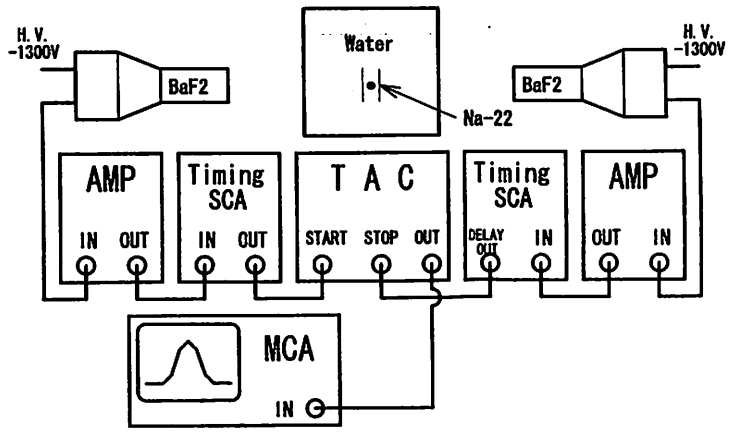

Fig. 1. Coincidence measurement system with Baf_2 scintilators for positron annihilation γ rays.

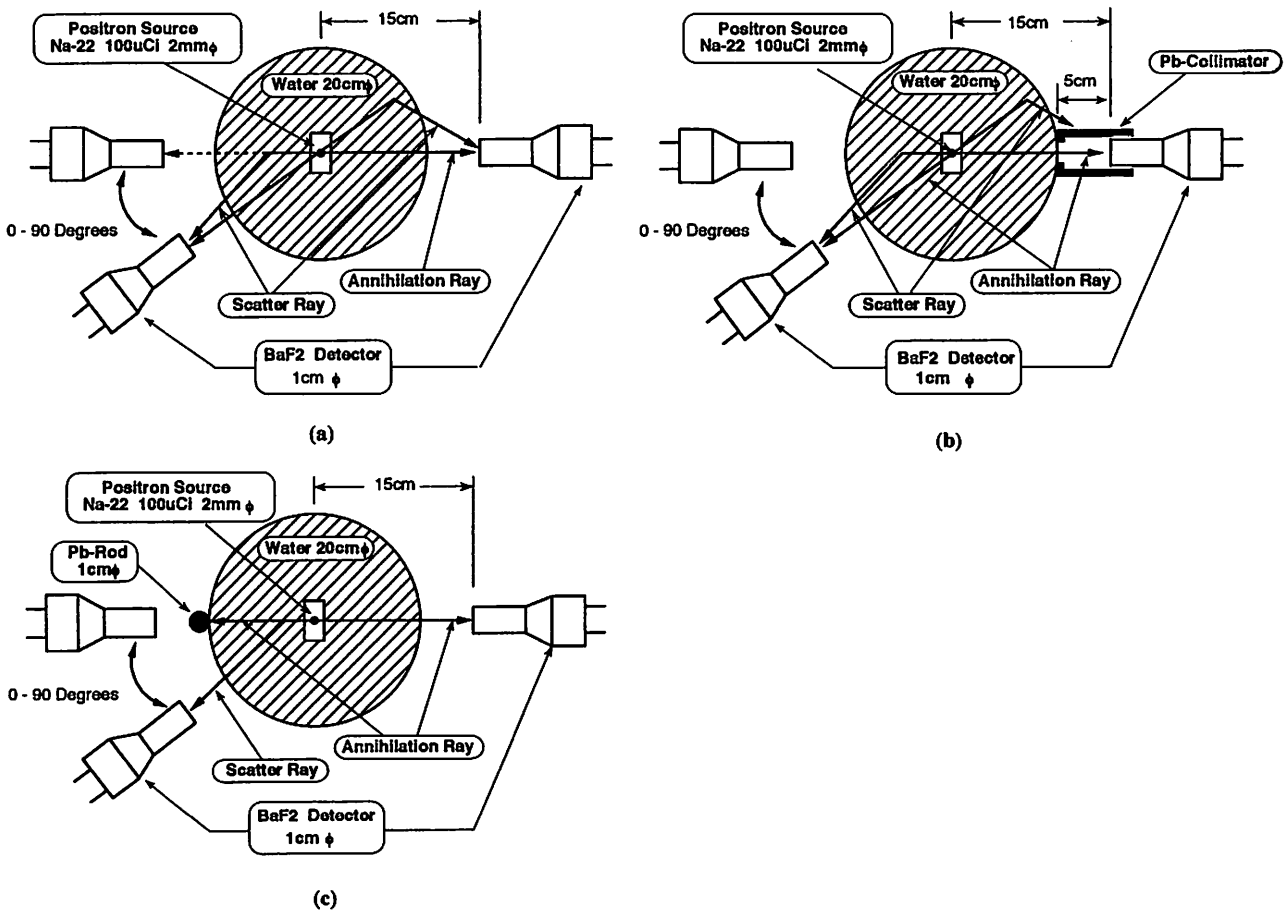

Fig. 2. Detection geometries for measurement of the Compton scattering.

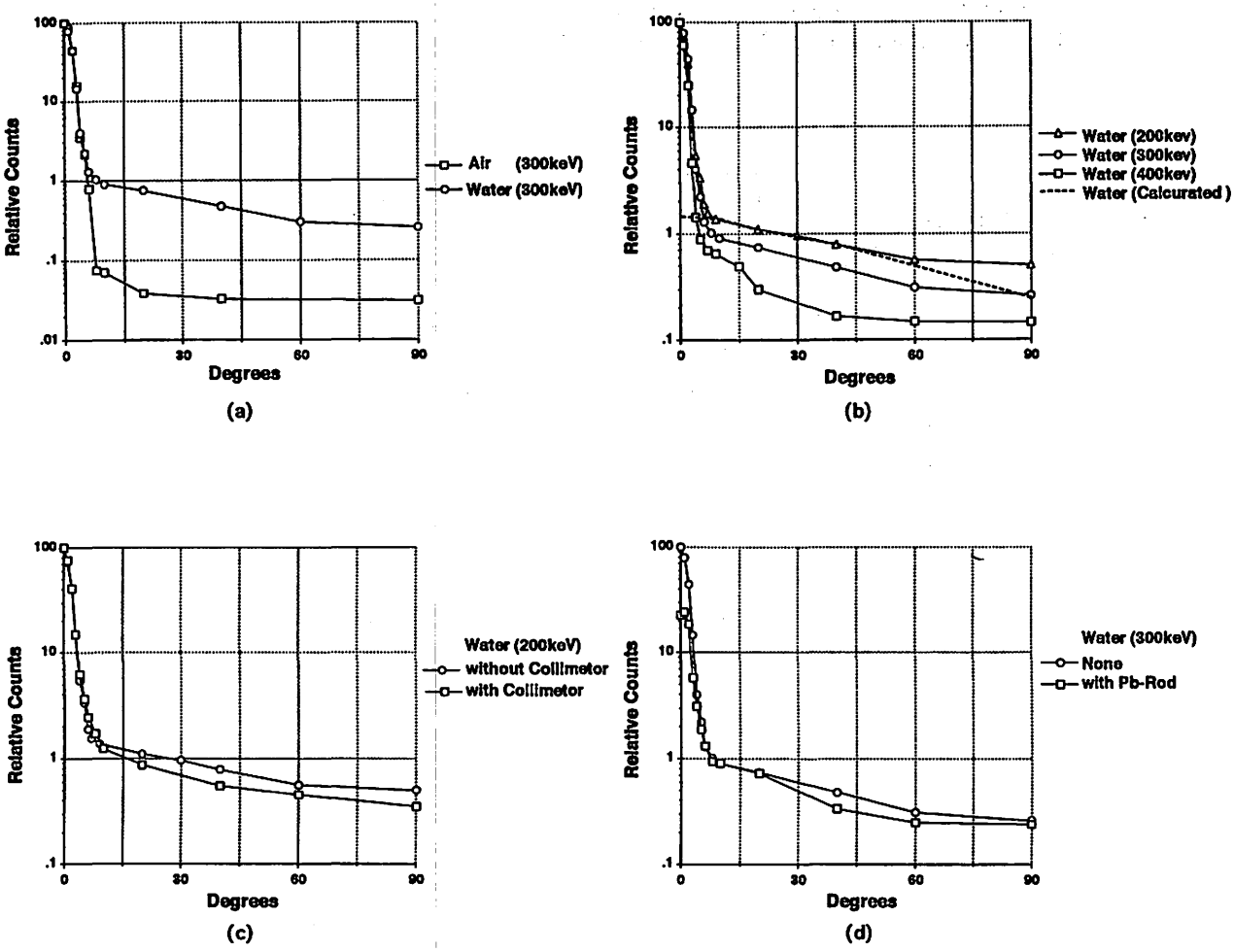

Fig. 3. Angular distributions measured under the detection conditions in Fig. 2 .

I. 21. Application of Neural-Network Technique to Analysis of PIXE Spectra

*Iwasaki S., Fukuda H., Yoshizaki K., Kitamura M., and Ishii K.**

Department of Nuclear Engineering, Tohoku University
*Cyclotron and Radioisotope Center, Tohoku University**

Introduction

Recently, artificial neural network techniques have been developed and successfully applied in the spectrum analysis in various fields. We have also proposed a analysis method based on the linear associative neural network (LANN) technique for the high speed analysis of the gamma-ray spectrum[1,2]. The principle of the LANN is very simple and calculation is very fast. In this paper, the LANN technique is introduced as a new method for the PIXE spectrum analysis; the method has high potential for the analysis in the on-line real-time and/or automatic modes.

LANN Method

The principle of the LANN technique has been described elsewhere,[1,2] but brief explanation is given here. The LANN can realize the direct mapping of the observed pulse height spectrum to elemental content of samples. Namely, the function of the network is the linear transformation of an input vector $\boldsymbol{x}=[x_1, \ldots\ldots, x_n]^T$, where T denotes the transposition and x_i is counts of channel i of the objective pulse height spectrum, to another space vector $\boldsymbol{y}=[y_1, \ldots, y_m]^T$, where y_j is the concentration of element j in the sample, as shown schematically in Figure 1. The mapping is carried out just by multiplying the mxn weight coefficients matrix **W**, whose elements are gained by the learning phase of the network before the analysis, to $\boldsymbol{x}$ as $\boldsymbol{y}=\mathbf{W}\boldsymbol{x}$. The values of the matrix elements of **W** are determined to satisfy the condition: $\|\mathbf{Y}-\mathbf{WX}\|^2=\min$.[3,4], where the nxm matrix **X** consists of $\boldsymbol{x}_j$'s, the reference spectra of the each element j's, and the mxm matrix **Y** consists of output $\boldsymbol{y}_j$'s corresponding to $\boldsymbol{x}_j$'s; for j=1, m, $\boldsymbol{y}_j$ is usually taken as a unit vector $\boldsymbol{y}_j=[y_{1j}=0, \ldots, y_{jj}=1, \ldots, y_{mj}=0]^T$. Thus, **Y** is a unit matrix, and the matrix **W** turns out to be $\mathbf{X}^+$: the Moore-Penrose pseudo-inverse matrix of **X**. The matrix elements of **W** are usually obtained by a supervised learning method of the network called Widrow-Hoff[4], or by a pure mathematical algorism.

Experimental

We conducted performance test of this method for two types of samples: the first ones were mixed metal samples consisting of iron and nickel of various compositions, and the other one was a thin SUS 316 sample. Here we show only the results for the SUS 316 sample. A sample of SUS316 and pure metal samples of chromium, manganese, iron and nickel, the principal elements of the SUS316 (a trace element copper not included) were prepared by the evaporation method on Mylar films in vacuum. The experiment was carried out in the PIXE course at Cyclotron and Radioisotope Center, Tohoku University using a proton beam of 3 MeV. We employed a graphite collimator of 3-mm diameter to limit the size of the proton beam on the samples. The beam after passing through the samples stopped in a Faraday cup at 3 m behind the sample position. A 100-μm Mylar absorber was inserted between the sample and X-ray detector to suppress the strong Bremsstrahlung continuum and elastically scattered protons. X-rays emitted from the samples were observed by a conventional type Si(Li) detector in the direction of 90 deg. with respect to the incident beam. The pulse signals were analyzed by a 1024-ch PHA, and the data were stored in a bulk memory of a micro-computer. We have measured a set of spectra for all alloys as well as the single elemental samples, and a sample of backing film alone.

Spectrum Analysis

First, we constructed an LANN having 1024 input units and 5 output units corresponding to the four principal elements of SUS316: Cr, Mn, Fe, and Ni, and Mylar backing. The reference spectra for the network learning were made by subtracting the Mylar data from each metal sample data after normalization by Coulomb numbers of the proton beam bombarded. Here, we adopted a conventional single-spectrum learning method[2]. The analysis of the objective spectra from the Fe-Ni alloys and SUS316 were made just by feeding those to the network.

The output of the LANN is compared to those of the peak fitting analysis using a sophisticated code SAPIX[5] as shown in Figure 2. Error bars for both results in the figures are due to the statistical uncertainties. The uncertainties for the network output dy_j's were evaluated by the following formula as variance matrix,

$$\langle dy\,dy^T\rangle = W\langle dx\,dx^T\rangle W^T,$$

where <.> denotes the ensemble average, $dy = W\,dx$, and $dy^T = dx^T W^T$. We adopted the assumption of independence between counts in each channel as follows,

$$\langle dx_i\,dx_k\rangle = (x_i x_k)^{1/2}\delta_{ik} \quad (\delta_{ik}=1, \text{ if } i=k;\ =0, \text{ otherwise}).$$

Both results are almost consistent for the Fe and Ni alloys. As for the SUS316, the agreement is good except the manganese case ((1) of Figure 2 for SAPIX). In the manganese case, the SAPIX result is not correct because the resulting K_β/K_α value for manganese is far from the data base value given in (Ref.6). In the network analysis, the K_β/K_α is in principle assured because the both K_α and K_β peaks were included in the experimental observed reference spectrum used for the network learning. Figure 3 presents the comparison of the constructed spectra using the output of the network and the reference spectra data with the objective SUS spectrum. Excellent agreement is shown except the small discrepancy both in the lower and higher tails of the Ni-K_β peak that correspond to the K_α and K_β peaks of copper, respectively, not included in the reference spectra as mentioned above. The simple use of the SAPIX code could not correctly resolve the overlapping of Cr-K_β and Mn-K_α peaks. These two peaks were too close with each other, and the separation problem was quite ill-posed. Conversely using the data of K_β/K_α for these elements, another result for Mn could be obtained as SAPIX(2) (Figure 2), and is consistent with the network result. Such additional information was necessary to resolve the ill-posedness. The present network analysis is almost free of this kind of problem because the each reference spectrum includes all X-ray peaks of a single element, not only peaks of K-X lines but also of L- and M-lines, if observed; whereby the independence among the spectra for the different elements is very high.

More detailed description on the present method and tests is given elsewhere[7].

Acknowledgments

The authors express their thanks to the member of the cyclotron crew at Cyclotron and Radioisotope Center, Tohoku University, and to Dr. K. Sera, Iwate Medical University, for the SAPIX code.

References

1) Iwasaki S., Fukuda H., and Kitamura M., Intelligent Engineering Systems Through Artificial Neural Networks, 3 (1993) 199 (ASME Press, New York).
2) Iwasaki S., Fukuda H., and Kitamura M., Internat. J. PIXE, 3, No.3 (1993) 267.
3) Kohonen T. , Self-Organization and Associative Memory, (Springer-Verlag, Berlin, 1984).
4) Hecht-Nielsen R. , Neurocomputing, (Addison-Wesley Pub. Co., New York, 1990).
5) Sera K., et al., Internat. J. PIXE, 2, No.3 (1992) 325.
6) Johansson S. A. E. and Campbell J. L., PIXE: A Novel Technique for Elemental Analysis, (John Wiley & Sons, Ltd., Chichester, 1988).
7) Iwasaki S., et al., Internat. J. PIXE, to be published in Vol. 4, Nos. 2&3.

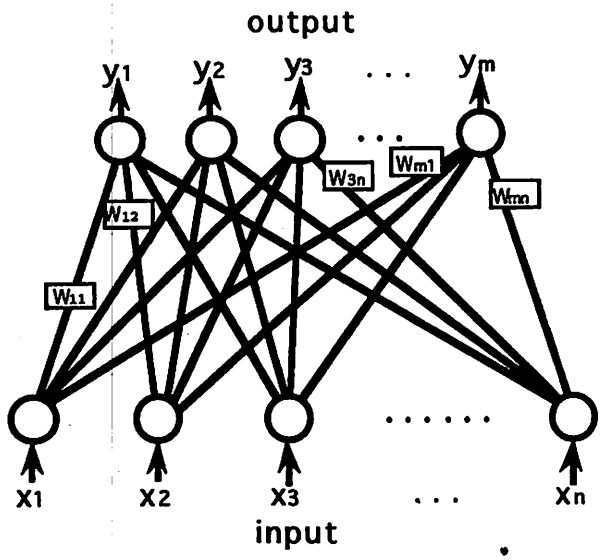

Fig. 1 Structure of linear associative neural network for the spectral analysis. The symbol (O) represents a unit of the network, and w_{ji} is weight coefficient of unit j for i input value.

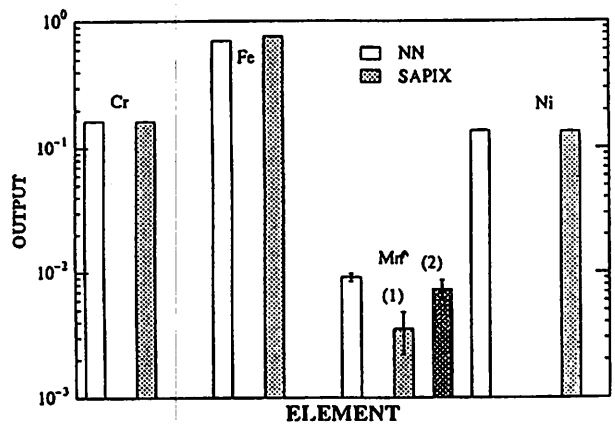

Fig. 2 Comparison of the results for SUS 316 with those of the SAPIX code. See text for the two results (1) and (2) of manganese.

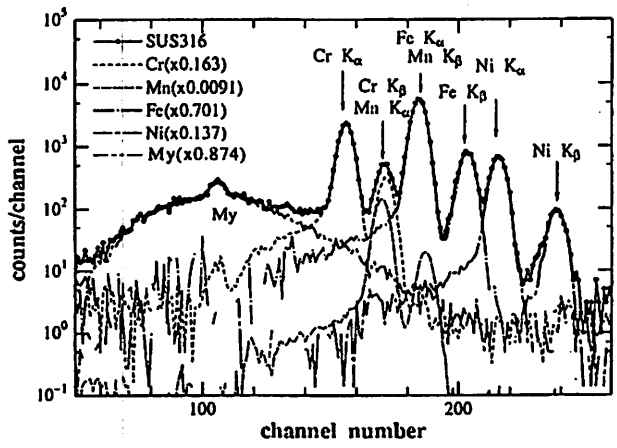

Fig. 3 Comparison of the spectrum for the SUS 316 (see. Fig. 2) with the reconstructed ones.

II. CHEMISTRY

II. 1. Extraction Behavior of Technetium(Vll) in the Primary Amine - Heptane - Aqueous (H, NH_4)F Solution System

Ito K.

Institute for Advanced Materials Processing, Tohoku University

Technetium-99 is one of the fission products produced in a nuclear reactor and has a very long half-life(210,000 y) and long β-activity decay chain. Primary amine extraction is favorable for the separation of technetium from uranium in a nitric acid solution[1,2] and in a hydrofluoric acid solution[3]. The extraction behavior of technetium(Vll) in a primary amine (Primene JMT) - heptane containing 1-octanol - aqueous fluoride solution system has been studied for the purpose of obtaining enhanced extraction of Tc by the determination of distribution ratios (D_{Tc}) and of volume ratios (R) between the organic and aqueous phases, and of pH.

The Primene JMT in heptane solution was mechanically shaken for 1 h at 25 °C with an equal volume of aqueous solution containing $^{95m}TcO_4^-$. After equilibration, the aqueous and organic phases were separated by centrifugation, and portions of the two phases were submitted to γ-counting $^{95m}TcO_4^-$ using a well-type NaI(Tl) scintillation counter. From the values, the distribution ratios were determined. The volume ratios were measured from the total volumes of organic and aqueous phases after equilibration. The pH measurements were carried out using a plastic strip derived from MACHERY-NAGEL Co. Ltd. Germany.

Changes of the distribution ratio of technetium(Vll) and of the volume ratio between organic and aqeous phases in the solvent extraction process are indicated in Figure 1-(a) as functions of concentrations both of Primene JMT in heptane solution and of hydrofluoric acid in 1M (H, NH_4)F aqueous solution. The values of volume ratios remained nearly constant at unity in the Primene JMT concentration region of below 0.26 M, however, the decrease of R values corresponded to that of D_{Tc} values except in the case of 0.1M HF - 1M (H, NH_4)F. In the decreasing region of R and D_{Tc}, the reaction mixture produced a micelle, which dissolved in the aqueous phase, increasing the aqeous phase volumes. When using 0.1M HF, this third phase did not occur, however, the distribution ratios reached not more than 50 in the technetium extraction stages.

Replacement, in the organic phase, of single heptane by a mixed solvent of heptane and 1-octanol, upgraded extraction performance in the case of 0.5M HF as shown in Figure 1-(b). Moreover the organic volume reveals a swelling of the organic phase, indicating the

increase of R values as shown in Figure 1-(b). The swelling of the organic phase indicates the formation of microemulsion[4].

In the Primene JMT concentration region of over 0.65 M, the pH values were nearly neutral, indicating poor amine extraction performance, since amine extraction needs protons. The low D_{Tc} values in the solution of 0.1M HF in 1M (H, NH_4)F appears to be responsible for the nearly neutral pH region of the aqueous phase as indicated in Figures 1-(a) and (b).

The effects of 1-octanol concentration in a heptane solution on the extraction performance at different concentrations of Primene JMT are shown in Figure 2. The figure indicates the changes of the D_{Tc} and R values with the concentrations of both Primene JMT and 1-octanol in the technetium extraction from aqueous 0.5M HF -1M (H, NH_4)F solution. The volume ratios increased steadily with the Primene JMT concentration in the JMT concentration region of over 0.65 M, and decreased with the increase of 1-octanol concentration. The D_{Tc} values at any given level of Primene JMT concentration decreased slightly with increasing 1-octanol percentages, which agreed with the results of the study by S.Yu[5]. The rate of increase for R decreased with increasing 1-octanol percentages in the organic phases.

References

1) CURE: Clean Use of Reactor Energy, WHC-EP-0268, (1990).
2) Ito K.; J. Radioanal. Nucl. Chem., Article, **171**, No.2 pp.371-382 (1993).
3) Ito K., Y. Akai-Imoto: J. Radioanal. Nucl. Chem., Article, **178**, No.1 pp.41-53 (1994).
4) Osseo-Asare K., Sep. Sci. Technol., **23**, pp.1269-1284 (1988).
5) Yu S., Wu Z. and J. Chen, *Iron removal from sulfuric acid solution by solvent extraction with mixtures of extractants*, pp. 334 - 352 in the *IRON CONTROL IN HYDROMETALLUGY*. Ed. by Dutrzac J. E. and Monhemius A. J., John Wiley & Sons, New York, 1992.

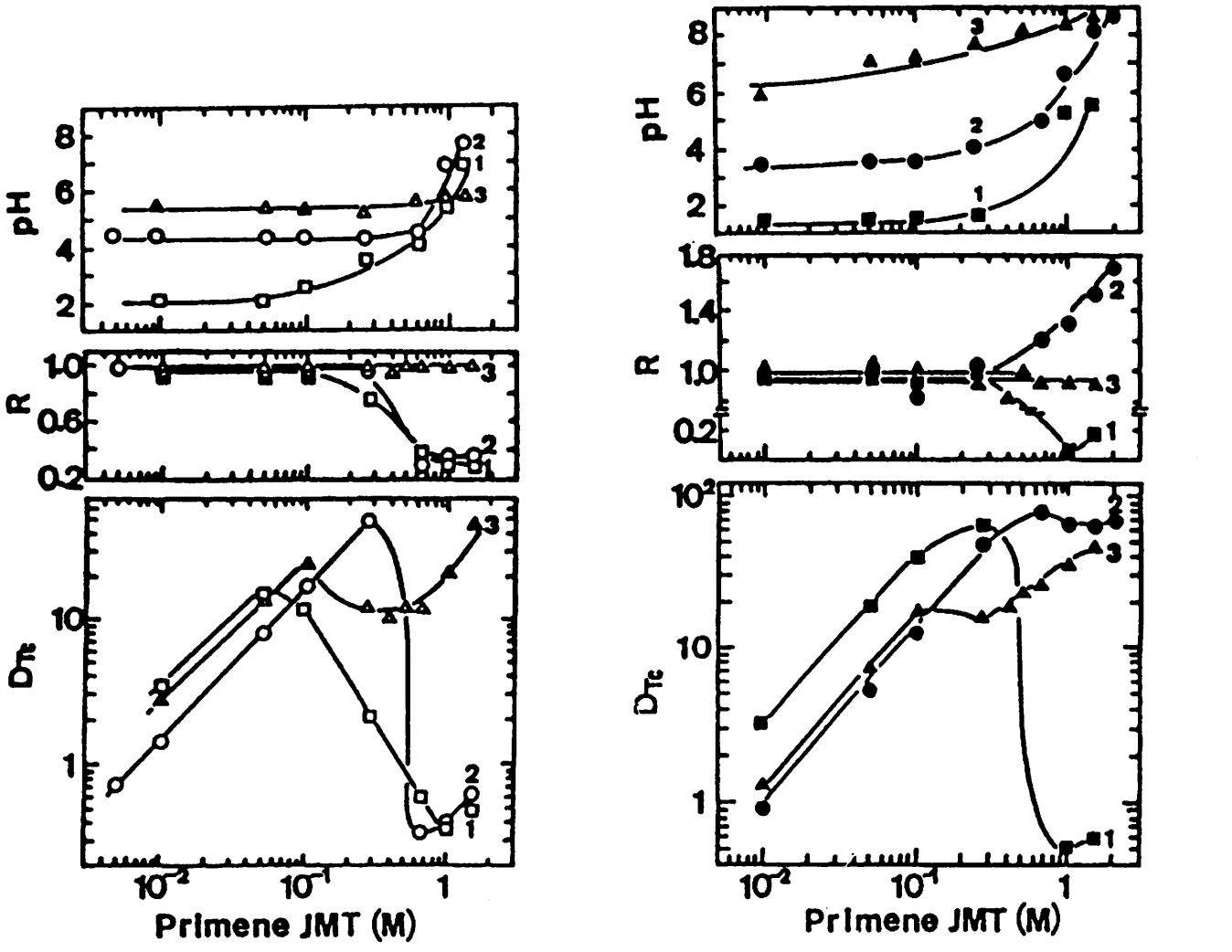

Fig. 1. Changes of distribution ratio D_{Tc} of technetium, volume ratio R between the organic and aqueous phases, and pH with Primene JMT and hydrofluoric acid concentrations in the Tc extraction from (H, NH_4)F aqueous solution by Primene JMT. 10^{-11}M TcO_4; 1: 1M HF, 2: 0.5M HF in 1M (H, NH_4)F, 3: 0.1M in 1M (H, NH_4)F.

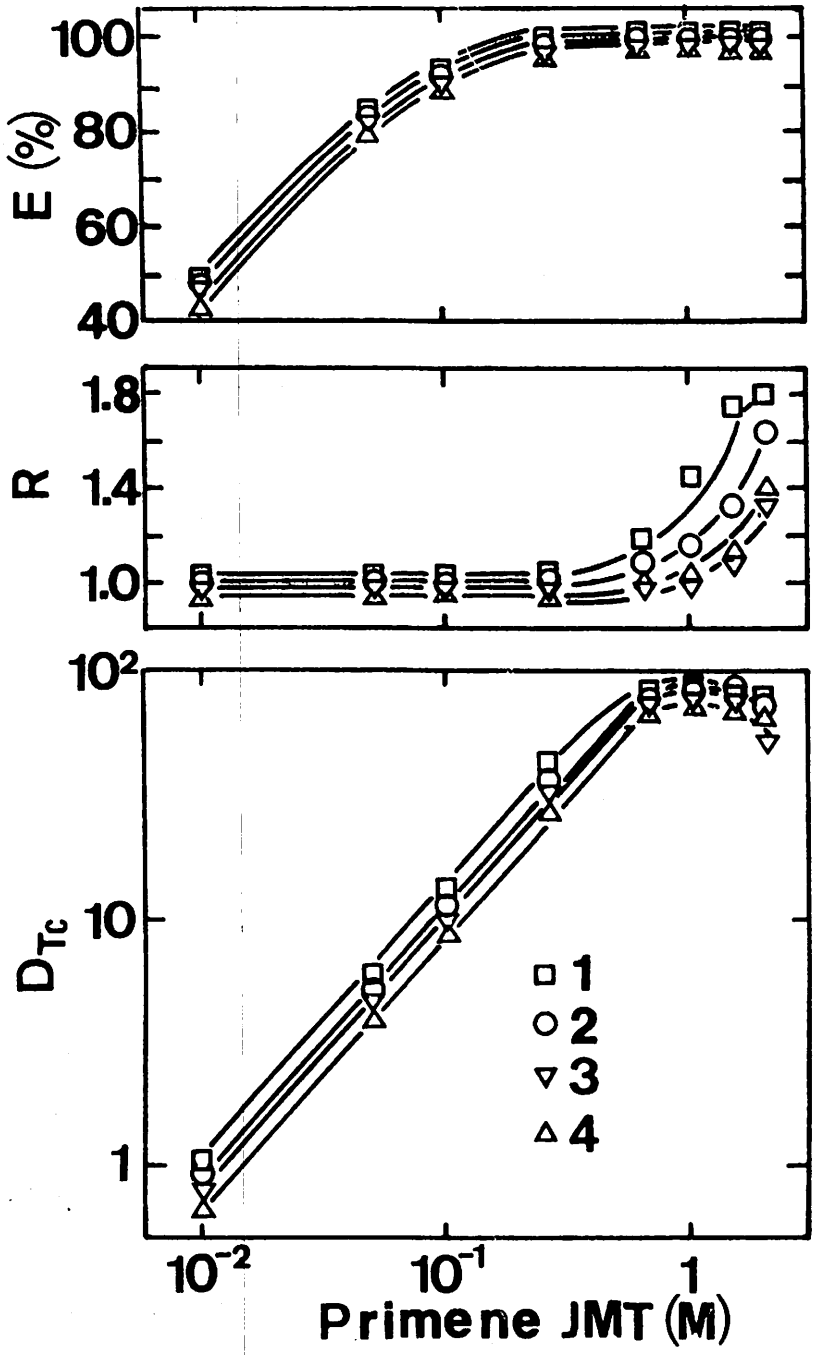

Fig. 2. Changes of D_{Tc} and R with concentrations of Primene JMT and 1-octanol in the Tc extraction from 0.5M HF - 1M (H, NH_4)F. 1: 5% 1-octanol, 2: 10% 1-octanol. 3: 20% 1-octanol, 4: 30% 1-octanol.

II. 2. Snthesis of Technetium Complexes in High Oxidation State I: Formation of Nitridotechnetium(VI) μ-oxo Dimer Compexes with Edta and Edda

*Takayama T., Kani Y., Sekine T., Kudo H., and Yoshihara K.**

Department of Chemistry, Faculty of Science, Tohoku University
*Tohoku Culture School**

Introduction

Growing interest has been paid to preparation of nitridotechnetium complexes, because the oxidation state of technetium in nitridotechnetium complexes ranges from +5 to +7 and the nitridotechnetium core (Tc≡N) is stable toward hydrolysis and ligand exchange reactions[1-4].

The formation of nitridotechnetium complexes like $[TcNCl_2(PPh_3)_2]$ and $[TcN(Et_2dtc)_2]$ was first reported by Kaden *et al.* [5] and by Baldas *et al.* [6]. The latter authors investigated interconversion between the monomer, μ-oxo dimer and di(μ-oxo) dimer of nitridotechnetium(VI) complexes in aqueous solution[7,8]. They have pointed out that the μ-oxo and di(μ-oxo) dimers are favorably formed under moderate conditions and the monomer tends to be formed only under high acidic conditions in the presence of coordinating anions. The μ-oxo dimers shows an intense visible absorption peak in the region around 470-510 nm due to a transition in the linear Tc-O-Tc three center p-bond system. For monomers and di(μ-oxo) dimers, no absorption peaks are observed in the same region.

We report the synthesis and properties of newly synthesized $^{99}Tc^{VI}N$-EDTA and $^{99}Tc^{VI}N$-EDDA complexes. The UV-Vis absorption peak of these complexes was found in the same region as that of the μ-oxo dimer complexes synthesized by Baldas *et al.*[7,8]. The result suggests that the $Tc^{VI}N$-EDTA complex has a Tc-O-Tc structure in the frame.

Experiental

PREPARATION OF $TC^{VI}N$-EDTA; SODIUM m-OXO-BIS[(ETHYLENEDIAMINE-N,N,N',N-TETRAACETATO)NITRIDOTECHNETATE(VI)] PENTAHYDRATE

$NA_4[TC_2N_2(\mu\text{-}O)(EDTA2] \cdot 5H_2O$

The starting material $[TcNCl_4]^-$ was prepared in the same manner as described by Baldas *et al.*[11]. Two milliliters of ammonium pertechnetate solution (7.60×10^{-2} M) was mixed with 10 ml of concentrated hydrochloric acid, and then 1 ml of aqueous solution

containing 0.1 g of sodium azide was added to the mixture. The solution was stirred for 15 min at 50 °C and then evaporated to dryness using a rotary evaporator. The residue was extracted with 10 ml of acetone and the insoluble salts were filtered off. The color of acetone solution obtained was orange.

When 60 mg of Na_2H_2edta, dissolved in 2 ml of water, was added to the orange acetone solution, the color of the solution changed immediately to reddish purple and the similar colored precipitate was formed. The precipitate was filtered, washed with acetone, and dried *in vacuo*. The yield of the product was 41.8 mg (55%). The product was recrystallized from a minimum amount of $NaClO_4$ solution. The addition of ethanol gave fine reddish purple powder which was soluble in water but insoluble in a variety of organic solvents (Found: C, 23.1; H, 3.36; N, 8.25; Tc, 20.7. $C_{20}H_{34}N_6O_{22}Na_4Tc_2$ requires C, 24.0; H, 3.43; N, 8.40; Tc, 19.8%).

PREPARATION OF TC^{VI}N-EDDA; μ-OXO-BIS[(ETHYLENEDIAMINE-N,N'-DIACETATO)NITRIDO-TECHNETIUM(VI)]PENTAHYRATE $[Tc_2N_2(\mu\text{-}O)(EDTA)_2] \cdot 5H_2O$

When 30 mg of H_2edda dissolved in 2 ml dil NaOH solution was added to the acetone solution of $[TcNCl_4]^-$ at room temperature, the color of the mixture rapidly changed to dark purple and then a purple precipitate appeared in 15 min. The precipitate collected by filtration was washed with acetone and dried *in vacuo*. The yield of the product was 33.6 mg (65%). The final product was slightly soluble in water, but insoluble in a variety of organic solvents (Found: C, 21.2; H, 4.04; N, 12.6; Tc, 29.5. $C_{12}H_{30}N_6O_{14}Tc_2$ requires C, 21.2; H, 4.44; N, 12.4; Tc, 29.1%).

Results and Discussion

The infrared spectrum of the Tc^{VI}N-EDTA complex gave absorption bands at 1041 cm^{-1} (Tc≡N) and 1634 cm^{-1} (C=O). The Tc^{VI}N-EDDA complex showed the absorption peaks at 1057 cm^{-1} (Tc≡N) and 1631 cm^{-1} (C=O), indicating the formation of nitridotechnetium complexes of EDTA and EDDA. The atomic ratio of C, H, N and Tc was 10 : 17 : 3 : 1 for the Tc^{VI}N-EDTA complex and 6 : 15 : 3 : 1 for the Tc^{VI}N-EDDA complex. The ratio of technetium nitrido core to the ligand was one to one for both the complexes.

The Tc^{VI}N-EDTA complex showed a reddish purple color in aqueous solution, with an absorption maximum at 504 nm (ε=4.94×10^3 $M^{-1}cm^{-1}$). The color of the Tc^{VI}N-EDDA complex was purple in aqueous solution, with an absorption maximum at 556 nm (ε=2.68 ×10^3 $M^{-1}cm^{-1}$). Both the complexes were stable in aqueous solution for several hours at an ambient temperature. The absorption peaks of the these complexes were found in the same region as the μ-oxo dimers synthesized by Baldas *et al.*[7,8], which can easily distinguish from

the monomer and di(μ-oxo) dimer these hae the absorption below 400nm. The fact suggests that both of the $Tc^{VI}N$-EDTA and $Tc^{VI}N$-EDDA complexes are μ-oxo dimers.

Chappuis *et al.* prepared a $Tc^{V}N$-EDDA complex starting from $[TcNCl_4]^-$ and H_2edda in a mixture of water and acetonitrile[10]. The UV-Vis spectrum of their product showed no absorption attributed to a m-oxo dimer. Their spectrum is obviously different from that of the $^{99}Tc^{VI}N$-EDDA complex prepared in the present work. There is a difference in the oxidation state of Tc between their complex (Tc^{V}) and ours (Tc^{VI}), even though both the complexes were synthesized from the same starting materials. It should be pointed out that the solvents used for preparation of these complexes are different. Although the $Tc^{V}N$-EDDA complex was prepared in a mixture of water and acetonitrile Chappius *et al.* , we used a mixture of water and acetone in preparation of the $Tc^{VI}N$-EDDA complex.

Electrophoresis of the $Tc^{VI}N$-EDTA complex indicated that technetium species moved toward only the anode side. The electrophoretic patterns observed at pH 4 and 10 were similar as shown in Figure 1. In the electrophoresis of $Tc^{VI}N$-EDDA, the technetium species were distributed from the neutral to anionic region. When perchlorate solution was used at pH 10, the fraction of neutral species was smaller than that at pH 4 (Figure 2). These results indicate that the neutral $Tc^{VI}N$-EDDA changed to an anionic form in the alkaline solution. The migration distance of the peak of anionic $Tc^{VI}N$-EDDA was two thirds of $Tc^{VI}N$-EDTA. This fact implies that the negative charge of $Tc^{VI}N$-EDTA is larger than anionic $Tc^{VI}N$-EDDA.

Consequently, it is conceivable that the $Tc^{VI}N$-EDTA and $Tc^{VI}N$-EDDA complexes are μ-oxo dimers, as shown in Figure 3. Although the $Tc^{VI}N$-EDDA complex is essentially a neutral species, the coordinated carboxyl group in the trans position of the nitrido ligands is dissociated by the attack of OH^- through the strong trans effects. Namely, the neutral $Tc^{VI}N$-EDDA complex is converted into the anionic form of $[Tc^{VI}N\text{-EDDA}]^{2-}$ in an alkaline solution as shown in Figure 4.

In conclusion both the $^{99}Tc^{VI}N$-EDTA and $^{99}Tc^{VI}N$-EDDA complexes obtained in the present work must be the m-oxo dimeric complexes.

References

1) Mutalib A. *et al.*, Radiochim. Acta **63** (1993) 123.
2) Baldas J. and Colmanet S. F., J. Chem. Soc., Dalton Trans. (1988) 1725.
3) Baldas J., Colmanet S. F. and Mackay M. F., J. Chem Soc., Chem. Commun. (1989) 1890.
4) Abram U. *et al.*, Inorg. Chim. Acta **109** (1985) L9.
5) Kaden L. *et al.*, Isotopenpraxis **17** (1981) 174.
6) Baldas J. *et al.*, J. Chem. Soc., Dalton Trans., (1981) 1798.
7) Baldas J. *et al.*, Inorg. Chim. Acta **204** (1993) 199.
8) Baldas J. *et al.*, Radiochimica Acta **63** (1993) 111.
9) Baldas J. *et al.*, J. Chem. Soc., Dalton Trans. (1984) 2395.
10) Chappuis. P. Ph. et al., J. Radional. Nucl. Chem., Lett 175 (1993) 113

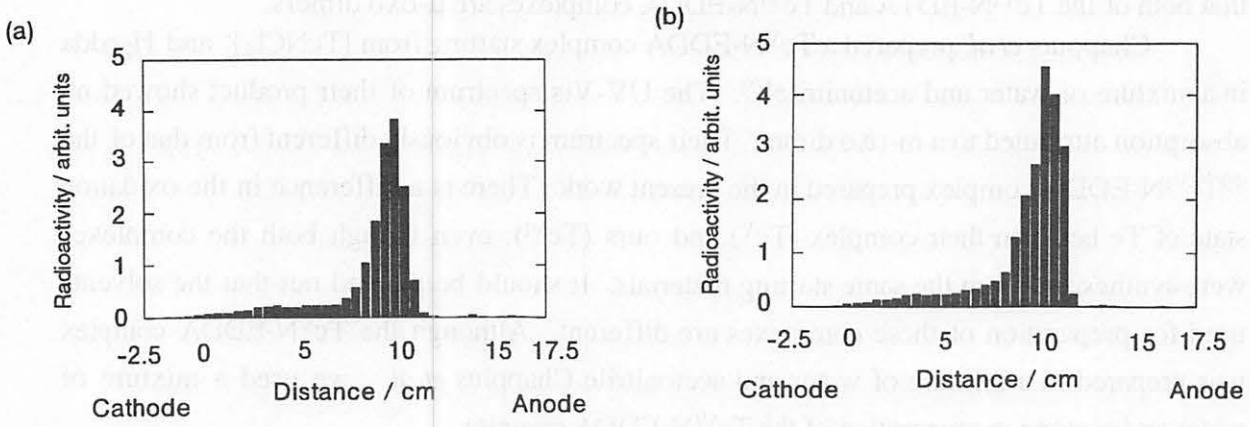

Fig. 1. Electrophoretic patterns of $Tc^{VI}N$-EDTA complex in 0.05M perchlorate solution at (a) pH 4 and (b) pH 10.

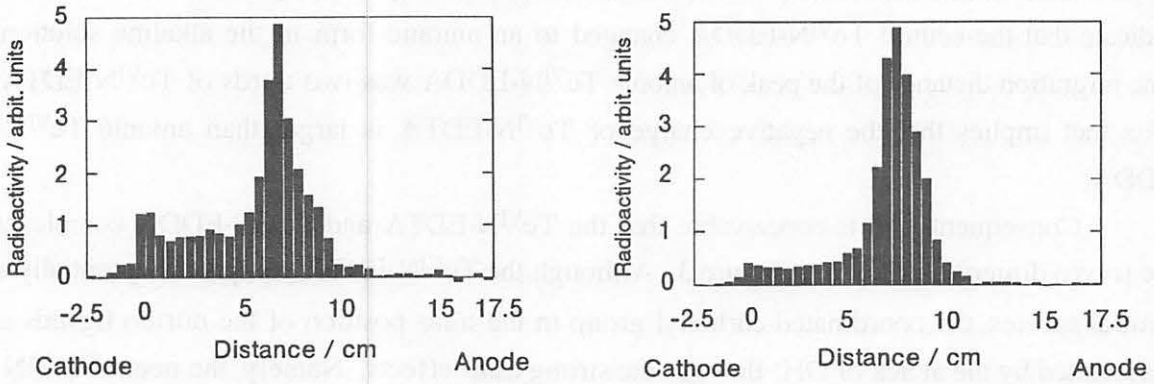

Fig. 2. Electrophoretic patterns of $Tc^{VI}N$-EDDA complex in 0.05M perchlorate solution at (a) pH 4 and (b) pH 10.

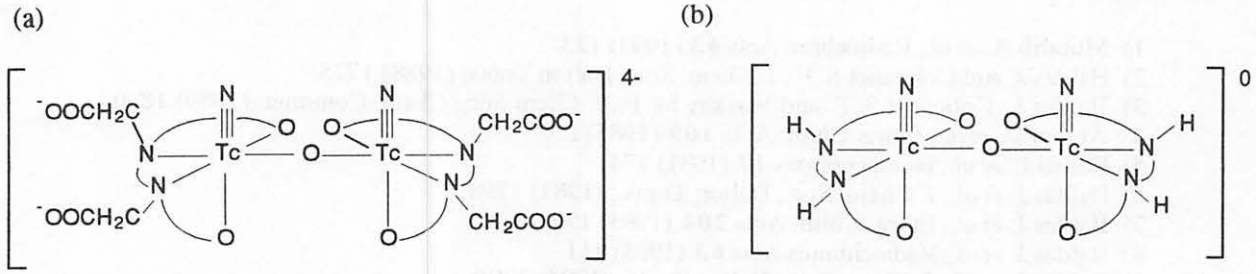

Fig. 3. A possible dimeric form of (a) $Tc^{VI}N$-EDTA and (b) $Tc^{VI}N$-EDDA complexes.

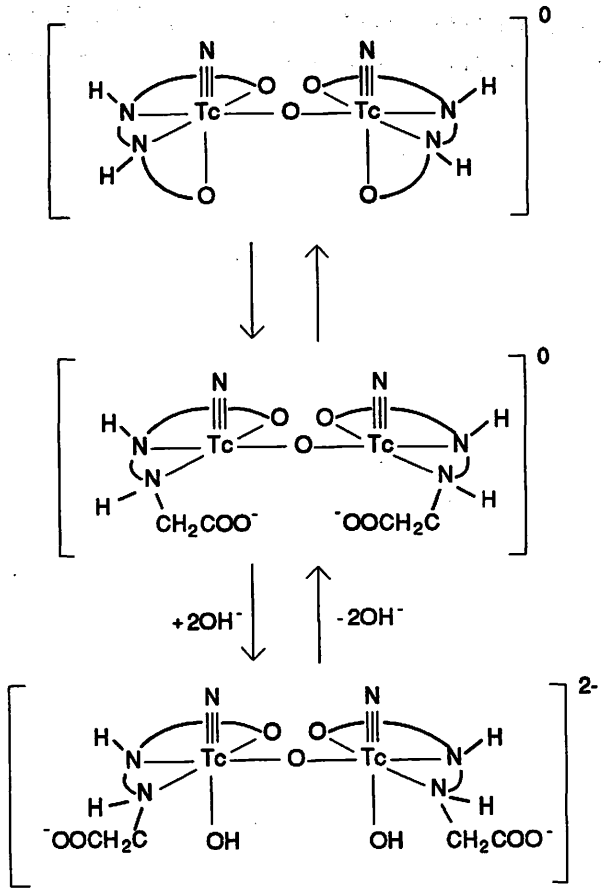

Fig. 4. The convertion of the $Tc^{VI}N$-EDDA complex in alkaline solution.

II. 3. Synergistic Extraction of Mn(II) with 2-Thenorytrifluoroacetone and Terpyridine

Satake S., Tsukahara S. and Teramae N.

Department of Chemistry, Faculty of Science, Tohoku University

Introduction

Manganese is one of the elements that exist widely in biological and geological environment. Mn^{2+} has less extractability among the first transition series, and its quantitative extraction can not often be attained with only a bidentate acidic chelating reagent. Since Mn(II) tends to have two auxiliary ligands in a crystal with an acidic chelating reagent, the extracted species of Mn(II) would contain two molecules of water and its hydrophobicity would not be very high. For an extracted metal ion the coordination number of which is not saturated with chelating reagents only, the synergistic extraction using a neutral ligand have been frequently adopted to increase extractability.

For the synergistic extraction of Mn(II), tributyl phosphate, trioctylphosphine oxide or pyridine derivatives have been used as unidentate ligands, and 1,10-phenanthroline or 2, 2'-bipyridine (bpy)[1] was examined as bidentate ligands. The adduct formation constants of these bidentate ligands are larger than that of unidentate ligand of similar structure, and thus the extractability is more improved. A neutral ligand having a coordination site of more than two is expected to show a further large synergistic effect, but no report on such a ligand has appeared.

We reported that a tridentate ligand, 2, 2': 6', 2"-terpyridine (terpy)[2] showed a large synergistic effect in extraction of lanthanoids(III). In this study, 2-thenoyltrifluoroacetone (Htta) is employed as an acidic chelating reagent and the synergistic extraction of Mn(II) with terpy is characterized.

Experimental

Htta and terpy were purchased and purified by sublimation[2]. Benzene was stirred with concentrated H_2SO_4 and distilled over CaH_2. Water was double-distilled and deionized. A radioisotope ^{54}Mn, used as a tracer, was purchased from New England Nuclear Co. A radioactive solution of Mn(II) was prepared by adding the radioisotope to a sample of a standard solution of Mn(II), evaporating to dryness, and redissolving the residue in a 1×10^{-3} M (1 M = 1 mol/dm^3) HCl solution containing 0.25 M ascorbic acid.

An aqueous solution (5 cm^3) containing 1×10^{-6}—1×10^{-5} M Mn(II) labeled with its radioisotope ^{54}Mn and 1×10^{-4}—1×10^{-3} M ascorbic acid was placed in a 20 cm^3 centrifuging tube. The pH of the aqueous phase was adjusted to 6—7 with 1×10^{-2} M of 2-(*N*-morpholino)ethanesulfonic acid (pK_a 6.15) and sodium hydroxide solutions. The ionic strength was fixed at 0.1 M with sodium perchlorate. A benzene solution (5 cm^3) containing 1×10^{-4}—3×10^{-3} M Htta and 8×10^{-6}—1×10^{-2} M terpy was added to the aqueous solution and shaken for 1 h. After centrifugation for phase separation, a sample (3 cm^3) of each phase was pipetted and γ-activity was measured with an NaI(Tl) well-type scintillation counter. The distribution ratio of Mn(II) was obtained as the γ-activity ratio. The equilibrium pH of the aqueous phase was measured with a glass electrode immediately after the phase separation.

From the organic phase separated after the first extraction, Mn(II) was back-extracted into a fresh aqueous phase whose pH and ionic strength were adjusted to 6—7 and 0.1 M, respectively (without ascorbic acid). The distribution ratio of Mn(II) was calculated as mentioned above.

All procedures were done in a thermostatted room at 25 ± 1 °C.

Theoretical

The distribution ratio (D_o) of a divalent metal ion (M^{2+}) with an acidic chelating reagent (HL) can be expressed as:

$$D_o = \frac{[\overline{ML_2}]}{[M^{2+}] + \sum_m [ML_m^{(2-m)+}]} = \frac{K_{ex} P_{HL}^2 [L^-]^2}{K_{HL}^2 (1 + \sum_m \beta_{L,m} [L^-]^m)} \qquad (1)$$

where K_{HL} and P_{HL} are the acid-dissociation constant and partition coefficient of HL, respectively, and the upper-bar denotes the organic phase. $\beta_{L,m}$ and L^- are the formation constant of $ML_m^{(2-m)+}$ and the acid-dissociated anion of HL in the aqueous phase, respectively, and K_{ex} denotes the extraction constant. In the region where the concentration of L^- is very low, the $\Sigma\beta_{L,m}[L^-]^m$ term is negligibly small in Eq. 1, and hence D_o is proportional to $[L^-]^2$.

In the synergistic extraction of M^{2+} with HL and a neutral ligand (S), the distribution ratio (D) can be expressed as:

$$D = \frac{[\overline{ML_2}] + \sum_n [\overline{ML_2S_n}]}{[M^{2+}] + \sum_m [ML_m^{(2-m)+}]} = \frac{K_{ex} P_{HL}^2 [L^-]^2 (1 + \sum_n \beta_{s,n} [\overline{S}]^n)}{K_{HL}^2 (1 + \sum_m \beta_{L,m} [L^-]^m)} \qquad (2)$$

where $\beta_{s,n}$ is the adduct (ML_2S_n) formation constant in the organic phase. The next equation is obtained from Eqs. 1 and 2:

$$D/D_o = 1 + \Sigma\beta_{s,n}[\bar{S}]^n \quad (3)$$

If ML_2S_n is the dominant species in the organic phase, D/D_o will be proportional to the n-th power of $[\bar{S}]$. The synergistic extraction constant ($K_{ex,s,n}$) for the following equilibrium:

$$M^{2+} + 2\overline{HL} + n\,\bar{S} \rightleftharpoons \overline{ML_2S_n} + 2H^+ \quad (4)$$

can be calculated as $K_{ex} \cdot \beta_{s,n}$.

Results and Discussion

EXTRACTION OF MN(II) WITH HTTA

The extraction of Mn(II) was done with various Htta concentrations in benzene and the plots of log D_o against log[tta$^-$] are shown in Figure 1. The equilibrium concentration of tta$^-$ in the aqueous phase is calculated with the initial concentration of Htta in the organic phase, $K_{HL}(10^{-6.23})$ and $P_{HL}(10^{1.62})$. The plots show linear relationship with a slope of 2.0. This indicates that two molecules of tta$^-$ participate in the extraction of Mn(II) according to Eq. 1. It was sometimes reported that Mn(II) was oxidized during the extraction[1], but the oxidation of Mn(II) is negligible in this case. This is also supported by the fact that plots for the back-extraction (without ascorbic acid) are located on this line.

K_{ex} is calculated with Eq. 1 as $10^{-10.06}$, which agrees well with the literature value[1], $10^{-10.07}$. K_{ex} is vary small, therefore quantitative extraction is not attained with Htta only (cf. Figure 1).

SYNERGISTIC EXTRACTION OF MN(II) IN HTTA-TERPY SYSTEM

The synergistic extraction of Mn(II) was done with various concentrations of Htta and terpy. To prevent Mn(II) from oxidizing, ascorbic acid was added also in the synergistic extraction systems.

The plots of log D against log[tta$^-$] are shown in Figure 1. A large synergistic effect is observed as compared with Htta only, that is, D is 10,000 times larger. In the presence of terpy, the plots also give a linear relationship with slopes of 2.0. Therefore it proves that two molecules of tta$^-$ participate in the synergistic extraction of Mn(II). Plots of the back-extraction agree with those of the forward extraction, and this indicates that the oxidation state of Mn is kept to divalent.

The plots of log (D/D_o) against log[$\overline{\text{terpy}}$] are shown in Figure 2, where the D_o value is calculated with Eq. 1 using the K_{ex} value. We had made sure that the equilibrium concentration of terpy in the benzene phase was equal to the initial concentration in these pH ranges[2]. The slope of the plots in the Htta-terpy system is 1.0, which implies that the dominant extracted species is $Mn(tta)_2(terpy)$. The $\beta_{s,1}$ and $K_{ex,s,1}$ values are calculated as $10^{6.96}$ and $10^{-3.10}$.

ADDUCT FORMATION CONSTANT AND COORDINATION NUMBER OF MN(II)

Terpy has three nitrogen atoms for coordination. In fact, it was suggested that terpy functioned as a tridentate ligand for light lanthanoids in the organic phase[2], and three nitrogens of terpy coordinate fully to a europium(III) β-diketonato complex in a crystal state[3]. The $\beta_{s,1}$ value of Mn for terpy (log $\beta_{s,1}$ 6.96) is smaller than that for bidentate ligand, bpy (log $\beta_{s,1}$ 8.00)[1], the basicity of which is nearly equal to terpy[2]. This indicates that only two nitrogen atoms of terpy coordinate to Mn and that a remaining free pyridyl-group causes either steric hindrance or an increment of the activity of the extracted complex. (The latter influence of the free pyridyl group would be brought on by exposure of the polar N-atom of this group to the non-polar phase.) The coordination number of Mn(II) is sometimes more than six[4,5]. In this study, this phenomenon was expected, but the coordination number of Mn(II) would be normally six (*i.e.*, octahedral) as mentioned above. In other words, the four coordination sites of Mn(II) are filled with two molecules of tta$^-$ and the other two sites are occupied with terpy, which functions as a bidentate ligand.

The extraction equilibrium of Mn(II) is clarified in a novel synergistic extraction system, *i.e.*, the Htta-terpy systems. Mn(II) is extracted into benzene as $Mn(tta)_2(terpy)$. Large synergistic effects observed in this system allow the quantitative extraction of Mn(II), which is hard to attain with Htta only.

References

1) Nakamura S. and Suzuki N., J. Radioanal. Nucl. Chem. **82** (1984) 33.
2) Suzuki N., Satake S. and Tsukahara S., J. Radioanal. Nucl. Chem. **172** (1993) 239.
3) Holz R. C. and Thompson L. C., Inorg. Chem. **27** (1988) 4640.
4) Brooker S. and McKee V., J. Chem. Soc., Dalton Trans. (1990) 2397.
5) Davis J. H. and Reid S., Inorg. Chim. Acta **105** (1985) L13.

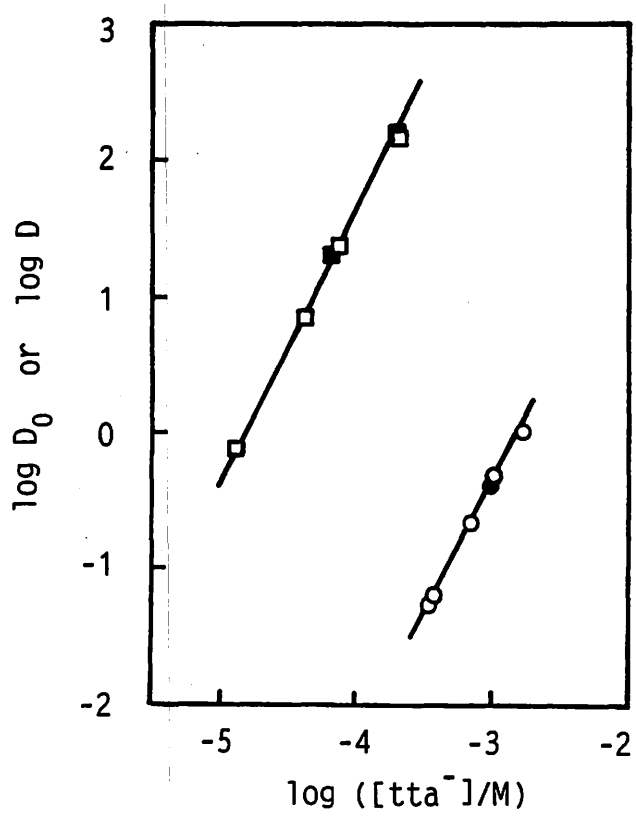

Fig. 1 Dependence of D_0 or D of Mn(II) on the concentration of tta$^-$ in the Htta (○, ●) and Htta-terpy (□, ■) systems.

Htta, 1.3×10^{-4}—2.8×10^{-2} M; terpy, 1.1×10^{-3} M; pH 6.5—6.9.
Open symbols, forward extraction with 1.0×10^{-3} M ascorbic acid.
Blackened symbols, back-extraction without ascorbic acid.

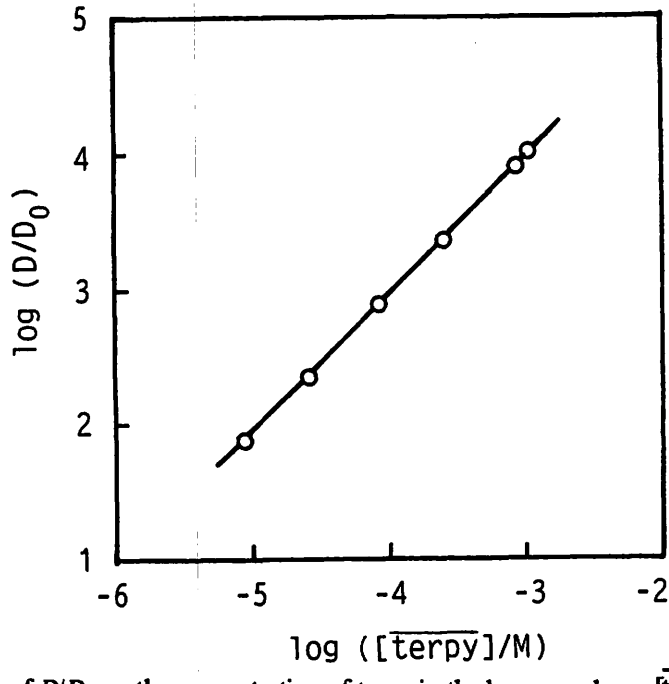

Fig. 2 Dependence of D/D_0 on the concentration of terpy in the benzene phase, [$\overline{\text{terpy}}$].

II. 4. Production of Several C-11 Labeled Fullerens by Charged Particle Irradiation and Recoil Implantation

*Masumoto K., Ohtsuki T., Sueki K. *, Kikuchi K.**

Laboratory of Nuclear Science, Faculty of Science, Tohoku University
*Department of Chemistry, Faculty of Science, Tokyo Metropolitan University**

Recently fullerens and their derivatives occupy the attention of many scientists of the world due to their interesting physical and chemical properties. The production of labeled fullerens is interesting and important for studying the behavior of trace amount of fullerens. In this work, the recoil implantation of radioactive carbon into fulleren network has been tried by cyclotron irradiation to study their reaction mechanism and open a new labeling method.

The production of ^{11}C labeled fullerens was already succeeded in our previous experiment using photonuclear reaction[1]. In this case, ^{11}C is produced from carbon of fullerens by $^{12}C(\gamma,n)^{11}C$ reaction. As the recoil enegy of ^{11}C is extremely larger than the chemical bonding energy, it can be considered in our common sense that ^{11}C produced by photonuclear reaction can not stay in the skelton of fullerens and carbon network is broken by recoil energy. Beyound our expectation, it was confirmed by HPLC separation coupled with the UV- and BGO-detectors that the 60-70% and 30% of total ^{11}C activity remained in C_{60} and C_{70}, respectively. Futhermore, 80-90% of labeled ^{11}C existed in fulleren dimer. This ^{11}C labeled fulleren dimer is isolated in the state of carrier-free, because it could only be detected by BGO-scintillation detectors and could not be detected by UV-spectrometer. Two important question are raised, that is, 1) why such a high yield of ^{11}C-labeled fullerences can be produced ? and 2) why ^{11}C-labeled fullerences prefer the coalescence reaction ?

It is very important to confirm whether the same experimental result can be obtained by chraged-particle irradiation, in order to make clear the labeling mechanism. As ^{11}C was produced by using $^{11}B(p,n)^{11}C$, $^{14}N(p,\alpha)^{11}C$ and $^{10}B(d,n)^{11}C$ reactions, the mixture of fullerene/boron or fullerene/nitrogen compound was irradiated with proton or deuteron. Therefore the possible production process of labeled fullerene by charged-particle irradiation is the substitution reaction between carbon atom of fullerene and ^{11}C recoiled out of boron or nitrogen.

Experimental

Fullerenes, C_{60} and C_{70} are dissolved into CS_2 and mixed with the same amount of boron, Si_3N_4, CH_2N_4 After evaporation of CS_2, 10mg of sample was wrapped with

aluminium foil of 10 μm thickness. Irradiation was done at the No.1 irradiation facility for radioisotope production of Cyclotron Radioisotope Center, Tohoku University. Samples were irradiated by 12 MeV proton and 10 MeV deuteron for 20 min at the average current of 1 μA. Sample surface was cooled by He-gas and the hidden side was cooled with water indirectly.

Irradiated samples were dissolved into CS_2 and filtrated by milipore filter to remove recoil sources such as boron powder and insoluble byproducts. After CS_2 was removed, CS_2 soluble fraction was dissolved into toluene-hexane mixture (7:3) and injected into HPLC column (Bucky-clutcher, 250 mm×10 mm id) to separate C_{60} and/or C_{70} and their derivatives. Flow rate was adjusted at 3ml/min. After separation, the absorbance and radioactivity of eluate were measured by UV-detector at 290 nm and BGO-scintillation detectors in series. After the absorbance measurement, a elution tube was coiled and sandwiched between a pair of BGO-scintillation detectors which were coupled with coincidence counting circuit to detect 511keV anihilation gamma-ray from labelled compounds. Eluate was collected by the fraction collector every 1 min and checked a radiochemical purity with the Ge-detector.

Results and Discussion

It was found from the result of 12 MeV proton irradiation of a pure C_{60} that the activity of ^{13}N and ^{11}C produced by the $^{13}C(p,n)^{13}N$ and $^{12}C(p,pn)^{11}C$ reaction respectively were negligible.

Figure 1 shows the radiochromatogram after proton irradiation of the C_{60} and boron mixture. Horizontal and vertical axes are the retention time and radioactivity detected by the coincidence counting system. The count rate at each elution time was normalized as the count rate at the injection time according to the half-life of ^{11}C. The first peak appeared at the retention of 6 min was attributed as C_{60} molecule labelled with ^{11}C, such as $^{11}CC_{59}$. The second large peak appeared at 10 min seems to be a C_{60}-dimer. The third broad peak, which may be a C_{60}-trimer was observed around 20 min after injection. The peak area ratio of above three peaks was 1:5:1. The same chromatograph was also obtained in the case of the C_{60} mixture with Si_3N_4 and CH_2N_4

Figure 2 shows the result of the C_{70} and boron mixture. The first and second large peaks are assigned as C_{70} monomer and dimer. The second peak was broader than that of single component. It seems to be the compound peak of three types of geometrical isomer of C_{70} dimer, because the C_{70} molecule resembles a rugby ball in shape. Three small peaks apeared at 6, 10 and 14 min were caused by the small amount of C_{60} impurity and expected to be C_{60}-monomer, C_{60}-dimer and C_{60}-C_{70}, respectively.

Above results are the same as the results of bremsstrahlung irradiation[1]. Therefore, the ^{11}C labeling induced by nuclear reactions is mainly caused by the substitution reaction

between a stable carbon in fullerene and ^{11}C. When fulleren network is opened by the attack of ^{11}C, the open end of carbon network can easily combine with neiboring fullerene molecules.

Yeretzian *et al.* reported the coalescence products observed in a hot and dense vapor generated by laser desorption of a fullerene film.[2] McElvany *et al.* found that the coalescense reaction can be catalyzed by ozone and produces odd mass molecule, such as C_{119} (C_{60} + C_{59}), C_{129} (C_{60} + C_{69} or C_{59} + C_{70}) and C_{139} (C_{70} + C_{69}).[3] They could not isolate these compound as chemically stable species. On the other hand, the Buckyclutcher column can separate these compound according to their molecular size. Our results are the first evidence that the chemically stable fullerene dimer and trimer can exist in liquid phase.

In the case of deuteron irradiation of C_{60}, ^{13}N labeled compound appeared at the retention time of 6 and 14 min The retention time of the first peak is that of the C_{60} itself and the second peak seems to be a new ^{13}N labelled compound. As the insertion of hetero atom into fullerene cage is a recent theme of the fullerene chemistry, recoil implantation method is very effective to study this kind of work. The ^{13}N labeling experiment will be continued to confirm the structure of ^{13}N labeled compound.

As this labeling method is very simple, easy and rapid, this method is very useful for preparing a complex molecule labeled with a short lived radioisotope, such as ^{11}C and ^{13}N. This work will open not only several application fields, such as tracer chemistry and nuclear medicine, but also a new fullerene chemistry for the insertion of heteroatom into fulleren cage and/or the production of higher fullerenes.

Acknowledgement

The authors thank the crew of the Cyclotron and Radioisotope Center for their kind operation of cyclotron irradiation.

References

1) Ohtsuki T., Masumoto K., Sueki K., Kobayashi K. and Kikuchi K., to be published.
2) Yoretzian C., Hansen K., Diederich F. and Whetten R., Nature **359** (1992) 44-46
3) McElvany S. W., Callahan J. H., Ross M. M., Lamb L. D., Huffman D. R., Science **260** (1993) 1632-1634.

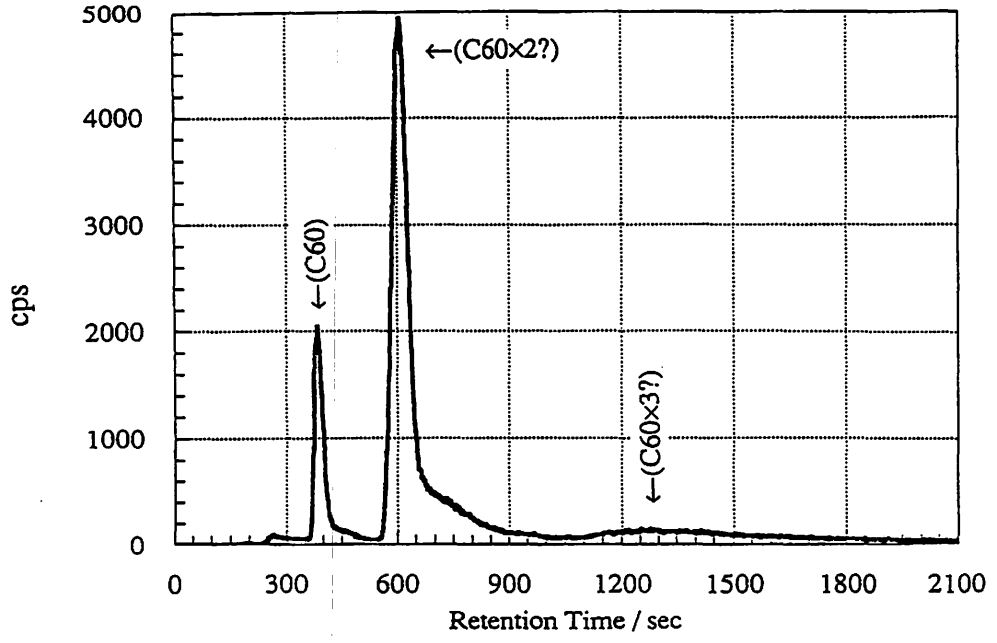

Fig. 1. Radiochromatogram of the C_{60} and boron mixture bombarded by 12 MeV proton.

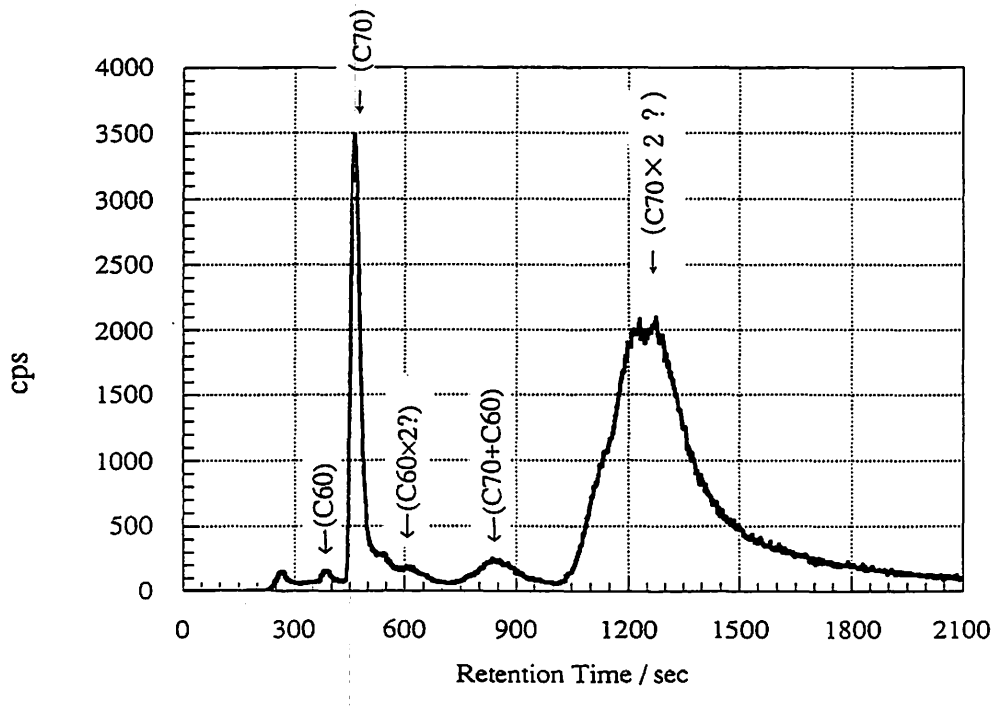

Fig. 2. Radiochromatogram of the C_{60} and boron mixture bombarded by 10 MeV deuteron.

II. 5. Application of PIXE to Analysis of Minerals in Plant Roots

*Yokota S., Ishii K. * and Mae T.*

Department of Applied Biological Chemistry, Faculty of Agriculture, Tohoku University
*Cyclotron and Radioisotope Center, Tohoku University**

Introduction

Acid soils widely spread all over the world, while, few area of such regions is now utilized as arable lands because of its low productivity of crops. In acid soils, growth of plants is severely inhibited by acidity (low pH, high concentration of hydrogen ion (H^+)) and phytotoxicity of soluble aluminum (Al) in soil solution. Development of new line of crops tolerant of acid soils is demanded for food production in near future. However, mechanism of phytotoxicity of hydrogen ion (low pH) and Al to plant root is still remained unclear. The aim of our work is to observe short-term events occurring in roots exposed to low pH or Al stress. It was reported that effects of those two stress factors appeared within 6 h as retardation of root elongation in alfalfa (1). In this study, changes in composition of some minerals (P, K, and Cl), which play important roles in plant cells, were analyzed by PIXE method. While there are some other chemical methods for the determination of content of individual minerals in root tissue, PIXE method was applied because of the following two advantages; (1) many elements can be measured simultaneously in less than 5 min for a sample using only a small fragment of root-tip without any pretreatments (such as, wet digestion), and (2) contamination from reagents or instruments for pretreatments can be avoided.

Material and Methods

PLANT MATERIAL

Twelve seedlings of alfalfa (*Medicago sativa* L. natsuwakaba) with a 4-5 mm radicle were transferred to 100-ml non-stressed or stressed (low pH or Al) rooting solution and grown at 22 °C under continuous lighting.

STRESS TREATMENT

Composition of rooting solutions is; (1) Basal solution: 1 mM $CaCl_2$ in distilled water, (2) Control: pH of solution (1) was adjusted to 5.0 with 0.01 N HCl, (3) Low pH: pH of solution (1) was adjusted to 4.3 with 0.1 N HCl, (4) +Al: $AlCl_3 \cdot 6H_20$ was added to the

solution (1) (final Al concentration and pH were 20 μM and 5.0, respectively, without any pH adjustment). Culture pots were placed in a growth chamber (22 °C, continuous lighting) and sampled 4, 8 and 20 h after transfer of plants to the rooting solutions.

PIXE ANALYSIS

PIXE spectra were obtained using a measuring system of Tohoku University Cyclotron and Radioisotope Center (Sumitomo Co., model CGR-MeV680 AVF cyclotron). Protons were accelerated to 3 MeV, and X-rays were detected with a Si(Li) detector. The beam was collimated to 3 mm in radius on the sample. One or two fragments of root-tip (4-5 mm in length) were placed on very thin PVF (polyvinyl formal) membrane prepared by the method developed by Iwata et al.(2) and allowed to be air-dried.

Results and Discussion

OVERVIEW OF MINERAL COMPOSITION IN ROOT-TIP

PIXE spectra are shown in Figure 1 after normalization by the peak count of phosphorus (P-K_α, 2.015 keV). Measuring time for each sample was less than 10 min (normally 5 min). Only a piece of root-tip was sufficient to obtain a PIXE spectrum. Root of the control treatment showed continuous elongation (data not shown) without any significant change in the K/P ratio (Figure 1). This means that balance of these elements is physiologically maintained in the root-tip grown under the non-stressed condition. Increase in the relative Cl content in the control root come probably from $CaCl_2$ and HCl added to the rooting solution. Under the low pH or Al conditions, alteration of mineral composition (K/P ratio) occurred within 4 h after exposure to these stresses.

K/P RATIO

The K/P ratio fell down dramatically within 4 h after exposure to the low pH solution (pH 4.3). In the Al treatment, the degree of decrease in K/P ratio was less than that in the low pH treatment. Decrease in K caused by Al or low pH stress was previously reported for other plant species (3, 4, 5). Phosphorus is a component of large and constitutive molecules, i.e. DNA, RNA and proteins. Most of potassium in cells exists as a free cation (K^+) and balance of its influx and efflux is very important for maintenance of cellular homeostasis. For example, K^+ is known to play a key role for regulation of osmotic potential. The decrease in K/P ratio and K content would be a reflection of disorder in homeostasis in cells. However, it is not sure whether the decrease is due to destruction of plasmamembrane as an ion barrier or change in physiological active export (or incorporation) of K^+.

K/Cl RATIO

Chlorine is an essential microelement for plant growth (6). The KCl ratio was lower in both low pH and Al treatments than that of the control (Figure 1). Chlorine exists as a free ion (Cl^-) in cells as well as K^+, while, K/Cl ratio in the low pH and Al treatments was quite different each other. It might come from the differences in permeability of plasmamembrane to K^+ and Cl^- (7). In fact, the barrier function of plasmamembrane remained under Al stress but not under low pH stress as was reported in our previous work (1).

TIME DEPENDENCE OF ALTERATION OF MINERAL COMPOSITION

Almost all alteration of the mineral composition had been completed within 4 h after exposure of the germinating seeds to the three kinds of rooting solutions (control, low pH and Al). The ratio of Al to P increased gradually for 20 h or more. These results suggest that the alteration of mineral composition of root is brought about by contact of H^+ or Al ion with the root, and is not by gradual accumulation of H^+ or Al in the root.

Ca CONTENT

Calcium plays important roles in many physiological processes in cells, and is one of macro essential elements for plants. Relation between Al and destruction of Ca homeostasis has been examined (7). In PIXE, accurate amount of Ca is difficult to be estimated as overlapping of Ca-K_α (3.68 keV) and K-K_β is not negligible. If appropriate correction for Ca-peak count is available, it will also be able to discuss the relation between alteration of Ca (if any) and Al stress from the PIXE spectra.

Concluding remarks

By application of PIXE, alterations of mineral composition of alfalfa root-tip exposed to low pH or Al stress were observed, and difference in the toxic effect between low pH and Al in short-term to plant root is suggested. Using micro-PIXE in air, target sites of hydrogen ion or Al on the surface of root-tip will be found. It will lead much information for elucidation of the mechanism of low pH and Al stress in plant roots. By PIXE method, it is possible to detect light elements (from Na to Ca) using only a small fragment of plant root-tip in a short time. PIXE will be very useful when the number of sample is limited.

References

1) Yokota S. and Ojima K., Plant Soil (in press, 1994).
2) Iwata Y. et al., Int. J. PIXE 2 (1992) 381.
3) Holst W. J. et al., J. Plant Physiol. **140** (1992) 174.
4) Ryan P. R. et al., Plant Physiol. **99** (1992) 1193.
5) Delhaize E. et al., Plant Physiol. **103** (1993) 685.
6) Terry N., Plant Physiol. **60** (1977) 693.
7) Bennet J. R. and Breen C. M., Plant Soil **134** (1991) 153.

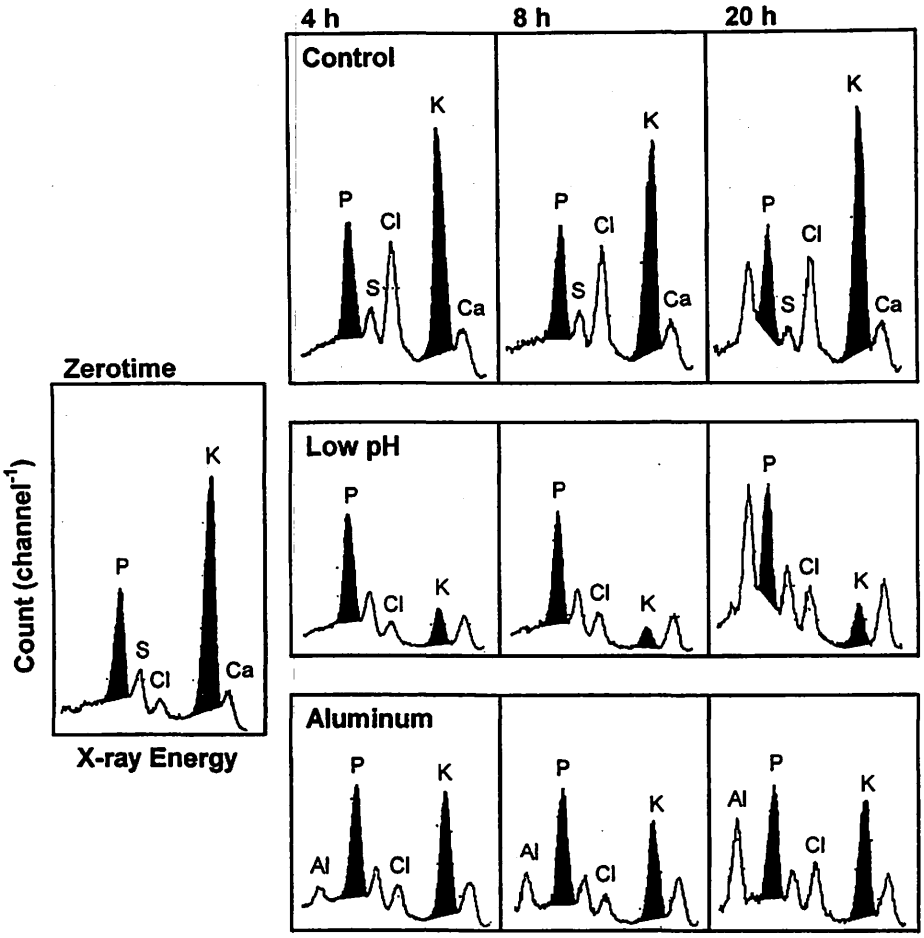

Fig. 1. PIXE spectra of root-tip of alfalfa under low pH or Al. Each spectrum chart was normalized to the count/channel of phosphorus at 2.015 keV(P-K_α).

III. BIOLOGY AND MEDICINE (Basic)

III. 1. On-Column Preparation of [^{11}C]Fatty Acid and [^{11}C]Amino Acid

*Iwata R., Ido T., and Tada M.**

CYRIC Tohoku University
*Institute of Development, Aging and Cancer, Tohoku University**

Extraction is one of troublesome procedures in PET radiopharmaceutical preparation which usually requires the use of a remote-controlled or automated system. This procedure is conveniently substituted for solid phase extraction with a short silica gel or C_{18} column. However, solid phase extraction is not always applicable. For example, in the [^{11}C]acetic acid preparation liquid-liquid extraction is the only practical way for the separation from the reaction mixture. Column extraction with a commercially available granular kieselguhr of giant pores, Extrelut® (Merck), is a feasible method for automation of liquid-liquid extraction. Extrelut can hold water and allow a hydrophobic solvent to flow to extract a lipophilic compound from the aqueous layer. In this report we describe excellent appliactions of column extraction to on-column preparation of [^{11}C]fatty acids, [^{11}C]acetate and [^{11}C]palmitate, from [^{11}C]CO_2 and [^{11}C]amino acid, 1-aminocyclopentane-1-[^{11}C]caroxylic acid ([^{11}C]ACPC).

On-column preparation of [^{11}C]fatty acids

Figure 1 shows the semi-automated synthesis system used for the on-column preparation of [^{11}C]fatty acid. Two glass columns (*I.D.* 4 mm, *O.D.* 6 mm, *L.* 10 cm) were closely packed with Extrelut to a length of approx. 4 cm and the first column (reaction column) was served as support for the Grignard reagent, and the second used to catch overflowed aqueous HCl from the first column. The third column was a disposable Extrelut column (Extrelut-1; Merck) for [^{11}C]acetic acid or a Sep-pak silica (Waters) for [^{11}C]palmitic acid. A short disposable column of Na_2SO_4 (Sample drying device; Whatman) was placed between Valve 4 and the third column.

Prior to use, the valves, lines and columns were washed with dilute HCl followed by water and acetonitrile, flushed with anhydrous THF, and fully dried by flowing He. Just before the radiosynthesis started, 0.2 mL of the Grignard solution had been carefully injected directly onto Extrelut in the first column through the stop valve while He was flowing through the column. The [^{11}C]carbon dioxide, which had been trapped and concentrated in a copper spiral immersed in liquid Ar, was introduced with a He current at 30 mL/min into the reaction

column. The 6-way valve was then switched to the reagent line and the 3 N HCl was injected into the column to quench the reaction mixture and to bring the radioactive product into the free acid form. The aqueous phase overflowing from the reaction column was caught by the second Extrelut column to protect the final product solution from contamination with Mg^{2+}. The columns were then heated to 70 °C and flushed with a He flow for 2 min to remove the [^{11}C]carbon dioxide remaining unchanged. The extractant was flowed through the columns to extract the free [^{11}C]fatty acid from the acidified aqueous solution and transferred through the Na_2SO_4 onto the third column, where the [^{11}C]acetic acid was extracted back into the $NaHCO_3$ phase or the [^{11}C]palmitic acid was adsorbed by the silica gel. The product was finally eluted with ethanol from the column into a flask, and the product solution was evaporated to dryness to remove the organic solvents.

The present method based on column extraction with Extrelut enables to perform rapid and efficient syntheses of the [^{11}C]fatty acids. They were usually completed within 15 min. Table 1 demonstrates that the system provides radiochemically pure [^{11}C]acetic acid and [^{11}C]palmitic acid in yields high enough for clinical PET use. Column extraction offers a convenient way to accomplish remotely operated extraction by a simple on-line procedure. Another remarkable feature is that Extrelut allows a gas to flow through the column without washing away the liquid phase and to interact efficiently with the liquid phase. The flowing [^{11}C]carbon dioxide reacts almost quantitatively with the Grignard reagent even at room temperature. Since the method consists of simple on-line processing, the synthetic procedure is suitable for automation. In addition, as the purification is based on extraction, the present method can be applied to the preparation of a wide variety of [^{11}C]fatty acids by the Grignard reaction. Moreover, the washing and drying procedure allows the system to be used for repeated preparation without change of the Extrelut columns.

On-column preparation of [^{11}C]amino acids

The synthesis of [^{11}C]ACPC was first reported by Hayes *et al.*[1] using the modified Bücherer-Strecker reaction as shown in Scheme I. This rapid synthesis requires a high reaction temperature and pressure with addition of carrier cyanide, whereas the alternative method, which we developed later, employs moderate reaction conditions and needs no carrier addition[2] (see Scheme II). Both routes, however, are not so easily adaptable to automated synthesis; for example, the former requires a pressure-tight reaction vessel, whereas the latter needs liquid-liquid extraction.

Figure 2 is flow chart of the remote-oparated sustem employed for the on-column preparation of [^{11}C]ACPC from [^{11}C]HCN. Extrelut was packed in the first column for the trapping and substitution reaction of [^{11}C]HCN. The aqueous substrate solution in an amount sufficient for overflowing was injected into the column, and air was then passed to push out the exceeding aqueous solution. The second Extrelut column was a glass column (I.D. 5 mm, Pharmacia HR5/5) for acid hydrolysis. It was first charged with Extrelut to a length of 3 cm,

then plugged at both ends with a small portion of quartz wool, and finally firmly fitted with plungers. An acid solution was loaded in the same way as the first column.

The [^{11}C]HCN, converted from [^{11}C]CO_2 and carried with a He flow, was passed through the first Extrelut column and the sodalime column. The radioactivity accumulating on the Extrelut column was monitored with the radiation detector. When it reached a maximum, the 6-way valve was switched and the column was heated with the hot blower at *ca.* 60 °C for 3 min to complete the substitution reaction. A 5 mL portion of diethylether was then sequentially passed through the first and second Extrelut columns. The radioactive substituted product, 1-aminocyclopentane-1-[^{11}C]nitrile ([^{11}C]ACPN), was in this way extracted from the reaction mixture to the ether layer and then from the ether layer to the acid solution. The hydrolysis with 6 N HCl was carried out after the back-extraction of [^{11}C]ACPN into the second Extrelut column. After hydrolysis at 160 °C, most of the HCl was eliminated from the column by sweeping with a He flow at a rate of 200 mL/min for 2 min while the column was cooled from 160 to 80 °C. The residue remaining in the column was washed out with 1 mL of water, and the washing was applied to solid phase extraction with a short disposable column of cation exchange resin (H^+, SCX, Whatman). The column was washed with an additional 2 mL of water and the [^{11}C]ACPC retained was then eluted with 6 mL of saline.

Results at optimization of the on-column preparation of [^{11}C]ACPC are summarized in Table 2. One of the advantages of the present system has been amply demonstrated in the column extraction with Extrelut. Efficient extraction and back-extraction can be accomplished at the same time by the single procedure of flushing ether through two columns, and this excellent feature can facilitate a synthesis automation.

In our previous study, HCl was chosen for the acid hydrolysis of the [^{11}C]ACPN because this volatile acid could be easily removed by evaporation and consequently no further purification was necessary. This procedure was repeated on-column in the present study and it was found that the yields by on-column hydrolysis were comparable to those by conventional methods. Ten-min heating provided over 80% conversion yields. The HCl used for the hydrolysis was very effectively removed from the column by the He flow. The washing from the column was usually around 3 without adjustment of pH. Most of the [^{11}C]ACPN and unknown ^{11}C-imtermediate product remaining in the second Extrelut column after the hydrolysis was swept away together with the HCl, while the [^{11}C]ACPC stayed in the column. The [^{11}C]ACPC could be simply purified by solid phase extraction with a disposable SCX column and finally obtained in saline without solvent evaporation. Thus, the [^{11}C]ACPC was prepared in decay-corrected radiochemical yield of over 60% within 40 min.

References

1) Hayes R. H., Washburn L. C., Wieland B. W., et al., J. Nucl. Med. **17** (1976) 748.
2) Iwata R., Ido T., Takahashi T., Nakanishi H. and Iida S., Appl. Radiat. Isot. **38** (1987) 97.

Table 1. Production of the [^{11}C]fatty acids by the column extraction method.

Fatty acid	Column temperature	[^{11}C]CO_2 trapping efficiency	Radiochemical yield	Radiochemical purity
[^{11}C]Acetic acid	-5°C	>99%	91~96%	>99%
	Room temp.	99%	60~72%	>99%
[^{11}C]Palmitic acid	-5°C	<10%	~1%	96%
	0°C	87%	34~40%	≥98%
	Roomtemp.	98%	43~55%	≥98%

Table 2. Summary of the on-column preparation of [^{11}C]ACPC.

Trapping yield of [^{11}C]CO_2 by the reaction column	98~99%
Extraction yield of [^{11}C]ACPN from the reaction column	95%
Bact-extraction yield of [^{11}C]ACPN into the hydrolysis column	86%
Hydrolysis yield	82%
Overall radiochemical yield	>60%
Radiochemical purity	~98%
Overall synthesis time	40 min

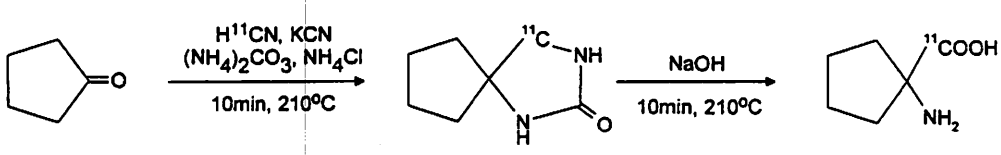

Scheme I

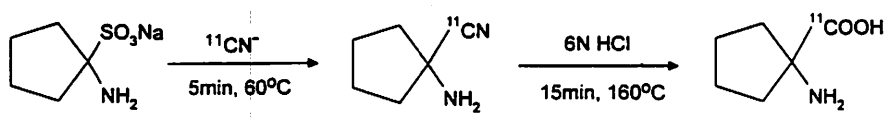

1 2 3

Scheme II

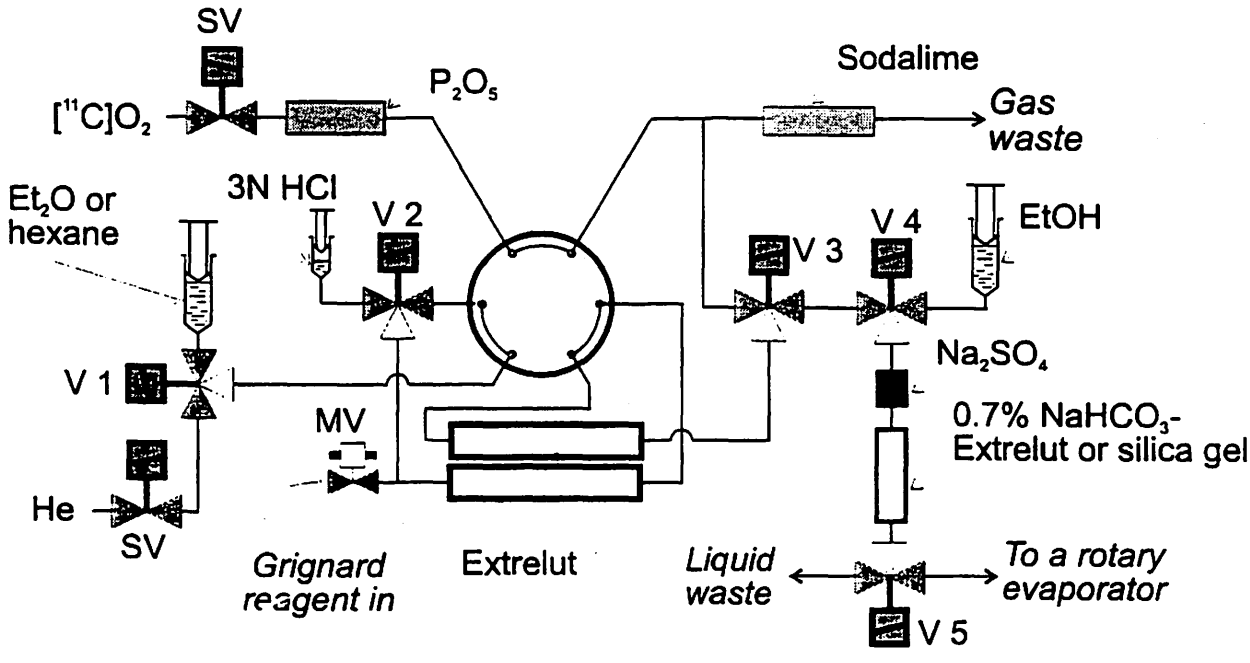

Fig. 1. Semi-automated system for the on-column preparation of [^{11}C]fatty acids.

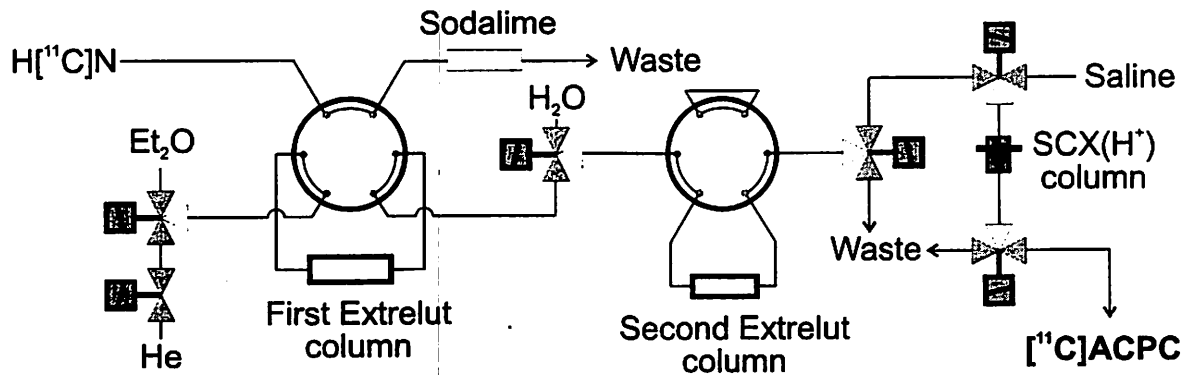

Fig. 2. Semi-automated system for the on-column preparation of [^{11}C]amino acid.

III. 2. Convenient Synthesis of ω-O-Tosylfatty Acid Esters

*Takahashi T. *,Ido T., Mukoyoshi M. and Iwata R.*

Cyclotron and Radioisotope Center, Tohoku University
*Radioisotope Center, Niigata University**

Introduction

In previous papers[1-2], we reported that ω-O-tosylfatty acid methyl esters were good precursors for [^{18}F]fluorofatty acid synthesis. While, for ω-O-tosylfatty acid ester synthesis, commonly ω-hydroxyfatty acids and ω-bromofatty acids are commercially available as starting materials. From this viewpoint, in order to establish the general synthetic method of starting materials for [^{18}F]fluorofatty acid synthesis, we have studied the mutual conversion among ω-hydroxy-, ω-bromo- and ω-O-tosyl-fatty acid derivatives. In this paper, the simple and easy conversion methods of ω-hydroxyfatty acids and ω-bromofatty acids into ω-O-tosylfatty acid esters are described.

Materials and Methods

16-Hydroxyhexadecanoic acid (1a) and silver p-toluenesulfonate (silver tosylate) were purchased from Aldrich Chem. Co. Inc., 11-bromoundecanoic acid (2b), 8-bromo-n-octanoic acid (2c), ethyl bromoacetate, γ-octanolactone, p-toluenesulfonyl chloride (tosyl chloride), were from Tokyo Kasei Kogyo Co. Ltd, 25% hydrogen bromide in acetic acid solution was from Wako Pure Chem. Ind. Ltd.

The total synthetic scheme of ω-O-tosylfatty acid esters is shown in figure 1.

Synthesis of ω-O-tosylfatty acid esters from ω-hydroxyfatty acids (Method A): As a typical example, the synthetic procedure for methyl 16-O-tosylhexadecanoate is described.

Methyl 16-hydroxyhexadecanoate (3a): To a suspension of 16-hydroxyhexadecanoic acid (1a) (3.0 g, 11 mmol) in abs. MeOH (90 mL), $SOCl_2$ (21 mL) was added dropwise at 0 °C. The mixture was stirred at 0 °C for 15 min after then refluxed for 1hr. After removal of the solvent, the residue (crude **3a**) was used for the next synthesis without further purification.

Methyl 16-O-tosylhexadecanoate (6a): To a solution of the crude **3a** dissolved in abs. CH_2Cl_2 (200 mL), a solution of tosyl chloride (6.0 g, 31 mmol) dissolved in abs. CH_2Cl_2 (200 mL) and triethylamine (6 mL) were added. The mixture was stirred at room temperature for 5 days. After removal of the solvent, water (100 mL) and conc. HCl (40 mL) were

added, followed by ether extrabtained by the evaporation was purified by column chromatography (Hexane/ CH_2Cl_2=1/1 (V/V)) to give **6a** (2.0 g). Yield : 41% (from **1a**). m.p. : 56-58 °C. i. r. ($CHCl_3$) : 1730 cm^{-1} (COOMe). MS (m/e): 440 (M^+), 409 (M^+-OMe). ^{1}H-NMR ($CDCl_3$) : δ 0.94-1.84 (26H, m), 2.30 (2H, t, -CH_2-COOMe), 2.44 [3H, s, p-CH_3 (tosyl)], 3.66 (3H, s, -COOCH_3), 4.00 (2H, t, Tos-O-CH_2-), 7.26 [arom. 2H (tosyl), d; J=9 Hz], 7.77 [arom. 2H (tosyl), d; J=9 Hz].

Synthesis of ω-O-tosylfatty acid esters from ω-bromofatty acids (Method B): The conversion of ω-bromofatty acid esters into ω-O-tosylfatty acid esters (route (g)) was carried out by a method similar to that described in the literature[3]. As a typical example, the synthetic procedure for methyl 11-O-tosylundecanoate is described.

Methyl 11-bromoundecanoate (4b): **4b** was synthesized from 11-bromoundecanoic acid (2b) (1.0 g, 3.8 mmol) in a manner similar to the synthesis of **3a**. The obtained residue was purified by column chromatography (Hexane/CH_2Cl_2=1/1) to give **4b** (701 mg). Yield : 67% (from **2b**). i. r. (neat) : 1740 cm^{-1} (COOMe). MS (m/e) : 278, 280 (M^+), 247, 249 (M^+-OMe), 199 (M^+-Br). ^{1}H-NMR ($CDCl_3$) : δ 1.04-2.00 (16H, m), 2.30 (2H, t, -CH_2-COOMe), 3.40 (2H, t, Br-CH_2-), 3.66 (3H, s, -COOCH_3).

Methyl 11-O-tosylundecanoate (6b): To a solution of **4b** (696 mg, 2.5 mmol) dissolved in dry acetonitrile (4 mL), silver tosylate (839 mg, 3.0 mmol) was added. After refluxing with protection from light for 1 day, the reaction mixture was poured into water (50 mL), followed by ether extraction (50 mL×3). The residue obtained by the evaporation was purified by preparative TLC (Hexane/CH_2Cl_2=3/7) to give **6b** (742 mg). Yield : 80% (from **4b**). m.p. :<30 °C. i. r. ($CHCl_3$) : 1730 cm^{-1} (COOMe). MS (m/e) : 370 (M^+). ^{1}H-NMR ($CDCl_3$) :δ 0.92-1.88 (16H, m), 2.30 (2H, t, -CH_2-COOMe), 2.44 [3H, s, p-CH_3 (tosyl)], 3.66 (3H, s, -COOCH_3), 4.00 (2H, t, Tos-O-CH_2-), 7.32 [arom. 2H (tosyl), d; J=9 Hz], 7.76 [arom. 2H (tosyl), d; J=9 Hz].

Then, as a special example for the preparation of bromofatty acid methyl esters, the synthesis of methyl 4-bromooctanoate is described below.

Methyl 4-bromooctanoate: γ-Octanolactone (1.0 g, 7.0 mmol) was dissolved in 25% HBr/AcOH (25 mL) and the mixture was heated at 100 °C for 14 hr. After cooling to room temperature, excess HBr/AcOH was evaporated *in vacuo*. The residue (crude 4-bromooctanoic acid) was used for the next esterification without further purification. Methyl 4-bromooctanoate was synthesized from the crude 4-bromooctanoic acid in a manner similar to the synthesis of **3a** ($SOCl_2$ (25 mL) and MeOH (25 mL) were used). The obtained residue was purified by column chromatography (Hexane/CH_2Cl_2=1/1) to give methyl 4-bromooctanoate (1.3 g). Yield : 78% (from γ-octanolactone). i. r. ($CHCl_3$) : 1740 cm^{-1} (COOMe). MS (m/e) : 236, 238 (M^+), 205, 207 (M^+-OMe), 157 (M^+-Br).

Results and Discussion

As starting materials for ω-O-tosylfatty acid ester synthesis, ω-hydroxyfatty acids and ω-bromofatty acids are commercially available. For example, in the cases of 16 carbon-membered and 11 carbon-membered fatty acids, 16-hydroxyhexadecanoic acid and 11-bromoundecanoic acid can be available, respectively.

In the conversion of ω-hydroxyfatty acids into ω-O-tosylfatty acid methyl esters (method A), the procedures described here are general. The chemical yields of methyl 16-O-tosylhexadecanoate and methyl 11-O-tosylundecanoate were 41-64% and 49-60% (from ω-hydroxyfatty acids), respectively. While, in the conversion of ω-bromofatty acids into ω-O-tosylfatty acid esters (method B), experimental data in O-tosylation with silver tosylate (route (g)) are shown in Table 1. We previously reported the conversion of ω-bromofatty acids into ω-O-tosylfatty acid methyl esters by way of ω-benzyloxyfatty acid methyl esters (previous method) (Figure 1 ; route (c) → route (e) → route (f))[1]. For example, in the comparison of method B with previous method in methyl 11-O-tosylundecanoate synthesis, the total yield using method B is 54% (route (d) : 67% , route (g) : 80%), while that using previous method is 26% (route (c) : 60% , route (e) : 65% , route (f) : 66%). This result shows the usefulness of O-tosylation with silver tosylate. Furthermore, in the reaction of methyl 4-bromooctanoate with silver tosylate, several attempts to prepare methyl 4-O-tosyloctanoate were unsuccessful. On the basis of the main process of elimination in the reaction of silver tosylate with a secondary or tertiary halide reported by Emmons et al.[4], formation of the unsaturated fatty acid methyl ester (methyl octenoate) is possible.

The synthesized ω-O-tosylfatty acid esters were characterized by i.r. spectra, ^{1}H-NMR spectra and mass spectra. Generally, their ester groups showed a strong i.r. band at 1730-1740 cm^{-1} and the presence of OMe or OEt was supported by mass spectra. Additionally, by ^{1}H-NMR spectra, both triplet signals of the following two methylene partial structures, Tos-O-$\underline{CH_2}$- and -$\underline{CH_2}$-COOR (R=Me, Et) were observed at δ 4.00 and 2.30, respectively.

Now, route (g) (method B) has been applied to the conversion of 3-benzyl-1-butanoyl-2-(16-bromopalmitoyl)glycerol into 3-benzyl-1-butanoyl-2-(16-O-tosyl palmitoyl)glycerol, which is a starting material for the synthesis of 1-butanoyl-2-(16-[^{18}F]fluoropalmitoyl)glycerol, a potential tracer for second messenger system imaging by PET. This result has been suggested that O-tosylation with silver tosylate was widely effective for the synthesis of terminal O-tosyl-compounds.

References

(1) Takahashi T., Ido T. and Iwata R., Appl. Radiat. Isot. **42** (1991) 801.
(2) Takahashi T., Ido T. and Iwata R., Appl. Radiat. Isot. **43** (1992) 822.
(3) Kornblum N., Jones W. J. and Anderson G. J., Am. Soc. **81** (1959) 4113.
(4) Emmons W. D. and Ferris A. F., Am. Soc. 75 (1953) 2257.

Table 1. Experimental data in the conversion of ω-bromofatty acid esters into ω-O-tosylfatty acid esters.

Starting Materials	Products	yield (%)
$Br-(CH_2)_{15}-COOMe$ (4a)	$Tos-O-(CH_2)_{15}-COOMe$ (6a)	69
$Br-(CH_2)_{10}-COOMe$ (4b)	$Tos-O-(CH_2)_{10}-COOMe$ (6b)	80
$Br-(CH_2)_7-COOMe$ (4c)	$Tos-O-(CH_2)_7-COOMe$ (6c)	66
$Br-CH_2-COOEt$	$Tos-O-CH_2-COOEt$	85
$C_4H_9-CH(Br)-(CH_2)_2-COOMe$	$C_3H_7-CH=CH-CH_2CH_2-COOMe$ [a] or $C_4H_9-CH=CH-CH_2-COOMe$	—

a) not identified

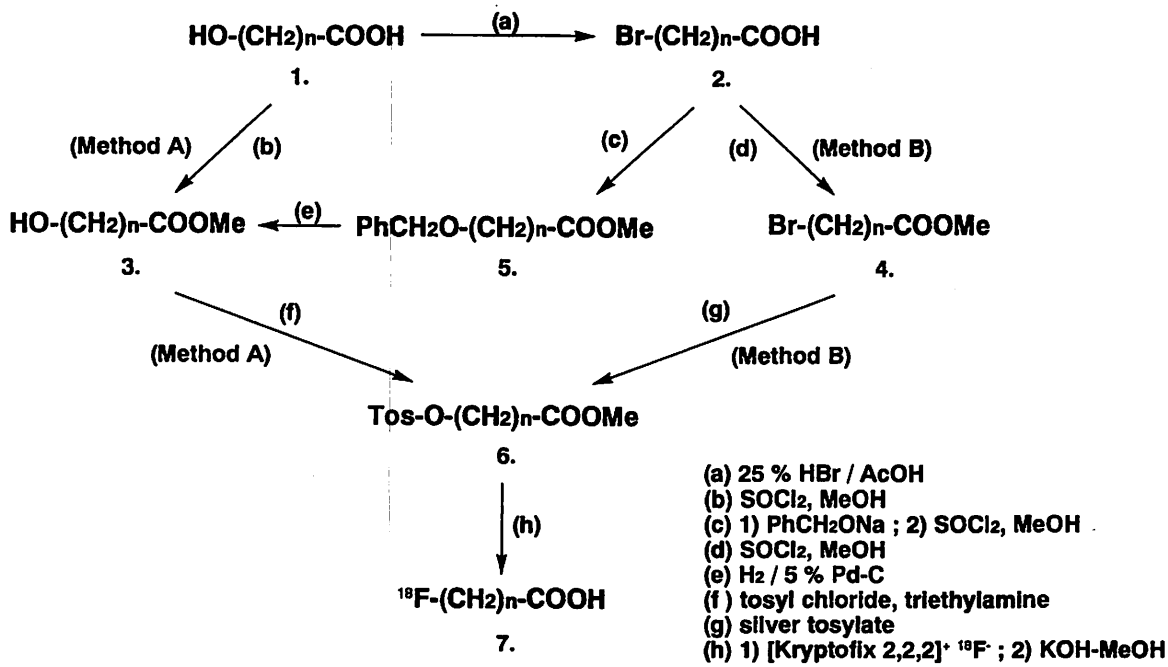

Fig. 1. Total synthetic scheme of ω-O-tosylfatty acid esters.

III. 3. Autoradiographic Analysis of Muscarinic Acetylcholine Binding Sites in the Exo-Focal Remote Areas of the Postischemic Rat Brain

Nagasawa H., Araki T., and Itoyama Y.**

Department of Neurology, Miyagi National Hospital
**Department of Neurology, Tohoku University School of Medicine*

Introduction

Transient cerebral ischemia leads to neuronal damage in selectively vulnerable areas. The extent of neuronal damage is dependent on the duration of ischemia[1,2]. Neuronal degenerative processes occur especially in the hippocampus of the rat[3] and the mongolian gerbil[4] induced by transient forebrain ischemia. Transient focal ischemia also induces neuronal degeneration in specific brain areas in the rat. Postischemic delayed neuronal damage has been reported in the ipsilateral thalamus and substantia nigra which lay outside ischemic areas of rat brain after middle cerebral artery (MCA) occlusion[5,6]. In these reports, the histological appearance of these remote areas was characterized by degeneration of most neurons with no necrotic changes of neuroglia and blood vessels. The mechanism of such a delayed phenomenon in the exo-focal remote areas is unclear, but it has been speculated that it might be caused by a transsynaptic process neuroanatomically associated with ischemic foci and that intracellular and transsynaptic signal transduction systems might play important roles in this mechanism[7-11].

Acetylcholine is a major neurotransmitter in the central nervous system and is thought to contribute to memory and cognitive processes[12]. The anatomical distribution of muscarinic acetylcholine binding sites in the brain has been mapped by an autoradiographic method using the radiolabeled antagonist [^{3}H]quinuclidinyl benzilate. Autoradiographic studies suggest that acetylcholine is very rich in the cerebral cortex, the striatum, the hippocampus, and the thalamus. In the present study, we examined chronological changes of acetylcholine binding sites of the rat brain after 90 min of MCA occlusion and after such occlusion followed by different periods of recirculation in order to clarify the damage to the cholinergic system in the postischemic brain areas during the chronic stage of ischemia.

Materials and Methods

ISCHEMIA MODEL

Adult male Wistar rats of the SPF strain weighing 280 - 300 g were allowed free access to food and water before and after all procedures. Six rats were used in each experiment. A detailed description of the surgical procedure has been previously reported[13]. In brief, after induction of anesthesia with a gas mixture of 70% N_2O and 2% halothane (the balance being O_2), the right middle cerebral artery (MCA) was occluded with a silicone rubber cylinder attached to a nylon surgical thread introduced from the bifurcation of the internal carotid artery immediately after ligation of the ipsilateral common and external carotid arteries. The cylinder was made of 4-0 nylon surgical thread (Nitcho Kogyo Co., Ltd., Tokyo, Japan), 16 mm long. This cylinder was coated with silicone (Xantopren, Bayer Dental, Leverkusen, FRG) which was mixed with a hardener (Elastomer Activator, Bayer Dental) to increase the thickness of the distal 5 mm to 0.25-0.30 mm. After introduction of the embolus, the internal carotid artery was ligated just distal to the point of insertion. The embolus extended from the bifurcation of the internal carotid artery to the proximal portion of the anterior cerebral artery (ACA). The origin of the right MCA and that of the right posterior communicating artery were occluded by the silicone rubber cylinder. In 6 sham-operated control rats, the right internal and external carotid arteries were ligated. Surgery was performed within 15 min with no bleeding. Body temperature was kept at normal limits with a heating pad. Following surgery, anesthesia was discontinued and all rats exhibited neurological deficits characterized by left hemiparesis with upper extremity dominancy and right Horner's syndrome. After 90 min of MCA occlusion, the 6 rats were decapitated with no recirculaion, and in the other rats, recirculation was achieved by pulling the thread out of the internal carotid artery under the same anesthetic conditions as during surgery. Once again, the rats were allowed free access to food and water. Although the ipsilateral common and external carotid arteries had been ligated, the ischemic area could be reperfused via the cerebral arterial circle (circle of Willis) through the contralateral carotid and basilar arteries, and by collateral circulation of the cortical branches of the cerebral arteries. The rats were killed by decapitation 3 h, 6 h, 1 day, 3 days, 1 week, 2 weeks, and 4 weeks after recirculation. After decapitation, the brains were quickly removed and frozen in powdered dry ice, and stored at -80 °C until assay. Serial coronal sections 12 μm in thickness were cut on a cryostat and thaw-mounted onto gelatin-coated slides. Adjacent sections were stained with cresyl violet and Luxol fast blue, as well as with hematoxylin and eosin, in order to confirm the ischemic areas.

Muscarinic acetylcholine receptor autoradiography

Muscarinic acetylcholine receptors were quantified using [^{3}H]quinuclidinyl benzilate ([^{3}H]QNB, spec. act. 41.5 Ci/mmol, Amersham, International plc, Buckingham, UK) according to the method of Onodera et al.[14]. Sections were incubated with 1 nM [^{3}H]QNB

in phosphate buffer (pH 7.4) at room temperature for 90 min. The slides were then washed in the buffer at 4 °C for 5 min and dried under a cold stream of air. Non-specific binding was determined using 1 μM atropine (Sigma, Chemical Company, St. Louis, USA). Autoradiograms were prepared from the sections by exposing them to [^{3}H]sensitive hyperfilm (Amersham, Sweden AB, Solna, Sweden) with a tritium standard microscale (Amersham, International plc, Buckingham, UK) for 2 weeks in standard X-ray cassettes.

Areas of the brain were identified with reference to the atlas of Paxinos and Watson[15]. The optical density of the brain regions was measured with a computer-assisted image analyzer (Zeiss, IBAS image analyzer system, FRG) without the examiner knowing the experimental protocol. The relationship between optical density and radioactivity was obtained with reference to the [^{3}H]microscales co-exposed with the sections using a third-order polynomial function. The optical density of the brain regions measured in the present study was in the range where optical density and radioactivity of the [^{3}H]microscales showed a near linear relationship.

Statistical analysis

Values were expressed as means ±S.D. fmol/mg tissue using six animals. Data regarding the QNB binding sites in each structure of the brain were analyzed using Duncan's multiple range test with $p<0.05$ and $p<0.01$ considered to be statistically significant.

Results

Chronological alterations of [^{3}H]QNB binding sites in each structure of rat brain after 90 min of MCA occlusion and after such occlusion followed by different periods of recirculation are summarized in Table 1. Representative autoradiograms are shown in Figure 1. After 90-min ischemia followed by 3-day recirculation, significant decreases of the [^{3}H]QNB binding sites were first observed in the anterior neocortex (FrPaSS) and the lateral part of the caudate putamen (CPu-L), both of which were supplied by the occluded MCA. Thereafter, [^{3}H]QNB binding sites of the ischemic side decreased to approximately 20% in the FrPaSS and to 30% in the CPu-L of each control value 4 week after the ischemic insult (Table 1). Moreover, 3 days after the ischemia, a significant reduction of [^{3}H]QNB binding sites was observed in the ipsilateral thalamus, the amygdala, and also 1 week after the ischemia, in the substantia nigra, areas remote from the precedent ischemic areas. Thereafter, the binding sites decreased progressively in the thalamus and the substantia nigra on the ischemic side. There were no significant changes of [^{3}H]QNB binding sites in the contralateral non-ischemic hemisphere.

Discussion

The present study indicated that two different alterations of muscarinic acetylcholine binding sites associated with the mechanisms of neuronal damage took place in the

postischemic rat brain. First, in the ischemic foci, the ipsilateral FrPaSS and the CPu-L, [^{3}H]QNB binding sites decreased after 90 min of ischemia followed by 3 days of recirculation. We previously reported that more rapid changes of second messenger systems than of muscarinic acetylcholine binding sites were observed concurrent with abnormal calcium accumulation in the FrPaSS and the CPu-L on the ischemic side using the same ischemia model[10-11]. In this model of ischemia, the anterior neocortex (FrPaSS) and lateral segment of the caudate putamen (CPu-L), which were supplied by the occluded MCA, were the regions most frequently damaged as so-called ischemic foci[13]. The reduction of muscarinic acetylcholine binding sites in the FrPaSS and the CPu-L is explained by the direct damage to intracellular components including cell membrane following damage of second messenger systems and disruption of calcium homeostasis by ischemia-induced energy failure.

Second, in the exo-focal postischemic brain areas, the ipsilateral thalamus and the amygdala, a significant decrease of [^{3}H]QNB binding sites was observed 3 days after the ischemia. Moreover, in the ipsilateral substantia nigra, [^{3}H]QNB binding sites decreased significantly compared with the value of sham-operated control rats 1 week after the ischemia. The alteration of [^{3}H]QNB binding sites in the substantia nigra was minimal because of their initial low binding activity.

These changes of muscarinic acetylcholine binding sites observed in the thalamus and the substantia nigra on the ischemic side were concurrent with the abnormal calcium accumulation detected there in our previous study[5]. Moreover, both phenomena, i.e., the reduction of [^{3}H]QNB binding sites and abnormal calcium accumulation, in two remote areas on the ischemic side preceded the histologic findings of delayed neuronal damages. In contrast with the FrPaSS and the CPu-L, the ipsilateral thalamus and the substantia nigra were remote from these ischemic areas, and both areas had not been directly affected by the original ischemic insult[5]. Delayed neuronal damages in the exo-focal remote areas might be caused by a transsynaptic process associated with the ischemic foci[5]. Iizuka et al. reported that delayed neuronal degeneration of the ipsilateral thalamus was observed after somatosensory cortical infarct of rats using the Fink-Heimer silver staining method[16]. Reduction of muscarinic acetylcholine binding sites in the thalamus on the ischemic side may be explained by retrograde neuronal degeneration due to thalamocortical fiber damage in ischemic cortical regions.

We realize that the mechanisms of delayed neuronal damage in the exo-focal brain areas may be variable and are complicated in remote areas, i.e., the thalamus, the amygdala, and the substantia nigra on the ischemic side. Yamada et al. reported that basic fibroblast growth factor prevented neuronal degeneration of the thalamus after MCA occlusion in rats[17]. This indicates that trophic substances may play an important role in the mechanism of neuronal damage of the thalamus which might be caused by retrograde degeneration of the thalamo-cortical pathway after ischemic insult. On the other hand, in the substantia nigra, we

speculate that delayed neuronal degeneration may be induced by disinhibitory overexcitation caused by diminished inhibitory regulation from the caudate putamen, which was affected by the precedent ischemia[5,11]. Further detailed investigation is required in order to clarify the mechanisms of delayed neuronal degeneration caused by neuronal network disturbances after ischemia.

It is well known that thalamic damage results in some behavioral neurological disturbances, such as amnesic syndromes, dementia, or aphasic syndrome[18,19]. There have been few studies on clinical symptoms in multi-focal brain damages during the chronic stage after stroke, and such delayed neuronal degeneration in the exo-focal remote areas after ischemia have only recently been revealed by animal experiments. Based on the present study, we suggest that multi-focal postischemic alterations of muscarinic acetylcholine binding sites may exacerbate the clinical symptoms of patients during the chronic stage of stroke. However, further study is required to confirm the clinical meaning of multi-focal neuronal degeneration after stroke.

References

1) Smith M. L. et al., Acta Neurol. Scand. **69** (1984) 385.
2) Araki T., Kato H. and Kogure K., Acta Neurol. Scand. 80 (1989) 548.
3) Pulsinelli W. A., Brierley B. J. and Plum F., Ann. Neurol. **11** (1982) 491.
4) Kirino T., Brain Res. **239** (1982) 57.
5) Nagasawa H. and Kogure K., Brain Res. **524** (1990) 196.
6) Tamura A. et al., Brain Res. **510** (1990) 154.
7) Siejö B. K., J. Cereb. Blood Flow Metab. **1** (1981) 155.
8) Raichle M. E., Ann. Neurol. **13** (1983) 2.
9) Kogure K., Tanaka J. and Araki T., Neurochem. Pathol. **9** (1988) 145.
10) Nagasawa H. and Kogure K., Brain Res. **563** (1991) 7.
11) Nagasawa H. and Kogure K., J. Neurosci. Res. **31** (1992) 507.
12) Bartus R. T. et al., Science **217** (1982) 408.
13) Nagasawa H. and Kogure K., Stroke **20** (1989) 1037.
14) Onodera H., Sato G. and Kogure K., Brain Res. **415** (1987) 309.
15) Paxinos G. and Watson C., The rat brain in stereotaxic coordinates, ed 2. Sydney, Academic Press, Inc. (1986).
16) Iizuka H., Sakatani K. and Young W., Stroke **21** (1990) 790.
17) Yamada K. et al., J. Cereb. Blood Flow Metab. **11** (1991) 472.
18) Graff-Radford N. R. et al., Neurology **34** (1984) 14.
19) Bogousslavsky J., Regli F. and Uske A., Neurology **38** (1988) 837.

Table 1. Time-course of [^{3}H]QNB binding in each structure of the rat brain after 90 min of MCA occlusion followed by different of recirculation.

Structure	Control	90-min ischemia	3 hours	6 hours	1 day
Ischemic side					
FrPaM	367.4 ± 24.1	366.4 ± 33.9	363.1 ± 20.0	364.1 ± 35.1	355.7 ± 20.7
FrPaSS	348.5 ± 31.2	352.3 ± 38.9	340.0 ± 32.5	357.4 ± 36.5	337.4 ± 37.4
CPu(L)	397.7 ± 21.3	414.4 ± 43.2	415.1 ± 48.5	405.3 ± 43.2	409.8 ± 37.1
CPu(M)	395.4 ± 37.3	382.3 ± 43.9	390.5 ± 32.9	397.2 ± 38.2	364.9 ± 22.2
Hippocampus	350.2 ± 18.3	375.0 ± 12.4	359.5 ± 43.8	383.4 ± 48.3	339.1 ± 38.9
Thalamus	139.0 ± 19.1	141.0 ± 21.6	134.0 ± 26.9	143.8 ± 22.8	123.2 ± 34.9
Amygdala	284.9 ± 12.1	281.8 ± 26.2	338.6 ± 36.2	317.9 ± 47.6	283.0 ± 35.2
Substantia nigra	62.9 ± 19.2	69.4 ± 18.9	64.9 ± 11.3	58.9 ± 10.0	66.4 ± 12.6
Pons	98.1 ± 15.8	95.3 ± 28.4	103.0 ± 32.3	104.7 ± 34.9	93.7 ± 15.2
Non-ischemic side					
FrPaM	340.9 ± 29.2	369.4 ± 27.5	357.1 ± 25.9	359.5 ± 34.2	348.5 ± 13.9
FrPaSS	346.4 ± 30.8	359.0 ± 28.1	351.8 ± 21.1	352.8 ± 40.2	345.7 ± 23.1
CPu(L)	387.8 ± 28.5	380.2 ± 41.6	415.7 ± 49.3	394.4 ± 40.4	358.3 ± 46.6
CPu(M)	383.5 ± 42.5	385.9 ± 33.2	377.7 ± 49.2	389.3 ± 41.9	347.1 ± 27.8
Hippocampus	347.6 ± 16.1	370.9 ± 31.4	363.6 ± 45.7	378.3 ± 42.9	336.4 ± 42.7
Thalamus	145.6 ± 25.4	155.5 ± 25.5	158.9 ± 35.9	151.8 ± 20.9	146.1 ± 26.9
Amygdala	291.4 ± 39.9	325.2 ± 40.3	323.1 ± 47.3	311.8 ± 40.7	278.4 ± 21.5
Substantia nigra	66.3 ± 14.7	64.5 ± 14.2	63.5 ± 11.4	69.4 ± 10.8	63.2 ± 10.5
Pons	112.2 ± 10.6	103.3 ± 18.0	97.2 ± 21.2	96.1 ± 20.1	93.9 ± 15.6

Values are given in Mean ± S.D. fmol/mg tissue using six animals.
FrPaM: frontoparietal cortex, motor area, supplied by anterior cerebral artery;
FrPaSS: frontoparietal cortex, somatosensory area, supplied by middle cerebral artery;
CPu(L): lateral segment of caudate putamen; CPu(M): medial segment of caudate putamen;
*p<0.05; **p<0.01, significant difference from sham-operated control values using Ducan's multiple range test.

Table 1. Time-course of [^{3}H]QNB binding in each structure of the rat brain after 90 min of MCA occlusion followed by different of recirculation(continued).

Structure	3 days	1 week	2 weeks	4 weeks
Ischemic side				
FrPaM	354.3 ± 23.8	353.8 ± 45.9	355.9 ± 34.4	348.0 ± 29.4
FrPaSS	248.9 ± 23.3**	198.0 ± 19.6**	91.4 ± 18.5**	74.0 ± 15.6**
CPu(L)	327.9 ± 27.8*	250.4 ± 48.4**	158.1 ± 30.1**	122.9 ± 42.0**
CPu(M)	366.7 ± 24.1	370.2 ± 45.1	361.1 ± 28.2	362.1 ± 34.9
Hippocampus	362.3 ± 42.2	374.2 ± 40.2	351.3 ± 35.3	347.7 ± 28.7
Thalamus	91.1 ± 23.5**	96.6 ± 34.1**	98.2 ± 22.7**	54.8 ± 16.1**
Amygdala	178.9 ± 39.4*	229.8 ± 37.3*	203.6 ± 28.3*	99.2 ± 20.9**
Substantia nigra	62.6 ± 22.7	38.9 ± 17.6*	44.0 ± 13.1*	43.9 ± 18.6*
Pons	92.9 ± 31.4	93.5 ± 11.7	99.1 ± 11.7	86.9 ± 18.5
Non-ischemic side				
FrPaM	351.5 ± 37.6	357.2 ± 27.1	358.3 ± 26.5	349.7 ± 27.4
FrPaSS	354.6 ± 43.7	350.4 ± 23.6	353.8 ± 33.6	358.2 ± 26.9
CPu(L)	385.8 ± 27.4	378.8 ± 44.9	402.8 ± 37.4	387.0 ± 26.2
CPu(M)	381.5 ± 43.7	370.6 ± 38.3	384.2 ± 37.1	375.9 ± 32.8
Hippocampus	353.2 ± 34.7	366.2 ± 35.3	344.2 ± 40.6	329.4 ± 21.9
Thalamus	141.7 ± 22.7	161.0 ± 24.8	149.6 ± 37.1	146.2 ± 17.2
Amygdala	265.9 ± 43.0	316.9 ± 36.1	304.2 ± 23.5	300.7 ± 26.1
Substantia nigra	60.8 ± 13.1	60.7 ± 10.8	69.9 ± 28.6	62.3 ± 13.6
Pons	97.2 ± 26.2	90.0 ± 13.3	85.9 ± 23.9	103.9 ± 29.8

Values are given in Mean ± S.D. fmol/mg tissue using six animals.
FrPaM: frontoparietal cortex, motor area, supplied by anterior cerebral artery;
FrPaSS: frontoparietal cortex, somatosensory area, supplied by middle cerebral artery;
CPu(L): lateral segment of caudate putamen; CPu(M): medial segment of caudate putamen;
*p<0.05; **p<0.01, significant difference from sham-operated control values using Duncan's multiple range test.

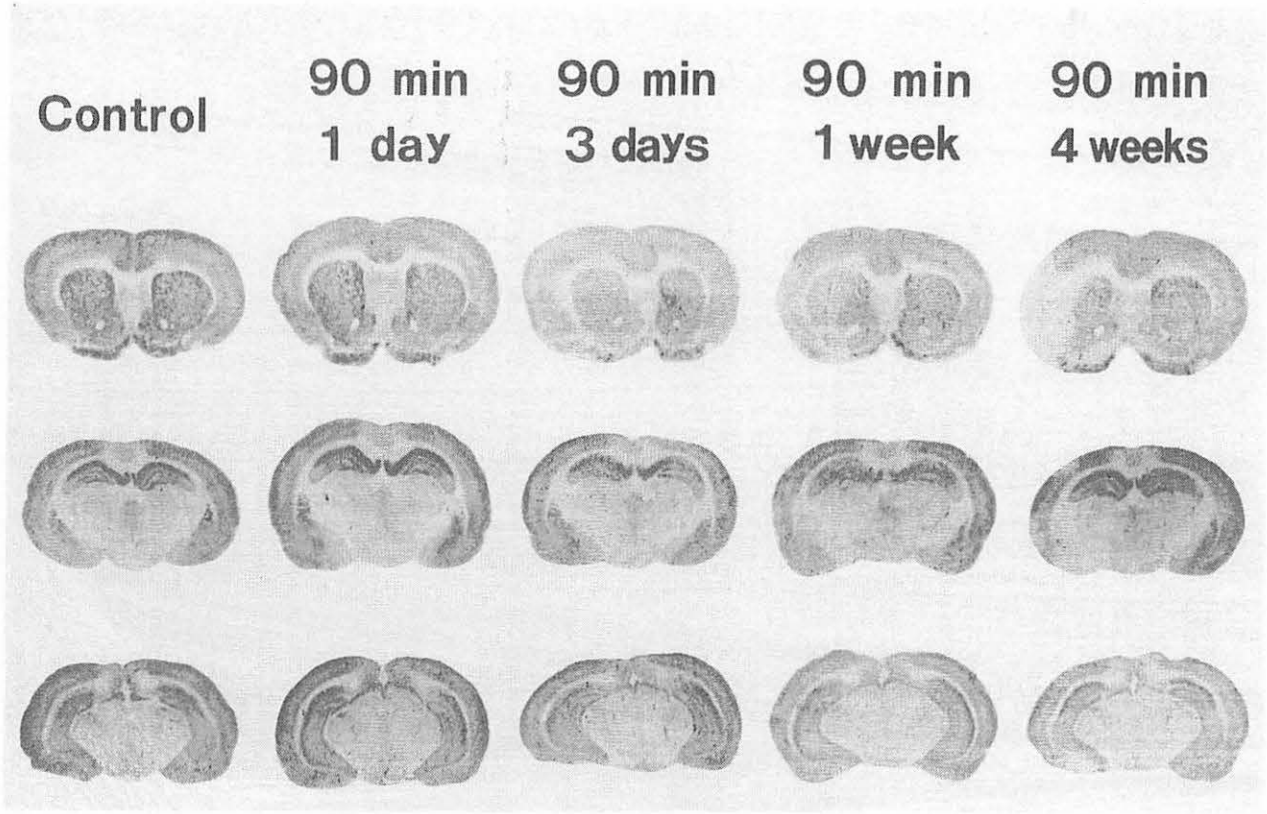

Fig. 1. [^{3}H]QNB autoradiograms of the brains of sham-operated control rats and those obtained after 90 min of MCA occlusion followed by 1-day, 3-day, 1-week, and 4-week recirculation. Representative autoradiograms show coronal sections at the level of the caudate putamen (top), the thalamus (middle), and the substantia nigra (bottom). Three days after the ischemia, a significant reduction of the binding sites was first detected not only in the cerebral cortex and the lateral segment of the caudate putamen, but also in the ipsilateral thalamus (arrowhead) on the ischemic side and these findings continued up to 4-week recirculation.

III. 4. Effect of Blood Glucose on ^{18}F-FDG Uptake in Experimental Inflammatory Tissue

Yamada S., Kubota K., Kubota R., Tamahashi N., and Ido T.***

Department of Nuclear Medicine and Radiology,
Institute of Development, Aging and Cancer, Tohoku University
*Clustercore Institute of Biology**
*Cyclotron and Radioisotope Center, Tohoku University***

Introduction

It had been believed that ^{18}F-FDG was an inadequate tracer to detect inflammation[1], until clinical PET studies of high ^{18}F-FDG uptake by abscess were reported[2,3]. However, in previous study, we demonstrated that ^{18}F-FDG accumulated in the abscess rim and the surrounding tissue by autoradiography[4,5]. In this study, we examined the effect of blood glucose level on ^{18}F-FDG uptake in inflammatory tissue by tissue distribution study.

Materials and Methods

Male Donryu rats weighing 100-120 g were used. To induce inflammation, animals were inoculated with 0.2 ml of turpentine oil subcutaneously in the left groin. Animals were selected 4 days after inoculation since maximum ^{18}F-FDG uptake was observed on the same day during the longitudinal study[5] and they were divided into two groups (n=6, each). Six rats of one group were subcutaneously injected with 2 units of insulin, and were injected with 740 kBq (20 μCi) of ^{18}F-FDG through the tail vein 5 min later. Other 6 rats as control group were injected with the same dose of ^{18}F-FDG without insulin injection. They were killed by cervical dislocation 1 hour later. The inflammatory tissue sample, including inoculated turpentine-oil, was excised and trimmed off the neighboring subcutaneous tissue. The muscle, heart and liver were excised and blood collected from the heart. Each sample was weighed and the ^{18}F radioactivity was counted with a well-type NAI(TI) autogamma counter and corrected for decay. Data were expressed as the differential uptake ratio (DUR). Simultaneously, blood glucose concentrations were measured by standard enzymatic methods.

Results and Discussion

Table 1 shows the blood glucose of two groups. Mean blood glucose in control group was significantly higher than that in insulin group. Table 2 summarizes results of ^{18}F-

FDG uptake in various tissues of rats 4 days after the inoculation of turpentine oil. The uptakes in blood, liver and inflammation in control group were significantly lower than those in insulin group, respectively. There was no significant difference in heart between control and insulin groups. However, the uptake in muscle in control group was significantly higher than that in insulin group. In this study, ^{18}F-FDG uptakes in blood and liver were directly affected by injected insulin. ^{18}F-FDG uptake in inflammatory tissue is thought to depend on the blood flow[5]. Therefore, the decreased ^{18}F-FDG uptake in inflammatory tissue in insulin group may reflect on the decreased blood glucose level. The increased uptake in muscle in insulin group may reflect the increased movement due to hypoglycemia and the insulin effect.

References

1) Som P. et al., J. Nucl. Med. **24** (1983) 288.
2) Tahara T. et al., J. Comput. Assist. Tomogr. **13** (1989) 829.
3) Sasaki M. et al., J. Comput. Assist. Tomogr. **14** (1990) 486.
4) Yamada S. et al., CYRIC Annual Report 1992, (1992) 114.
5) Yamada S. et al., J. Nucl. Med. (1995) in press.

Table 1. Blood glucose.

	Blood glucose (mg/ml)
Control group	133±17
Insulin group	52±20

* Mean±SD for 6 rats.

Table 2. ^{18}F-FDG uptake in rats 4 days after inoculation of turpentine oil.

	Blood	Heart	Muscle	Liver	Inflammation
Control group	0.26±0.02	8.73±2.01	0.87±0.16	0.27±0.04	1.59±0.23
Insulin group	0.09±0.01	7.56±0.56	1.45±0.14	0.11±0.02	0.76±0.14
	(p<0.001)	(NS)	(p<0.001)	(p<0.001)	(p<0.01)

* Mean±SD for 6 rats. NS: not significant.

( ): p value between Control group and Insulin group.

III. 5. Effects of a Cyclic AMP-Selective Phosphodiesterase Inhibitor, Rolipram, on Age-Related Changes in Neurotransmission and Transduction Systems in the Rat Brain

Kato H., Chen T., Araki T., Kogure K. and Itoyama Y.*

Department of Neurology, Tohoku University School of Medicine
*Institute of Neuropathology, Kumagaya, Japan**

Introduction

Recent studies have shown age-related changes in neurotransmitter systems in mammalian brain[1,2]. In particular, age-dependent changes are known to occur in the hippocampus, which is important in cognitive function such as learning and memory. Calcium ions also play critical roles in various neuronal functions. Age-related changes in calcium metabolism may affect neuronal function, especially neurotransmitter release. Both stimulated and basal releases of a number of neurotransmitters have been shown to change during senescence[3-5].

Rolipram is a clinically effective antidepressant with selective cAMP phosphodiesterase (PDE) inhibiting properties. Rolipram inhibits a Ca^{2+}/calmodulin independent cAMP selective PDE isoenzyme[6-8] leading to increased brain cAMP levels[9]. In this study, we investigated the regional age-related changes in the binding sites of muscarinic acetylcholine, presynaptic cholinergic terminals, protein kinase C, and of a voltage-dependent L-type calcium channel blocker using *in vitro* ligand autoradiography together with the effects of chronic treatment with rolipram on the regional age-related changes in these binding sites in the rat brain.

Materials and Methods

EXPERIMENTAL ANIMALS

Male Wistar rats (CLEA JAPAN INC., Tokyo, Japan), 15 weeks and 80 weeks old, were used. Rolipram (Meiji Seika Kaisha, Ltd., Yokohama, Japan), or vehicle (distilled water), was administered orally at a dose of 0.01 mg/kg or 0.1 mg/kg once a day for 4 weeks. The animals were killed by decapitation and the brains were frozen in powdered dry ice. Sagittal sections, 12 μm in thickness, were cut on a cryostat and thaw mounted onto gelatin-coated slides.

IN VITRO RECEPTOR BINDING AUTORADIOGRAPHIC ASSAYS

Muscarinic cholinergic receptors were quantified using the radiolabeled antagonist [^{3}H]quinuclidinyl benzilate (QNB; specific activity 43 Ci/mmol, Amersham) as reported previously[10]. Autoradiographic localization of [^{3}H]hemicholinium-3 (HC3) binding in the brain was performed according to the method of Forloni and Angeretti[11] with minor modifications. Autoradiography with [^{3}H]phorbol 12,13-dibutyrate (PDBu) was carried out essentially as described by Worley et al.[12]. Binding sites for 1, 4-dihydropyridine calcium antagonists were located with [^{3}H]nimodipine essentially as reported previously[13].

The sections were apposed to Hyperfilm-^{3}H (Amersham) for 2-4 weeks with a set of tritium standards. The optical density of the brain regions was measured using a computer-assisted image analyzer (IBAS Image Analyser System, Zeiss).

Results

[^{3}H]QNB BINDING

In young animals, high [^{3}H]QNB binding was noticed in the hippocampal CA1 sector, the nucleus accumbens, the dentate gyrus, and the striatum, followed by the frontal cortex and the hippocampal CA3 sector (Table 1). In old animals, the [^{3}H]QNB binding was relatively similar to that of young animals. However, a significant decrease was seen in the thalamus and the cerebellum compared with young rats. Chronic treatment with rolipram of the higher dose induced significant decreases in [^{3}H]QNB binding in the frontal cortex, the striatum, and the hippocampal CA3 of the old rats, but no changes were seen in the young rats (Table 1).

[^{3}H]HC3 BINDING

In young animals, high density of [^{3}H]HC3 binding was found in the striatum and the accumbens nucleus. In the hippocampus, the density of [^{3}H]HC3 binding was intermediate (Table 2). In old animals, the density of [^{3}H]HC3 binding was relatively similar to that of young animals, but the frontal cortex showed a slight reduction. After rolipram treatment, [^{3}H]HC3 binding in old rat brains was largely unchanged except for slight changes in the striatum and the thalamus (Table 2). No effects of the treatment was found in young rats.

[^{3}H]PDBu BINDING

In young rats, the highest density of the [^{3}H]PDBu binding was noted in the hippocampal CA1 sector, the molecular layer of the cerebellum, the dentate gyrus, and the hippocampal CA3 sector. The accumbens nucleus, the frontal cortex, the parietal cortex, and the striatum exhibited relatively high [^{3}H]PDBu binding sites (Table 3). In old rats, significant elevations in the [^{3}H]PDBu binding were found in the hippocampal CA1 sector, the dentate gyrus, and the molecular layer of the cerebellum compared with young rats. Chronic treatment with the higher dose of rolipram caused a significant reduction in

[^{3}H]PDBu binding in the hippocampal CA3 sector, the accumbens nucleus, the molecular layer of cerebellum, the frontal cortex, the striatum, the dentate gyrus, and the thalamus. However, there were no significant alterations in [^{3}H]PDBu binding in young rats (Table 3).

[^{3}H]NIMODIPINE BINDING

In young rats, the dentate gyrus exhibited high binding activity. The thalamus, the hippocampal CA3 sector, the accumbens nucleus, the striatum, and the neocortex had also relatively high [^{3}H]nimodipine binding sites (Table 4). In old animals, significant reductions in [^{3}H]nimodipine binding were found in the striatum, the thalamus, the hippocampal CA3 sector, the dentate gyrus, and the frontal cortex compared with young rats (Table 4). Chronic treatment with the lower dose of rolipram significantly increased [^{3}H]nimodipine binding in the hippocampal CA1 sector, the dentate gyrus and the moleculer layer of the cerebellum, but no alterations were found in the young rats.

Discussions

The hippocampus has a high density of muscarinic cholinergic receptors and receives cholinergic innervation[14]. We found that [^{3}H]QNB binding showed no striking changes in the hippocampus between 19 weeks and 84 weeks of age in Wistar rats. After rolipram treatment, the hippocampal CA3 sector showed a significant decrease in [^{3}H]QNB binding in old rats, but not in young rats. Several studies have suggested that the impairments in learning and memory in aged rats are associated with an age-dependent decline of cholinergic function in the forebrain[15]. It is likely that decreased [^{3}H]QNB binding after chronic rolipram treatment in old rats results from improved acetylcholine neurotransmission.

[^{3}H]HC3 binding serves as a specific marker for cholinergic terminals[16]. The distribution of [^{3}H]HC3 binding sites is closely consistent with the localization of presynaptic markers of the cholinergic system[17]. In the present study, [^{3}H]HC3 binding sites were largely unchanged during senescence and only showed a slight decrease in the frontal cortex in old rats. After rolipram treatment, we observed only slight changes in the brain. These findings suggest that presynaptic acetylcholine terminals are resistant to senescence and pharmacological intervention.

We observed significant elevations in [^{3}H]PDBu binding in old rats in the hippocampal CA1, the dentate gyrus, and the cerebellar molecular layer compared with young animals. PKC is known to play a role in modulating neuronal transmission, intracellular signal transduction, and synaptic plasticity[18]. PKC may be involved in the generation of long-term potentiation in the hippocampus, which is related to learning and memory[19-21]. Although the dysfunction of a second-messenger system in the course of aging processes is not fully understood, the elevations of this second-messenger in most brain areas seen in old rats may result from decreased neurotransmission activity. Furthermore, rolipram modulated the alterations in the [^{3}H]PDBu binding.

Age-related reductions in [^{3}H]nimodipine binding sites were found in various brain regions. This observation suggests that the density of calcium channels is altered during aging. An altered calcium homeostasis is an important contributing factor in the expression of a number of neuronal functions altered during aging, such as neurotransmitter release, enzymatic functions, and transport systems[22]. Noteworthy is that the age-related reductions in [^{3}H]nimodipine binding in old rats were modulated following rolipram treatment.

Thus, the present study demonstrated age-related alterations in the binding sites of muscarinic acetylcholine, PKC, and a voltage-dependent L-type calcium channel blocker in various brain regions, whereas presynaptic cholinergic terminals were largely unchanged during aging. Rolipram modulated these age-related changes in these binding sites in old rats. These changes in neurotransmission and second-messenger systems may be caused by changes in brain cAMP levels. In contrast, we found that rolipram did not influence these binding sites in young rats. Because the acetylcholine, PKC, and calcium channel systems are believed to contribute to learning and memory processes, further studies should be performed to investigate the precise mechanisms for such effects.

References

1) Najlerahim A., Francis P. T., Bowen, D. M., Neurobiol. Aging, **11** (1990) 155.
2) Wenk G. L., et al., Neurobiol. Aging, **12** (1991) 93.
3) Freeman G. B., Gibson G. E., Neurobiol. Aging, **8** (1987) 147.
4) Mclntosh H. H., Westfall T. C., Neurobiol. Aging, **8** (1987) 233.
5) Meyer E. M., et al., J. Neurochem., **47** (1986) 1244.
6) Davis C. W., Biochim. Biophys. Acta, **797** (1984) 354.
7) Ilien B., Ruckstuhl M., Landry Y., J. Pharmacol., **13** (1982) 307.
8) Schwabe U., et al., Mol. Pharmacol., **12** (1976) 900.
9) Schneider H. H., Biochem. Pharmacol., **33** (1984) 1690.
10) Araki T., et al., J. Neurol. Sci., **106** (1991) 206-.
11) Forloni G., Angeretti N., Brain Res., **570** (1992) 354.
12) Worley P. F., Baraban J. M., Snyder S. H., J. Neurosci., **6** (1986) 199.
13) Bellemann P., Schade A., Towart R., Proc. Natl. Acad. Sci., **80** (1983) 2356.
14) Fibiger H. C., Brain Res. Rev., **4** (1982) 327.
15) Bartus R. T., et al., Science, **217** (1982) 408.
16) Happe H. K., Murrin L. C., J. Neurochem., **60** (1993) 1191.
17) Schramm M., Sekinger Z., Science, **225** (1984) 1350.
18) Araki T., et al., Res. Exp. Med., **192** (1992) 221.
19) Akers R.F., et al., Science, **231** (1986) 587.
20) Hu G.Y., et al., Nature, **328** (1987) 426.
21) Malenka R. C., Madison D. V., Nicoll R.A., Nature, **321** (1986) 175.
22) Gibson G. E., Peterson C., Neurobiol. Aging, **8** (1987) 329.

Table 1. Effect of rolipram on age-related alterations in [^{3}H]QNB binding (fmol/mg) in the rat brain.

	19 weeks old			84 weeks old		
	Vehicle	0.01mg	0.1mg	Vehicle	0.01mg	0.1mg
Frontal cortex	352±41	369±28	347±30	331±29	305±13	271±25##
Striatum	377±45	400±29	390±42	351±28	357±24	303±27#
Nucleus accumbens	444±40	455±47	447±23	411±27	402±38	386±38
Hippocampus						
CA1 sector	469±39	482±19	485±16	473±16	474±28	437±31
CA3 sector	307±35	303±14	287±37	282±28	274±20	245±13#
dentate gyrus	398±35	379±22	391±42	402±42	398±23	362±34
Thalamus	135±36	119±21	105±29	83±20*	80±22	67±19
Hypothalamus	45±13	28±19	28±13	22±23	26±11	31±11
Substantia nigra	83±40	52±21	50±15	43±11	50±15	45±17
Cerebellum	38±7	27±10	29±7	26±6**	35±7	32±6

Values are expressed as means±SD. n=5-6.
*p<0.05 , **p<0.01 vs. vehicle treated young animal (Student's t-test).
#p<0.05 , ##p<0.01 vs. vehicle treated old animal (Bonferroni's multiple comparison test).

Table 2. Effect of rolipram on age-related alterations in [^{3}H]Hemicholinium-3 binding (fmol/mg) in the rat brain.

	19 weeks old			84 weeks old		
	Vehicle	0.01mg	0.1mg	Vehicle	0.01mg	0.1mg
Frontal cortex	19±2	21±2	17±3	16±2*	16±3	17±3
Parietal cortex	19±3	21±1	18±1	17±2	17±2	18±3
Striatum	75±15	93±15	88±11	73±7	79±13	93±14#
Accumbens nucleus	74±6	86±10	70±9	62±13	61±5	70±12
Hippocampus						
CA1 sector	21±2	23±3	20±1	21±2	19±3	22±2
CA3 sector	24±2	25±4	21±2	23±2	21±3	22±2
Dentate gyrus	54±9	57±9	43±9	55±9	53±12	55±4
Thalamus	16±3	17±3	13±3	19±4	14±2#	16±1
Hypothalamus	2±0.5	3±2	1±0.5	2±1	1±1	2±1
Brain stem	11±4	9±1	8±2	7±2	7±2	7±3
Cerebellum	5±2	5±1	4±0.4	4±1	3±2	3±1

Values are expressed as means±SD. n=5-6.
*p<0.05 vs. vehicle treated young animal (Student's t-test).
#p<0.05 vs. vehicle treated old animal (Bonferroni's multiple comparison test).

Table 3. Effect of rolipram against age-related alterations in [^{3}H]PDBu binding (fmol/mg) in the rat brain.

	19 weeks old			84 weeks old		
	Vehicle	0.01mg	0.1mg	Vehicle	0.01mg	0.1mg
Frontal cortex	876±95	925±94	862±56	897±81	839±79	748±99$^{\#}$
Parietal cortex	810±57	822±86	795±88	908±98	924±54	808±89
Striatum	756±95	794±99	728±21	783±80	692±75	657±50$^{\#}$
Accumbens nucleus	890±98	994±95	893±66	943±99	836±82	701±47$^{\#\#}$
Hippocampus						
CA1 sector	998±39	1052±55	988±66	1090±92*	1084±43	1086±69
CA3 sector	906±84	988±67	945±71	973±86	936±73	820±61$^{\#\#}$
Dentate gyrus	915±43	988±21**	927±30	1006±86*	937±99	860±57$^{\#}$
Thalamus	648±59	686±75	598±66	638±71	510±84$^{\#}$	446±62$^{\#\#}$
Hypothalamus	168±29	163±34	128±23	126±21*	124±33	114±55
Brain stem	205±23	188±39	179±13	177±29	168±36	150±18
Cerebellum						
Average	684±86	687±92	681±80	686±50	604±66	602±72
Molecular layer	933±89	1008±46	997±98	1068±95*	1018±55	897±38$^{\#\#}$

Values are expressed as means±SD. n=5-6.
*p<0.05, **p<0.01 vs. vehicle treated young animal (Student's t-test).
$^{\#}$p<0.05, $^{\#\#}$p<0.01 vs. vehicle treated old animal (Bonferroni's multiple comparison test).

Table 4. Effect of rolipram against age-related alterations in [^{3}H]nimodipine binding (fmol/mg) in the rat brain.

	19 weeks old			84 weeks old		
	Vehicle	0.01mg	0.1mg	Vehicle	0.01mg	0.1mg
Frontal cortex	35±6	33±7	33±5	27±5*	29±6	26±6
Parietal cortex	32±7	22±9	36±8	29±6	35±7	30±6
Striatum	35±5	32±4	37±7	23±4**	27±7	23±3
Accumbens nucleus	40±6	36±6	44±3	28±11	36±4	32±3
Hippocampus						
CA1 sector	23±5	17±9	28±6	14±10	27±8$^{\#}$	21±5
CA3 sector	39±5	35±10	41±8	30±7*	39±8	30±9
Dentate gyrus	52±3	50±8	58±6	42±9*	54±8$^{\#}$	48±7
Thalamus	44±4	38±4	43±10	29±8**	31±9	26±7
Brain stem	6±7	6±5	6±6	7±5	6±4	2±2
Cerebellum						
Average	7±7	8±8	13±5	8±5	10±4	9±7
Molecular layer	4±4	5±7	5±5	1±1	9±5$^{\#}$	5±4

Values are expressed as means±SD. n=5-6.
*p<0.05, **p<0.01 vs. vehicle treated young animal (Student's t-test).
$^{\#}$p<0.05, vs. vehicle treated old animal (Bonferroni's multiple comparison test).

III. 6. Rolipram, a Cyclic AMP-Selective Phosphodiesterase Inhibitor, Modulates Age-Related Changes in the Excitatory Amino Acid Neurotransmission System in the Rat Brain

Kato H., Araki T., Chen T., Liu X.-H., Kogure K. and Itoyama Y.*

Department of Neurology, Tohoku University School of Medicine
Institute of Neuropathology, Kumagaya, Japan*

Introduction

Rolipram, which has been known as an antidepressant, inhibits a Ca^{2+}/calmodulin-independent cyclic adenosine monophosphate (cyclic AMP)-selective phosphodiesterase isozyme[1], leading to an increase in brain cyclic AMP levels[2]. Specific binding sites for [^{3}H]rolipram have been visualized and quantified by *in vitro* autoradiography, which showed high binding site densities in the CA1 subfield of the hippocampus[3]. Rolipram has also been shown to have a neuroprotective action against cerebral ischemia[4].

Chronic treatment with this compound is expected to modify signal transmission and transduction systems in the brain via the alteration of brain cyclic AMP levels. It is important to reveal the changes in the brain of animals treated chronically with rolipram considering its potential clinical application as an antidepressant or an agent for stroke patients. The purpose of this study, therefore, was to reveal the effects of chronic treatment with rolipram on the excitatory amino acid (EAA) neurotransmission system. For this purpose, we performed *in vitro* ligand binding autoradiography with [^{3}H]MK-801 and D-[^{3}H]aspartate to investigate the *N*-methyl-D-aspartate (NMDA) subtype of glutamate receptors and sodium dependent glutamate transport sites, respectively. By use of young and aged Wistar rats, we evaluated the age-related alterations in the EAA neurotransmission system and compared the effects of rolipram between young and aged rats.

Materials and Methods

CHRONIC ROLIPRAM TREATMENT

We used male Wistar rats (Clea Japan Inc., Tokyo, Japan) 15 weeks old (young) and 80 weeks old (aged), weighing approximately 400 g and 500 g, respectively. Rolipram (Meiji Seika Kaisha, Ltd., Yokohama, Japan) at a dose of 0.01 mg/kg or 0.1 mg/kg or its vehicle (distilled water) was administered *per os* once a day over 4 weeks. Twenty four hours after the final administration, the animals were sacrificed by decapitation, when the

young rats were 19 weeks old and the aged rats were 84 weeks old. The brains were rapidly removed and frozen in dry ice powder. Frozen sections were cut at a thickness of 20 μm on a cryostat and mounted onto a gelatin-coated slides and dried under a cold air stream. The sections were kept at -80 ℃ until assay.

[^{3}H]MK-801 BINDING

NMDA receptors were quantified using the radiolabeled non-competitive antagonist [^{3}H]MK-801 (20.3 Ci/mmol, New England Nuclear) as reported previously[5,6]. Sections were rinsed in 50 mM Tris-HCl buffer (pH 7.4) with 190 mM sucrose, air-dried, and then incubated with 30 nM [^{3}H]MK-801 in the same buffer for 20 min at room temperature. The sections were then washed twice in the buffer for 20 sec. Non-specific binding was determined using 100 μM MK-801 (Research Biochmicals Inc.).

D-[^{3}H]ASPARTATE BINDING

Sodium-dependent excitatory amino acid transport sites were quantified using D-[^{3}H]aspartate (12.8 Ci/mmol, New England Nuclear) as reported previously[7]. Sections were preincubated in 50 μM Tris-HCl buffer (pH 7.4) containing 300 mM NaCl for 10 min at 30 ℃, and then incubated with 100 nM D-[^{3}H]aspartate in the buffer for 10 min at 0-4 ℃. The sections were then washed three times in the buffer for 30 sec at 4 ℃. Non-specific binding was determined using 100 μM D,L-threo-β-hydroxyaspartate (Sigma).

AUTORADIOGRAPHY

The sections were dried under a stream of cold air and apposed to Hyperfilm-^{3}H (Anersham) for 2-4 weeks. The optical density of the regions of interest was measured using a computer-assisted image analyzer system (IBAS image analyser system, Zeiss). The relation between optical density and radioactivity was determined using a third order polynomial function with reference to tritium standards (^{3}H-microscale, Amersham) exposed along with the tissue sections. The binding were represented as mean values ±S.D. (fmol/mg tissue). Statistical comparisons were made with the analysis of variance and the Bonferroni's test, and the Student's t-test.

Results

[^{3}H]MK-801 BINDING

In normal brains, the highest [^{3}H]MK-801 binding was seen in the CA1 subfield of the hippocampus, followed by the dentate gyrus. Moderate binding was seen in the CA3 subfield of the hippocampus and the neocortex (Table 1). We observed no significant differences in [^{3}H]MK-801 binding between young and aged rats. Chronic rolipram treatment at both high and low doses led to an increase in the [^{3}H]MK-801 binding in the striatum, the dentate gyrus, the thalamus, and the cerebellum in aged rats (Table 1). In young

rats, treatment with the higher dose of rolipram increased [^{3}H]MK-801 binding in the dentate gyrus but otherwise caused no alterations.

D-[^{3}H]ASPARTATE BINDING

In normal brains, the highest D-[^{3}H]aspartate binding was seen in the CA1 subfield of the hippocampus, followed by the CA3 subfield of the hippocampus, the dentate gyrus, and the molecular layer of the cerebellum (Table 2). We observed no significant differences in D-[^{3}H]aspartate binding between young and aged rats. Chronic rolipram treatment caused remarkable reductions in the D-[^{3}H]aspartate binding in allmost all brain regions examined largrly in a dose-dependent fashion and the reductions were similarly seen in young and aged rats (Table 2).

Discussions

In the present study, we found no significant changes in [^{3}H]MK-801 and D-[^{3}H]aspartate binding between brains of young (19 weeks old) and aged (84 weeks old) animals. Earlier studies have reported age-related reductions in binding to NMDA receptors in rodent brains[8-11]. Furthermore, an age-related loss in the number of high affinity glutamate transport (uptake) sites has been reported[12-15]. However, the binding sites within the channel protein labeled by [^{3}H]MK-801 is relatively preserved during the aging process, showing different effects of aging on the NMDA receptor and its channel protein[16]. Furthermore, strain-dependent reductions in glutamate binding to the NMDA receptor are observed in aged mouse brain[17]. Therefore, the reasons why we observed no significant age-related alterations in [^{3}H]MK-801 and D-[^{3}H]aspartate binding may be that (1) [^{3}H]MK-801 binding sites are relatively resistant during senescence as compared to NMDA binding sites, and (2) brains of Wistar rats may be relatively resistant to aging processes compared with Fisher-344 rats which is frequently used.

One of the major findings of this study is that chronic treatment with rolipram, a cyclic AMP-selective phosphodiesterase inhibitor, altered EAA neurotransmission in the brain. The alterations observed after rolipram treatment were (1) increases in [^{3}H]MK-801 binding and (2) decreases in D-[^{3}H]aspartate binding. These alterations suggest up-regulation of NMDA receptors and down-regulation of EAA transport sites, respectively. These alterations also suggest that EAA neurotransmission in the brain is regulated by receptor activation and uptake of EAA. Because rolipram increases brain levels of cyclic AMP, the rolipram-induced elevations in [^{3}H]MK-801 binding and reductions in D-[^{3}H]aspartate binding may imply a compensatory up-regulation and down-regulation, respectively, following decreased extracellular EAA levels in response to the activated second messenger system by elevated levels of cyclic AMP. Thus, a close linkage between brain cyclic AMP levels and EAA neurotransmission is suggested.

With regard to the effects of chronic roliram treatment on [^{3}H]MK-801 binding, differences were observed between young and aged animals although similar changes were observed in D-[^{3}H]aspartate binding. Rolipram increased [^{3}H]MK-801 binding in many regions of the aged rats but only in the dentate gyrus of the young rats. This observation suggests greater sensitivity of aged rats to this kind of drugs. Similar effects have been reported on treatment with MK-801. Ingram et al.[18] reported that aged rats show a dose-dependent impairment in maze performance while young rats exhibit no detrimental effects.

In conclusion, chronic treatment with rolipram, a cyclic AMP-selective phosphodiesterase inhibitor, resulted in increases in [^{3}H]MK-801 binding and decreases in D-[^{3}H]aspartate binding in various brain regions. Greater sensitivity of this treatment in aged rats was also observed. These findings suggest that EAA neurotransmission in the brain can be regulated by pharmacological treatment such as rolipram. Further investigations of the compensatory responses of neurotransmission and second messenger systems to pharmacological treatment are required to define the compensatory mechanisms that are related to aging and therapeutic action of the drugs.

References

1) Schwabe U., et al., Mol. Pharmacol., **12** (1976) 900.
2) Schneider H. H., Biochem. Pharmacol., **33** (1984) 1690.
3) Kaulen P., et al., Brain Res. **503** (1989) 229.
4) Kato H., et al., Eur. J. Pharmacol., **272** (1995) 107.
5) Bowery N. G., Wong E. H. F., Hudson A. L., Br. J. Pharmacol., **93** (1988) 944.
6) Kato H., et al., Neuroscience, **52** (1993) 245.
7) Anderson, K. J., et al., Neuroscience, **38** (1990) 311.
8) Clark A. S., Magnusson K. R., Cotman C.W., Behav. Neurosci., **106** (1991) 324.
9) Pellymounter, M.A., Beatty, G., Gallagher M., Psychobiology, **18** (1990) 198.
10) Tamaru M., et al., Brain Res., **542** (1991) 83.
11) Wenk G. L., Neurobiol. Aging, **12** (1991) 93.
12) Price, M. T., Olney J. W., Haft R., Life Sci., **28** (1981) 1365.
13) Wheeler, D. D., Ondo J. G., Exp. Gerontol., **21** (1986) 159.
14) Freeman G. B., Gibson G. E., Neurobiol. Aging, **8** (1987) 147.
15) Aprikyan G. V., Gekchyan K. G., Gerontology, **34** (1988) 35.
16) Magnusson K. R., Cotman C. W., Brain Res., **604** (1993) 334.
17) Peterson C., Cotman C. W., Neurosci. Lett., **104** (1989) 309.
18) Ingram D. K., et al., Brain Res., **580** (1992) 273.

Table 1. Effects of chronic rolipram treatment on [^{3}H]MK-801 binding in various brain regions of young (19-week old) and aged (84-week old) Wistar rats.

	young (19-week old)			old (84-week old)		
	vehicle	0.01mg/kg	0.1mg/kg	vehicle	0.01mg/kg	0.1mg/kg
frontal cortex	209±36.2	194±39.8	227±13.4	217±29.9	252±46.9	247±38.7
parietal cortex	229±27.7	192±58.5	227±27.2	253±40.8	252±81.4	266±25.3
striatum	169±62.9	170±21.9	201±30.3	164±50.6	248±26.9*	233±40.6*
accumbens nucleus	205±84.7	240±39.6	274±61.9	206±35.6	305±41.9*	249±56.9
hippocampus, CA1 subfield	366±48.7	399±67.8	414±54.8	411±58.8	478±66.0	484±30.3
hippocampus, CA3 subfield	214±45.0	192±32.5	218±14.7	231±27.3	281±43.8	266±39.7
hippocampus, dentate gyrus	313±26.2	300±35.7	377±39.1*	325±65.4	387±45.5	403±16.8*
thalamus	187±43.9	148±17.0	207±37.8	175±46.5	243±47.5*	236±30.6*
cerebellum (average)	64±20.9	42±25.0	81±27.3	46±32.4	97±5.4**	116±25.5**

mean values ± SD, n=4-6, *p<0.05, **p<0.01 vs vehicle-treated animals (Bonferroni test)

Table 2. Effects of chronic rolipram treatment on D-[^{3}H]aspartate binding in various brain regions of young (19-week old) and aged (84-week old) Wistar rats.

	young (19-week old)			old (84-week old)		
	vehicle	0.01mg/kg	0.1mg/kg	vehicle	0.01mg/kg	0.1mg/kg
frontal cortex	416±79.8	224±34.5**	238±36.3**	478±58.7	268±63.7**	178±39.2**
parietal cortex	474±60.3	267±43.4**	262±48.4**	603±132.8	390±56.0*	265±67.1**
striatum	362±89.4	207±63.3**	206±40.2**	377±50.0	250±21.7**	191±38.5**
accumbens nucleus	414±111.9	272±95.1	211±54.3*	427±107.1	325±42.7	229±40.3**
hippocampus, CA1	894±113.1	600±146.4**	552±117.8**	811±83.3	620±154.2	598±109.6*
hippocampus, CA3	642±109.7	393±153.0*	373±69.7**	644±32.1	416±34.1**	399±152.3**
dentate gyrus	534±125.4	380±67.9	401±86.9	618±124.5	420±82.3*	401±113.4*
thalamus	256±57.1	147±28.9**	148±40.2**	209±48.5	119±19.6**	120±15.7**
cerebellum (average)	176±57.9	107±18.3*	133±16.6	189±30.7	100±8.8**	123±27.5**
cerebellum (molecular)	681±115.0	418±134.4*	597±134.3	571±50.2	530±124.8	301±59.2**

mean values ± SD, n=4-6, *p<0.05, **p<0.01 vs vehicle-treated animals (Bonferroni test)

III. 7. Changes of [^{3}H]hemicholinium-3 Binding in the Postischemic Gerbil Brain

Araki T., Kato H., Nagasawa H., Fujiwara T. and Itoyama Y.*

Department of Neurology, Tohoku University School of Medicine
*Division of Cyclotron Nuclear Medicine, Cyclotron and Radioisotope Center, Tohoku University**

Selective neuronal damage occurs in certain limited regions of the brain such as the hippocampal CA1 sector and dorsolateral striatum after a brief period of cerebral ischemia[1,2]. Mild damage is also found in the hippocampal CA3 sector and neocortex, if cerebral ischemia is prolonged[2-4]. The neuronal damage in these areas develops over a period ranging from hours to several days after transient cerebral ischemia. A previous study indicates that in the hippocampus, a considerable number of presynaptic terminals preserved their fine structure even when most of postsynaptic structures are destroyed after ischemia[5]. Furthermore, several studies suggest that choline acetyltransferase levels as an index of presynaptic cholinergic activity are unchanged after cerebral ischemia[6,7]. However, a recent study has shown that the presynaptic terminals of the cholinergic neurons are vulnerable to ischemic insult and that cholinergic dysfunction precedes postsynaptic CA1 pyramidal neuronal death in the hippocampus[8]. This observation suggests that the presynaptic terminals of the cholinergic neurons in vulnerable areas are also susceptible, if ischemic time is prolonged.

Hemicholinium-3 (HC3) is a very specific and potent inhibitor of the high affinity choline transport system (HAChT)[9,10]. Several studies indicate that [^{3}H]HC3 specifically binds to a site associated with the HAChT site. Furthermore, the autoradiographic distribution of [^{3}H]HC3 binding sites is closely consistent with the localization of presynaptic markers of the cholinergic system[11]. Therefore, HC3 is thought to be a valuable ligand for HAChT sites and a specific maker for presynaptic cholinergic terminals[12]. However, little is known about postischemic changes of [^{3}H]HC3 binding as a sensitive marker of presynaptic cholinergic terminals. In the present study, we examined sequential changes of [^{3}H]HC3 binding in the gerbil brain after transient cerebral ischemia using receptor autoradiography.

Materials and Methods

Ischemic insult: Male adult Mongolian gerbils weighing between 60 and 80 g were anesthetized with 2% halothane in a mixture of 30% oxygen and 70% nitrous oxide. Bilateral common carotid arteries were exposed and the carotid arteries were occluded with aneurysmal

clips for 10 min, and then the animals were allowed to survive for 1, 5, 24 and 48 h and 7 days after ischemia. Sham-operated gerbils were treated in the same manner, except for the clipping of the bilateral carotid arteries.

[^{3}H]HC3 receptor autoradiography : The gerbils were decapitated at different reperfusion times as described above, and the brains were removed quickly, frozen in powdered dry-ice and stored at -80 °C until assay. Coronal sections 12 μm in thickness were cut on a cryostat and thaw-mounted onto gelatin-coated slides. Autoradiographic localization of [^{3}H]HC3 binding in the brain was performed according to the method of Forloni and Angeretti[13] with minor modifications. The slides were incubated with 10 nM [^{3}H]HC3 (Specific activity 140.9 Ci/mmol, NEN) for 30 min at room temperature in 50 mM glycylglycine buffer, pH 7.8, containing 200 mM NaCl. Then the slides were washed two times in ice-cold fresh buffer for 2 min. Non-specific binding was determined in adjacent sections processed in the same manner except for that 10 μM unlabeled HC3 (Aldrich Chem. Co.) was added to the incubation medium. The sections were dried under a cold air stream and were exposed to Hyperfilm-[^{3}H] (Amersham) for 4 weeks in X-ray cassettes with a set of [^{3}H]microscales (Amersham). Quantitative autoradiographic analysis was measured by a computer-assisted image analyzer without the examiner knowing the experimental protocol, as described previously[14,15]. Binding assays were performed in duplicate. Values were expressed as the means ±SD. Statistical comparisons were made using ANOVA followed by Dunnett's multiple range test. Each group contained 5 to 8 gerbils.

Histopathology : Adjacent sections prepared for receptor autoradiography were also stained with Cresyl violet and Haematoxylin-eosin. Stained sections were examined with a light microscope, and ischemic neuronal damage was graded on a semiquantitative scale; 0: normal, 1: a few neurons damaged, 2: many neurons damaged and 3, majority of neurons damaged according to the method of Pulsinelli et al.[2]. The average of left and right values was expressed as the means ±SD. Statistical comparisons were made using the Mann-Whitney U-test. Each group contained 5 to 8 gerbils.

Results

[^{3}H]HC3 binding

Representative [^{3}H]HC3 autoradiograms in the gerbil brain 7 days after 10 min of ischemia are shown in Figure 1. Postischemic changes of [^{3}H]HC3 binding are summarized in Table 1. In sham-operated gerbils, high density of [^{3}H]HC3 binding was found in the striatum. In the hippocampus, the gray density of [^{3}H]HC3 binding was intermediate. This autoradiographic distribution of [^{3}H]HC3 binding is consistent with a previous report[13]. In animals subjected to ischemia, [^{3}H]HC3 binding was unchanged in the brain throughout the recirculation periods.

Histopathology

Representative photographs of Cresyl violet staining in the brain 7 days after 10 min of ischemia are shown in Figure 1. Distributions of ischemic brain damage are summarized in Table 2. Sham-operated gerbils showed no conspicuous neuronal alteration in the brain. Gerbils subjected to ischemia revealed no neuronal damage in the hippocampus and neocortex upto 48 h after ischemia. By contrast, the striatum showed conspicuous neuronal damage from 24 h after ischemia. Seven days after ischemia, severe neuronal damage was noted in selectively vulnerable areas. The most affected areas were the hippocampal CA1 sector and striatum. Mild damage was also found in the frontal cortex and hippocampal CA3 sector. However, the dentate gyrus showed no neuronal damage. The results are consistent with a previous report[16].

Discussion

Cerebral ischemia causes degeneration of specific neuronal populations that lie in the hippocampus, striatum and neocortex. Especially, most of the neurons in the hippocampal CA1 sector are destroyed after brief cerebral ischemia. On the other hand, numerous presynaptic terminals in the hippocampal CA1 region maintain their structural characteristics although the postsynaptic structures are almost absent following cerebral ischemia[5]. This postischemic preservation of presynaptic terminals in the hippocampal CA1 sector has been previously confirmed by several authors[5,17]. Johansen et al.[18] previously demonstrated the survival of presynaptic sites for 4 days after 20-min cerebral ischemia in rats. Kitagawa et al.[19] recently reported that preservation of immunohistochemical staining for synapsin I which serves as a marker protein for presynaptic sites upto 7 days following 30-min unilateral ischemia in gerbils. These observations seem to indicate that presynaptic terminals in the hippocampal CA1 sector are resistant to cerebral ischemia. Interestingly, a recent study indicates that the presynaptic terminals of the cholinergic neurons are vulnerable to severe ischemia and that cholinergic dysfunction precedes postsynaptic CA1 pyramidal neuronal cell loss in the hippocampus[8]. This finding is not in accord with previous reports[5,17,18,19]. Therefore, it is still obscure whether the presynaptic terminals of the cholinergic neurons are damaged in selectively vulnerable areas after ischemia.

It is well known that [^{3}H]HC3 binding sites serve as a specific marker for cholinergic terminals[20]. Furthermore, [^{3}H]HC3 has recently come into wide use a specific ligand in autoradiographic study to visualize the cholinergic terminals. In the present study, [^{3}H]HC3 binding showed no significant alterations in selectively vulnerable regions upto 7 days of recirculation. On the other hand, histological study revealed that ischemic neuronal damage was evident in the hippocampal CA1 and CA3 sector, striatum and frontal cortex 7 days after recirculation. These findings suggest that the presynaptic terminals can survive and maintain their structure not only in the hippocampal CA1 sector but also in the vulnerable regions such as striatum and cortex upto at least 7 days following ischemia, even when the postsynaptic

structures were destroyed and removed. Thus, our findings are not in accordance with the findings of Ishimaru et al.[8] indicating that cholinergic terminals in the hippocampal CA1 sector are vulnerable to cerebral ischemia. Although the reason for this discrepancy is presently unclear, the present data may indicate that cerebral ischemia can produce the cholinergic dysfunction in the hippocampus even when presynaptic terminals in this region are well preserved. However, the finding of Isimaru et al.[8] was not derived from focused observation of cholinergic function in the hippocampal CA1 sector after cerebral ischemia . Therefore, it is unclear whether cholinergic dysfunction plays a key role in the pathogenesis of ischemic neuronal death in the hippocampal CA1 sector. Further studies are needed to clarify the precise correlation between cholinergic dysfunction and hippocampal CA1 neuronal cell loss after cerebral ischemia.

The present study also showed that ischemic neuronal damage was found in the hippocampal CA3 pyramidal neurons which connect with mossy fiber terminals from the dentate gyrus and send off Schaffer collaterals to the CA1 pyramidal cells. Therefore, it is suggested that the presynaptic sites in the hippocampal CA1 sector may be damaged by cerebral ischemia. In the present study, however, the change in [^{3}H] HC3 binding was not observed in the hippocampal CA1 sector. For this reason, we speculate that most of the cholinergic terminals remaining after cerebral ischemia may restore [^{3}H]HC3 binding in the hippocampal CA1 sector to sham-operated level, since the neuronal damage to the hippocampal CA3 pyramidal neurons was mild as shown in Table 2. However, we cannot exclude the possibility that reactive astrocytes existing in the hippocampal CA1 sector may contribute to the maintenance of axonal terminals by supplying neurotropic factors required for the survival of the detached terminals and their original neurons[21]. Furthermore, it is still unclear whether detectable changes in [^{3}H]HC3 to the HAChT sites will occur under the experimental conditions, even when comparatively minor defects in the structural integrity of the presynaptic sites are evident. Though the precise mechanisms for our findings remain to be elucidated in further studies, the present study supports the hypothesis that presynaptic sites are resistant to cerebral ischemia, but postsynaptic sites are particularly vulnerable.

Conclusion

Our data demonstrate that transient cerebral ischemia causes no conspicuous alterations in [^{3}H]hemicholinium-3 binding as a marker of presynaptic cholinergic terminals in selectively vulnerable areas. The results suggest that presynaptic sites in selectively vulnerable areas can maintain their structural components, although most of the postsynaptic neurons are degenerated.

References

1) Kirino T., Brain Res. **239** (1982) 57.
2) Pulsinelli W. A. Brierley J. B. and Plum F., Ann. Neurol. **11** (1982) 491.
3) Jorgensen M. B. and Diemer N. H., Acta Neurol. Scand. **66** (1982) 536.
4) Smith M. L., Auer R. N. and Siesjo B. K., Acta. Neuropathol. **64** (1984) 319.
5) Kirino T., Tamura A. and Sano K., Brain Res. **510** (1990) 17.
6) Francis A .and Pulsinelli W., Brain Res.**243** (1982) 271.
7) Haba K., Ogawa N., Mizukawa K. et al., Brain Res. **540** (1991) 116.
8) Ishimaru H., Takahashi A., Ikarashi Y. et al., Neuro Report **5** (1994) 601.
9) Guyenet P., Lefresne P., Rossier J. et al., Mol. Pharmacol: **9** (1973) 630.
10) Simon J. R., Mittag T. W., Kuhar M. J. et al., Biochem. Pharmacol. **24** (1975) 1139.
11) Vickroy T. W., Roeske W. R., Gehlert D. R. et al., Brain Res. **329** (1985) 368.
12) Happe H. K. and Murrin L. C., J. Comp. Neurol. **321** (1992) 591.
13) Forloni G. and Angeretti N., Brain Res. **570** (1992) 354.
14) Araki T., Kato H., Kogure K. et al., Br. J. Pharmacol. **107** (1992) 437.
15) Araki T., Kato H., Kanai Y. et al., Neuroscience **53** (1993) 829.
16) Araki T., Kato H., Hara H. et al., Neuroscience **46** (1992) 973.
17) Bonnekoh P., Barbier A., Oschlies U. et al., Acta Neuropathol. **80** (1990) 18.
18) Johansen F. F., Jorgensen M. B., von Lubitz D. K. J. E. et al., Brain Res. **391** (1984) 373.
19) Kitagawa K., Matsumoto M., Sobue K. et al., Neuroscience **46** (1992) 287.
20) Happe H. K. and Murrin L. C., J. Neurochem. **60** (1993) 1191.
21) Kromer L. F., Science **235** (1986) 214.

Table 1. Changes in [^{3}H]hemicholinium-3 binding in the gerbil brain after transient cerebral ischemia.

	Sham-operated	Recirculation time 1 h	5 h	24 h	48 h	7 days
Frontal cortex	14±1	13±2	5±1	15±2	14±2	12±2
Striatum	139±8	142±17	148±9	145±12	143±26	131±6
Hippocampus						
CA1 sector						
Stratum oriens	13±2	14±2	14±2	16±3	13±1	11±1
Stratum radiatum	12±1	14±3	14±2	15±4	12±1	10±2
Stratum lacunosum-moleculare	13±1	14±2	14±2	16±4	12±1	11±2
CA3 sector	18±2	20±3	20±2	22±5	21±3	17±1
Dentate gyrus	21±2	22±3	23±4	26±6	22±1	23±1

Optical density was converted to fmol/mg tissue using [^{3}H]microscales. Values are expressed as means ±SD. $^*p<0.05$, $^{**}p<0.01$ vs sham-operated group (Dunnett's multiple range test). n = 5-8 animals.

Table 2. Distributions of neuronal damage in the gerbil brain 7 days after cerebral ischemia.

	Neuronal damage	
	Sham-operated	Ischemia
Frontal cortex	0.0±0.0	1.6±0.1*
Striatum	0.0±0.0	2.6±0.2*
Hippocampus		
CA1 sector	0.0±0.0	3.0±0.0*
CA3 sector	0.0±0.0	1.7±0.1*
Dentate gyrus	0.0±0.0	0.0±0.0

Neuronal damage was garaded from 0 to 3. Values are expressed as means±SD. *p<0.01 vs sham-operated group (Mann-Whitney U-test). n = 6 animals.

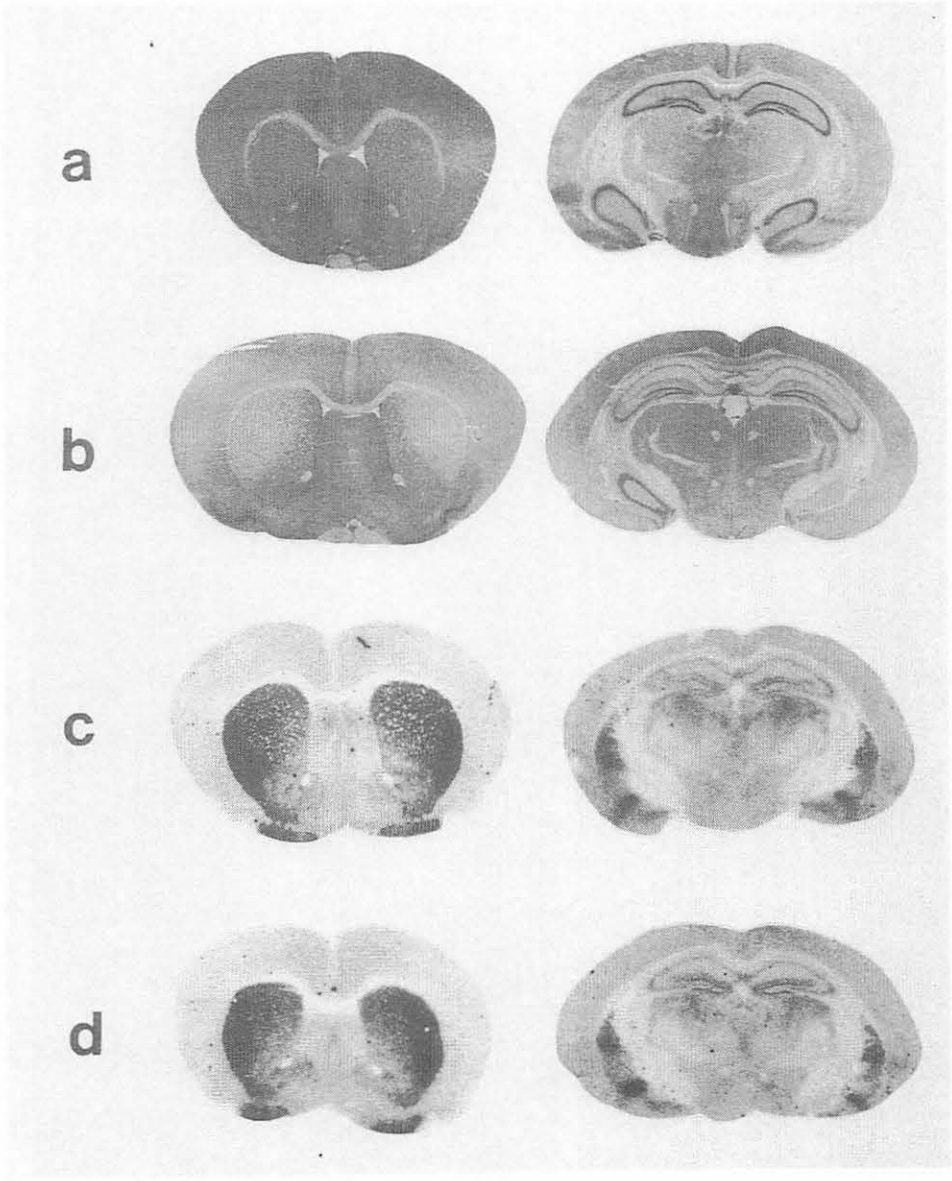

Fig. 1. Representative photographs with Cresyl violet staining (a,b) and autoradiograms of [^{3}H]hemicholinium-3 binding (c,d) in the postischemic gerbil brain. Left half: striatum. Right half: hippocampus. a,c: sham-operated group; b,d: 7 days after ischemia. Marked damage was noted in the striatum and hippocampal CA1 sector. A mild damage was also seen in the frontal cortex and hippocampal CA3 sector (a,b). However, [^{3}H]hemicholinium-3 binding was unchanged in these areas after ischemia (c,d).

III. 8. Alterations of Dopaminergic Receptors in the Gerbil Striatum after Transient Cerebral Ischemia

Araki T., Kato H., Fujiwara T. and Itoyama Y.*

Department of Neurology, Tohoku University School of Medicine
*Division of Cyclotron Nuclear Medicine, Cyclotron and Radioisotope Center, Tohoku University**

Selective vulnerability of certain neurons to cerebral ischemia is well established morphologically. Neurons known to be susceptible to ischemia include CA1 pyramidal cells of the hippocampus, the small- to medium- sized cells of the dorsolateral striatum and certain cells of neocortex[1-3]. There is considerable evidence that supports the role of excitatory amino acid toxicity in hippocampal CA1 neuronal cell death[4-6]. However, whether a similar mechanism is implicated in the pathogenesis of post-ischemic striatal neuronal damage is as yet unknown.

It is well known that N-methyl-D-aspartate (NMDA) receptor/channel activates the release of dopamine from striatum[7-9]. The NMDA receptors are normally activated by endogenous glutamate and its coagonist glycine, acting at its own receptor within the NMDA receptor/channel complex[10]. Several lines of evidence suggest that a massive release of dopamine occurs in the striatum as a result of cerebral ischemia[11,12]. A previous study also indicates that striatal dopamine depletion can protect striatal neurons from ischemic damage despite excessive release of an excitatory amino acid such as glutamate during and after transient ischemia[13]. From these observations, the changes in dopamine neurotransmission seem to play a key role in the development of ischemic striatal damage. Therefore, to elucidate further the mechanisms of regional ischemic vulnerability, we investigated whether the dopamine release from the striatum is associated with changes in dopaminergic receptors. For this purpose, we examined changes in dopamine D_1 and D_2 receptors and uptake sites in the striatum and neocortex after transient cerebral ischemia in gerbils.

Materials and Methods

Ischemic insult: Male adult Mongolian gerbils weighing 60 to 80 g were anesthetized with 2% halothane in a mixture of 30% oxygen and 70% nitrous oxide. Bilateral common carotid arteries were gently exposed and the arteries were occluded with aneurysm clips for 10 min, and then the gerbils were allowed to survive for 1, 5, 24 and 48 h and 7 days after transient ischemia. Sham-operated animals were treated in the same manner, except for the

clipping of the bilateral carotid arteries. Body temperature was maintained at 37-38 °C using a heating pad with a thermostat throughout the experiments.

Tissue preparation: The gerbils were decapitated at different reperfusion times as described above, and the brains were removed quickly, frozen in powdered dry-ice and stored at -80 °C until assay. Coronal sections 12 μm in thickness were cut on a cryostat and thaw-mounted onto gelatin-coated slides. Adjacent sections were stained with Cresyl violet and used for histopathology.

[^{3}H]SCH23390 binding: Autoradiographic distribution of dopamine D_1 receptors was measured using [^{3}H]SCH23390 ([N-methyl-^{3}H]R[+]-8-chloro-2,3,4,5-tetrahydro-3-methyl-5-phenyl-7-ol-benzazepine) by the method of Dawson et al.[14,15] with minor modifications[16,17]. Sections were incubated with 1 nM [^{3}H]SCH23390 (New England Nuclear; 71.1 Ci/mmol) in 50 mM Tris-HCl buffer (pH 7.4) containing 120 mM NaCl. 5 mM KCl, 2 mM $CaCl_2$ and 1 mM $MgCl_2$ for 30 min at room temperature. The sections were then dipped in the buffer at 4 °C, followed by 25-min rinses in fresh buffer at 4 °C. Non-specific binding was determined using 1 μM non-labeled SCH23390 (Research Biochemicals Inc.).

[^{3}H]Nemonapride (YM-09151-2) binding assay: Autoradiographic localization of dopamine D_2 receptors was performed according to the method of Unis et al.[18] with slight modifications. Briefly, the sections were incubated with 0.4 nM [^{3}H]YM-09151-2 (New England Nuclear; 86.1 Ci/mmol) for 60 min at room temperature in 50 mM Tris-HCl buffer (pH 7.4) containing 120 mM NaCl, 5 mM KCl, 5 mM $MgCl_2$, 1 mM EDTA, 10 μM paraglycine hydrochloride and 0.1% ascorbic acid. After incubation, the sections were rinsed in fresh buffer for 2 min at 4 °C and dipped in distilled water at 4 °C. Non-specific binding was determined using 1 μM haloperidol (Sigma).

[^{3}H]Mazindol binding assay: Autoradiographic distribution of dopamine uptake sites was performed according to the method of Przedborski et al.[19] with minor modifications. Briefly, the sections were pre-incubated for 15 min at 4 °C in 50 mM Tris-HCl buffer (pH 7.9) containing 120 mM NaCl and 5 mM KCl. The sections were then incubated with 15 nM [^{3}H]mazindol (New England Nuclear; 24.0 Ci/mmol) for 60 min at 4 °C in 50 mM Tris-HCl buffer (pH 7.9) containing 300 nM NaCl, 5 mM KCl and 0.3 μM desmethylimipramine (DMI, Sigma). DMI was used to block the binding of [^{3}H]mazindol to norepinephrine uptake sites. After incubation, the sections were washed 2 times in fresh ice-cold buffer for 3 min, dipped in ice-cold distilled water. Non-specific binding was determined using 30 μM Benztropine (Sigma).

The sections were quickly dried under a cold air stream and were exposed to Hyperfilm-^{3}H (Amersham) for two to four weeks in X-ray cassettes with a set of ^{3}H microscales (Amersham). The optical density of the brain regions was measured with a computer-associated image analyzer, as described previously[16]. Binding assays were performed in duplicate. Values were expressed as the means ±S. D. Statistical comparisons

were made using an analysis of variance (ANOVA) followed by Dunnett's multiple comparison test. Each group containing five to eight animals.

Histopathology: Adjacent sections prepared for receptor autoradiography were also stained with cresyl violet and hematoxylin-eosin. Stained sections were examined with a light microscope, and ischemic neuronal damage was graded on a semiquantitative scale: 0, normal; 1: a few neurons damaged; 2, many neurons damaged; 3, majority of neurons damaged, as descried previously[17]. The average of left and right values was expressed as the means ±S. D. Statistical comparisons were made using the Mann-Whitney U-test. Each group contained five to eight animals.

Results

RECEPTOR AUTORADIORAPHY

Representative autoradiographs of dopamine D_1 and D_2 receptors and uptake sites are shown in Figure 1. Post-ischemic changes in dopamine D_1 and D_2 receptors and uptake sites are summarized in Table 1

Dopamine D_1 receptor: In sham-operated gerbils, [^{3}H]SCH23390 binding was greatest in the striatum. The frontal cortex had a very low density of the binding. Gerbils subjected to ischemia showed no significant alteration in [^{3}H]SCH23390 binding in the striatum and frontal cortex up to 24 h after recirculation. Forty-eight hours after ischemia, a significant reduction in [^{3}H]SCH23390 binding was seen in the dorsolateral striatum. Thereafter, a marked reduction in [^{3}H]SCH23390 binding was found in the striatum 7 days after ischemia. In contrast, the frontal cortex exhibited no significant alteration in [^{3}H]SCH23390 binding throughout the recirculation periods.

Dopamine D_2 receptor: In sham-operated gerbils, high density of [^{3}H]nemonapride binding was found in the striatum. In the frontal cortex, the gray density of [^{3}H]nemonapride binding was very low. In animals subjected to ischemia, [^{3}H]nemonapride binding was unchanged in the striatum and frontal cortex throughout the recirculation periods except for a transient elevation in the dorsolateral striatum after 48h.

Dopamine uptake site: In sham-operated gerbils, [^{3}H]mazindol binding was predominantly located in the striatum. The frontal cortex had a very low density of the binding. In animals subjected to ischemia, [^{3}H] mazindol binding was statistically unchanged in the striatum and frontal cortex throughout the recirculation periods.

Histopathology: Representative photographs of cresyl violet staining in the striatum and neocortex 7 days after ischemia are shown in Figure 1. Distributions of ischemic neuronal damage are summarized in Table 2. Sham-operated gerbils showed no neuronal damage in the striatum and frontal cortex. Gerbils subjected to ischemia also revealed no conspicuous neuronal damage in the frontal cortex up to 48 h after ischemia. In contrast, the striatum showed conspicuous neuronal damage from 24 h after ischemia. Seven days after ischemia, severe damage was noted in the striatum. The damage to the frontal cortex was mild.

Discussion

Dopamine is a well-documented neurotransmitter in the central nervous system (CNS). The distinction between dopamine receptor subtypes in the CNS has been based on anatomical, biochemical and pharmacological characteristics[15,20,21,22]. The dopamine receptors are predominantly located in the striatum and substantia nigra and are found at least in two main types, D_1 and D_2, coupled via different G-proteins to different second messenger[23]. The dopamine has been implicated as a possible cause for neuronal damage in experimental animals. A previous study suggests that the reduction in dopamine D_1 receptors was found in the dorsolateral striatum 7 days after transient cerebral ischemia in rats, whereas the dopamine D_2 receptors were not affected in this area[24]. Recent studies also indicate that dopamine and L-DOPA caused neuronal death in tissue culture[25] and intrastriatal injection of dopamine caused dose-dependent loss of neurons[26]. The involvement of the dopamine system in neuronal damage is also supported by the fact that depletion of dopamine either by inhibition of synthesis or release prevented striatal neuronal necrosis[13,27]. These observations seem to indicate that the changes in dopamine neurotransmission play any roles in the pathogenesis of striatal neuronal damage.

In the present study, transient cerebral ischemia in gerbils caused severe decrease in [^{3}H]SCH23390-labeled dopamine D_1 receptors in the striatum where severe neuronal damage was noted. However, the reduction in [^{3}H]SCH23390-labeled dopamine D_1 receptors was not seen in the striatum at early stage prior to histological neuronal damage. On the other hand, the frontal cortex, where ischemic neuronal damage was mild, showed no significant change in [^{3}H]SCH23390-labeled dopamine D_1 receptors throughout the recirculation periods. In contrast, [^{3}H]nemonapride-labeled dopamine D_2 receptors were unchanged in the striatum and frontal cortex throughout the recirculation periods, except for a transient elevation in the receptors 48 h after ischemia. This finding with [^{3}H]nemonapride-labeled dopamine D_2 receptors was similar to that with [^{3}H]spiperone-labeled dopamine D_2 receptors, as shown in Figure 1. A previous study indicates that lesions of the substantia nigra with either 6-hydroxydopamine (6-OHDA) or ibotenic acid can produce a marked reduction in [^{3}H]sulpiride-labeled dopamine D_2 receptors, but no change in [^{3}H]SCH23390-labeled dopamine D_1 receptors in the substantia nigra[28]. Therefore, the reduction in [^{3}H]SCH23390-labeled dopamine D_1 receptors found in our study is associated with the neuronal loss of striatal cells that possess dopamine D_1 receptors, as shown in Figure 1. In contrast, [^{3}H]nemonapride-labeled dopamine D_2 receptors were unaffected in the striatum after ischemia. This finding suggests that [^{3}H]nemonapride-labeled dopamine D_2 receptors are highly located on the presynaptic sites of striatal neurons which are resistant to ischemia. On the other hand, both dopamine D_1 and D_2 receptors showed no significant changes in the frontal cortex after ischemia. For this reason, it is conceivable that we did not observe any significant changes in both dopamine D_1 and D_2 receptors in the frontal cortex because the dopaminergic presynaptic structures were preserved after ischemia or the density of these

receptors was particularly low in this region. Therefore, our data suggest that changes of both dopamine D_1 and D_2 receptors cannot fully explain the mechanism of neuronal damage in the striatum after transient cerebral ischemia.

[^{3}H]Mazindol is a highly specific and selective ligand for dopamine uptake sites when the binding is performed in the presence of DMI to block the binding to norepinephrine uptake sites[19,29]. Several lesion studies demonstrate that [^{3}H]mazindol binding is located on the presynaptic terminals of dopaminergic axons originating substantia nigra in rats[29,30]. The present study also showed that [^{3}H]mazindol binding in gerbils was greatest in the striatum which is innervated by a dopaminergic projections from substantia nigra. Following ischemia, no significant change in [^{3}H]mazindol binding was found in the striatum and frontal cortex throughout the recirculation periods. The results support the evidence that [^{3}H]mazindol-labeled dopamine uptake sites are predominantly located on the presynaptic terminals of striatal neurons.

Recently, attention has been focused on the abnormal metabolism of dopamine in the pathogenesis of several neuronal disorders such as Parkinson's disease, schizophrenia and stroke. This has been attributed to the toxic oxygen species, semiquinones and quinones, which result from autoxidation and metabolism of dopamine[31-33]. Especially, the enzymatic deamination of dopamine by monoamine oxidase (MAO) leads to the production of free radicals[34]. The formation of free radicals during hypoxic and ischemic states is widely accepted[35,36]. These free radicals are known to have the capacity to initiate destructive reactions on membrane lipids as well as on other cellular structures. A previous study suggests the activation of dopamine metabolism through MAO during and after cerebral ischemia[37]. Furthermore, numerous studies demonstrated that lipid peroxidation inhibitors and MAO inhibitors can prevent neuronal damage after cerebral ischemia[38-40]. The study using the microdialysis technique also demonstrated that dopamine extracellular concentration in the striatum increased to a very large degree, but this elevation was not dependent on ischemic duration[41]. Based on these observations and our present results, we speculate that oxidative stress including free radicals may play a key role in causing ischemic striatal damage. However, recent studies indicate the possibility of reciprocal interactions between dopamine and glutamate in the striatum which is richly populated with both glutametargic and dopaminergic terminals[9,42,43]. Therefore, further studies are needed to investigate the precise mechanisms for ischemic striatal damage.

Conclusion

The results obtained here revealed a significant reduction of striatal dopamine D_1 receptors after transient cerebral ischemia. However, the reduction in the dopamine D_1 receptors was not found in the striatum at an early stage prior to histological neuronal damage. In contrast, dopamine D_2 receptors and uptake sites were mostly unaffected in the striatum, suggesting that the dopaminergic presynaptic structures are preserved after cerebral

ischemia. Furthermore, the frontal cortex showed no significant changes in the dopamine D_1 and D_2 receptors and uptake sites throughout the recirculation periods. These results suggest that dopamine neurotransmission is not always responsible for evolution of ischemic striatal damage, but that some other factors of the products of dopamine metabolism including free radicals and glutamatergic neurotransmission may play an important role in the pathogenesis of ischemic striatal damage. Thus our observations may have important implications for the understanding and therapeutic intervention of striatal and neocortex damage after cerebral ischemia.

References

1) Kirino T., Brain Res. **239** (1982) 57.
2) Pulsinelli W. A., Brierley J. B. and Plum F., Ann. Neurol.**11** (1982) 491.
3) Smith M. L., Auer R. N. and Siesjo B. K., Acta Neuropathol. **64** (1984) 319.
4 Wieloch T., Lindvall O., Blomqvist P. et al., Neurol. Res.**7** (1985) 24.
5) Rothman S. M. and Olney J. W., Trends. Neurosci. **10** (1987) 299.
6) Benveniste H., Jorgensen N. B., Sandberg M. et al., J. Cereb. Blood Flow Metab. **9** (1989) 629.
7) Robarts P. J. and Anderson S. D., J. Neurochem. **32** (1979)1539.
8) Snell L. D. and Johnson K. M., J. Pharmacol. Exp. Ther. **238** (1979) 938.Exp. Ther. **255** (1990) 40.
10) Kleckner N. W. and Dingledine R., Science **241** (1988) 835.
11) Globus M. Y.-T., Busto R., Ditrich W.D. et al., J. Neurochem. **51** (1988)1455.
12) Slivka A., Brannan T. S., Weinberger J. et al., J. Neurochem. **50** (1988) 1714.
13) Globus M. Y.-T., Ginsberg M. D., Dietrich W. D. et al., Neurosci. Lett. **80** (1987) 251.
14) Dawson T. M., Gehlert D. R.,Yamamura H. I. et al., Eur. J. Pharmacol. **108** (1985) 323.
15) Dawson T. M., Gehlert D. R., McCabe R. T. et al., J. Neurosci. **6** (1986) 2352.
16) Araki T., Kato H., Kogure K. et al., Br. J. Pharmacol. **107** (1992) 437.
17) Araki T., Kato H., Hara H. et al., Neuroscience **46** (1992) 973.
18) Unis A. S.,Vincent J. G. and Dillon B., Life Sci. **47** (1990) PL-151.
19) Przedborski S., Kostic V., Jackson-Lewis V. et al., J. Neurochem. **57** (1991) 1951.
20) Stoof J. C. and Kebabian J. W., Life Sci. **35** (1984) 2282.
21) Filloux F. M., Wamsley J. K. and Dawson T. D., Eur. J. Pharmacol. **138** (1988) 61.
22) Civelli O., Bunzow J. R., Grandy D. K. et al., Eur. J. Pharmacol. **207** (1991) 277.
23) Wachtel S. R., Hu X.-T. , Galloway M. P. et al., Synapse **4** (1989) 327.
24) Benfenati F., Merlo Pich E., Grimaldi R. et al., Brain Res. **498** (1989)376.
25) Tanaka M., Sotomatsu A., Kanai H. et al., J. Neurol. Sci. **101** (1991) 198.
26) Filloux F. and Townsend J. J., Exp. Neurol. **119** (1993) 79.
27) Phebus L. A. and Clements J. A., Life Sci. **44** (1989) 1335.
28) Filloux F., Dawson T. M. and Wamsley J. K. et al., Brain Res. Bull. **20** (1988) 447.
29) Javick J. A., Strittratter S. M. and Snyder S. H., J. Neurosci. **5** (1985) 1513.
30) O'Dell S. J. and Marshall J. F., Brain Res. **460** (1988) 402.
31) Graham D. G., Mol. Pharmacol. **14** (1978) 633.
32) Graham D. G., Neurotoxicology **5** (1984) 83.
33) Halliwell, B., J. Neurochem. 59 (1992) 1609.
34) Spina M. B. and Cohen G., Proc. Natl. Acad. Sci. USA **86** (1989) 1398.
35) Demoppoulos H. D., Flamm E. S., Pietronigro D. D. et al., Acta Neurol. Scand. **492** (1980) 91.
36) Siesjo B. K., J. Cereb. Blood Flow Metab. **1** (1981) 155.
37) Damsma G., Boisvert D. P., Mudrick L. A. et al., J. Neurochem.**54** (1990) 801.
38) Yamamoto M., Shima T., Uozumi T. et al., Stroke **14** (1983) 977.
39) Hall E. D., Braughler J. M., Yonkers P. A. et al., J. Pharmacol. Exp. Ther. **258** (1991) 688.
40) Matsui Y. and Kumagae Y., Neurosci. Lett. **126** (1991) 175.
41) Baker A. J., Zornow M. H., Scheller M. H. et al., J. Neurochem. **57** (1991) 1370.
42) Wahl F., Plotkine M., Boulu R. et al., NeuroReport **5** (1993) 151.
43) Werling L. L., Jacocks H. M. III., Rosenthal R. E. et al., Brain Res. **606** (1993) 99.

Table 1. Alteration in [^{3}H]SCH23390, [^{3}H]nemonapride and [^{3}H]mazindol bindings in the gerbil brain after transient cerebral ischemia

	Sham-operated	Recirculation time				
		1 h	5 h	24 h	48 h	7 days
[^{3}H]SCH23390 binding						
Frontal cortex	13±2	14±1	13±3	14±2	13±3	12±3
Striatum						
Lateral	299±21	274±9	258±24	244±79	224±49[a]	64±11[b]
Medial	303±31	289±18	283±20	273±40	280±14	173±75[b]
[^{3}H]Nemonapride binding						
Frontal cortex	14±3	16±2	13±2	13±1	13±2	11±3
Striatua						
Lateral	103±4	99±12	99±6	108±9	119±14[a]	112±10
Medial	91±2	87±15	84±6	87±11	88±7	77±18
[^{3}H]Mazindol binding						
Frontal cortex	24±4	26±7	25±9	20±6	22±7	22±5
Striatum						
Lateral	88±9	93±6	92±7	103±18	106±17	76±16
Medial	104±9	95±13	91±10	100±20	111±17	119±18

Optical density was converted to fmol/mg tissue using [^{3}H]microscales. Values are expressed as means±S.D. [a]$p<0.05$, [b]$p<0.01$ vs. sham-operated group (Dunnett's multiple range test). Striatum (Lateral): the dorsolateral part of striatum, Striatum (Medial): the ventromedial part of striatum. n= 5-8 animals.

Table 2. Distributions of neuronal damage in the gerbil brain 7 days after cerebral ischemia.

	Neuronal damage	
	Sham-operated (6)	Ischemia (6)
Frontal cortex	0.0±0.0	1.6±0.1[a]
Striatum	0.0±0.0	2.6±0.2[a]

Neuronal damage was garaded from 0 to 3. Values are expressed as means±SD. *$p<0.01$ vs sham-operated group (Mann-Whitney U-test). Figures in parentheses indicate the number of gerbils.

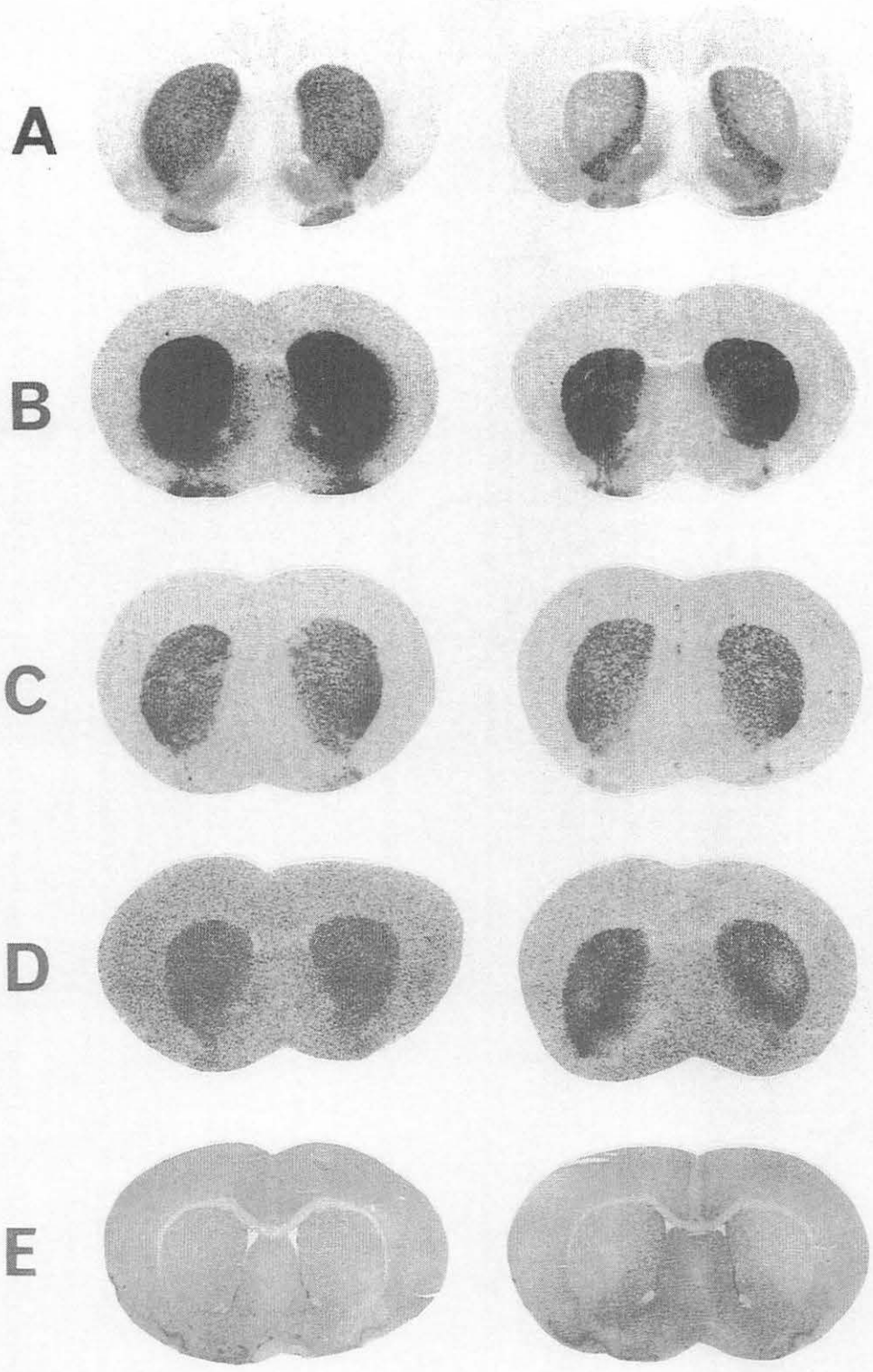

Fig. 1. Representative autoradiograms of [^{3}H]SCH23390 (A), [^{3}H]nemonapride (B), [^{3}H]spiperone (C) and [^{3}H]mazindol (D) bindings and photographs with Cresyl violet (E) in the gerbil striatum and frontal cortex following transient cerebral ischemia. Right half: sham-operated, Left half: 7 days after ischemia. In sham-operated gerbils, [^{3}H]SCH23390, [^{3}H]nemonapride, [^{3}H]spiperone and [^{3}H]mazindol bindings were greatest in the striatum, whereas the frontal cortex showed particularly low densities of these bindings. Seven days after ischemia, a marked reduction in [^{3}H]SCH23390 binding was noted in the striatum, whereas [^{3}H]nemonapride, [^{3}H]spiperone and [^{3}H]mazindol bindings were unaffected in this region. No significant changes in these bindings were found in the frontal cortex (A-D). Sham-operated gerbils showed no neuronal damage in the striatum and frontal cortex. Seven days after ischemia, marked damage was noted in the striatum and mild damage was seen in the frontal cortex (E).

III. 9. Alterations in Brain Distribution of [^{11}C]Methamphetamine in Methamphetamine Sensitized Dog

Mizugaki M., Nakamura H., Hishinuma T., Tomioka Y., Ishiwata S., Suzuki H., Ido T., Iwata R.*, Funaki Y.*, Itoh M.*, Fujiwara T.*, Yanai K.*, Sato M.**, Numachi Y.** and Yoshida S.***

Department of Pharmaceutical Sciences, Tohoku University Hospital.
Cyclotron and Radioisotope Center,Tohoku University.*
*Department of Psychiatry, Tohoku University School of Medicine**.*

Introduction

The repeated administration of methamphetamine (MAP) to experimental animals produces progressive and enduring augmentation of hyper locomotion and stereotyped behavior[1,2]. This phenomenon is termed behavioral sensitization or reverse tolerance. Since these sensitized animals have been considered a model of MAP psychosis similar to paranoid schizophrenia[3], knowledge of the neuronal mechanisms underlying sensitization may provide information on the neurochemical basis of MAP psychosis. We previously reported the significant increase in [^{11}C]MAP radioactivities in the striatum and hypothalamus of MAP sensitized mice[4] and [^{14}C]MAP radioactivities in the striatum and the limbic forebrain area of the MAP sensitized rats[5]. Furthermore, *in vivo* measurement of these alterations in brain kinetics of MAP using positron emission tomography (PET) is of interest for elucidating biochemical mechanisms of behavioral sensitization.

In this report, we newly produced a MAP sensitized dog by repeated MAP treatment and showed the alteration in brain distribution of [^{11}C]MAP in a MAP sensitized dog using PET.

Materials and Methods

CHEMICALS AND SYNTHESIS OF [^{11}C]MAP

Anhydrous *N*,*N*-dimethyl formamide (DMF) was purchased from Amersham Japan Co. Ltd. Other chemicals used were of regent grade purchased from Wako Pure Chemical Co. Ltd, Osaka, Japan.

[^{11}C]MAP was synthesized as our previous report[6].

ANIMAL AND DRUG SCHEDULE

A 7-year-old male beagle dog weighing 12.5 kg was used for this study. In the sensitization study, the dog was given daily injection of MAP hydrochloride for 14 days [s.c.

injection (1 mg/kg) for the first 7 days and s.c. injection (1.5 mg/kg) for 7 days] and was then free from MAP for 7 successive days. The locomotion and behavior of the model animal was monitored by video-camera and the change was clarified. This protocol was approved by the Tohoku University animal care committee.

PET STUDY

The dog was initially anesthetized with ketamine (10 mg/kg, s.c.) and maintained under pentobarbital (25 mg/kg, i.v.) anesthesia. Catheters were inserted in the arterial vein for arterial blood sampling and in the venous vein of the fore leg for administration of [^{11}C]MAP. Vital signs (blood pressure, pulse rate, blood pH, O_2 tension, CO_2 tension), monitored and recorded throughout the PET study, were kept within a physiological range. After an intravenous injection of [^{11}C]MAP (6.7-11.3 mCi) into the animal, dynamic scan was carried out parallel to the orbitomeatal (OM) line using PET scanner (PT931, CIT Inc, Noxvile USA at the Cyclotron and Radioisotope Center, Tohoku University, Sendai, Japan) for 90 min. The following regions of interest were selected: parietal cortex, occipital cortex, temporal cortex, frontal cortex, cerebellum. Tissue concentration of [^{11}C]MAP was measured using a ROI program.

DOG PLASMA METABOLITE ANALYSIS

Arterial blood samples were collected in heparinized tubes at 5, 10, 20, 40 and 50 min after injection of [^{11}C]MAP and centrifuged (3000 rpm×3 min). Plasma samples (0.5 ml) were added to 1 ml of methanol and the mixture sonicated and centrifuged (15,000 rpm×45 sec). The supernatant with the addition of unlabeled MAP was injected into analytical HPLC system. The [^{11}C]MAP fraction were collected and counted in an automated NaI counter. The percentage of [^{11}C]MAP activity in plasma activity was calculated.

Results

BEHAVIORAL SENSITIZATION

In dog, an acute injection of MAP (1mg/kg) initially induced the rotational locomoter activity and stereotyped behavior (looking at the ceiling). The repeated administration of MAP produced an increase in the incidence of the stereotyped behavior and a concomitant decrease in that of the locomoter activity. Furthermore, we observed the decreased latency to the onset of stereotyped behavior following injection of MAP. At 7 days after the second PET study, we tried a challenge test of MAP. A challenge dose of MAP (1 mg/kg) reproduced the hyperlocomotion and stereotyped behavior. The behavioral changes produced by repeated administration of MAP are summarized in Figure 1.

PET STUDY

Figure 2 shows PET images of [^{11}C]MAP of the normal and the sensitized dog brains at 10-20 min after administration. The accumulation of [^{11}C]MAP was more clearly visible in the sensitization model than that in the normal condition. Figure 3 shows the time course of tissue distribution of [^{11}C]MAP in the normal and the sensitized dog brains. [^{11}C]MAP rapidly reached the brain and the maximal uptake was observed at 5-15 min after injection. No significant differences of distribution were noted in the five regions. The maximal level of accumulation of [^{11}C]MAP in the sensitized dog brain was 1.4 times higher than that in the control dog brain.

DOG PLASMA METABOLITE ANALYSIS

We analyzed the metabolites of [^{11}C]MAP in the plasma (Figure 4). The clearance of [^{11}C]MAP from the plasma was rapid. At 10 min after the injection, approximately 40% of the total [^{11}C] activity was in the form of [^{11}C]MAP. No difference was found in metabolism of MAP between the MAP sensitized dog and the control dog.

Discussion

In most studies of behavioral sensitization, rats or mice were used as model animals. But it is necessary for PET study to used more large animals. So, we newly produced a MAP sensitized dog by repeated MAP treatment, and confirmed the enduring behavioral sensitization by the challenge test after the second PET study. Wallach and Gershon reported sensitization to amphetamine in dog[7], but they only mentioned a decreased latency to onset of the stereotyped behavior in their paper. We observed the behavioral change produced by repeated administration of MAP in detail and clarified the sensitizing effects of MAP on the dog behavior (Figure 1).

[^{11}C]MAP was distributed uniformly in the five regions of dog brain (Figure 3). Sakai *et al.* reported that the major metabolite of MAP in blood after i.v. administration was *p*-hydroxyl-MAP in rat, but the phenolic metabolites were not detected in brain because these were unable to pass trough the blood-brain barrier[8]. Only MAP and amphetamine were detected in brain. Consequently, we think the activity of each region reflects the distribution of MAP. This result about uniform distribution is similar to a PET study in monkey[9]. The clearance of [^{11}C]MAP in dog brain, however, a little faster than that of monkey. They reported 50% of radioactivity remained as [^{11}C]MAP at 60 min after the injection in arterial monkey plasma. In the other hand, approximately 20% of arterial plasma radioactivity was in the form of [^{11}C]MAP at 50 min after the injection in dog (Figure 4). This species difference of MAP metabolism may cause the difference of biological half-life of MAP between dog and monkey brain.

We visualized a significant increase of [^{11}C]MAP in whole brain of MAP sensitized dog (Figure 2). This significant increase of [^{11}C]MAP uptake into the sensitized dog brain

can't be due to the decreased metabolism of MAP in the sensitized dog (Figure 4). Similar results about increased uptake have been obtained using mice and rats in our previous studies[4,5]. These findings of a lasting increase in [^{11}C]MAP radioactivity in the brain of sensitized animals indicate that subchronic MAP administration causes some functional change in uptake site of MAP.

MAP sensitized animals are widely used as experimental models of stimulant-induced psychosis. The present study suggests that this alteration of [^{11}C]MAP kinetics can be utilized as a marker of MAP abuse in man.

Acknowledgment

This research was supported by a scientific research fund from the Ministry of welfare of the Japanese Government.

References

1) Seagal D. S. and Mandell A. J., Pharmacol. Biochem. Behav. **2** (1974) 249.
2) Nishikawa T. et al., Eur. J. Pharmacol. **88** (1983) 190.
3) Robinson T. E. and Becker J. B., Brain Res. Rev. **11** (1986) 157.
4) Mizugaki M. et al., Nucl. Med. Biol. **20** (1993) 487.
5) Numachi Y. et al., Ann. N. Y. Acad. Sci. **654** (1992) 153.
6) Mizugaki M. et al., CYRIC Annual Report 1993 P93.
7) Wallach M. B. and Gershon S., Psychopharmacol. Bull. **7** (1971) 30.
8) Sakai T. et al., Xenobiotica **15** (1985) 31.
9) Shiue C. Y. et al., Nucl. Med. Biol. **20** (1993) 973.

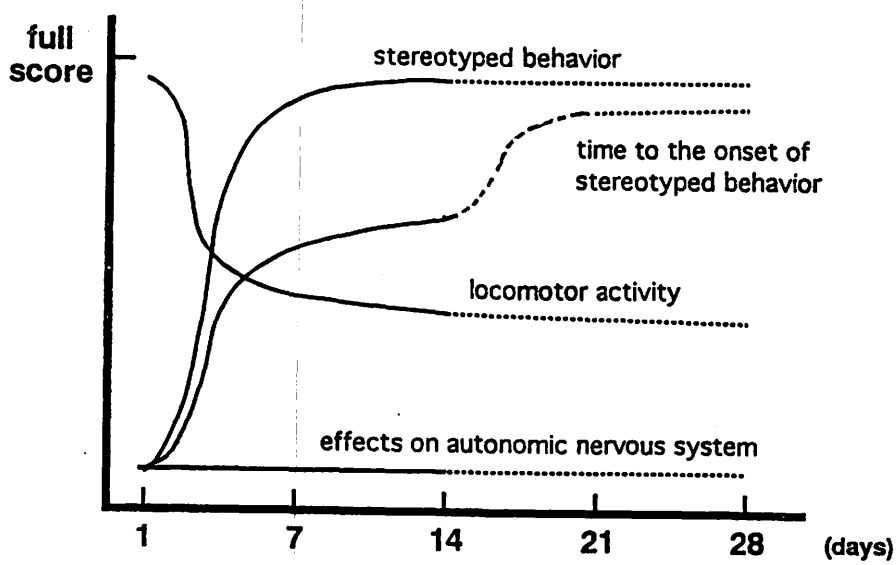

Fig. 1 The effects of repeated MAP administration on the dog behavior.

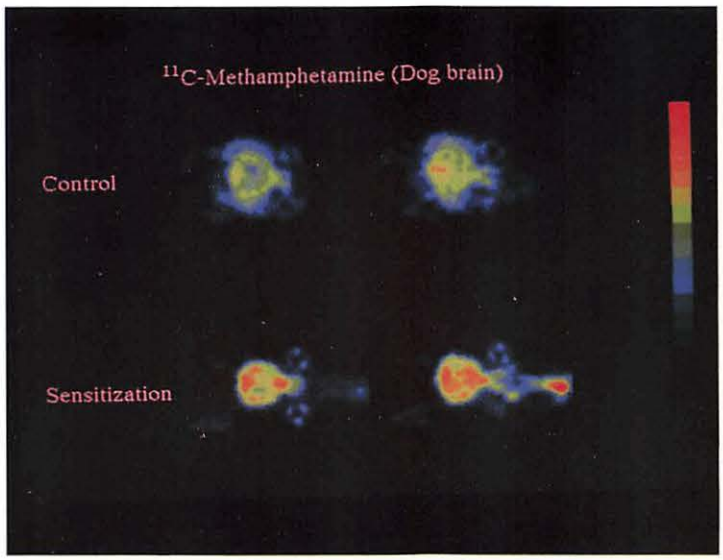

Fig. 2 [^{11}C]MAP PET images in control and sensitized dog brain at 10-20 min after the injection.

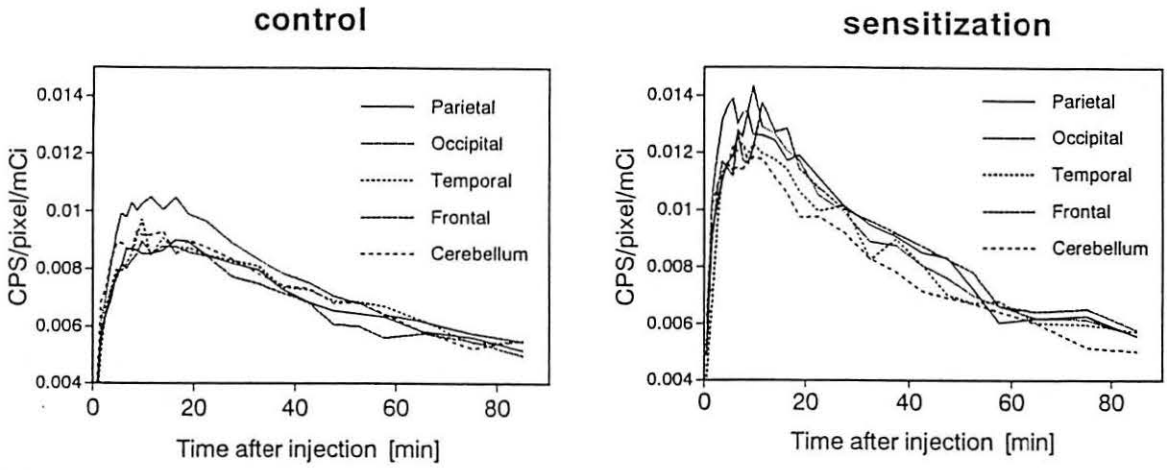

Fig. 3 Time course of tissue distribution of [^{11}C]MAP in control and sensitized dog brain.

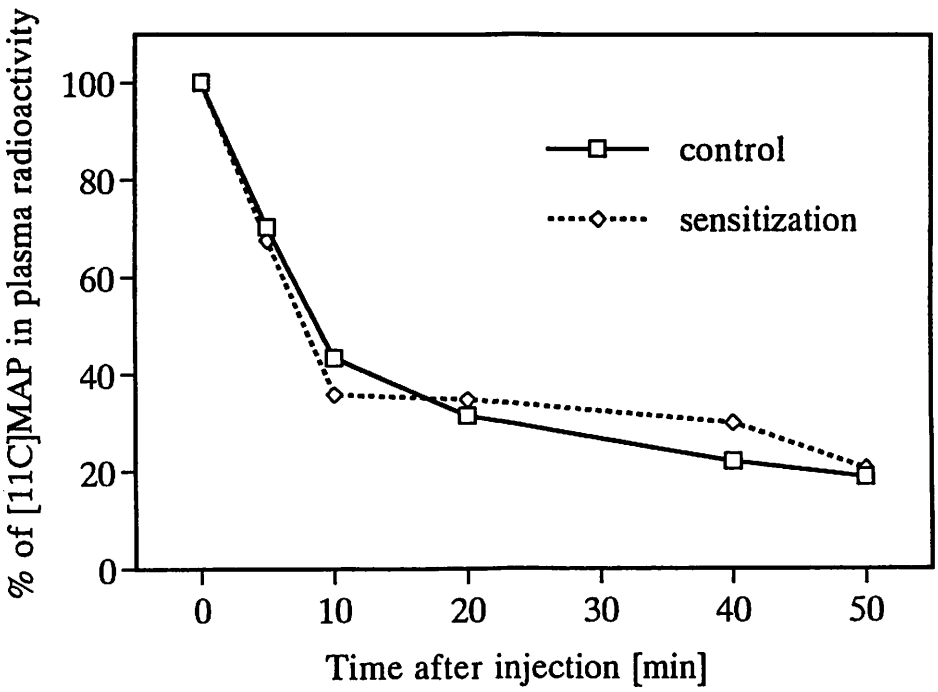

Fig. 4 HPLC analysis of [^{11}C]MAP in plasma. The percent of [^{11}C]MAP activity in plasma activity is indicated.

III. 10. Multi-focal Disturbances of the Postischemic Rat Brain by Measuring Blood Flow, Glucose Metabolism and Adenosine A_1 Binding Activity

Nagasawa H., Araki T., and Itoyama Y.**

Department of Neurology, Miyagi National Hospital,
*Department of Neurology, Tohoku University School of Medicine**

Introduction

It is well known that transient cerebral ischemia produces selectively neuronal damage in brain areas[1-3]. Neuronal degenerative processes occur especially in the hippocampus of the rat[4] and the Mongolian gerbil[5] induced by transient forebrain ischemia. Transient focal ischemia also induces neuronal degeneration in specific brain areas in the rat. Postischemic delayed neuronal damage has been reported in the ipsilateral thalamus and substantia nigra which lay outside ischemic areas of rat brain after middle cerebral artery (MCA) occlusion[6,7]. In those reports, the histological appearance of these remote areas was characterized by degeneration of most neurons with no necrotic changes of neuroglia and blood vessels. The mechanism of such a delayed phenomenon in the exo-focal remote areas is unclear, but it has been speculated that it might be caused by a transsynaptic process neuroanatomically associated with ischemic foci and that intracellular and transsynaptic signal transduction systems might play important roles in this mechanism[8-11].

Adenosine plays neuromodulatory roles in the central nervous system[12,13]. Especially, adenosine A_1 receptor inhibit adenylate cyclase activity[14] and mediate excitatory neuronal pathways by reducing neuronal activity[12]. The anatomical distribution of the adenosine receptor binding sites has been mapped in the rat brain by an autoradiographic method using a potent adenosine A_1 agonist [^{3}H]N^6-cyclohexyladenosine ([^{3}H]CHA)[15-17]. In the present study, we examined chronological changes of adenosine A_1 receptor binding sites of the rat brain, especially focusing on these changes in the exo-focal remote brain areas, after 90 min of MCA occlusion and after such occlusion followed by different periods of recirculation. We also investigated the mechanism involved by measuring regional cerebral blood flow (rCBF) and glucose metabolism.

Materials and Methods

ISCHEMIA MODEL

Seventy-eight adult male Wistar rats of the SPF strain weighing 280-300 g were allowed free access to food and water before and after all procedures. Six rats were used for each experiment group. A detailed description of the surgical procedure has been previously reported[18]. In brief, after induction of anesthesia with a gas mixture of 70% N_2O and 2% halothane (the balance being O_2), the right MCA was occluded with a silicone rubber cylinder attached to a nylon surgical thread introduced from the bifurcation of the internal carotid artery immediately after ligation of the ipsilateral common and external carotid arteries. The cylinder was made of 4-0 nylon surgical thread (Nitcho Kogyo Co., Ltd., Tokyo, Japan), 16 mm long. This cylinder was coated with silicone (Xantopren, Bayer Dental, Leverkusen, Germany) mixed with a hardener (Elastomer Activator, Bayer Dental) to increase the thickness of the distal 5 mm to 0.25-0.30 mm. After introducing the embolus, the internal carotid artery was ligated just distal to the point of insertion. The embolus extended from the bifurcation of the internal carotid artery to the proximal portion of the anterior cerebral artery (ACA). The origin of the right MCA and that of the right posterior communicating artery were occluded by the silicone rubber cylinder. In eighteen sham-operated control rats, the right internal and external carotid arteries were ligated. Surgery was performed within 15 min with no bleeding. Body temperature was kept at normal limits with a heating pad. Following surgery, anesthesia was discontinued and all rats exhibited neurologic deficits characterized by left hemiparesis with upper extremity dominancy and right Horner's syndrome. After 90 min of MCA occlusion, recirculation was achieved in 54 rats by pulling the thread out of the internal carotid artery under the same anesthetic conditions as during surgery. Once again, the rats were allowed free access to food and water. Although the ipsilateral common and external carotid arteries had been ligated, the ischemic area could be reperfused via the cerebral arterial circle (circle of Willis) through the contralateral carotid and basilar arteries, and by collateral circulation of cortical branches of the cerebral arteries.

Adenosine A_1 receptor autoradiography

Adenosine A_1 receptor binding sites were measured using [^{3}H]cyclohexyladenosine ([^{3}H]CHA, spec. act. 34.4 Ci/mmol, Dupon NEN Products, Boston USA) according to the method of Onodera et al[19]. The rats were killed by decapitation 3 h, 6 h, 1 day, 3 days, 1 week, 2 weeks, and 4 weeks after recirculation. After decapitation, the brains were quickly removed and frozen in powdered dry ice. Serial coronal sections 12 μm in thickness were cut on a cryostat (HM500, Zeiss, Germany) and thaw-mounted onto gelatin-coated slides. Sections were incubated with 5 nM [^{3}H]CHA and 2 units/ml adenosine deaminase (Boehringer-Mannheim, Mannheim, Germany) in 50 mM Tris-HCl buffer (pH 7.4) at room temperature for 90 min. Following incubation, sections were washed in the buffer at 4 °C for 5 min and rapidly dried under a cold stream of air. Nonspecific binding was determined

using 10 μM L-phenylisopropyl-adenosine (Boehringer-Mannheim). Autoradiograms were prepared from the sections by exposing them to [^{3}H]sensitive hyperfilm (Amersham, Sweden AB, Solna, Sweden) with a tritium standard microscale (Amersham, International plc, Buckingham, UK) for 2 weeks in standard X-ray cassettes. The optical density of the brain regions was measured with a computed-assisted image analyzer (Zeiss, IBAS image analyzer system, Germany) without the examiner knowing the experimental protocol. The relationship between optical density and radioactivity was obtained with reference to [^{3}H]microscales co-exposed with the sections using a third-order polynominal function. The optical density of the brain regions measured in the present study was in the range where optical density and radioactivity of the [^{3}H]microscales showed a near linear relationship.

Cerebral blood flow and glucose metabolism

Regional CBF was measured in 6 sham-operated rats and in 6 rats 2 weeks of recirculation after 90 min of MCA occlusion. A tracheotomy was performed in 12 rats under the same anesthetic conditions and the rats were ventilated. Pancuronium bromide (0.6 mg/kg i.p.) was administered, and both femoral arteries and a femoral vein were cannulated. After surgical preparation, 2% halothane was discontinued and the rats were ventilated with 70% N_2O and 30% O_2, allowing normoxia and normocapnia. CBF was measured by the [^{14}C]iodoantipyrine quantitative autoradiographic technique according to Sakurada et al. In brief, 20 μCi (0.6 ml) of 4-iodo-N-methyl-[^{14}C]iodoantipyrine (Amersham) was infused intravenously over 30 seconds. During the infusion, several 20-μl samples of arterial blood from the free-flowing femoral artery catheter were collected in sample tubes. The [^{14}C]iodoantipyrine concentration in the blood samples was determined by a liquid scintilation counter (Aloka) after allowing 24 hours for decolorization in a mixture with 1 ml tissue and gel solubilizer (Protosol) and 100 μℓ H_2O_2. The rats were decapitated approximately 30 seconds after the start of infusion. The brains were quickly removed and frozen in powdered dry ice. Each brain was sectioned (20 μm) in a cryostat (HM500, Zeiss, Germany) at -20 °C, and the sections were exposed to x-ray film (NMC-1, Kodak) with an autoradiographic carbon-14 standard microscale (Amersham) in x-ray cassettes for two weeks. Regional cerebral blood flow was calculated using a blood-brain coefficient of 0.8 and the equation derived by Sakurada et al.[20]

Regional cerebral glucose utilization (rCGU) was measured in other 6 rats after 90 min of ischemia followed by 2 weeks of recirculation and in 6 sham-operated rats. After the same surgical preparation as for the measurement of rCBF, samples of arterial blood were taken immediately prior to measurement of rCGU for determination of blood glucose level, PaO_2, $PaCO_2$, and pH. Regional CGU was measured by the 2-[^{14}C]deoxyglucose (Amersham) quantitative autoradiographic technique and rCGU was calculated using the equation of Sokoloff et al.[21] Cerebral [^{14}C] tissue concentrations of the autoradiograms were determined by means of a computerized microdensitometric system (Chromoscan, USA).

Statistical analysis

Values of adenosine A_1 binding sites were expressed as the means ±SD fmol/mg tissue using six animals. Data regarding the adenosine A_1 binding site, rCBF and rCGU in each structure of the brain were analyzed using Duncan's multiple range test with $p<0.05$ and $p<0.01$ considered to be statistically significant.

Results

ADNOSINE A_1 RECEPTOR BINDING ACTIVITY

The values of sham-operated control animals and chronological alteration of [^{3}H]CHA binding sites in each structure of rat brain after 90 min of MCA occlusion and after such occlusion followed by different periods of recirculation are summarized in Table 1. Representative autoradiograms of [^{3}H]CHA are shown in Figure 1. After 90-min ischemia followed by 1-day recirculation, significant decreases of the [^{3}H]CHA binding sites were first observed in the anterior neocortex (FrPaSS) ($p<0.05$) and the lateral segment of caudate putamen (CPu-L) ($p<0.01$), both of which were supplied by the occluded MCA. Therefore, [^{3}H]CHA binding sites of the ischemic side decreased to approximately 20% in the FrPaSS and to 35% in the CPu-L of each control value 4 weeks after the ischemic insult (Table 1). On the contrary, there was no alteration on day 1, but 3 days after recirculation, a significant reduction of [^{3}H]CHA binding sites was first detected in the ipsilateral thalamus ($p<0.05$), the amygdala ($p<0.05$), and the substantia nigra ($p<0.05$), which those areas were not directly affected by the original ischemic insult. Thereafter, the binding sites decreased progressively in the thalamus and the substantia nigra on the ischemic side (Figure 1). There were no significant changes of [^{3}H]CHA binding sites in the contralateral non-ischemic hemisphere.

Cerebral blood flow and glucose metabolism

In the measurement of rCBF and rCGU, there were no significant differences in physiological variables between the MCA occlusion and sham-operated groups. After 90 min of MCA occlusion followed by 2 weeks of recirculation, representative [^{14}C]iodoantipyrine and 2-[^{14}C]deoxyglucose autoradiograms of the thalamus and the substantia nigra are presented in Figure 2 and 3, respectively. There were no significant differences of rCBF in the exo-focal remote areas, the thalamus, the amygdala and the substantia nigra on the ischemic side compared with the each corresponding region of the contralateral hemisphere and sham-operated group (Table 2). However, rCGU in the ventral posterior nucleus of the thalamus on the ischemic side decreased inhomogeneously, to a variable extent, but was not significant compared with the corresponding region of the contralateral hemisphere and sham-operated group. On the other hand, CGU in the substantia nigra on the ischemic side

increased significantly ($p<0.01$) in comparison with the corresponding region of the contralateral hemisphere (Table 3).

Discussion

It has been well known that adenosine and adenosine nucleotide play important roles in energy metabolism within cells as cyclic adenosine monophosphate and adenosine triphosphate (ATP). In experimental animals, a protective action of adenosine against ischemic neuronal damage has been demonstrated[22]. Furthermore, the adenosine receptor antagonist theophylline enhances ischemic neuronal damage in the gerbil hippocampus[23]. In general, adenosine is thought to prevent ischemic brain damage through several actions, such as enhanced resynthesis of ATP[24], inhibition of excitatory amino acid release[25], and reduction of free radical formation[26]. Therefore, adenosine may play an important role in the pathogenesis of ischemic brain damage[27].

The present study indicated that two different alterations of adenosine A_1 binding sites associated with the mechanisms of neuronal damage took place in the postischemic rat brain. First, in the frontoparietal cortex, somatosensory areas (FrPaSS), and the lateral segment of caudate putamen (CPu-L), adenosine A_1 binding activity decreased after 90 min of ischemia followed by 1 day of recirculation. In this model of ischemia, the FrPaSS and the CPu-L, which were supplied by the occluded MCA, were the regions most frequently damaged so-called ischemic foci[18]. We previously reported that more rapid changes of second messenger systems than adenosine A_1 binding activity were observed concurrent with abnormal calcium accumulation in the FrPaSS and the CPu-L on the ischemic side using the same ischemia model[10,11]. Regional CBF and glucose metabolism decreased persistently in those ischemic foci 2 weeks of recirculation after the ischemic insult. The reduction of adenosine A_1 binding activity in the FrPaSS and the CPu-L is explained by the direct damage to intracellular components including cell membrane following damage of second messenger systems and disruption of calcium homeostasis by ischemia-induced energy failure.

Second, in the exo-focal postischemic brain areas, the ipsilateral thalamus, the amygdala, the substantia nigra, significant decreases of adenosine A_1 binding activities were observed 3 days after the ischemia. These changes of adenosine A_1 binding activity observed in the thalamus and the substantia nigra on the ischemic side were concurrent with the abnormal calcium accumulation detected there in our previous study[6]. Moreover, both phenomena, i.e., the reduction of adenosine A_1 binding activity and abnormal calcium accumulation, in two remote areas on the ischemic side preceded the histologic findings of delayed neuronal damages. In contrast with the FrPaSS and the CPu-L, the ipsilateral thalamus and the substantia nigra were remote from these ischemic areas, and both areas had not been directly affected by the original ischemic insult[6]. Delayed neuronal damages in the exo-focal remote areas might be caused by a transsynaptic process associated with the ischemic foci[6].

However, regional glucose metabolism was quite different in two individual area, rCGU decreased in the thalamus and the amygdala, but increased in the substantia nigra, although there were no significant differences of rCBF in those exo-focal remote areas. We realize that the mechanisms of delayed neuronal damage in the exo-focal remote areas may be variable and are complicated in remote areas, i.e., the thalamus, the amygdala, and the substantia nigra on the ischemic side.

Iizuka et al. reported that delayed neuronal degeneration of the ipsilateral thalamus was observed after somatosensory cortical infarct of rats using Fink-Heimer silver staining method[28]. Reduction of adenosine A_1 binding activity in the thalamus on the ischemic side may be explained by retrograde neuronal degeneration due to thalamo-cortical fiber damage in ischemic cortical regions. Yamada et al. reported that basic fibroblast growth factor prevented neuronal degeneration of the thalamus after MCA occlusion in rats[29]. This indicates that trophic substances may play an important role in the mechanism of neuronal damage of the thalamus which might be caused by retrograde degeneration of the thalamo-cortical pathway after ischemic insult.

On the other hand, in the ipsilateral substantia nigra, it is not easy to explain the mechanism of the delayed reduction of adenosine A_1 receptor binding activity 3 days after the ischemic insult and increased glucose metabolism 2 weeks after the ischemia. We speculate as a possible hypothesis that the phenomenon in this area may be explained as being due to abnormal function of some neurotransmitters in the transsynaptic process associated with ischemic foci[11,30]. As for the substantia nigra, it consists of fibrous connections originating in the caudate putamen and projecting over the globus pallidus, forming the strio-nigral pathways[31]. The neuro-inhibitory transmitter GABA plays an important functional role in the strio-nigral pathway[32-34]. The increase of glucose metabolism in the substantia nigra on the ischemic side may be explained as being a result of altered neuronal function and hypermetabolism and is caused by diminished inhibitory output from the caudate putamen, which was affected by the precedent ischemic insult. We also speculate that the delayed neuronal degeneration in this area may be induced by disinhibitory overexcitation caused by diminished inhibitory regulation from the caudate putamen. Further detailed investigation is required in order to clarify the mechanisms of delayed neuronal degeneration in the exo-focal remote areas, which may be caused by neuronal network disturbances after ischemia.

Based on the present study, we conclude that postischemic alteration of adenosine A_1 binding activity was involved not only in the ischemic foci due to ischemia-induced energy failure, but also in the exo-focal remote areas prior to the histologic changes, which neuronal damage might be caused by the transsynaptic delayed degeneration associated with the ischemic foci. Furthermore, we suggest that multi-focal neuronal dysfunction in the postischemic brain areas may exacerbate the clinical symptoms of patients during the chronic stage of stroke.

References

1) Smith M.L. et al., Acta Neurol. Scand. **69** (1984) 385.
2) Araki T., Kato H. and Kogure K., Acta Neurol. Scand. **80** (1989) 548.
3) Bonnekoh P. et al., Acta Neuropathol. **80** (1990) 18.
4) Pulsinelli W.A., Brierley J.B. and Plum F., Ann. Neurol. **11** (1982) 491.
5) Kirino T., (1982) Brain Res. **239** (1982) 57.
6) Nagasawa H. and Kogure K., Brain Res. **524** (1990) 196.
7) Tamura A. et al., Brain Res. **510** (1990) 154.
8) Kogure K., Tanaka J. and Araki T., Neurochem. Pathol. **9** (1988) 145.
9) Nagasawa H. and Kogure K., Brain Res. **563** (1991) 7.
10) Nagasawa H. and Kogure K., J. Neurosci. Res. **31** (1992) 507.
11) Nagasawa H., Araki T. and Kogure K., J. Neurosci. Res. **33** (1992) 485.
12) Phillis J. W. and Wu P. H., Prog. Neurobiol. **16** (1981) 187.
13) Snyder S. H., Annu. Rev. Neurosci. **8** (1985) 103.
14) Van Calker D., Muller M. and Hamprecht B., J. Neurochem. **33** (1979) 999.
15) Lewis M.E. et al., Eur. J. Pharmacol. **73** (1981) 109.
16) Goodman R. R. and Snyder S. H., J. Neurosci. **2** (1982) 1230.
17) Goodman R. R. et al., Science **220** (1982) 967.
18) Nagasawa H. and Kogure K., Stroke **20** (1989) 1037.
19) Onodera H., Sato G. and Kogure K., Brain Res. **415** (1987) 309.
20) Sakurada O. et al., Am. J. Physiol. **234** (1978) H59.
21) Sokoloff L. et al., J. Neurochem. **28** (1977) 897.
22) Dragunow M. and Faull R. L. M., Trends Pharmacol. Sci. **9** (1988) 193.
23) Rudolphi K. A., Keil M. and Hinze H. J., J. Cereb. Blood Flow Metab. **7** (1987) 74.
24) Foker J. E., Einzig S. and Wang T., J. Thorac. Cardiovasc. Surg. **80** (1980) 506.
25) Fastbom J. and Fredholm B. B., Acta Physiol. Scand. **125** (1985) 121.
26) Cronstein B. N. et al., J. Clin. Invest. **78** (1986) 760.
27) Phillis J. W. and O'Regan M. H., Brain Res. Bull. **22** (1989) 537.
28) Iizuka H., Sakatani K. and Young W., Stroke **21** (1990) 790.
29) Yamada K. et al., J. Cereb. Blood Flow Metab. **11** (1991) 472.
30) Nagasawa H., Kogure K. and Ido T., Tohoku J. Exp. Med. **169** (1993) 87.
31) Szabo J., Exp. Neurol. **27** (1970) 1.
32) McNair J., Sutin J. and Tsubokawa T., Exp. Neurol. **37** (1972) 395.
33) Nagy J., Carter D. and Fibiger H., Brain Res. **158** (1978) 15.
34) Yosida M., Rabin A. and Anderson M., Brain Res. **32** (1971) 225.

Table 1. Time-course of [^{3}H]CHA binding sites in each structure of the rat brain after 90 min of MCA occlusion followed by different periods of recirculation.

Structure	Control	90-min ischemia	3 hours	6 hours	1 day
Ischemic side					
FrPaM	233.8 ± 14.8	237.3 ± 15.4	233.2 ± 31.6	230.5 ± 30.7	225.9 ± 38.3
FrPaSS	236.9 ± 18.3	226.5 ± 19.4	241.6 ± 35.1	230.3 ± 24.1	192.8 ± 33.6*
CPu(L)	214.4 ± 29.3	206.3 ± 13.5	226.8 ± 36.8	198.1 ± 18.0	138.6 ± 17.7**
CPu(M)	214.9 ± 29.9	191.7 ± 19.1	220.7 ± 36.8	212.0 ± 37.4	236.6 ± 39.4
Hippocampus	311.1 ± 22.1	316.1 ± 37.8	349.7 ± 34.5	319.9 ± 24.1	356.7 ± 35.5
Thalamus	298.8 ± 36.8	290.6 ± 21.4	319.6 ± 39.0	281.1 ± 33.9	310.0 ± 38.0
Amygdala	121.5 ± 9.6	138.3 ± 9.0	141.2 ± 29.0	137.2 ± 14.9	129.3 ± 27.8
Substantia nigra	129.3 ± 15.4	113.1 ± 13.6	115.4 ± 27.3	114.8 ± 15.1	115.1 ± 20.1
Pons	93.4 ± 9.0	112.2 ± 12.2	102.4 ± 13.1	105.3 ± 13.1	100.1 ± 22.3
Non-ischemic side					
FrPaM	233.6 ± 21.7	236.5 ± 19.6	235.5 ± 24.9	232.9 ± 30.7	230.3 ± 47.6
FrPaSS	221.8 ± 24.6	225.3 ± 22.6	247.1 ± 22.3	228.5 ± 26.4	222.0 ± 38.4
CPu(L)	214.5 ± 34.4	220.6 ± 18.3	227.6 ± 18.4	221.0 ± 25.8	238.1 ± 22.8
CPu(M)	210.3 ± 35.9	205.2 ± 15.1	227.9 ± 12.2	217.5 ± 20.6	237.5 ± 24.9
Hippocampus	316.2 ± 39.3	319.1 ± 37.1	336.7 ± 33.6	336.4 ± 26.7	345.1 ± 36.6
Thalamus	295.6 ± 36.9	304.2 ± 33.1	312.1 ± 30.3	278.1 ± 27.4	285.9 ± 27.4
Amygdala	124.4 ± 20.6	133.7 ± 21.5	115.7 ± 19.1	144.7 ± 22.3	134.9 ± 25.8
Substantia nigra	117.0 ± 21.2	118.3 ± 6.7	120.9 ± 20.1	113.4 ± 17.7	120.4 ± 33.9
Pons	99.6 ± 8.4	111.1 ± 10.3	106.7 ± 12.5	103.5 ± 14.8	103.4 ± 17.4

Values are given in Mean ± S.D. fmol/mg tissue using six animals.
FrPaM: frontoparietal cortex, motor area, supplied by anterior cerebral artery;
FrPaSS: frontoparietal cortex, somatosensory area, supplied by middle cerebral artery;
CPu(L): lateral segment of caudate putamen; CPu(M): medial segment of caudate putamen;
*p<0.05; **p<0.01, significant difference from control values using Duncan's multiple range test.

Table 1. Time-course of [^{3}H]CHA binding sites in each structure of the rat brain after 90 min of MCA occlusion followed by different periods of recirculation (continued).

Structure	3 days	1 week	2 weeks	4 weeks
Ischemic side				
FrPaM	236.4 ± 36.8	233.8 ± 22.6	240.1 ± 23.8	238.7 ± 33.4
FrPaSS	74.2 ± 6.9**	82.9 ± 24.6**	55.1 ± 11.3**	52.2 ± 7.0**
CPu(L)	97.4 ± 24.6**	102.1 ± 19.7**	81.5 ± 12.7**	71.6 ± 8.4**
CPu(M)	233.9 ± 20.6	234.2 ± 38.3	233.2 ± 20.5	231.3 ± 22.1
Hippocampus	353.2 ± 27.3	322.8 ± 18.9	368.5 ± 22.3	362.2 ± 36.1
Thalamus	225.1 ± 17.9**	179.0 ± 28.4**	163.6 ± 29.0**	166.5 ± 12.5**
Amygdala	105.5 ± 22.3*	82.6 ± 20.6**	79.6 ± 28.1**	58.9 ± 15.6**
Substantia nigra	99.1 ± 15.4*	87.1 ± 11.9**	75.1 ± 12.2**	60.4 ± 14.4**
Pons	101.1 ± 24.9	109.2 ± 11.0	106.4 ± 7.3	118.6 ± 17.9
Non-ischemic side				
FrPaM	232.2 ± 27.6	236.5 ± 22.9	254.6 ± 33.3	250.6 ± 29.3
FrPaSS	261.1 ± 35.4	254.9 ± 30.9	259.1 ± 37.4	231.8 ± 35.1
CPu(L)	249.7 ± 23.5	250.0 ± 21.0	250.7 ± 21.9	258.6 ± 30.7
CPu(M)	228.0 ± 29.0	236.1 ± 26.7	239.6 ± 25.2	232.1 ± 27.6
Hippocampus	350.0 ± 27.7	347.7 ± 22.3	348.2 ± 23.8	332.8 ± 20.3
Thalamus	285.6 ± 26.8	309.1 ± 25.1	304.0 ± 34.8	302.5 ± 37.1
Amygdala	154.7 ± 28.1	152.5 ± 16.1	150.0 ± 20.0	150.2 ± 14.8
Substantia nigra	115.5 ± 11.6	114.3 ± 17.9	130.4 ± 10.7	130.2 ± 11.2
Pons	100.4 ± 12.5	104.3 ± 11.0	113.4 ± 10.6	118.1 ± 13.1

Values are given in Mean ± S.D. fmol/mg tissue using six animals.
FrPaM: frontoparietal cortex, motor area, supplied by anterior cerebral artery;
FrPaSS: frontoparietal cortex, somatosensory area, supplied by middle cerebral artery;
CPu(L): lateral segment of caudate putamen; CPu(M): medial segment of caudate putamen;
*p<0.05; **p<0.01, significant difference from control values using Duncan's multiple range test.

Table 2. Regional cerebral blood flow of the sham-operated control rats and measured after 90-min ischemia followed by 2-week recirculation.

Structure	sham-operated control group	90-min ischemia followed by 2-week recirculation
Ischemic side		
FrPaM	1.39 ± 0.09	1.36 ± 0.14
FrPaSS	1.70 ± 0.18	0.55 ± 0.08**
CPu(L)	1.65 ± 0.15	0.99 ± 0.17**
CPu(M)	1.63 ± 0.12	1.62 ± 0.10
Hippocampus	1.01 ± 0.10	0.90 ± 0.09
Thalamus (VPN)	1.62 ± 0.12	1.47 ± 0.14
Amygdala	1.19 ± 0.17	0.51 ± 0.08**
Substantia nigra	1.05 ± 0.08	0.98 ± 0.16
Pons	1.42 ± 0.12	1.34 ± 0.12
Non-ischemic side		
FrPaM	1.41 ± 0.09	1.42 ± 0.09
FrPaSS	1.68 ± 0.15	1.63 ± 0.23
CPu(L)	1.62 ± 0.12	1.78 ± 0.05
CPu(M)	1.60 ± 0.13	1.77 ± 0.07
Hippocampus	1.05 ± 0.09	0.94 ± 0.12
Thalamus (VPN)	1.59 ± 0.11	1.60 ± 0.11
Amygdala	1.17 ± 0.15	1.33 ± 0.19
Substantia nigra	1.07 ± 0.10	0.96 ± 0.08
Pons	1.40 ± 0.13	1.39 ± 0.08

Values are given in mean ± SD ml/g/min using six animals. FrPaM, frontoparietal cortex, motor area, supplied by anterior cerebral artery; FrPaSS, frontoparietal cortex, somatosensory area, suuplied by middle cerebral artery; CPu(L), lateral segment of caudate putamen; CPu(M), medial segment of caudate putamen; Thalamus (VPN), ventral posterior nucleus of thalamus. **$p<0.01$, significant difference from control values using Duncan's multiple range test.

Table 3. Local cerebral glucose utilization of the sham-operated control rats and measured after 90-min ischenia followed by 2-week recirculation.

Structure	Sham-operated control group	90-min ischemia followed by 2-week recirculation
Ischemic side		
FrPaM	70.39 ± 6.17	67.56 ± 6.56
FrPaSS	69.44 ± 3.83	57.39 ± 7.17*
CPu(L)	73.11 ± 7.22	61.83 ± 7.83*
CPu(M)	76.06 ± 9.89	60.61 ± 9.28
Hippocampus	66.83 ± 7.28	63.00 ± 9.39
Thalamus (VPN)	66.72 ± 6.67	59.78 ± 4.65
Amygdala	53.22 ± 7.06	45.17 ± 9.11*
Substantia nigra	45.72 ± 8.44	57.56 ± 5.61**
Non-ischemic side		
FrPaM	71.39 ± 7.11	64.94 ± 8.44
FrPaSS	61.17 ± 3.89	65.67 ± 7.78
CPu(L)	72.33 ± 7.44	74.28 ± 7.89
CPu(M)	73.67 ± 9.77	74.44 ± 9.61
Hippocampus	66.61 ± 7.78	62.72 ± 7.00
Thalamus (VPN)	67.06 ± 6.28	71.61 ± 7.61
Amygdala	54.33 ± 5.39	59.17 ± 8.61
Substantia nigra	47.00 ± 6.72	45.94 ± 6.17

Values are given in mean ± SD umol/100g/min using six animals.
FrPaM: frontoparietal cortex, motor area, supplied by anterior cerebral artery; FrPaSS: frontoparietal cortex, somatosensory area, supplied by middle cerebral artery; CPu(L): lateral segment of caudate putamen; CPu(M), medial segment of caudate putamen; Thalamus (VPN): ventral posterior nucleus of thalamus.
*$p<0.05$; **$p<0.01$, significant difference from control values using Duncan's multiple range test.

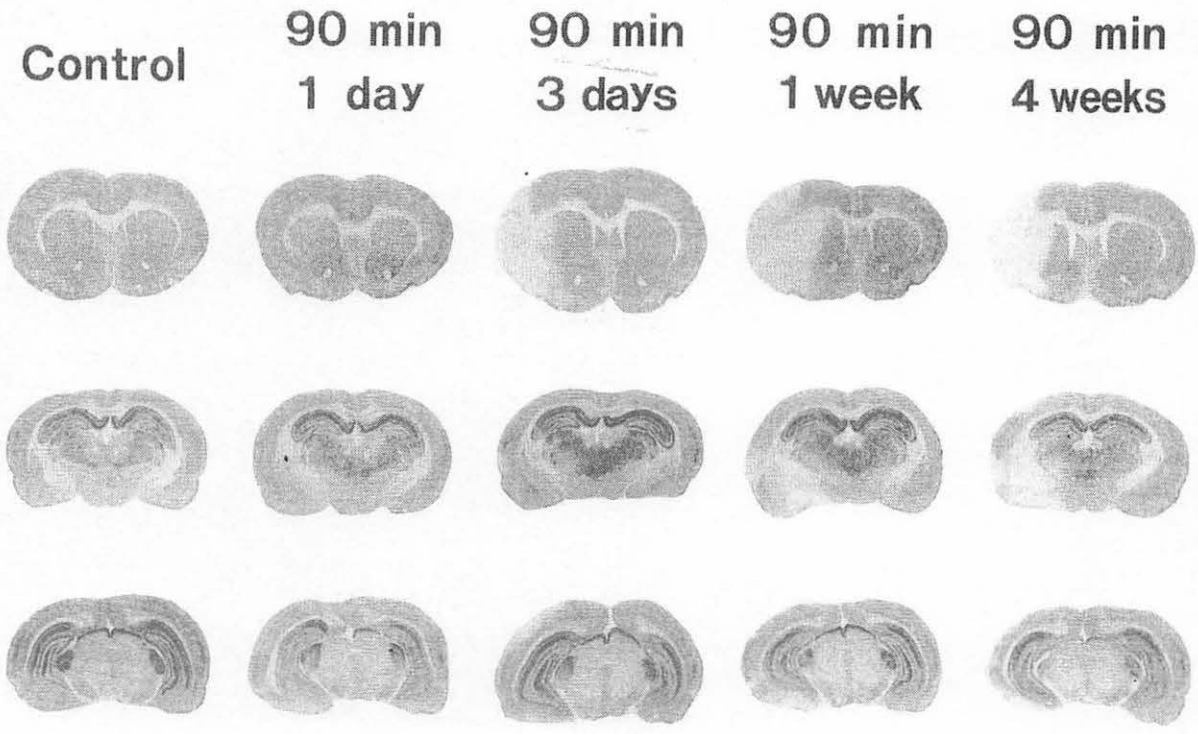

Fig. 1. [^{3}H]CHA autoradiograms of the brains of sham-operated control rats and those obtained after 90 min of MCA occlusion followed by 1-day, 3-day, 1-week, and 4-week recirculation. Representative autoradiograms show coronal sections at the level of the caudate putamen (top), the thalamus (middle), and the substantia nigra (bottom).

Fig. 2. [^{14}C]iodoantipyrine autoradiograms of the rat brain after 90 min of MCA occlusion followed by 2 weeks of recirculation. Representative autoradiograms show coronal sections at the level of the caudate putamen (top), the thalamus (middle), and the substantia nigra (bottom).

Fig. 3. 2-[^{14}C]Deoxyglucose autoradiograms of rat brain after 90 min of MCA occlusion followed by 2 weeks of recirculation. Regional cerebral glucose utilization (rCGU) decreases slightly and inhomogeneously in the ventral posterior nucleus of the thalamus of the ischemic side (arrowhead), whereas an increase in rCGU is seen in the ipsilateral substantia nigra (arrow).

III. 11. Autoradiographic Study of ^{67}Ga Citrate and ^{18}F-FDG in Experimental Inflammatory Tissue.

Yamada S., Kubota K., Kubota R., Tamahashi N., and Ido T.***

Department of Nuclear Medicine and Radiology,
Institute of Development, Aging and Cancer, Tohoku University
Clustercore Institute of Biology*
Cyclotron and Radioisotope Center, Tohoku University**

Introduction

In previous report[1], longitudinal tissue distribution study of double tracer of ^{18}F-FDG and ^{67}Ga citrate showed that both uptakes in inflammatory tissue increased progressively to a peak on day 4 after inoculation of turpentine oil and then decreased. Section of inflammatory tissue 4 days after inoculation when the maximum uptake was observed showed characteristic changes of chronic inflammation. ^{67}Ga citrate has been widely used for the detection of inflammation[2-5]. In this study, we examined morphologically the biodistribution of ^{18}F-FDG and ^{67}Ga citrate in the inflammatory tissue by double-tracer macro-autoradiography (macro-ARG).

Materials and Methods

A male Donryu rat weighing about 100 g was used. To produce experimental inflammatory tissue, the rat was subcutaneously inoculated with 0.2 ml of turpentine oil in the left groin. The rat 4 days after inoculation was injected with 7.4 MBq (200 μCi) of ^{67}Ga citrate through the tail vein. Twelve hours later, the rat was injected with 148 MBq (4 mCi) of ^{18}F-FDG and killed 1 hour later. Inflammatory tissue was dissected immediately and the sample was embedded in OCT compound (Miles Inc. U.S.A.) and frozen with dry-ice. The frozen sample was sectioned in a cryostat at -20 °C. It was immediately processed for macro-ARG as described previously[6]. Briefly, 10 μm-thick section was mounted on clean glass slide, air-dried and contacted with ARG film (MARG ^{3}H-type, Konica, Japan). After exposure for 1 hour, the ARG film for ^{18}F-FDG macro-ARG was photographically processed. Fortyeight hours later, when ^{18}F ($T_{1/2}$=109.7 min) had fully decayed, the slide was contacted with ARG film. After exposure for 9 days, the film for ^{67}Ga ($T_{1/2}$=3.2 day) citrate macro-ARG was also processed. Section on the slide was stained with hematoxylin and eosin, and examined under a light microscope.

Results and Discussion

Double-tracer macro-autoradiograms with the corresponding section of inflammatory tissue 4 days after inoculation of turpentine oil is shown in Figure 1. ^{67}Ga citrate macro-ARG (Figure 1-A) demonstrated a high density of silver grains in the outer side of the zone surrounding abscess center, that corresponded histologically to "abscess wall" (Figure 1-C). On the other hands, ^{18}F-FDG macro-ARG (Figure 1-B) showed a high density in the inner side of abscess wall. There was a notable different distribution between ^{67}Ga citrate and ^{18}F-FDG. Our previous tissue distribution study showed that both ^{67}Ga citrate and ^{18}F-FDG accumulate highly in inflammatory tissue characterized by chronic phase, but this double-tracer macro-ARG showed a different distribution. The outer side of abscess wall histologically consists of round cells of macrophages and matured fibroblasts and the inner consists of phagocytes of macrophages and neutrophils, young endothelial cells of vessels and young fibroblasts. Our results suggest that there is a possibility of identifying a role (tissue repair or response to tissue injury) in inflammatory response in inflammatory tissue using ^{67}Ga citrate and ^{18}F-FDG.

References

1) Yamada S. et al., CYRIC Annual Report 1992, (1992) 122.
2) Ito Y. et al., Radiology **100** (1971) 357.
3) Higasi T. et al., J. Nucl. Med. **13** (1972) 196.
4) Littenberg RL. et al., Ann. Int. Med. **79** (1973) 403.
5) Heshiki A. et al., Am. J. Roentgenol. **122** (1974) 744.
6) Kubota R. et al., J. Nucl. Med. **33** (1992) 1972.

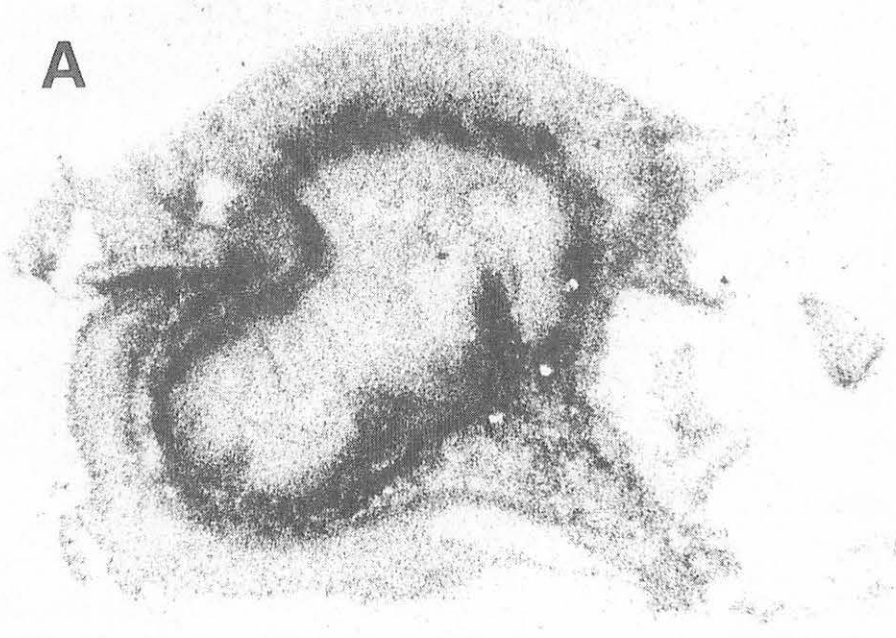

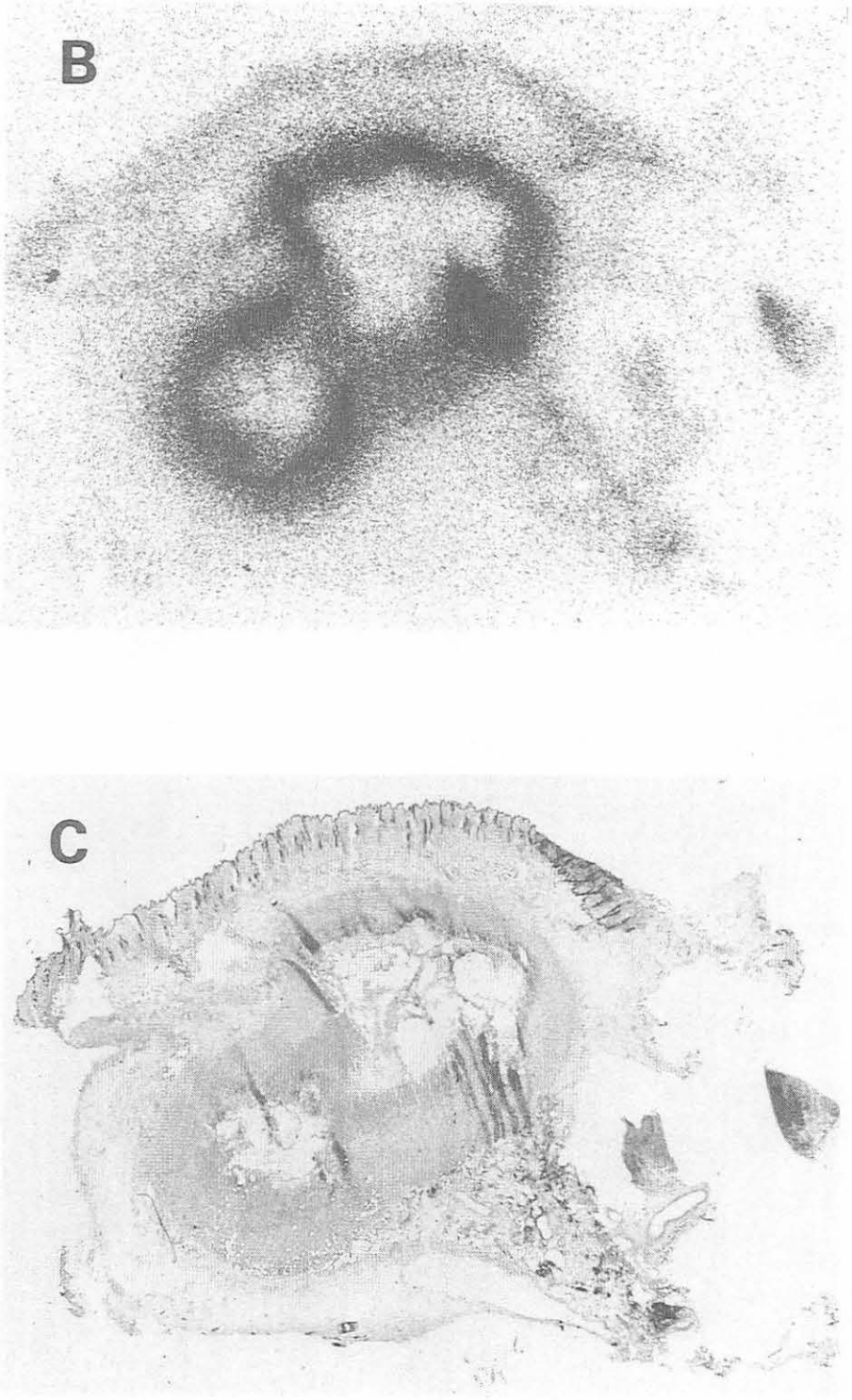

Fig. 1. Double-tracer macro-autoradiograms (^{67}Ga citrate: A, ^{18}F-FDG: B) and the corresponding section (C) of inflammatory tissue 4 days after inoculation of turpentine oil.

III. 12. Magnesium Behavior in Mice Affected by Different Dietary Magnesiunm or Calcium Level

Kawamura M., Ido T., Iwata R.*, Funaki Y.*, and Kimura S.***

Faculty of Agriculture, Tohoku University
** Cyclotron and Radioisotope Center, Tohoku University*
*** Showa Women's University, Graduate School*

Magnesium, the second most important intracellular cation is found in all tissues and may affect many function of the body. Magnesium deficiendy can affect not only trace elements but other nutrients. So far, we developed biodistribution studies and whole body-macroradioruminography of ^{28}Mg in normal mice[1-3]. In this study we conducted experiments on mice to obtain information on the effect of different dietary magnesium or calsium level on magnesium behavior.

The preparation of no-carrier-added ^{28}Mg (half-life 20.9h, β,γ) from a pure A1 target irradiated by an α-particle beam has been developed for its biological use. ^{28}Mg was synthesized following the method of R. Iwata et al[4]. Forty eight male ddy mice, weight 20-22g were randomly divided into four groups. Animals were fed for 6 days. The dietary magnesium or calcium level is shown in Table 1. Biodistribution studies of doubly labeled of ^{28}Mg, ^{45}Ca and whole body-macroradioluminography of ^{28}Mg were performed in mice. The tissues were wet ashed with nitric acid and perchloric acid in borosilicate test tube placed in a hot block bath. Magnesium and calcium were analyzed by an inductively coupled plasma atomoc emission spectrometer (ICP S-5000, Shimazu Co., Ltd., Kyoto, Japan).

Growth curves (Fig. 1) showed significantly lower gain in magnesium deficient groups (group 3, group 4) compared with magnesium sufficient groups. Organ weights are shown in Table 2. Figure 2 shows the radioluminographs of a mouse fed the diet varied with calcium-magnesium ratio 120 min after the injection of ^{28}Mg. The radioluminographs of a mouse fed the magnesium deficient diet (group 3 and 4) revealed high accumulation of ^{28}Mg in heart and gut compared with the other groups. Tissue distribution of doubly labeled ^{28}Mg and ^{45}Ca are shown in Table 3. ^{28}Mg had a significantly high accumulation in the heart, liver, small intestine and bone of group 3 compared with the other groups. The distribution of ^{45}Ca were not changed between four groups under this experimental conditions. Uptake ratio of $^{45}Ca/^{28}Mg$ are shown in Table 4. Magnesium and calcium concentrations in liver, heart, kidney, and bone are shown in Table 5-8. The magnesium concentration was significantly lower in liver and kidney of group 2, 3, and 4, in heart and

bone of group 4 than in these of group 1. The calcium concentration was significantly lower in liver of group 2 than in these of group 1. In contrast, its concentration was significantly higher in heart of group 4 in kidney of group 3 than in these of group 1.

Studies are in progress in our laboratory to investigate the possible mechanism under lying these changes of magnesium behavior in animals.

Acknowledgements

The authors appriciate the cooperation of the staff members of the Cyclotron and Radioisotope Center.

References

1) Kawamura M. et al., CYRIC Annual Report 1993, p136.
2) Kawamura M. et al., Biomed. Res. Trace Elements **4** (1993) 127.
3) Biryou Eiyouso Kenkyu, Mimeographycal Report in Japanese, **11** (1994) 171.
4) Iwata R. et al., J. Radioanal. Chem. Article, **159** (1992) 233.

Table 1. Experimental group.

Group	Diet		Data *(g / 100g of diet)	
	Mg	Ca	Mg	Ca
1	+	+	0.04	0.503
2	+	++	0.04	0.965
3	-	+	0.003	0.459
4	-	++	0.003	0.946

+ : adequate - : deficient ++ : double of adequate * : analyzed by inductively coupled plasma (SHIMAZU ICPS-5000)

Table 2. Organ weights of mice fed the diet varied with Ca-Mg ratio.

Group \ Organ	Liver	Heart	Lungs	Kidneys	Brain
1	1.06 ± 0.07	0.104 ± 0.003	0.058 ± 0.011	0.40 ± 0.02	0.43 ± 0.01
2	0.96 ± 0.02	0.097 ± 0.003 *	0.060 ± 0.004	0.36 ± 0.01	0.42 ± 0.01
3	0.84 ± 0.03 **	0.089 ± 0.003 ***	0.066 ± 0.007	0.41 ± 0.03	0.42 ± 0.02
4	0.84 ± 0.02 **	0.094 ± 0.004 *	0.091 ± 0.018	0.29 ± 0.01 ***	0.45 ± 0.02

Data are means± S.E. values from six mice
*P<0.05 compared with group 1
**P<0.01 compared with group 1
***P<0.001 compared with group 1

Table 3. Tissue distributions of ^{28}Mg in mice fed the diets varied with Ca-M.

	120 min (DAR)			
Tissue	Group 1	Group 2	Group 3	Group 4
Blood	0.43 ± 0.30	0.59 ± 0.02	0.39 ± 0.10	0.69 ± 0.44
Heart	2.08 ± 0.19	2.18 ± 0.39	2.79 ± 0.22*	2.59 ± 0.47
Lung	0.78 ± 0.12	0.79 ± 0.17	0.83 ± 0.14	0.83 ± 0.04
Liver	1.27 ± 0.18	1.21 ± 0.08	2.22 ± 0.07*	1.81 ± 0.44
Spleen	0.92 ± 0.03	0.98 ± 0.02	0.92 ± 0.12	1.04 ± 0.20
S.Intestine	1.55 ± 0.18	1.88 ± 0.13	2.35 ± 0.35*	2.13 ± 0.14
Kidney	2.30 ± 0.27	2.36 ± 0.36	2.49 ± 0.06	2.63 ± 0.54
Muscle	0.41 ± 0.08	0.41 ± 0.01	0.42 ± 0.05	0.64 ± 0.17
Bone	2.55 ± 0.48	2.47 ± 0.35	1.21 ± 0.03*	1.47 ± 0.19*
Brain	0.19 ± 0.01	0.20 ± 0.03	0.29 ± 0.02	0.30 ± 0.04

Data are means± S.E. values from three or four mice
*P<0.05 compared with control mice

Table 4. Tissue distributions of ^{45}Ca in mice fed the diets varied with Ca-l.

	120 min (DAR)			
Tissue	Group 1	Group 2	Group 3	Group 4
Blood	0.05 ± 0.08	0.04 ± 0.01	0.05 ± 0.02	0.03 ± 0.01
Heart	0.07 ± 0.01	0.07 ± 0.02	0.14 ± 0.04	0.05 ± 0.04
Lung	0.21 ± 0.03	0.32 ± 0.01	0.42 ± 0.13	0.23 ± 0.08
Liver	0.25 ± 0.15	0.34 ± 0.21	0.30 ± 0.17	0.17 ± 0.12
Spleen	0.08 ± 0.02	0.11 ± 0.05	0.09 ± 0.02	0.04 ± 0.02
S.Intestine	0.32 ± 0.08	0.65 ± 0.30	0.30 ± 0.07	0.12 ± 0.11
Kidney	0.24 ± 0.02	0.15 ± 0.03	0.33 ± 0.20	0.09 ± 0.08
Muscle	0.25 ± 0.13	0.22 ± 0.12	0.26 ± 0.09	0.29 ± 0.18
Bone	5.64 ± 2.07	4.75 ± 1.54	4.17 ± 0.08	4.52 ± 0.27
Brain	0.37 ± 0.18	0.21 ± 0.10	0.29 ± 0.19	0.14 ± 0.05

Data are means± S.E. values from three mice

Table 5. Uptake ratio of $^{45}Ca/^{28}Mg$ in mice fed the diets varied with Ca-Mg.

Tissue	Ratio *			
	Group 1	Group 2	Group 3	Group 4
Heart	3.56	3.31	3.44	2.46
Liver	2.72	2.41	2.62	2.08
Kidneys	2.49	3.10	4.49	2.85
Bone	199.40	167.4	1265.69	1242.48

$$*\text{Ratio} = \frac{\text{Ratio of tissue uptake } (^{45}Ca/^{28}Mg)}{\text{Ratio of injected solution } (^{45}Ca/^{28}Mg = 0.39)}$$

Table 6. Magunesium and calcium levels in liver.

Group	Mg (mg/g)	Ca (mg/g)	Ca/Mg
1	0.224 ± 0.005	0.128 ± 0.006	0.57
2	0.208 ± 0.007*	0.111 ± 0.007*	0.54
3	0.193 ± 0.010**	0.136 ± 0.013	0.70
4	0.207 ± 0.013*	0.122 ± 0.013	0.59

Data are means± S.E. values from six mice
*P<0.05 compared with group 1
**P<0.01 compared with group 1

Table 7. Magunesium and calcium levels in heart.

Group	Mg (mg/g)	Ca (mg/g)	Ca/Mg
1	0.178 ± 0.007	0.075 ± 0.010	0.42
2	0.171 ± 0.005	0.078 ± 0.009	0.45
3	0.165 ± 0.005	2.119 ± 1.252	12.81
4	0.160± 0.003*	0.750 ± 0.263**	4.68

Data are means± S.E. values from six mice
*P<0.05 compared with group 1
**P<0.01 compared with group 1

Table 8. Magunesium and calcium levels in kidneys.

Group	Mg (mg/g)	Ca (mg/g)	Ca/Mg
1	0.187 ± 0.002	0.109 ± 0.007	0.58
2	0.178 ± 0.005*	0.106 ± 0.009	0.59
3	0.147 ± 0.005***	1.763 ± 0.791*	12.01
4	0.170 ± 0.004***	0.112 ± 0.008	0.66

Data are means± S.E. values from six mice
*P<0.05 compared with group 1
***P<0.001 compared with group 1

Table 9. Magunesium and calcium levels in bone.

Group	Mg (mg/g)	Ca (mg/g)	Ca/Mg
1	1.562 ± 0.380	83.728 ± 19.196	53.61
2	1.609 ± 0.081	95.100 ± 4.185	59.12
3	0.991 ± 0.136	81.674 ± 8.381	82.38
4	0.870 ± 0.069*	82.831 ± 6.499	95.20

Data are means± S.E. values from six mice
*P<0.05 compared with group 1

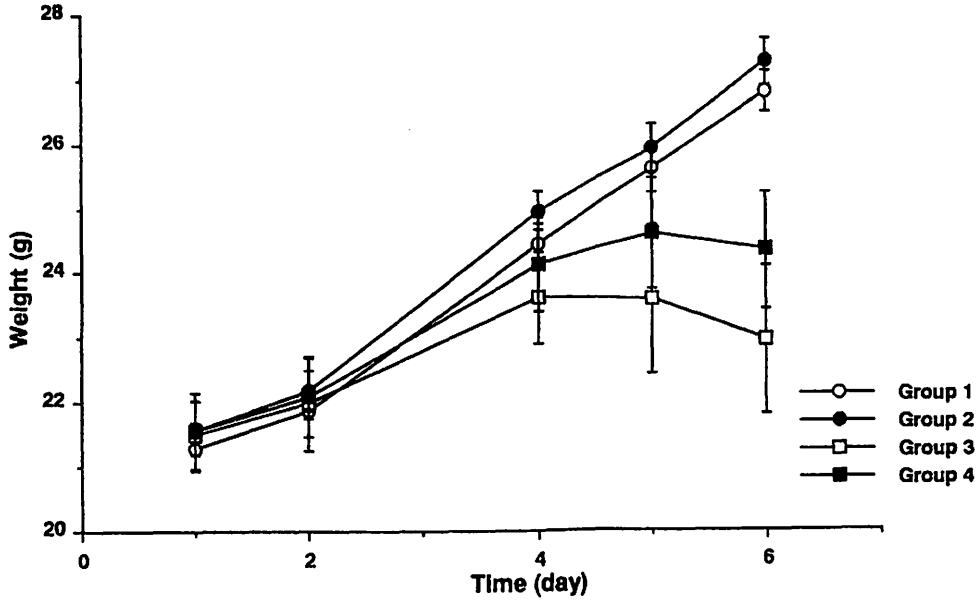

Fig. 1 Body weights of mice fed the diets varied with Ca-Mg ratio.

Group	Reg (mg/g)	Chr (mg/g)	Chr/Reg
1	0.12e + 0.00a	0.14e + 0.00f	0.86
2	0.16d + 0.01b	0.18d + 0.00e	0.89
3	0.19c + 0.01b	0.22c + 0.01d	0.86
4	0.23b + 0.01a	0.26b + 0.00c	0.88

Group	Reg (mg/g)	Chr (mg/g)	Chr/Reg
1	0.12e + 0.00a	0.14e + 0.00f	0.86
2	0.16d + 0.01b	0.18d + 0.00e	0.89
3	0.19c + 0.01b	0.22c + 0.01d	0.86
4	0.23b + 0.01a	0.26b + 0.00c	0.88

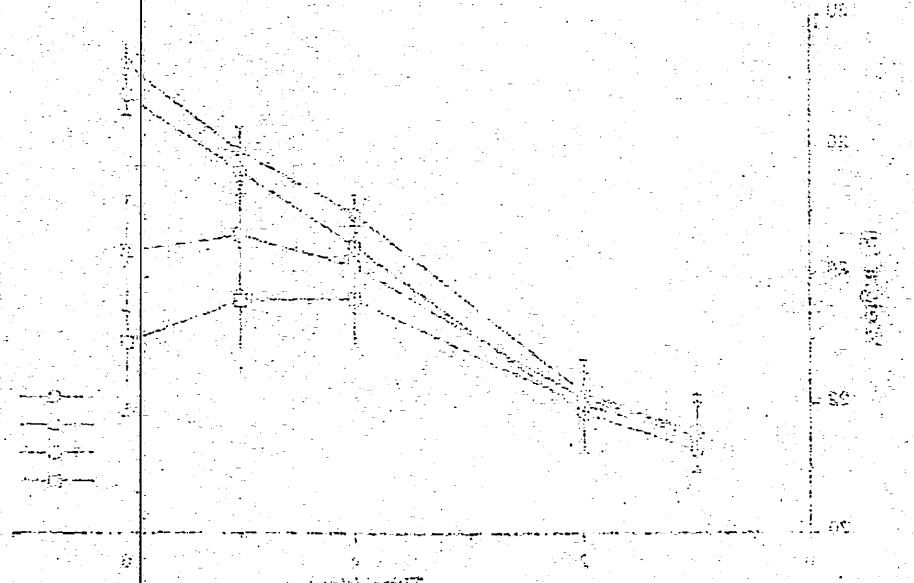

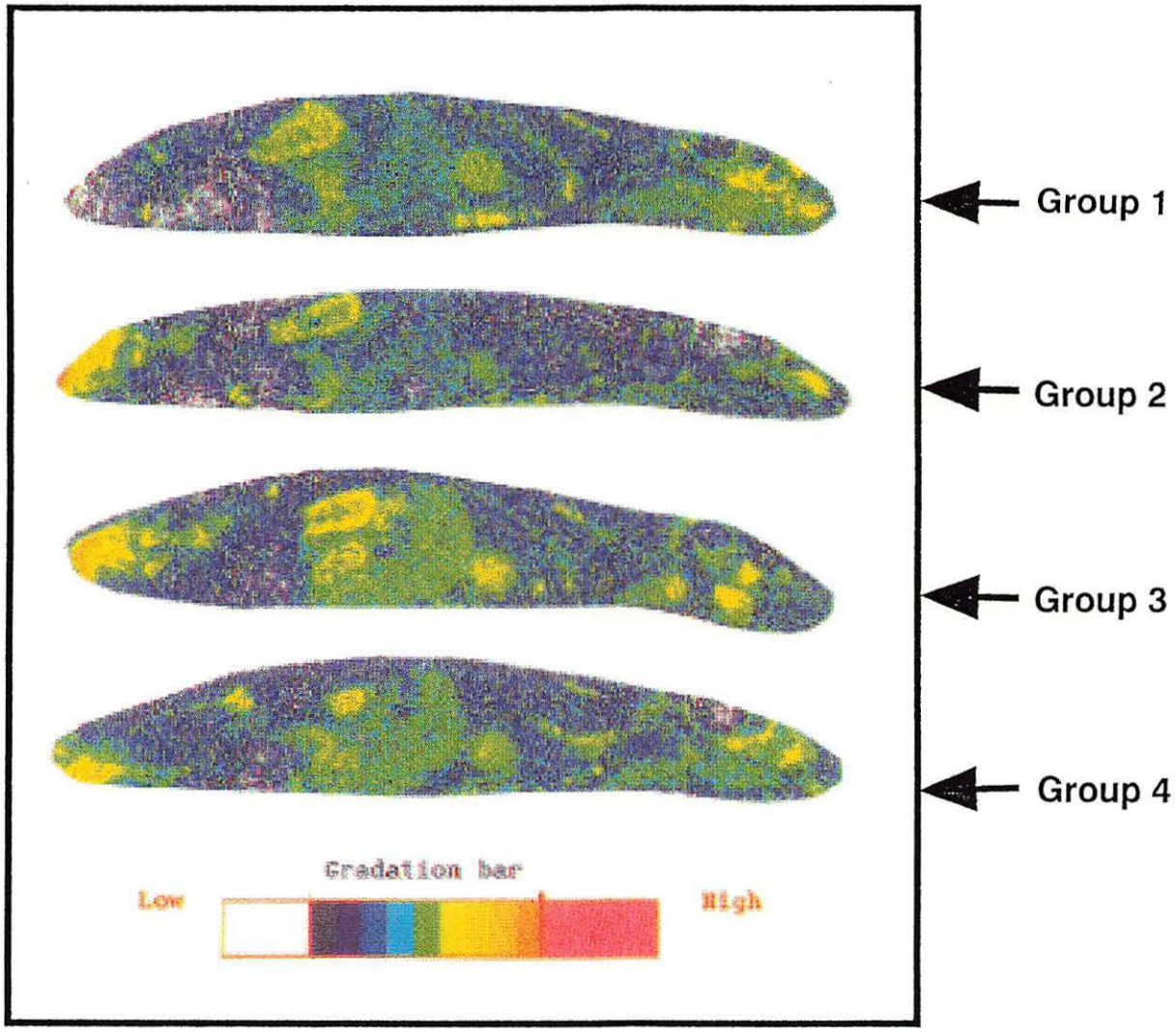

Fig. 2 Radioluminograms of ^{28}Mg in mice.

IV. MEDICINE (Clinical)

IV. 1. Comparative Study of Sample Extraction in Metabolite Analysis for Quantitative PET Studies

Nakagawa N., Yanai K., Fujiwara T., Iwata R. and Ido T.*

Cyclotron and Radioisotope Center, Tohoku University
*Department of Pharmacology I, School of Medicine, Tohoku University**

Introduction

Metabolite analysis of radiopharmaceuticals in plasma is an important factor for quantitative measurement in the PET study on neurotransmitter receptors which requires exact input concentrations of the radio-ligand[1,2]. The metabolite analysis has not been investigated in detail from the methodological point of view. Especially the interaction of radiopharmaceutical and its metabolites with plasma proteins should be re-examined.

In ordinary metabolite analysis, plasma protein is precipitated by an organic solvent[3] or lowering pH below 2[4]. Since the protein denaturation is unlikely to occur in vivo, the true concentration of radiopharmaceutical and its metabolites in plasma cannot be given by this conventional method. In addition, there is the possibility of over-estimating the free fraction of radiopharmaceutical due to compulsive separation of plasma bound drug from proteins by the protein denaturation.

Dialysis is known as an alternative separation method of drug and its metabolites from plasma protein. We determined free drug in human plasma by on-line dialysis using the automated sequential trace enrichment of dialyzate sample preparation[5]. Dialysis and ultrafiltration are the most widely used techniques for separation of a free drug from plasma protein. We compared the extraction efficiency by dialysis, ultrafiltration and the conventional method using methanol (MeOH) or perchloric acid ($HClO_4$).

Materials and methods

Human plasma samples were taken before the administration of [^{11}C]doxepin (^{11}C-DOX) or [^{11}C]benztropine (^{11}C-BZT). ^{11}C-DOX and ^{11}C-BZT were prepared as described previously.

Figure 1 shows a schematic diagram of the dialysis system used in this study. The system was equipped with a flat-bed dialyser (100μl donor channel volume, 175μl recipient channel volume) and a trace enrichment column (Hypersil ODS). The trace enrichment

column was packed with ODS (Hypersil). A donor solution was prepared by adding 0.01% Triton X-100 to saline. Saline was also used as the recipient solution.

Two parameters were determined in order to operate the dialysis system. A volume of 2450μl was used as a optimal enrichment volume which caused no breakthrough of the dialyzates. The plasma was dialyzed for 13.5 min to obtain an enough amount of the dialyzates for the subsequent analysis.

Ultrafiltration was performed with minicolumns molecular mass cut-off 30000 (Molcut II TK, Millipore Japan, Ltd.).

BZT was measured on a silica column (Radial PAK Resolve, 8×100mm, 10μm particle size, Waters) with a mixture of acetonitrile:0.01M diammonium hydrogenphosphate (60:40, v/v) at a flow rate of 4.0ml/min. An ODS column (Radial PAK NOVA C18, 8×100mm, 4μm particle size, Waters) was used for DOX with a mixture of acetonitrile:0.1M ammonium formate (45:55, v/v) at a flow rate of 1.5 ml/min. The HPLC eluate was monitored with a spectrophotometer at the UV length of 254 nm. DOX (50μM to 1mM) and BZT (70μM to 2mM) were spiked to each human plasma as carrier to detect the corresponding radioactive peaks of the labeled drugs and to make them pass through the membrane easily. As a conventional method, DOX and BZT were extracted with $HClO_4$[4] and MeOH[3], respectively.

Results and discussion

The comparison of the free fraction of DOX in the plasma by $HClO_4$ and dialysis extraction method is shown in Figure 2. The percentage of free fraction obtained by dialysis in human plasma at each concentration of DOX was calculated at 19.5±1.6% to 27.8±1.4%. The percentage in the supernatant obtained by $HClO_4$ extraction was 22.5±3.2% to 32.2±4.3%. Figure 3 shows the comparison of free fraction of DOX using ultrafiltration and $HClO_4$ extraction. The free fractions of ultrafiltration and $HClO_4$ extraction were 17.6±2.0% and 34.8±2.1%, respectively.

The free fractions of BZT in the plasma study are also shown in Figure 4 and Figure 5. The percentage of free fraction determined using dialysis method in human plasma was also calculated at 22.6±1.3% to 32.9±0.7% at each concentration. The percentage in the supernatant obtained by MeOH extraction was also 73.4±2.7% to 83.3±1.7%. The free fraction by ultrafiltration and MeOH extraction was 13.8±3.9% and 93.6±3.3%, respectively.

There was no significant differences of free fractions of DOX in the plasma determined by acid extraction, dialysis and ultrafiltration methods. On the other hand, marked difference was observed in the free fraction of BZT measured by methanol, ultrafiltration and dialysis method. It is assumed that the protein-bound fraction of drugs is not able to pass through the blood-brain barrier (BBB) and that the free fraction can penetrate through the BBB. Our data indicates that the free fraction of ^{11}C-ligands in the plasma

depends on the extraction methods. The methods of metabolites analysis should be re-examined in order to measure the binding of ^{11}C-ligands quantitatively.

References

1) Yanai K. et al., J. Neurochem. **55** (1990) 409-420.
2) Yanai K. et al., J. Neurochem. **59** (1992) 128-136.
3) DEWEY. S. L. et al., Synapse **5** (1990) 213-223.
4) HATANO K. et al, J. Nucl. Med. **30** (1989) 515-522.
5) ANDRESEN. A. T. and ERASMUSSEN K., J. Chromatogr **621** (1993) 189-198.

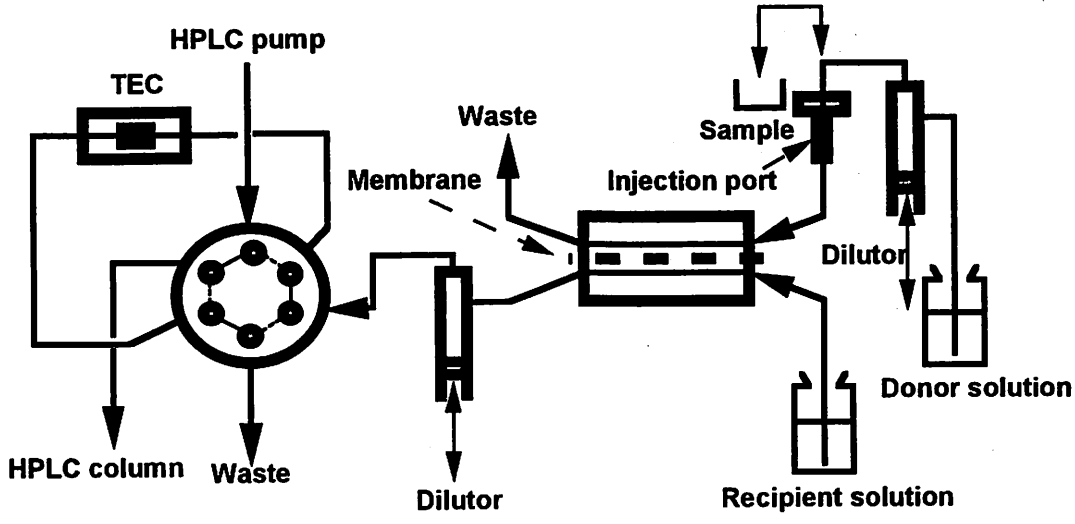

Fig. 1. Schematic diagram of the dialysis system.

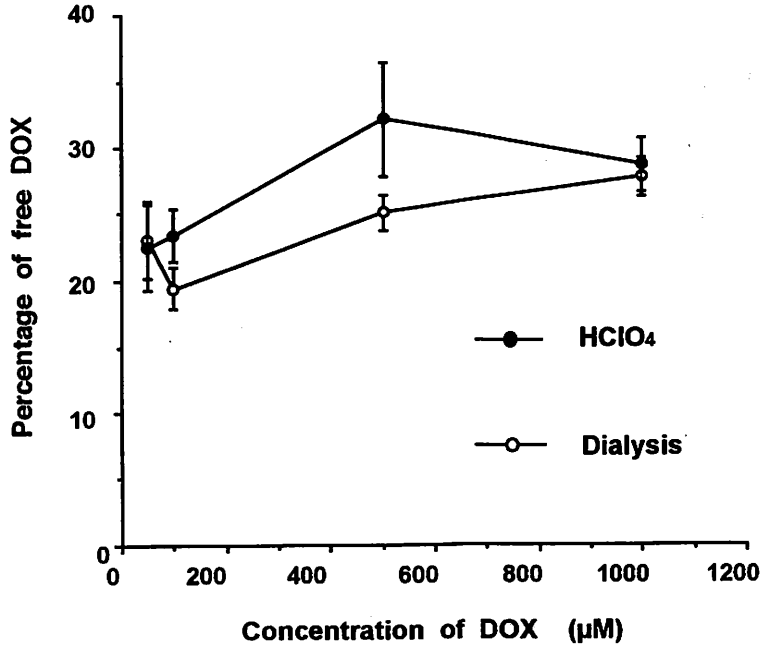

Fig. 2. The free fraction of DOX determined by $HClO_4$ and dialysis extraction methods in human plasma spiked with DOX. The two lines represent the observed values (mean ± S. E, n=3).

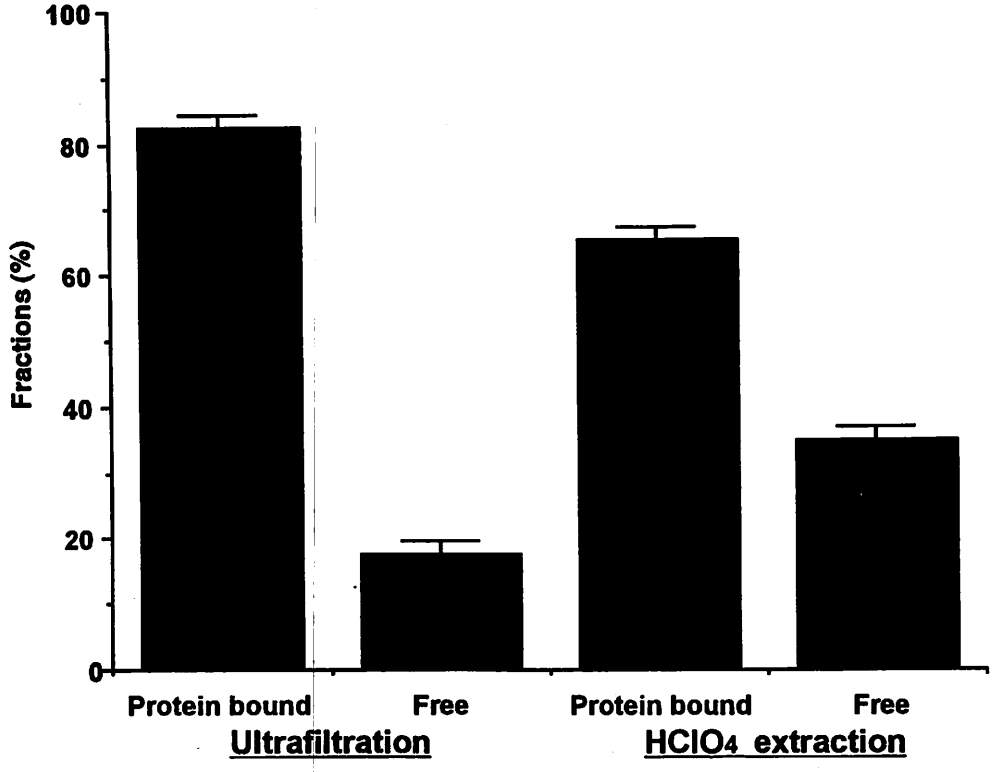

Fig. 3. The percentage of protein-bound and free fraction of DOX determind by ultrafiltration and $HClO_4$ extraction methods. These columns represent the observed values (mean ± S. E, n=3).

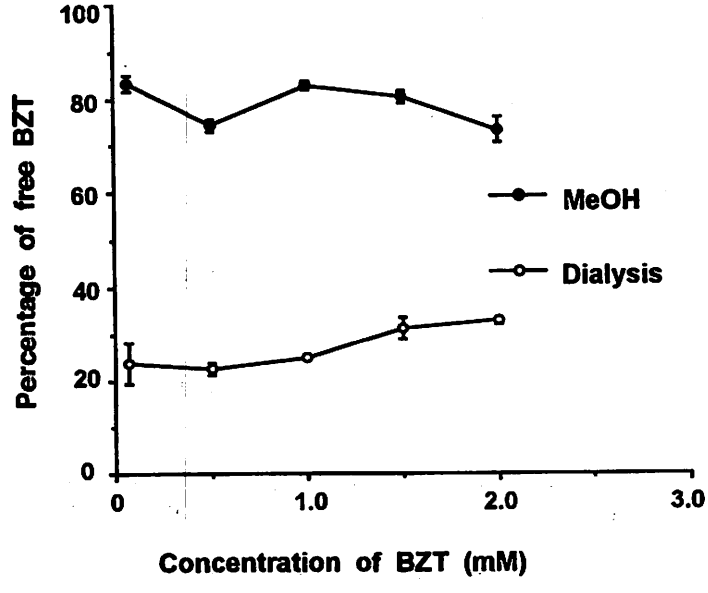

Fig. 4. The free fraction of BZT determind by MeOH and dialysis extraction methods in human plasma spiked with BZT. The two lines represent the observed values (mean ± S. E, n=3).

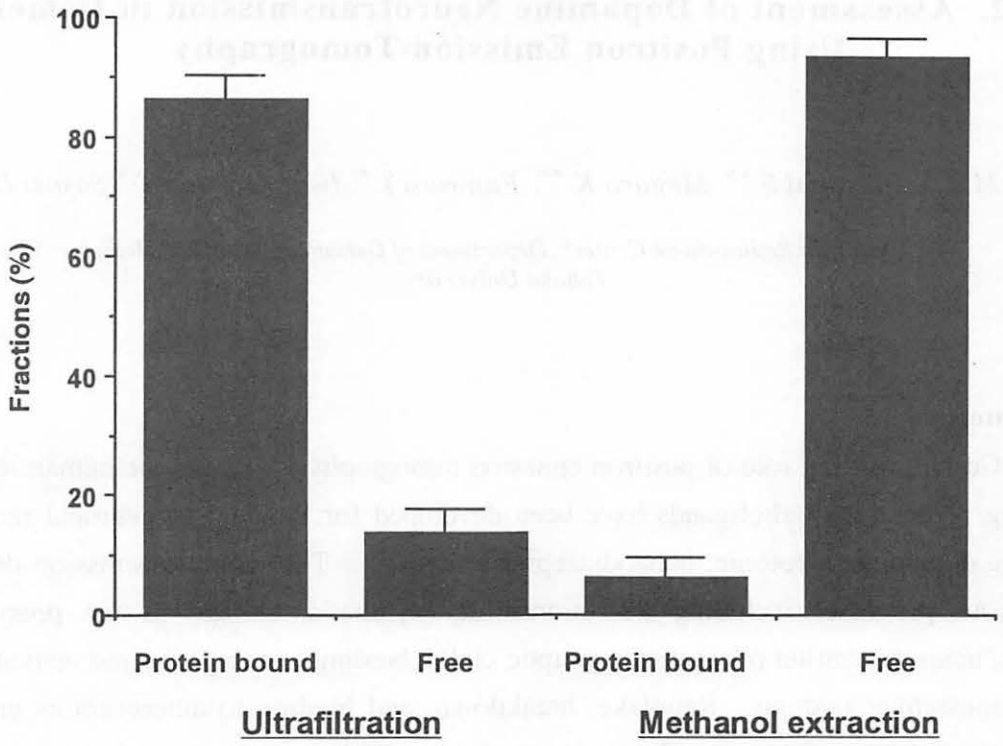

Fig. 5. The percentage of the protein-bound and free fractions of BZT determined by ultrafiltration and MeOH extraction methods. These columns represent the observed values (mean±S. E, n=3).

IV. 2. Assessment of Dopamine Neurotransmission in Dementia Using Positron Emission Tomography

Itoh M., Yamaguchi S.**, Meguro K.**, Fujiwara T.*, Iwata R.* Ido T.* Sasaki H.***

Cyclotron Radioisotope Center, Department of Geriatrics, School of Medicine, ** Tohoku University*

Introduction

Current leading role of positron emission tomography(PET) may be human receptor mapping. Numerous radioligands have been developed for imaging of neuronal receptors covering dopamine, serotonin, benzodiazepine and so on. The neurotransmission depends on various processes including neurotransmitter synthesis, storage in the presynaptic neurons, neurotransmitter release into synaptic clefts, binding to receptors, and activation of second messenger systems. Reuptake, breakdown, and binding to autoreceptors are also crucial for neurotransmission. Dysfunction of any single or complex of above process inevitably leads to neurological or psychological disorders. Parkinson's disease is a typical example of this type of dysfunction. Selective degeneration of dopaminergic neurons within pars compacta of the substantia nigra is the pathological process of this entity[1]. 6-[^{18}F]fluoro-L-dopa(FDOPA)[2], an analogue of L-dopa, is incorporated into dopaminergic nerve endings, converted to fluorodopamine[3] and stored in synaptic vesicles. Injection of FDOPA and PET measurement is a powerful tool to assess overall function of presynaptic dopaminergic neurotransmission[4]. Loss of FDOPA incorporation was demonstrated in Parkinson's patients[5]. Enhanced activity or supersensitivity of D2 receptors in such patients was also shown by PET[6].

Alzheimer's dementia is a progressive disease and its definitive diagnosis is only given at autopsy because of lack of clinical diagnosstic markers. There had been increasing interests in the neurochemical changes in dementia brain. Deficiencies in several transmitter systems such as acetylcholine (Ach), noradrenaline, dopamine (DA), serotonin, and some neuropeptides were reported[7]. Therefore in vivo measurement of neurotransmitter function by PET may be a possible clinical tool for dementia diagnosis. We discuss here altered dopaminergic neurotransmission in AD/SDAT and vascular dementia which was revealed by PET measurements.

Methods

DOPAMINE METABOLISM MEASUREMENT

6-^{18}F-L-FDOPA was synthesized according to the method described by Adam et al.[8]. Following an intravenous bolus injection of FDOPA to subjects, positron tomography was carried out by using PT931 (CTI Inc,USA) with 7 mm axial and transaxial resolution[9]. Emission scans were performed every 5 minutes for 60 min after injection. Tissue FDOPA concentration was measured defining ROIs on three image planes that included the striatum[10]. The influx rate (Ki) of FDOPA into the selected regions was then calculated employing the graphical analysis described by Patlak et al.[11,12]using concentration of the cerebellum radioactivity as the input function. A linear fitting was carried out using data between 25 and 60 min post FDOPA injection.

DOPAMINE RECEPTOR MEASUREMENT

Dopamine D2 receptor binding potenial was measured by using ^{11}C labeled benzamide derivative, N-[1-benzyl-2-methyl-pyrrolidinyl]-5-chloro-2-methoxyl-4-methylaminobenzamide, NMAB)[13,14]. A three compartment model was used for brain kinetics of NMAB. The influx of NMAB from capillary to brain parenchyma was expressed as Ki, a parameter including blood flow and permeability-surface area product for NMAB at BBB. Characteristic of specific bindings of NMAB was represented by k3, which is a bimolecular association constant of Bmax(receptor density) times kon, and k4, a dissociation constant. Nonlinear least square fitting of brain activity to the model estimates from the above parameters yielded estimation of the rate constants. The ratio of k3/k4 was used as an index of the D2 receptor function.

SUBJECTS

Studies were performed on thirty-two subjects over 50 years old including 11 normal subjects (6 males and 5 females; average age: 63.3 ± 9.2), 12 patients with Alzheimer's and senile dementia (AD/SDAT) (5 males and 7 females; average age: 67.0 ± 11.3) and 9 patients with vascular dementia (5 males and 4 females; average age: 74.1 ± 6.9). The diagnosis of dementia was based on DSM-III-R[15]. The dementia subtypes were judged mainly on the clinical profiles of symptoms, referenced to the Ischemic Score[16] and CT/MRI findings. The severity of the dementia was evaluated using the mini-mental state battery (MMS).

Results

The Ki of FDOPA influx into the striatum and other cortical regions (average of both sides) in normal subjects and two types of dementia were summarized in Figure 1 Two way ANOVA revealed Ki differed significantly between the striatum and all cortical regions (F-value = 155.3, $p<0.01$). Ki to the occipital cortex was negligible (0.00006 ± 0.00207 min^{-1}) and significantly smaller than the frontal and temporal cortex ($p<0.01$ by the multiple

comparison). The striatal Ki of the normal group was 0.0116 ± 0.0017 min^{-1} and showed no age-related decline (Ki = - 0.00003•Age ± 0.01333, r = -0.152). The striatal Ki differed significantly among study groups (F-value = 5.03, $p<0.01$, by ANOVA). Vascular dementia group showed reduced striatal Ki (0.0081 ± 0.0026 min^{-1}) than normals (0.0110 ± 0.0031 min^{-1}, $p<0.05$, by the multiple comparison). The multiple regression analysis revealed Ki could be predicted by age and dementia severity as evaluated with the mini-mental state as Ki = - 0.000046. Age + 0.000382•MMS + 0.008076 ($r^2 = 0.590$, $p<0.01$) for AD/SDAT and Ki = - 0.000088• Age + 0.000226•MMS + 0.010483 ($r^2 = 0.401$, $p<0.05$) for the vascular dementia. The MMS term in AD/SDAT was most significant with its t-value as 3.168 ($p<0.01$). The correlation analysis supported dependence of Ki on MMS (Figure 2).

NMAB uptake, assessed by the raio of the k3/k4, was 1.18 ± 0.96 for normal control, 2.28 ± 1.26 for AD/SDAT, and 5.74 ± 2.51 for vascular dementia. Student t-statistic revealed the vascular group had significantly higher binding potenials than the control ($p<0.01$). PET images of typical cases were shown in Figure 3.

Discussion

Dopaminergic neurons has not only crucial to motor regulation but a part of the system is linked to the neocortex and limbic brain[17]. The nucleus accumbence or the ventral striatum connects to the amygdala, ventral pallidum, thalamus, the limbic and premotor cortex and functions as an interface between the limbic and the motor system. It is thought to be related to the temporal control of behavior, reward-related learning and memory function[18]. The dopaminergic projections from A_{10} of the ventral tegmentum to the nucleus accumbens may play a mediating role for incentive motivation[19]. The striatal ACh neurons receive an input from extrinsic DA neurons of the mesencephalic tegmentum and give output to interneurons containing somatostatin/NPY, neurotensin or GABA. DA controls ACh-mediatedmediated transmission in an inhibitory manner through D2 receptors[20]. D2 receptor upregulation induced by a partial meso-diencephalic hemitransection in mice was counteracted by nicotine treatment[21]. These results confirms close interraction between dopaminergic and cholinergic system. It is reasonable to assume, therefore, that the dopaminergic system plays fundamental roles, in the process of higher brain function.

Postmortem studies revealed that there are some age-related reductions in the concentration of DA in the caudate nucleus in the group of patients older than 65[22]. PET observation of a normal aged population also found a gradual decline in FDOPA uptake with age[23]. However, a recent study opposed this age-related decline[24]. Our data support the latter observation. We reported stability of blood flow and oxygen metabolism in the neurologically normal populations up to 80 years of age[25]. Little change in FDOPA uptake in normal subjects supports well preserved homeostasis in brain metabolism in normal population. Disturbed DA metabolism in demented subjects, therefore, is hardly explained by the age-related reductions.

DA and HVA of human postmortem specimens were reported significantly reduced in AD/SDAT patients (for a review, see Gottfries, C. G.)[26]. The aromatic amino acid decarboxylase, an enzyme that catabolize L-dopa to dopamine, was reported to decrease in senile dementia[27]. Thus, DA metabolism must be disturbed in AD/SDAT especially at the final stage. In the case of vascular dementia, the concentration of DA also decreased in the caudate nucleus compared with the brains of age-matched controls[28].

Tyrrell, et al.[28] reported a greater variance in Ki values of FDOPA in the patients' group than in normal subjects despite of no significant changes in FDOPA uptake into the caudate and putamen in Alzheimer type dementia patients with extrapyramidal signs. Thus it was suggested that some AD/SDAT patients had lower FDOPA uptake compared to the normal subjects. It is noteworthy that mildly demented AD/SDAT patients had relatively higher FDOPA uptake in our study (Figure 2). This may explain the larger variance in Ki values and suggests increased dopamine metabolism in early course of the AD/SDAT. There are some reports about reciprocal activities between cortical and subcortical DA neurons. Underactivity of the frontal cortical DA system may result paradoxically, in overactivity of the subcortical DA projection (see review by Robbins TW)[29]. Although precise reason for DA hyperactivity in our early AD/SDAT patients is not known, it may reflect a disturbed neuronal function including the striatal DA system.

Intercorrelation between level of dopamine metabolism and D2 receptor function in our study was not straightforward (Figure 4). Diminished DA synthesis might be partly compensated by upregulation of D2 receptors in vascular dementia subjects. However, D2 receptor function varied rather independently from the level of dopamine metabolism in AD/SDAT subjects. Reduction of dopamine synthesis as well as D2 receptor function seen in a part of AD/SDAT patients which may reflect hypoactivity of DA neurotransmission. The other patients showed hyperactivity of both DA synthesis and D2 receptors. These data support heterogeneity of AD/SDAT[30] and PET assessment of DA function may predict outcome of neuroleptic treatments for dementia symptoms.

References

1) Bernheimer X., Birkmayer W., Homykiewicz O., Jellinger K, Seitelberger F. J. Neurol Sci 20: 515- 455, 1973.
2) Gamett E. S., Firnau G., Chan P. K. H., Sood S., Belbeck L., Proc Natl. Acad. Sci. USA 75: 464-467, 1978.
3) Horne M. K., Cheng C. H., Wooten G. F., Pharmacology 28: 12-26, 1984.
4) Garnett E., S., Firnau . G, Nahrnias C., Nature 305:137-138,1983.
5) Garnett E., S., Nahrnias C, Firnau G., Can J Neurol Sci 11: 174-179, 1984.
6) Rinne U. K., Laihinen A, Rinne J. O, et al. Movement Disorders 5: 5S-59, 1990.
7) Nordberg A., Cerebrovasc Brain Metabol Rev 4:303-328, 1992.
8) Adam M., J., Abeysekera B., Ruth T., J, Grierson J., R,. Pate BD., J Nucl Med 26: 125, 1985.
9) Watanuki S., Ishii K., Orihara H., Fukuda H., Matsuzawa T., CYRIC Annual Report 1986: 250-244,.1986.
10) Itoh M, Meguro K, Fujiwara T, Hatazawa J, et al. Ann Nucl Med 8:248-251, 1994.
11) Patlak C. S., Blasberg RG. J Cereb Blood Flow Metabol 5:584-590, 1985.

12) Patlak CS, Blasberg R. G., Fenstermacher J. D., J Cereb Blood Flow Metabol 3 :1-7, 1983 .
13) Hatano K., Ishiwata K, Kawashima K, et al. J Nucl Med 30:515-522, 1989.
14) Hatazawa J, Hatano K, Ishiwata K, Itoh M, Ido T, et al. J Nucl Med 32: 713-718, 1991.
15) American Psychiatric Association. Amer Psychiat Ass, Washington DC, USA, pp103-122, 1987.
16) Hachinski VC, IliffLD, Zilka E, DuBoulay GH, et al. Arch Neurol 32:632-637, 1975.
17) Scatton B, Zivkovic B. Psychopharmacology ofthe limbic system. Trimble MR & Zarifian E (eds). Oxford University Press, Oxford, ppl74-197, 1984.
18) Salamone JD. The mesolimbic dopamine system:from motivation to action. Willner P, Scheel Krueger J (eds) John Wiley & Sons, Chichester pp599-614, 1991.
19) Gray JA. Neurobiology of learning, emotion and affect, Madden J (ed). Raven, N. Y., pp273306, 1991
20) Di Chiara G, Morelli M, Consolo S. TINS 17(6)228-232, 1994
21) Janson AM, Hedlund PB, Fuxe K, Von Euler G. Brain Res 655:25-33, 1994.
22) Carlsson A, Winblad B. J Neural Transm 38:271-276, 1976.
23) Leenders KL, Salmon EP, Turton D, Tyrrell P, et al. Arch Neurol 47, 1290-1298, 1990.
24) Taldkawa S, Dahwan V, Chaly T, Robeson W, et al. J Cereb Blood Flow Metab 13:S410, 1993.
25) Itoh M, Hatazawa J, Miyazawa H, Matsui H, et al. Gerontology 36: 43-48, 1990
26) Gottfriies CG. J Neurosci Res 27:541-547, 1990.
27) Bowen DM, Smith CB, White P, Davison AN. Brain 99: 459-496, 1976.
28) Tyrrell PJ, Sawle GV, Ibanez V, Bloomfield PM, et al. Arch Neurol 47:1318-1323, 1990.
29) Robins TW. The mesolimbic dopamine system:From motivation to action, Willner P, Sheel-Krueger (edts), Jon Wiley & Sons, Chichester, pp497-528, 1991.
30) Mayeux R, Stern Y, Spanton S. Neurology. 35:453-461, 1985.

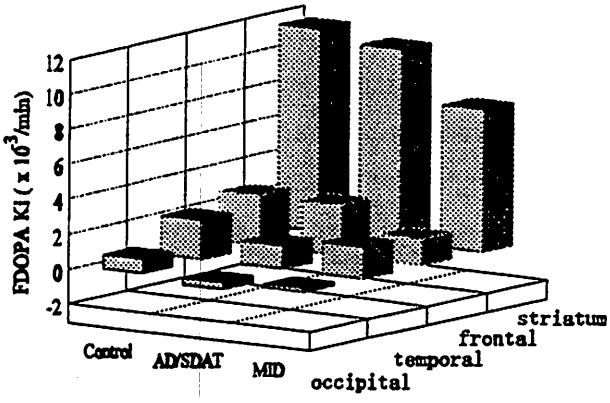

Fig. 1. The mean FDOPA influx rate (min^{-1}) into the brain regions in control, AD/SDT, MID groups. The columns represent the striatum, frontal cortex, temporal cortex, occipital cortex from right to left.

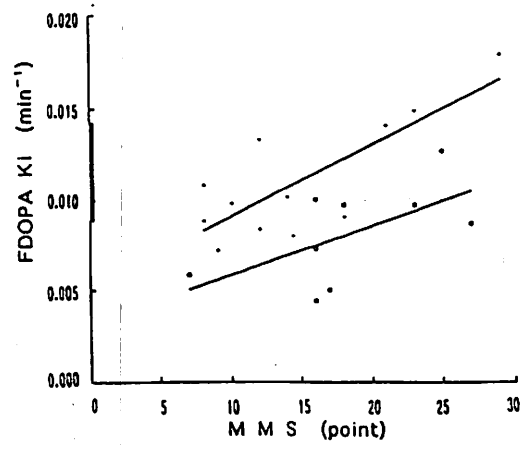

Fig. 2. Correlation of FDOPA Ki into the striatum with dementia severity as assessed by mini-mental state battery (MMS points, abscissa) in MID(□) and AD/SDAT(■). The values are averages of right and left striatum. From Itoh M, et al.[10]

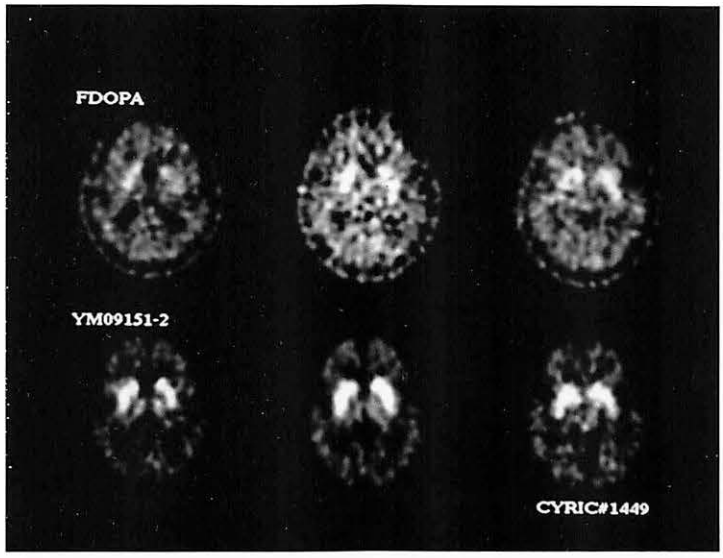

Fig. 3. Uncoupling of FDOPA influx into the striatum (upper row) and dopamine D2 receptor activity (bottom row) in a vascular dermentia case.

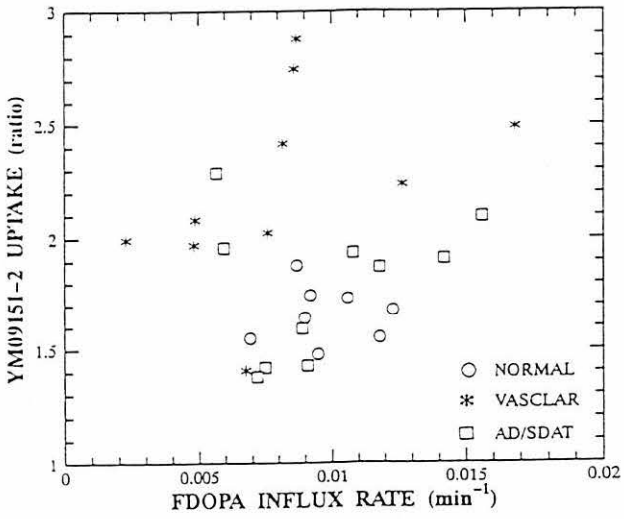

Fig. 4. Scatter diagram comparing FDOPA influx rate (abscissa) into the striatum and dopamine D2 receptor function in dementia. The values for the right and left striatum are separately plotted.

IV. 3. Less Invasive Method for Accurate CMRglc Measurement

Ono S., Koyama M., Goto R., Ito H., Kawashima R., Seo S., Watanuki S.*, Ito M.*, and Fukuda H.*

Department of Nuclear Medicine and Radiology, Institute of Development, Aging, and Cancer, Tohoku University
Cyclotron and Radioisotope Center, Tohoku University.*

Introduction

In order to investigate brain glucose metabolism quantitatively, now we are supposed to perform ^{18}F-FDG PET study with frequent arterial blood sampling. The aim of this study was to reduce the frequency of blood sampling for measurement of cerebral metabolic rate for glucose (CMRglc) with the autoradiography (ARG) method in the ^{18}F-FDG PET method by utilization of standardized plasma time activity curves (TACs) and calibration of those TACs by the actual plasma radioactivity. In the preliminary study, we obtained a result of 0.93 as the correlation coefficient and less than 20% as the errors between the original and the developed method[1]. In this article, we will show the improved results by optimization of the methods of plasma-calibration.

Subjects and Methods

Twenty three volunteers (age 19 to 81 average 48.7 y.o.) who gave a written informed consent were involved in this study and it was approved by the Research Ethics Committee of the Tohoku University School of Medicine. From randomly selected 11 cases, standardized plasma TACs were produced. Other data analysis of CMRglc calculated from the plasma-calibrated standardized as well as the original plasma TACs was performed on all of those 23 subjects.

The subjects were laid in the supine position on a bed of the PT931/04 PET scanner (CTI) with their eyes closed. The angle of the scans were adjusted along the orbitomeatal (OM) line and the center of the imaging volume was set to OM +56mm. We obtained 7 continuous PET images of the 8 mm thickness (Full Width at Half Maximum). We injected them intravenously with ^{18}F-FDG (107.3 to 259.0 MBq) in the 1 minute extended bolus fashion. After 10 minutes transmission scan for absorption correction, dynamic emission scanning was started. However in this study, we used the 10 minutes emission scan of 45 minutes after start only. Also, frequent arterial blood sampling was carried out from a small catheter inserted into their right brachial artery at every 15 seconds in the first 2 minutes with

gradually increasing intervals. Those blood samples were centrifuged immediately into plasma and the plasma samples were weighed and counted to make the plasma TACs. We calculated CMRglc from that 10 minutes scan of 45 minutes after and from the original and the plasma-calibrated standardized TACs with the ARG method of Sokoloff et al.[2] and Phelps et al.[3]. The rate constant K_1 used was 0.102 ml/g/min, k_2 0.130 /min, k_3 0.062 /min, and k_4 0.0068 /min. We employed the value 0.42 as the lumped constant.

Eleven plasma TACs were standardized by the factors of the injected FDG dose alone or that with the body weight. We optimized the methods of calibration of those standardized TACs by plasma radioactivity, using the time integrals of those TACs (AUC) by error and regression analysis of AUCs of the standardized and original TACs. Then CMRglc images of 23 subjects were calculated using those plasma TACs of selected calibration. We placed spatially equal one large region of interest (ROI) on them and compared the ROI values from those standardized plasma TACs (Y) with the original (X) by correlation coefficients (r) or coefficients of variation (COVs).

Results and Discussion

Figure 1 shows an example of the original and the standardized TACs with and without plasma-calibration. If only with restoration of the standardized TACs by the individual standardization factors and without plasma radioactivity calibration, the standardized TACs were far from the original TACs and they could not produce reliable values of CMRglc. After the plasma radioactivity calibration, the standardized TACs became relatively close to the original TACs and they were supposed to produce more reliable CMRglc values. By one point calibration, we obtained the best result at 14 minutes of all 8 investigated sampling points (peak, 5, 10, 14, 20, 29, 39, 45 minutes); Y=0.978X+0.158 r=0.980. In two points calibration by adding radioactivity at different two points, the best result was Y=0.923X+0.447 r=0.981 (10 and 29 minutes). In two points calibration by dividing TACs into two parts at 10 minutes and calibrating the first and latter parts individually, the best result was Y=0.998X-0.016 r=0.990 (5 and 29 minutes). By this method, the mean and maximum COV was 1.7 and 6.0%, respectively. From those results, we concluded that the frequency of blood sampling can be reduced for CMRglc measurement with the ARG method into once or twice.

References

1) Ono S. et al., CYRIC Annual Report **1993** (1994) 218.
2) Phelps M. E et al., Ann. Neurol. **6** (1979) 371.
3) Sokoloff L et al., J. Neurochem. **28** (1977) 897.

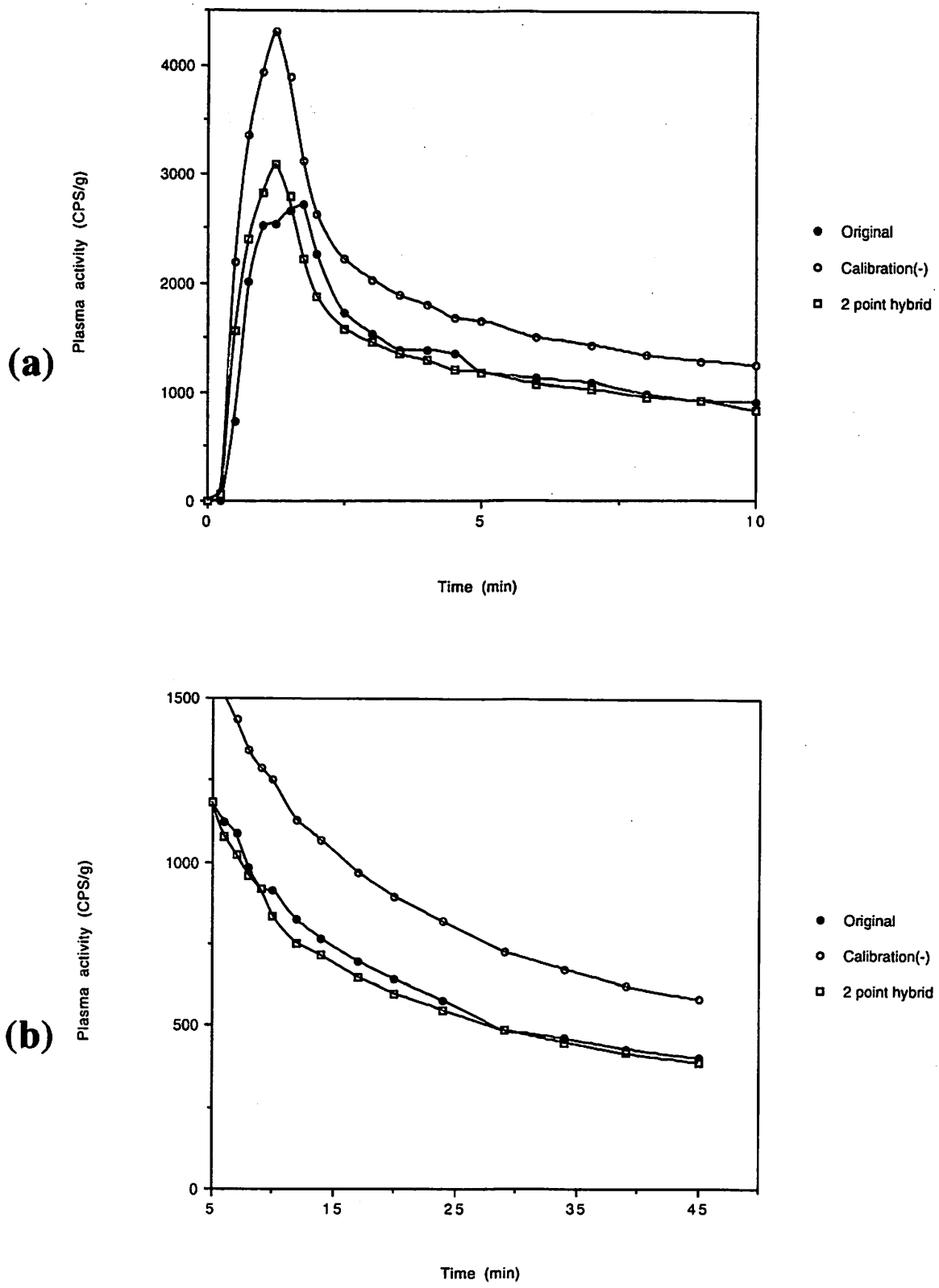

Fig. 1a An example of the original and the standardized TACs with and without plasma-calibration. (a)First part. (b)Latter part. If only with restoration of the standardized TAC by the individual standardization factor (in this case, the injected dose alone) and without plasma radioactivity calibration, the standardized TAC was far from the original TAC. After the plasma radioactivity calibration (in this case, the two points hybrid type calibration of 5 and 29 minutes after injection), the standardized TAC became relatively close to the original TAC and it was supposed to produce more reliable CMRglc values.

IV. 4. Mediastinal Tumors Studied with Positron Emission Tomography

Kubota K., Yamada S., Kondo T., Yamada K.,** Fukuda H., Fujiwara T.,*** Ito M.,*** and Ido T.,****

Department of Nuclear Medicine and Radiology, Institute of Development, Aging and Cancer, Tohoku University
*Department of Thoracic Surgery, Institute of Development, Aging and Cancer, Tohoku University**
*Sendai Kosei Hospital,***
*Cyclotron Radioisotope Center, Tohoku University****

Introduction

Mediastinal masses include a wide variety of tumors, and remain an interesting diagnostic challenge for radiologists. Computed tomography (CT) has proved to be an excellent diagnostic tool for investigating the mediastinum[1,2]. The CT demonstration of fat, calcium or water attenuation in a tumor often suggests a specific diagnosis. However, the ability of CT in differentiating soft tissue mediastinal masses is limited due to a considerable overlap in the CT characteristics between malignant and benign tumors[3,4].

Positron emission tomography (PET) has proved excellent in detecting malignant tumors of the central nervous system and non-CNS tumors[5]. Both 2-deoxy-2-fluoro-[^{18}F]-D-glucose (FDG) and L-[Methyl-^{11}C]methionine (Met) have been used with PET for the diagnosis of head and neck, breast, and lung cancers, while FDG has also been used in detecting liver tumors and pancreas cancer. To our knowledge, the use of FDG and Met in primary mediastinal tumors has not yet been evaluated. In order to predict the malignant nature of these tumors preoperatively, we performed PET studies using FDG or Met, and compared the results with the pathological diagnosis and the results of CT examination.

Materials and Methods

The study protocol was approved by the Ethics Committee for Clinical Research of Tohoku University and informed consent was obtained from each patient.

A total of 28 patients (mean age: 48 ± 20 (±SD), range: 14-83, 16 women and 12 men) with mediastinal tumors were studied with PET imaging. Nineteen patients had anterior, 5 patients had middle, and four patients had posterior mediastinal tumors. None received chemo- or radiotherapy before the PET study. Histologic diagnosis was confirmed

in all patients after the PET study by surgical pathology (18 patients) or biopsy (10 patients), and the histological diagnosis was compared with results of the PET study.

Twenty-two patients were studied with FDG while Met was used in seven patients (one patient had both FDG and Met-PET studies). After fasting for five hours, the blood glucose level was measured before the injection of FDG or Met. PET scans were performed using PT931/04 scanner (Siemens-CTI, Knoxville, TN). After a transmission scan, a bolus dose of FDG or Met was injected intravenously. The mean dose of FDG was 4.3 ± 0.8 mCi (159.1 ± 29.6 MBq) while that of Met was 19.7 ± 7.0 mCi (728.9 ± 258.0 MBq). Dynamic images were obtained first, followed by a 10 min static image which was acquired 40-50 min after injection of FDG or 30-40 min of Met. The tumor ROI, including the highest radioactivity point, was set on the static image. To avoid contamination of the non-tumor area, the tumor ROIs were checked carefully by superimposing both on transmission images and on the early post injection images, which showed vascular structures.

Eight muscle ROIs, located in the tumor slice, were placed in the paravertebral muscles bilaterally, shoulder, lateral and anterior chest wall muscles, as described previously[6]. The mean radioactivity per pixel within the tumor and muscle ROI was quantitatively analyzed by calculating the differential uptake ratio (DUR, synonym; standardized uptake value; SUV), as reported previously[6]. This involved expressing the radioactivity concentration in ROI relative to the injection dose and body weight. We also calculated the tumor to muscle radioactivity ratio (T/M). Students' *t* -test was used for statistical analysis.

Results

A high FDG uptake was clearly observed in nine of ten patients with malignancies, and also in one patient with sarcoidosis. A moderate level of FDG uptake was observed in benign thymomas, a myeloma and schwannoma, while a low FDG uptake was detected in a teratoma and various benign cysts. The mean FDG uptake was significantly higher in malignant tumors compared with that of benign tumor, using either DUR or T/M ratio (Table 1). However, the FDG uptake of muscle and blood glucose level in malignant tumors were not significantly different from those in benign tumors. Examples of typical PET images of thymic cancer (Figure 1) is presented.

Although the number of patients studied with PET and Met was small, the results of these studies were similar to those using FDG. Thus, malignant tumors showed a high Met uptake while benign tumors had a low Met uptake but statistically not significant. The muscle Met uptake and blood glucose levels in malignant and benign tumors were similar (Table 1).

The distribution of DUR in malignant and benign tumors with FDG and Met is shown in Figure 2. The use of FDG and Met enabled differentiation of most malignant tumors from benign tumors based on DUR analysis. However, an overlap between malignant and benign

tumors was evident. FDG tended to provide a better distinction between malignant and benign tumors compared with Met.

Our analysis demonstrated the presence of a significant linear correlation between the T/M ratio and DUR ($r=0.9896$, $p<0.001$) (Figure 3). Although the mean DUR in muscles examined with FDG (0.79 ± 0.07, $n=18$) was slightly lower than that with Met (0.90 ± 0.06, $n=7$), the correlation between T/M ratio and DUR with FDG was not significantly different from that with Met.

Discussion

The major finding of the present study is that the distribution of FDG or Met uptake in malignant mediastinal tumors, revealed by PET, was significantly higher than that in benign tumors. These results are in agreement with those reported recently on the excellent diagnostic performance of PET in differentiating the malignancy of lung nodules using FDG-PET[6]. The present results are also consistent with FDG-PET studies of other tumors, including breast[7] and pancreatic tumors[8]. These results suggest that the high uptake of FDG seems to be a general feature of a variety of cancers. Increased FDG uptake may reflect the high activity of hexokinase and glucose transport[9].

Calculation of the glucose metabolic rate using FDG based on the Sokoloff's model has been applied to oncology PET, mostly to brain tumor studies[10]. However, such method requires arterial blood sampling and estimation of the lumpt constant. Determination of the latter in individual tumors is impossible in humans. More simple evaluation methods without blood sampling, such as DUR or tumor/normal tissue ratio, have been recently introduced. The clinical value of these parameters has been demonstrated in several oncology studies. The use of DUR and tumor/muscle radioactivity ratio in the present study confirmed the presence of a significant linear relationship between the two parameters in benign and malignant tumors.

The level of FDG uptake of tumors is related to the grade of malignancy in brain and soft tissue tumors[10,11]. Furthermore, it has also been used as a prognostic indicator of malignancy in gliomas[12]. The FDG uptake by the tumor also correlates with the cell density in gliomas of grade 2 and 3[13]. Results of experimental studies indicate that the uptake of FDG is related to the number of viable cancer cells in vitro[14], and the amount of viable tissue in vivo[15]. FDG uptake varies also with the histologic differentiation of human abdominal tumors transplanted in nude mice[16]. In this regard, recent studies from our laboratory indicate that FDG uptake by cancer cells is higher in G_0/G_1 and G_2 phases of the cell cycle compared with the S and M phases[17], and that tumor growth rates correlated with the FDG uptake of tumors[18]. These results suggest that the uptake of FDG by mediastinal tumors may represent a biological marker of the clinical behavior of these tumors.

In conclusion, PET, particularly in combination with FDG, seems to be useful in the evaluation of malignancy in primary mediastinal tumors.

Acknowledgement

The authors thank Mr. Sugawara for photography, Mr. Watanuki and Mr. Seo for PET operation, and to the staff of the Cyclotron and Radioisotope Center, Tohoku University, for their assistance. We also thank Dr. F. G. Issa (Word-Medex) for his assistance in reading and editing the manuscript. This work was supported by grants-in-aid (06454320, 06670899) from the Ministry of Education, Science and Culture, Japan.

References

1) Davis R. D. Jr, Oldham H. N. Jr, Sabiston D. C. Jr., Ann. Thorac. Surg. **44** (1987) 229.
2) Brown L. R. and Aughenbaugh G. L., Am. J. Roentgenol **157** (1991) 1171.
3) Rendina E. A. et al., Thorax **43** (1988)441.
4) Rebner M. et al.,Computerized Radiol **11** (1987) 103.
5) Strauss L. G. and Conti P. S., J. Nucl. Med. **32** (1991) 623.
6) Kubota K. et al., J. Nucl. Med. **31** (1990)1927.
7) Adler L. P. et al., Radiology **187** (1993) 743.
8) Bares R. et al., Radiology **192** (1994) 79.
9) Haberkorn U. et al., Nucl. Med. Biol. **21** (1994) 827.
10) Di Chiro G., Invest. Radiol. **22** (1987) 360.
11) Adler L. P. et al., J. Nucl. Med. **32** (1991) 1508.
12) Patronas N. J. et al., J. Neurosurg. **62** (1985) 816.
13) Herholz K. et al., J. Neurosurg. **79** (1993) 853.
14) Higashi K., Clavo A. C., and Wahl R. L. J Nucl Med **34** (1993) 414.
15) Kubota K., Kubota R., Yamada S., J Nucl. Med. **34** (1993) 419.
16) Yoshioka T. et al., J. Nucl. Med. **35** (1994) 97.
17) Kubota R. et al., J. Nucl. Med. **35** (1994) 1067.
18) Kubota R. et al., J. Nucl. Med. **36** (1995) 484.

Table 1. FDG or Met uptake by benign and malignant mediastinal tumors.

	Tumor DUR	Muscle DUR	T/M ratio	Glucose (mg/dl)
FDG				
Malignant (10)*	7.15±2.27†	0.85±0.10‡	8.34±2.47†	101±9‡
Benign (12)	1.80±1.24	0.81±0.14	2.31±1.75	97±15
Met				
Malignant (4)	6.31±2.33‡	0.89±0.05‡	7.19±2.93‡	95±10‡
Benign (3)	2.93±0.97	0.90±0.08	2.97±1.41	86±15

Mean±s.d. *: number of patients. Glucose: blood glucose level.
†: $p<0.001$ compared to benign tumors.
‡: not significant compared to benign tumors. (Students' t-test)

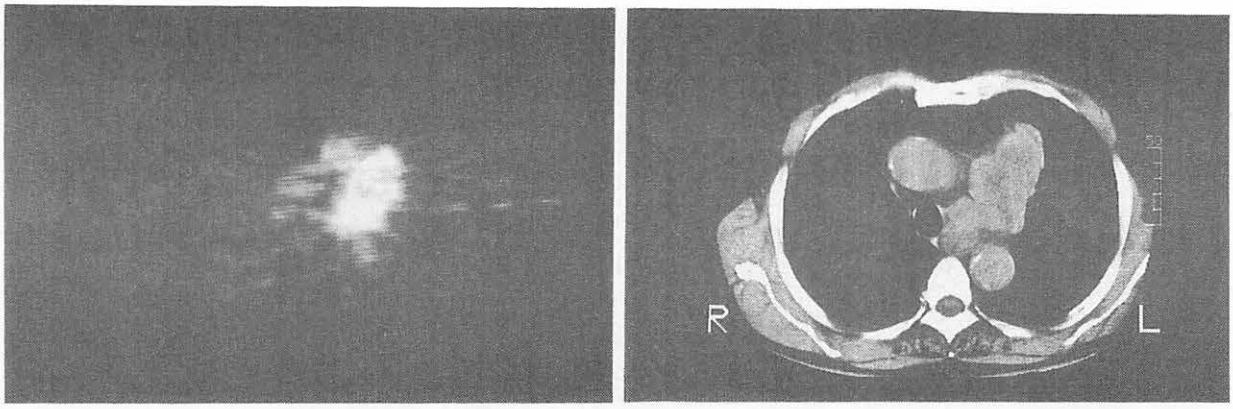

(a) (b)

Fig 1. A typical FDG-PFT image (a) and CT (b) of a thymic cancer. Fourty to fifty min after injection of 4 mCi (148 MBq) of FDG, showing an increased FDG uptake by tumor (DUR: 7.22).

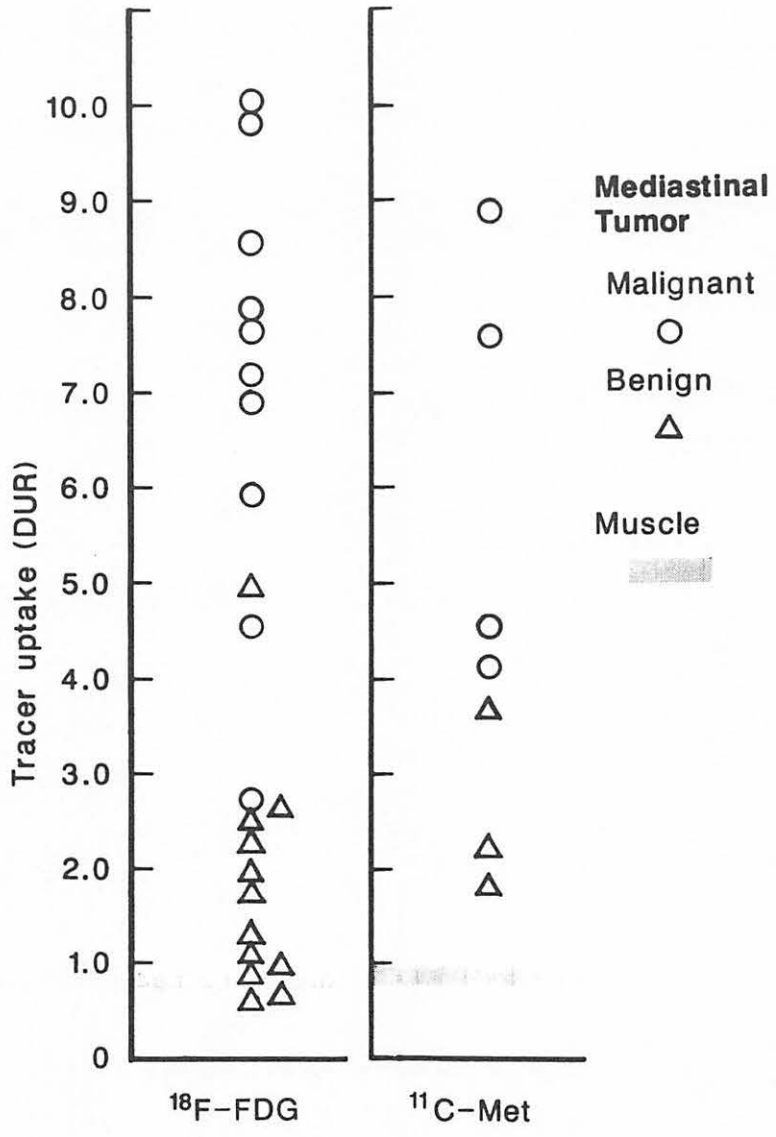

Fig 2. The distribution of DUR of FDG (left column) and Met (right column) in malignant (circle) and benign (triangle) primary mediastinal tumors. The standard deviation of muscle uptake of each tracer is shadowed in the graph.

Malignant
Benign
Malignant
Benign
0.0
0.2
0.4
0.6
0.8
1.0
0
0.1
0.2
0.3
0.4
0.5
0.6
0.7
0.8
0.9
1.0

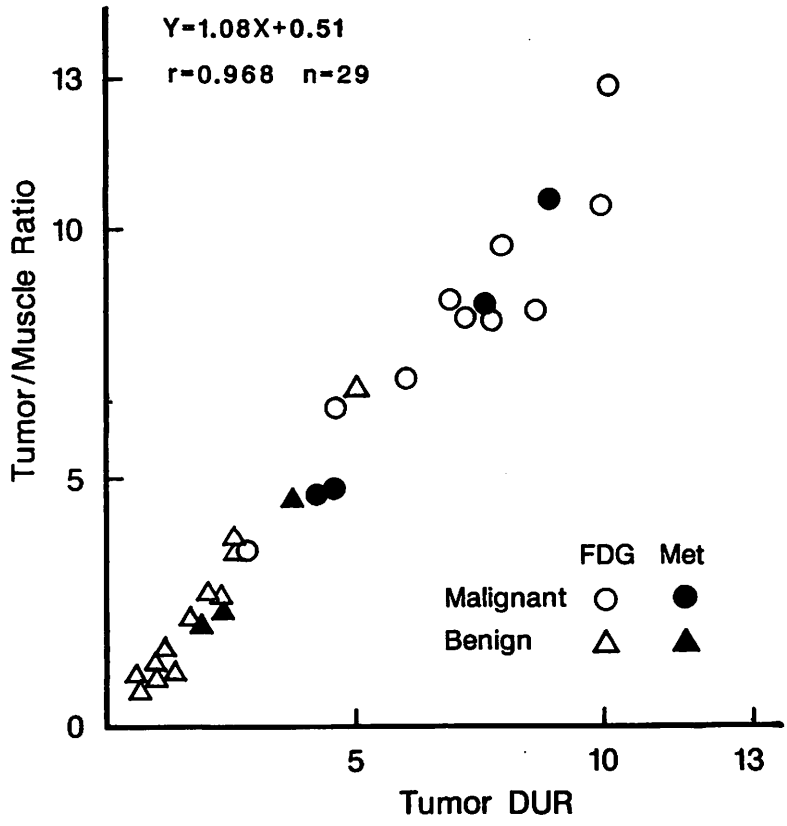

Fig 3. The correlation of tumor DUR and tumor/muscle ratio using FDG (open symbol) and Met (closed symbol) in primary mediastinal tumors. The tumor/muscle ratio increased linearly with DUR ($Y=1.08x+0.51$, $r=0.968$, $n=29$, $p<0.001$).

IV. 5. Effects of Hyperglycemia on Myocardial FDG Uptake

*Kubota K., Kubota R., Yamada S., *Tada M., **Takahashi T., **Iwata R.,*

Department of Nuclear Medicine and Radiology, Institute of Development, Aging and Cancer, Tohoku University
*Molecular Neurology, Institute of Development, Aging and Cancer, Tohoku University**
*Cyclotron Radioisotope Center, Tohoku University***

PET using 2-deoxy-2-[^{18}F]fluoro-D-glucose (FDG) has become a valuable method for the evaluation of various myocardial diseases[1]. In myocardial imaging with FDG, the increase in myocardial uptake of FDG after glucose loading has been well known. After glucose loading, the increase in insulin levels coupled with the decrease in FFA shifted the metabolic fuel of myocardium from fatty acid to glucose, resulting in an increase in FDG uptake[1-3]. Under fasting, distribution of FDG in myocardium is not uniform, that becomes homogeneous after glucose loading[4]. However, under severe hyperglycemia in diabetic patients, a defect in myocardial glucose utilization and non-uniformity of FDG distribution has been reported[5]. Exact correlation of myocardial FDG uptake and hyperglycemia is not clear. In order to study the effects of hyperglycemia on myocardial FDG uptake in vivo, FDG uptake in vivo was studied using rats under various pre-treatments which induce hyperglycemia.

Materials and methods

The experimental protocol was approved by the Laboratory Animal Care and Use Committee of Tohoku University.

Young male Donryu rats weighing (140-180g) were used for radioisotope study after various pre-treatments which may be expected to modify the blood glucose level. The control rats (n=48) were fasted for 12 hr. The glucose loading group (n=42) was given an oral ingestion of 0.6 ml of 50% glucose 15 min before the radioisotope injection. Also 8 other treatments were performed as shown in Table 1. Stereptozotocin (Szt) and dehydroascorbic acid have been known to induce experimental diabetes[6]. Dexamethasone (Dex), triiodothyronine and epinephrine have been known to induce hyperglycemia clinically. Ascorbic acid as the comparison to the dehydroascorbic acid, and dipyridamole as a popular coronary dilator were also included.

After various hyperglycemic treatments, rats were intravenously injected of 1.11MBq of FDG and killed 1hr later. Blood samples, myocardium, and skeletal muscle from thigh

were excised, weighed and radioactivity was measured using an automated gamma counter. Serum samples were separated and stored at -20 °C. The glucose level was measured by glucose oxidase method using an autoanalyzer. FDG uptake was expressed as differential uptake ratio (DUR)

$$DUR = \frac{\text{Sample radioactivity/Sample weight}}{\text{Injection dose/Body weight}}$$

Results

Table 1 shows the effects of pre-treatments on the blood glucose level. Treatments of ascorbic acid and dipyridamole showed no significant differences from the control. Glucose loading, dehydroascorbic acid, triiodothyronine, epinephrine and Szt-2 induced moderate level of hyperglycemia (significantly higher than the control, $p<0.001$). Szt-1 and Dex induced severe hyperglycemia (significantly higher than the glucose loading, $p<0.001$).

Figure 1 shows FDG uptake and serum glucose level. Myocardial uptake of FDG increased along the increase in serum glucose level from about 100mg/dl until about 200mg/dl. Thereafter, myocardial FDG uptake dropped suddenly and became almost constant irrespective of the serum glucose level. Skeletal muscle uptake of FDG also showed the same pattern, blood level of FDG was almost constant.

Discussion

At the moderate level of hyperglycemia (lower than 200 mg/dl), myocardial uptake of FDG was increased along the increase of glucose level. Dehydroascorbic acid has been known to induce hyperglycemia in vivo[6] and to inhibit brain uptake of glucose[7]. It increased FDG uptake by myocardium. Enhanced cardiac glucose utilization under hyperthyroidism has been induced by the secondary changes in glucose-lipid interaction at the tissue level rather than the changes in glucose transporter expression[8]. In this study, triiodothyronine induced moderate hyperglycemia and increased FDG uptake by myocardium in vivo. Epinephrine stimulated translocation of glucose transporter into plasma membrane of muscle[9]. In this study, moderate hyperglycemia and increased FDG uptake by myocardium was induced by epinephrine the same as that by glucose loading. Each treatment has been reported to induce hyperglycemia by each different mechanism. However, considering the effects of these treatments on the myocardial uptake of FDG, FDG uptake is simply increased along the increase in blood level of glucose.

In severe hyperglycemia, myocardial FDG uptake was dropped and became almost constant around 1.8-0.7 (DUR) independent of the glucose level. There must exist some specific change of glucose metabolism or transport at the level of 200 mg/dl. A shift of metabolic fuel from glucose to fatty acid, or impairment of glucose metabolism or transport may explain this low FDG uptake of myocardium under severe hyperglycemia.

Glucocorticoid suppressed myocardial glucose extraction in vivo[10], and Dex reduced skeletal muscle glucose uptake[11]. Dex-induced insulin resistance in rat skeletal muscle was not due to suppression of glucose transporter gene expression, and possible failure of translocation of glucose transporter-4 (GLUT4) containing intracellular vesicles to plasma membrane was suggested[11]. Szt is known to induce experimental diabetes due to selective destruction of the pancreatic β cells[6]. Several studies indicated that glucose uptake in heart and skeletal muscle was reduced in Szt-induced diabetes[12]. Recently, a dissociation of reduced glucose uptake rates and unaltered levels of GLUT 4 at early stage (7 days) of the Szt diabetes has been observed and impaired glucose transporter translocation or activity was suggested[13]. The reduced FDG uptake by myocardium and skeletal muscle under severe hyperglycemia induced by Dex or Szt treatments might be explained by reduced transport of glucose.

Irrespective to its mechanisms, our observation that myocardial FDG uptake showed two-phase correlation to the blood glucose level seems to be useful knowledge for FDG-PET imaging of myocardium under various disease or medication which may alter blood glucose level.

Acknowledgment

We are grateful to the staff of the Cyclotron and Radioisotope Center Tohoku University for their cooperation; and to Mr. Y. Sugawara for photography; and to Prof. H. Fukuda and to Prof. T. Ido for their support. This work was supported by grant-in-aid (04557047, 06454320, 06670899) from the Ministry of Education, Science and Culture, Japan.

References

1) Schwaiger M. and Hicks R. J. Nucl. Med **32** (1991) 565.
2) Yamada K. et al., Eur. J Nucl. Med. **10** (1985) 341.
3) Knuuti M. J. et al., J. Nucl. Med. **33** (1992) 1255.
4) Gropler R. J. et al., J. Nucl. Med. **31** (1990) 1749.
5) Voipio-Pulkki L. M. et al., J. Nucl. Med. **34** (1993) 2064.
6) Rerup C. C., Pharmacol. Rev. **22** (1970) 485.
7) Mooradian A. D. Diabetes **36** (1987) 1001.
8) Sugden M. C. et al, Biochem. J. **286** (1992) 513.
9) Bonen A. et al., Biochem. Biophys. Res. Comm. **187** (1992) 685.
10) Wahlqvist M. L. et al,. In: Tajuddin M. et al., ed. Advances in Myocardiology, Volume 2. Baltimore: University Park Press, (1980) 39.
11) Haber R. S. and Weinstein S. P. Diabetes **41** (1992) 728.
12) Kahn B. B. and Flier J. S. Diabetes Care **13** (1990) 548.
13) Kahn B. B. et al, J. Clin. Invest. **87** (1991) 2197.

Table 1 Effects of treatments on serum glucose.

Treatment		No. of rats	Glucose (mg/dl)*
Control		48	105±13
Glucose loading	50%, 0.6 ml p.o.	42	176±41†
Dehydroascorbic ac.	100mg i.p.	5	173±31†
Ascorbic ac.	100mg i.p.	7	104±14
Dipyridamole	3mg i.p.	7	102±8
Streptozotocin-1	6mg i.v.	6	393±64†§
Streptozotocin-2	4mg i.v.	10	165±14†
Dexamethasone	1mg s.c.×6	34	308±82†§
Triiodothyronine	10μg p.o.×3	7	152±8†
Epinephrine	50μg i.p.	7	163±6†

*: Mean±SD.

†: $p<0.001$ compared to the control (Student's t-test).

§: $p<0.001$ compared to the Glucose loading and the Dehydroascorbicacid.

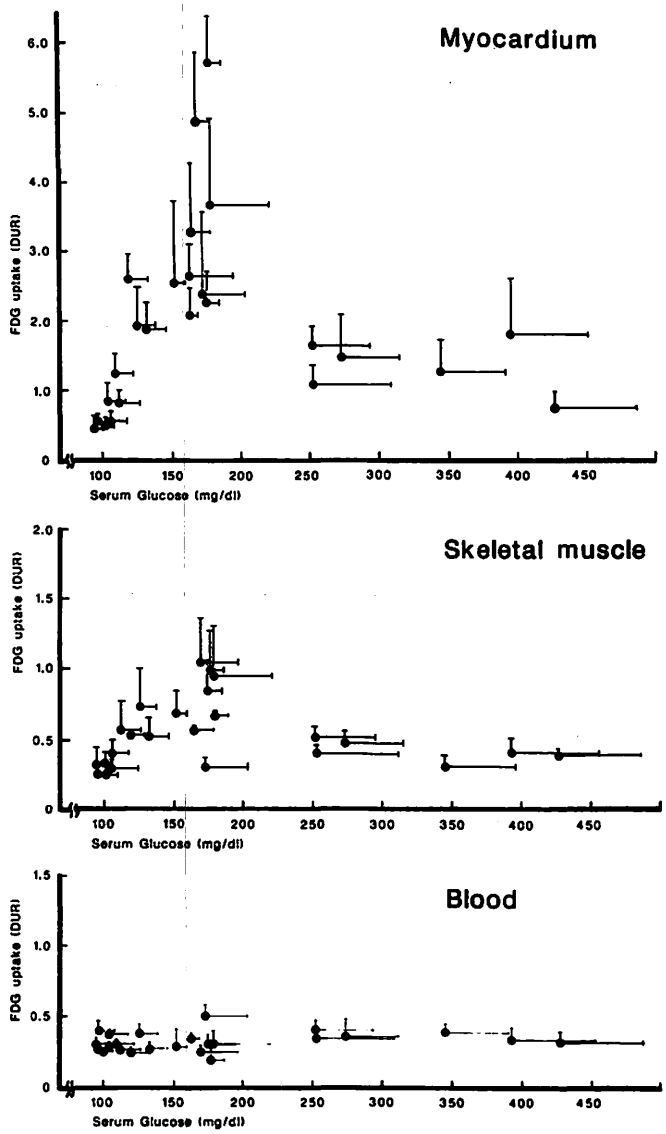

Fig. 1 FDG uptake by myocardium (A), and by skeletal muscle from thigh (B) correlated with the serum glucose level. Blood level of FDG (C) was almost constant. Each point represent mean and SD of 5 ~ 8 rats data. Data were obtained 60 min after injection of FDG, after various pre-treatments listed in Table 1.

IV. 6. Imaging of Hepatocellular Carcinoma Metastases with [F-18] Fluorodeoxygalactose: A Preliminary PET Study

Fukuda H., Yamaguchi K., Takahashi J., Kiyosawa M.**, Yoshioka S., Fujiwara T.***, Itoh M.***, Tada, M.****, Iwata R.*** and Ido T.****

Department of Nuclear Medicine and Radiology, Institute of Development, Aging and Cancer, Tohoku University
*Department of Radiology, Ryukyu University School of Medicine**
*Department of Opthalmology, Tokyo Medical and Dental University School of Medicine***
*Cyclotron and Radioisotope Center, Tohoku University****
*Department of Molecular Neurology, Institute of Development, Aging and Cancer, Tohoku University*****

Introduction

[F-18] fluorodeoxygalactose (^{18}FDGal), a positron labeled galactose analog, is phosphorylated by galactokinase, as is D-galactose, but trapped in the tissue after the second uridylation step of the metabolic pathway[1,2]. Therefore, ^{18}FDGal can be used for the evaluation of galactose metabolism in vivo using positron emission tomography[3,4]. The relevant metabolic enzymes occur in almost all tissues, but the hepatocyte has by far the greatest activity so that highest uptake of the tracer occurs in the liver[3-5], allowing its use as a liver specific tracer.

We earlier reported that uptake of ^{18}FDGal is very high in well differentiated hepatomas of mice and rats but very low in their poorly differentiated counterparts or in cancers other than hepatomas[5]. These results suggest that hepatomas originating from hepatocytes preserve galactose metabolic activity and point to a potential of this liver specific tracer for imaging and characterization of hepatocellular carcinomas (HCCs) using PET.

In the present investigation, a PET study with ^{18}FDGal was performed on 3 patients with extrahepatic metastases from HCC and their uptakes were compared to those of lung cancers.

Materials and Methods

PATIENTS

Table 1 gives a brief description of the patients examined in this study. Three HCC patients with extrahepatic metastases, respectively in the right orbit, sternal bone and 4th lumbar vertebrae and 5 lung cancer patients were examined. Diagnosis of HCC was determined based on the histology of materials taken at biopsy, the findings of X-ray CT , echogram and angiography as well as α-fetoprotein values. Histopathological diagnosis were

determined using biopsy specimens or operated materials and obtained from all patients except case 3 (HCC).

Informed consent for the present PET study was obtained in written form from each patient and approved by The Committee for Clinical Application of Radioactive Substances at Tohoku University.

PET STUDY

Seventy-four to 148MBq of ^{18}FDGal were injected intravenously into the patients. For HCC cases, sequential scans of the primary liver tumor site were performed every 5 min for 40-50 min. In the third case, a liver tumor scan was not available because the tumor had already been controlled by transarterial embolization. After the liver scan, one scan of the metastatic tumor site was added. As regions of interest (ROI), primary liver tumors and metastatic tumors were chosen.

For lung cancer cases, sequential scans were performed in the same way as for HCC cases and one scan added if metastases to the mediastinal lymphnode existed outside the scan field. Radioactivities measured in the region of interest for each image were expressed as differential absorption ratios (DAR).

Results

Table 1 summarizes data for uptakes of the tracer in the tumors at 40-60 min. The range of DAR values in HCC metastases was from 7.2 to 14.7. The uptakes of the primary liver tumors in case 1 and case 2 were 15.9 and 13.1, respectively. The primary liver tumor in case 3 was treated by transarterial embolization (TAE) and therefore a tumor scan could not be made at the time of the PET study. While the uptakes in lung cancers were 1.6-3.0 and very low compared to the HCC values. However, because of high tumor-to-background ratios (2.2-4.6), all these lung tumors could be clearly visualized.

Discussion

In a previous paper, we reported very high ^{18}FDGal uptake in a well differentiated spontaneous hepatoma of C3H mice and in the 5123D Morris hepatoma but only low values in poorly differentiated mouse and rat hepatomas (MH129P, AH109A, AH272) and tumors other than hepatomas (B-16 melanoma, FM3A mammary carcinoma)[5]. In the present study, we examined the potential clinical application of ^{18}FDGal for the imaging of metastases from HCCs.

We have also described in congress report that ^{18}FDGal uptakes in HCCs are very high compared to those in metastases to the liver from other cancers[8,9]. Although ^{18}FDGal uptake in HCCs were very high, the tumors were nevertheless visualized as cold lesions in most cases because the uptakes were even higher in the surrounding parenchyma. Consequently, tumor uptake values had been overestimated by partial volume and spillover

effects. In this study the matastatic HCC investigated were located in extrahepatic regions where background uptake was very low, and thus the values can be considered reliable since tumor size was large enough for a high recovery coefficient.

The uptakes of ^{18}FDGal were very high and comparable not only in primary tumors (15.9 and 13.1 by DAR) but also in metastases of HCCs (7.2-18.2), with the values being 30-77% of that for normal liver[4]. Lung cancers, in clear contrast, all demonstrated significantly lower values (1.6-3.0). The fact that the tumor uptake in case 2 was relatively low might be due to 20 Gy irradiation to the tumor before the PET study. Since ^{18}FDGal uptake decreases after by radiation in animal tumors (our unpublished data).

From the results of our clinical PET study, we speculated that not only the primary tumor but metastatic tumor of HCCs examined in this study maintained substantial activity of galactose metabolism, while the lung cancers, which origin is not hepatocells had only little activity of the metabolism.

In conclusion, ^{18}FDGal is a potential useful tracer for the detection of HCC metastases and differential diagnosis from cancers other than HCC. Using tissue specific tracers, characterization of the specific tumor can be performed as described in this paper, and this provide a powerful another approach with PET in oncology.

References

1) Ishiwata K. et al., Nucl. Med. Biol. 1988; 15:271-276.
2) Ishiwata K. et al., Nucl. Med. Biol. 1989; 16:247-254.
3) Fukuda H. et al., Eur. J. Nucl. Med. 1986; 11:444-448.
4) Fukuda H. et al., Jpn. J. Nucl. Med. 1987; 24:871-874.
5) Fukuda H. et al., Carbohydr Res. 1987; 161:314-317.
7) Fukuda H. et al., Jpn. J. Nucl. Med. 1987; 24:165-169.
8) Fukuda H. et al., J. Nucl. Med. 1987; 28:706.
9) Fukuda H. et al., Tumor Diagnostik & Therapie 1988; 9:171.

Table 1. Uptake of ^{18}FDGal in the tumor and background tissues.

Case No	Age/Sex	Diagnosis	Uptake (DAR) at 40-60 min		
			primary tumor	metastatic tumor	background tissue
1	51/M	HCC	15.9	14.7 (right orbit)	0.52 (left orbit)
2	52/M	HCC	13.1	7.2a (sternum)	0.70 (chest wall)
3	60/F	HCC	b	18.2 (L4)	0.50 (chest wall)
4	41/M	lung cancer (large cell)	1.61	_	0.75 (chest wall)
5	66/M	lung cancer (sq. cell)	1.66	_	0.45 (chest wall)
6	75/M	lung cancer (adeno)	1.95	_	0.65 (chest wall)
7	62/M	lung cancer (adeno)	3.03	_	0.75 (chest wall)
8	75/M	lung cancer (sq cell)	2.33	_	0.51 (chest wall)

a: 20 Gy irradiated by the time of PET study. b: a primary liver tumor scan was not available because the tumor had been treated and controlled by transarterial embolization, DAR: differential absorption ratio=Tissue activity / (injected activity/body weight), M=male, F=female, HCC=hepatocellular carcinoma, L4=4th lumbar vertebrae

IV. 7. Evaluation of TRH Therapy in a Patient with Spinocerebellar Degeneration by Measuring Glucose Metabolism with Positron Emission Tomography

Tanji H., Nagasawa H., Hayashi T., Onodera H., Itoyama Y., Itoh M., and Ido T.**

Department of Neurology, Tohoku University School of Medicine
*Cyclotron and Radioisotope Center, Tohoku University**

Introduction

Thyrotropin releasing hormone (TRH) has been used for treatment in patients with spinocerebellar degeneration (SCD). Positron emission tomographic (PET) study of SCD has revealed that the regional metabolic rate for glucose was decreased in the cerebellum[1-3] and degree of hypometabolism was correlated to the clinical severity of SCD[2-3]. In the present study, we measured cerebral metabolic rate for glucose (CMRGlc) in a patient with SCD using 2-[^{18}F]fluoro-2-deoxy-D-glucose (^{18}FDG) and PET in order to evaluate the effect of TRH therapy.

Patient and method

PATIENT

A 56-year-old female developed slowly progressive gait instability and speech disturbance for 2 years. There was no remarkable past illness or family history of SCD. On admission in 1994, neurological examination revealed saccadic eye movement, horizontal nystagmus, ataxic speech, moderate truncal ataxia and marked incoordination in four limbs with no pyramidal and extra-pyramidal tract signs, but involuntary movement or dementia were not observed. The general laboratory data, thyroid function, tumor markers and cerebro-spinal fluid examination were normal. Nerve conduction velocities in four limbs and electroencephalogram were also normal. Gallium scintigraphy of the whole body showed no abnormality. MRI revealed marked atrophy in both cerebellar hemispheres and vermis, and slight atrophy in the brainstem (Figure 1).

METHOD

The patient was diagnosed as sporadic type of SCD by her clinical symptoms and MRI findings. For the treatment, 2.0 mg of TRH was administered intravenously everyday. Regional CMRGlc of the brain was measured by PET using ^{18}FDG before and 3 weeks after the TRH treatment.

The study was approved by the Research Ethics Committee of the Tohoku University, School of medicine. The patient gave her written informed consent.

PET study was performed with a model PT-931 scanner (CTI Inc., USA), according to the FDG method[4-5] at the Cyclotron and Radioisotope Center, Tohoku University, Sendai, Japan. Before the study, a short 21-gauge cannula was placed in a brachial artery under local anesthesia for arterial blood sampling. The patient was then positioned in the scanner, with the orbitomeatal (OM) line parallel to the detector ring. A cross of light was projected onto markes on her head from three dimensions, and the head was set at the standard points of 16, 63 and 110 mm above and parallel to the OM line. The study was conducted in a quiet, semi-darkened room. Before the emission scanning, a 15-min transmission scan using a ^{68}Ge-^{68}Ga external ring source was performed. ^{18}FDG was synthesized according to the method of Ido et al.[6]. ^{18}FDG (96.2 MBq 1 st study, 115.4 MBq 2nd study) was injected as an intravenous bolus. Thirty to 60 min after the injection, a series of three emission scans was performed by using a PT-931 with an 8 mm axial and transaxial resolusion at the center of each standard point. Each emission datum was simultaneously collected from seven contiguous axial sections. A total of 21 slices parallel to the OM line with a slice thickness of 6 mm, encompassing virtually the whole brain including the cerebellum, was analyzed. Twenty blood samples were collected from the brachial artery according to the following protocol; from injection to 2 minutes, one sample every 20 seconds, then samples at 2.5, 3, 4, 5, 7.5, 10, 15, 20, 25, 30, 40, 50, and 60 min after the intravenous administration of ^{18}FDG. The blood plasma radioactivities of ^{18}FDG were measured with a cross-calibrated well-counter.

Values of regional CMRGlc were calculated using the operational equation derived by Phelps et al.[4] and Huang et al.[7] from that of Sokoloff et al.[8].

A lot of regions of interest (ROIs) were placed in the cerebellum and the frontal cortex, and mean value of CMRGlc in each structure was calculated.

We also examined the sway of gravity center of her body unbalanced by truncal ataxia using stabilography at the 19th and 26th day of TRH treatment

Results

Before the TRH treatment, CMRGlc was markedly decreased in the cerebellum. In the other regions of the brain, regional CMRGlc was almost normal and there was no difference between right and left hemispheres with focal abnormality (Figure 2). A marked decrease of CMRGlc in the cerebellum was also observed 3 weeks after the TRH treatment (Figure 3). The mean values of CMRGlc in the cerebellum were 4.92 and 4.90mg/100g/min, and the ratios of the cerebellum versus the frontal cortex were 0.50 and 0.51 before and after the TRH treatment, respectively (Table 1). There was not significant change of the CMRGlc in the cerebellum before and after the TRH treatment in this patient.

On the examination with stabilography, the degree of disequilibrium of her body when she was standing on the floor was less observed at 19th day of the TRH treatment, and such finding was further improved at 26th day of the treatment (Table 2).

Discussion

In the previous studies, values of CMRGlc were significantly reduced in the cerebellar hemispheres and vermis in patients with SCD[1-3]. However, marked atrophy was also observed in most of such patients by MRI, therefore these findings were speculated that hypometabolism in the cerebellum might be explained by partial volume effects. In some cases with slight atrophic change of the cerebellum, regional CMRGlc was reduced significantly[1]. It is suggested that the glucose hypometabolism of the cerebellum may not be explained only by the cerebellar atrophy but also by neuronal dysfunction of the cerebellum itself. In the present patient, the significant decrease of CMRGlc in the cerebellum was observed in accordance with previous reports. It may be due to both the cerebellar atrophy and the neuronal dysfunction of the cerebellum. TRH has been widely used for treatment in patients with SCD. It has been suggested that the mechanism of the effects of TRH may be related to improvement of abnormal noradrenaline metabolism in the cerebellum[9-10], but the details are still unknown. A few reports using PET or SPECT described an increase of cerebellar blood flow immediately after intravenous TRH administration[11-12], so cerebellar function might improve during short time after administration. However, the administrated TRH is rapidly metabolized in blood, and mechanisms of the chronic effects are unknown. In the present study, we tried to evaluate the chronic effects of TRH therapy and also investigate the mechanism by PET. In order to exclude the influence of cerebral blood flow, we calculated the ratios of the cerebellum versus the frontal cortex as a reference area, because TRH receptor binding sites are relatively low level in the frontal cortex[13]. Based on the present study, we concluded that TRH did not improve CMRGlc in the cerebellum, but evidently improved the sway of gravity center by stabilography with no significant changes of neurological findings. We speculate the reason why the effect of TRH was too small to improve glucose metabolism with PET. We also speculate the effect of TRH was not necessarily due to an improvement of cerebellar function, because TRH receptors are widely distributed throughout the central nervous system[13]. A further detailed study is needed to clarify the mechanism of pharmacological action of TRH in patients with SCD.

References

1) Gilman S. et al., Ann. Neurol. **23** (1988) 223.
2) Kluin K. J. et al., Ann. Neurol. **23** (1988) 547.
3) Rosenthal G. et al., Ann. Neurol. **24** (1988) 414.
4) Phelps M. E. et al., Ann. Neurol. **6** (1979) 371.
5) Reivich M. et al., Circ. Res. **44** (1979) 127.
6) Ido T. et al., J. Org. Chem. **42** (1977) 2341.
7) Hung S. C. et al., Am. J. Physiol. **238** (1980) E69.
8) Sokoloff L. et al., J. Neurochem. **28** (1977) 897.
9) Sobue I. et al., Lancet. **23** (1980) 419.
10) Arai M., Clin. Neurol. **28** (1988) 595.
11) Harada K. et al., Clin. Neurol. **28** (1988) 563.
12) Ono S. et al., Kakuigaku. **25** (1988) 393.
13) Manaker S. et al., Neurology. **36** (1986) 641.

Table 1. The mean values of metabolic rate for glucose in the cerebellum and the frontal cortex, and the ratios of the cerebellum versus the frontal cortex before and after the TRH treatment.

	Before TRH	After TRH	Control (n=6)
Cerebellum	4.92	4.90	7.02±1.89 *
Frontal cortex	9.76	9.60	
Cerebellum / Frontal cortex	0.50	0.51	

* Control value is given as mean±SD (mg/100g/min) from six normal subjects

Table 2. The areas of sway of gravity center of the patient measured by stabilography before and after TRH treatement.

	Before TRH	After TRH		Control (n=31)
		19th day	26th day	
Envelop. Area	27.94	8.95	4.94	1.90±0.76 *
Rectangle Area	79.18	33.05	15.10	5.23±1.86 *

* Control values are given as means±SD (cm^2) from 31 normal subjects

Fig. 1. MRI (Tl-weighted image) revealed marked atrophy in both cerebellar hemispheres and vermis, and slight atrophy in the brainstem.

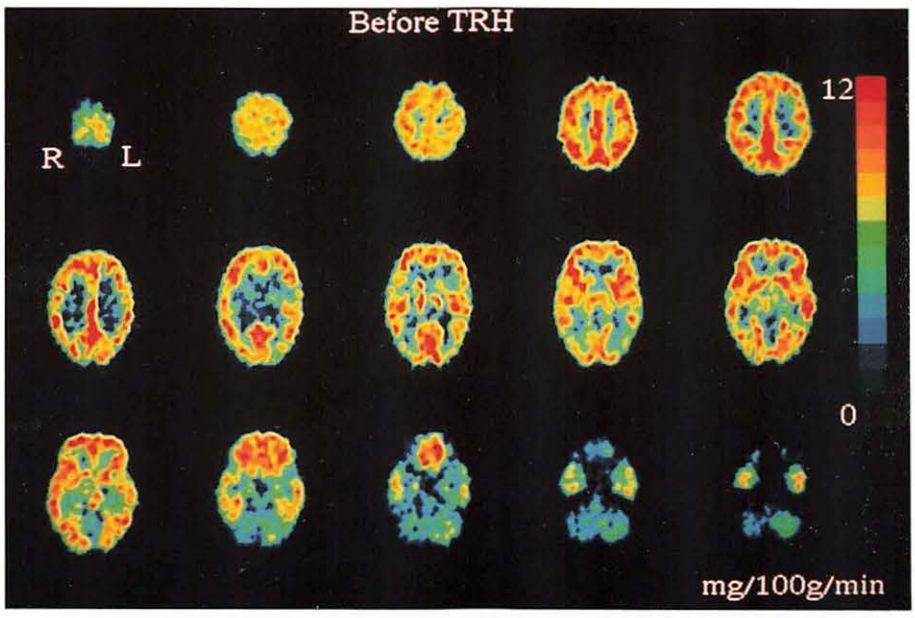

Fig. 2. Positron emission tomographic (PET) images of cerebral metabolic rate for glucose (CMRGlc) using 2-[^{18}F]fluoro-2-deoxy-D-glucose (^{18}FDG) before the TRH treatment. CMRGlc was markedly decreased in the cerebellum. In the other regions of the brain, regional CMRGlc was almost normal and there was no difference between right and left hemispheres with focal abnormality.

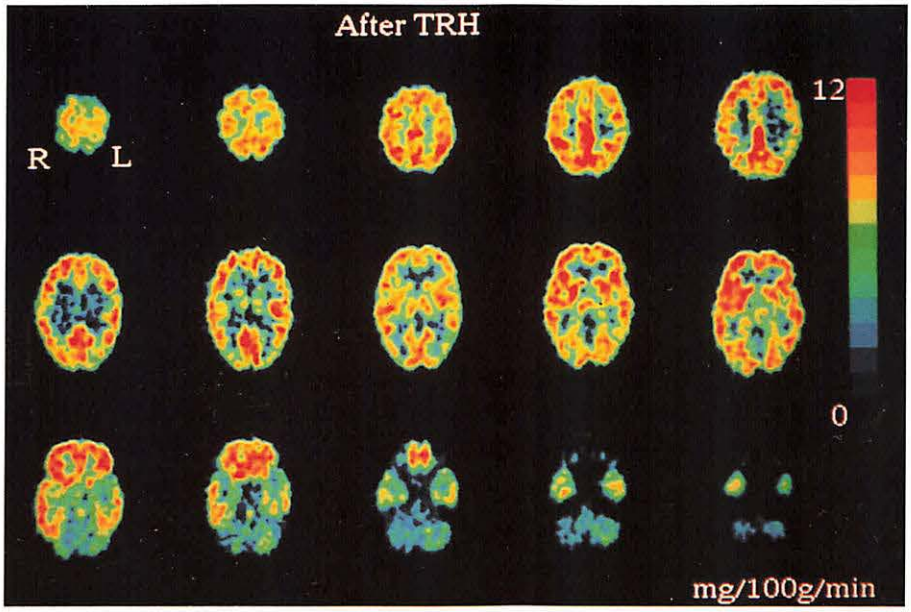

Fig. 3. PET images of CMRGlc using ^{18}FDG 3 weeks after the TRH treatment. A marked decrease of CMRGlc in the cerebellum was also observed.

IV. 8. Brain Dopamine Metabolism in Young Onset Parkinson's Disease Studied by Positron Emission Tomography

Nagasawa H., Tanji H., Saito H.*, Itoyama Y.*,*
*Fujiwara T.**, Iwata R.**, Itoh M.** and Ido T.***

Department of Neurology, Miyagi National Hospital
*Department of Neurology, Tohoku University School of Medicine**
*Cyclotron and Radioisotope Center, Tohoku University***

Introduction

Onset of idiopathic Parkinson's disease is unusual in patients below the age of 40. Quinn et al. studied 60 cases of parkinsonism with onset under the age of 40 and they proposed that cases of idiopathic Parkinson's disease beginning between 21-40 years should be called "young onset Parkinson's disease", which differentiated from cases of parkinsonism beginning before age 21 years defined as juvenile parkinsonism because of clinical features with familial cases[1]. There were several studies indicating some clinical features observed in young onset Parkinson's disease such as more prominent dystonia, earlier manifestation of levodopa-related dyskinesia and higher frequency of levodopa-dose-related motor fluctuations than seen in idiopathic Parkinson's disease of later onset[2].

Positron emission tomographic (PET) scanning using 6-[^{18}F]fluorodopa (FDOPA) is an efficient method of studying the nigrostriatal dopaminergic system in living subjects[3]. Intravenously injected FDOPA crosses the blood-brain barrier, is decarboxylated to fluorodopamine by L-aromatic amino acid decarboxylase, and remain in the nerve terminals during the scanning. Recent PET studies revealed striatal uptake of FDOPA was reduced in parkinsonism caused by loss of nigrostriatal neurons[4].

In the present study, we measured dopamine metabolism in patients with young onset Parkinson's disease using PET with FDOPA and analyzed the correlations between dopamine metabolism in the caudate nucleus and the putamen and clinical symptoms of the patients.

Subjects and methods

SUBJECTS

We studied 10 patients, 4 men and 6 women, who were diagnosed young onset Parkinson's disease by neurologists before age 40 years (Table 1). The age of onset of their initial Parkinson's symptoms was ranged from 24 to 39 years (mean±SD, 30.6±6.0). The mean duration of the disease was 7.5 years. All patients had effective responses to levodopa

therapy. Magnetic resonance imaging (MRI) and/or computed tomography (CT) scans of brain, obtained in all patients, were normal. No dementia was detected on formal neuropsychological testing. Patients were rated on overall disease severity rated from I to IV according to Hoehn and Yahr. The degree of main symptoms, bradykinesia, limb rigidity and tremor, was scored from 0 to 3 (0, absent; 1, mild; 2, moderate; 3, severe). Clinical assessment did not reveal any pyramidal, cerebellar, or oculomotor disturbances. The drug treatment was stopped at least 24 h before the PET study.

The control group consisted of 5 normal male volunteers with an age range of 27-40 years (mean±SD, 32.4±4.9), without a history of recent medical illness, neurological diseases, developmental disorder, or substance abuse. MRI and/or CT scans of the brain, obtained in the control group, were normal. Control subjects underwent a complete neurological examination and neuropsychological evaluation before PET scanning. The project was approved by the Research Ethics Committee of the Tohoku University School of Medicine. All subjects gave their written informed consent.

Positron Emission Tomography

[^{18}F]FDOPA scans were performed on a scanner, PT-931 (CTI Inc., USA), at the Cyclotron and Radioisotope Center, Tohoku University, Sendai, Japan. Patients and subjects were positioned in the scanner, with the orbitomeatal (OM) line parallel to the detector rings according to the brain slices by MRI. A cross of light was projected onto marks on the subjects' heads from three dimensions and the heads were positioned at 40 mm above and parallel to the OM line. All studies were conducted in a quiet, semi-darkened room with minimal background noise. The subjects' eyes were open and their ears were unplugged.

A 15-min transmission scan was collected using a ^{68}Ge-^{68}Ga external ring source. [^{18}F]FDOPA was synthesized by the method described by Adam et al. with a radiochemical purity of more than 99%. After an intravenous bolus injection of FDOPA (2.5-8.3mCi or 14.9-49.5 nmol) into the subjects, positron tomography was carried out using PT-931 with an 8 mm axial and transaxial resolution. A series of 5 min emission scans was performed over 60 min and emission data were simultaneously collected from seven contiguous axial sections, each about 6 mm in thickness from OM+66 to OM+22 mm.

Data analysis

After data collection, the latter six contiguous images of the same brain slice scanned between 30 and 60 min after administration of FDOPA were added and composite images were obtained in order to improve the contrast between dopaminergic and non-dopaminergic brain regions to aid the definition of anatomical regions of interest (ROIs). In each case, two different pairs of images, the PET images and the images obtained by MR, were registered and matched with each other using image scaling to bring the disparate pairs of image data

into congruence at the same brain slices. To ascertain the anatomical position of each brain structure, the positions of ROIs were manually defined using the overlapped images, i.e., PET images and MR images of the same brain slices according to the previous study[5]. Influx constants (Ki values min^{-1}) were calculated for the caudate nucleus and the putamen separately using a multiple graphical analysis method with cerebellar tissue input function[6,7]. The Ki value is a rate constant that reflects uptake and decarboxylation of FDOPA into [^{18}F]dopamine and its metabolites by the nigrostriatal nerve terminals.

The average values of influx constants within each structure are presented as means±SD. The Mann-Whitney U-test was used to compare the Ki values in each structure of the brain between patients and controls with $p<0.01$ considered to be statistically significant.

Results

Representative appearances of brain images at the level of the caudate nucleus and the putamen, obtained by MR or CT scan, FDOPA uptake, FDOPA influx rate and FDOPA distribution volume from a normal control and from the patients with young onset Parkinson's disease, are shown in Figure 1. FDOPA and its labeled metabolites were highly concentrated in the caudate nucleus and the putamen of both hemispheres of the normal control. On the contrary, in the patients with young onset Parkinson's disease, FDOPA uptake was markedly reduced both in the caudate nucleus and the putamen. The FDOPA uptake rate constant in the patients was significantly reduced ($p<0.01$) compared with normal controls as shown in Table 2.

There were not significant correlation between FDOPA influx rate and duration of illness (Figure 2A). However, FDOPA influx rate was well correlated with clinical stages according to Hoehn and Yahr (Figure 2B). The correlations between FDOPA influx rate in the caudate nucleus and the putamen and the degrees of the main clinical symptoms were analyzed. The FDOPA influx rate was more prominently correlated with the degree of rigidity than the degrees of bradykinesia and tremor (Figure 3).

Discussion

We selected apparent cases who had suffered from idiopathic Parkinson's disease beginning between age 21-40 years. The present study indicated that dopamine uptake was significantly reduced in both the caudate nucleus and the putamen of the patients with young onset Parkinson's disease as well as those seen in idiopathic Parkinson's disease of later onset from the previous study[5]. Moreover, dopamine metabolism was more prominently affected in the putamen than in the caudate nucleus.

The relationships between dopamine uptake and degree of clinical stages of the patients were quite variable. In some cases with young onset Parkinson's disease, dopamine uptake was markedly reduced in both caudate nucleus and the putamen, although their clinical

symptoms were mild and scored in 1 stage degree according to Hoehn and Yahr. In such cases, we speculate that dopamine receptor function might be highly sensitive and compensatory up-regulation of dopamine receptor binding sites might be modified levodopa responses and their clinical pictures of main symptoms.

Based on the present study, in the patients with young onset Parkinson's disease, FDOPA uptake rate constant was significantly reduced compared with normal controls. However, FDOPA influx rate in the presynaptic sites might not be always well correlated with individual clinical measures. We speculate that compensatory up-regulation in the postsynaptic receptor sites may be modified the degree of main clinical features and disease severity of young onset Parkinson's disease[9].

References

1) Quinn N., Critchley P. and Marsden D., Mov. Disord. **2** (1987) 73.
2) Globe L. 1., Neurology**41** (1991) 168.
3) Garnett E. S., Firnau G. and Nahmias C., Nature **305** (1983) 137.
4) Nahmias C., et al., J. Neurol. Sci. **69** (1985) 223.
5) Nagasawa H., et al., J. Neurol. Sci. **115** (1993) 136.
6) Patlak C. S., Blasberg R. G. and Fenstermacher J.D., J. Cereb. Blood Flow Metab. **3** (1983) 1 .
7) Patlak C. S. and Blasberg R. G., J Cereb. Blood Flow Metab. **5** (1985) 584.
8) Rinne U.K., et al., Mov. Disord. **5** (1990) 55.
9) Perlmutter J. S., Kilbourn M. R. and Raichle M. E., Neurology **37** (1987) 1575.

Table 1. Summary of patients with youn onset Parkinson's disease.

Patient No.	Age at Scan (yr)	Sex	Age of Onset (yr)	Duration (years)	Stage (H&Y)	Symptoms BR	T	R	Drugs
1	29	F	25	4	I	1	1	1	1, 3
2	37	F	27	11	III	3	2	2	1, 2
3	46	M	39	7	II	1	2	1	1, 2, 3
4	46	M	39	7	II	2	1	1	1, 3
5	44	M	38	6	III	3	1	3	1, 3
6	36	F	30	6	III	1	0	2	3
7	28	M	26	3	I	1	1	1	3
8	33	F	24	9	III	3	1	1	1, 3
9	36	F	26	11	III	2	1	1	1, 3
10	42	F	32	10	III	2	0	2	1, 2, 3

H & Y, Hoehn and Yahr; BK, Bradykinesia; T, Tremor; R, Rigidity.
Clinical scores: o, absent; 1, mild; 2, moderate; 3, severe.
Medications are signified numerically: 1, levodopa; 2, D_2 agonist (bromocriptine); 3, anticholinergic drugs (trihexyphenidyl).

Table 2. [^{18}F] Dopa influx rate measured by positron emission tomography in normal control and patients with young onset Parkinson's disease.

	Caudate Nucleus (Ki)	Putamen (Ki)
Normal control (N=5)	0.0176 ± 0.0039	0.0164 ± 0.0044
Young onset PD (N=10)	0.0132 ± 0.0031**	0.0093 ± 0.0024**

Values are given in mean ± SD. Ki=[^{18}F]dopa influx constant (min^{-1}).
N: number of subjects. **: $p<0.01$ significant compared with control using the Mann-Whitney U-test.

(A)

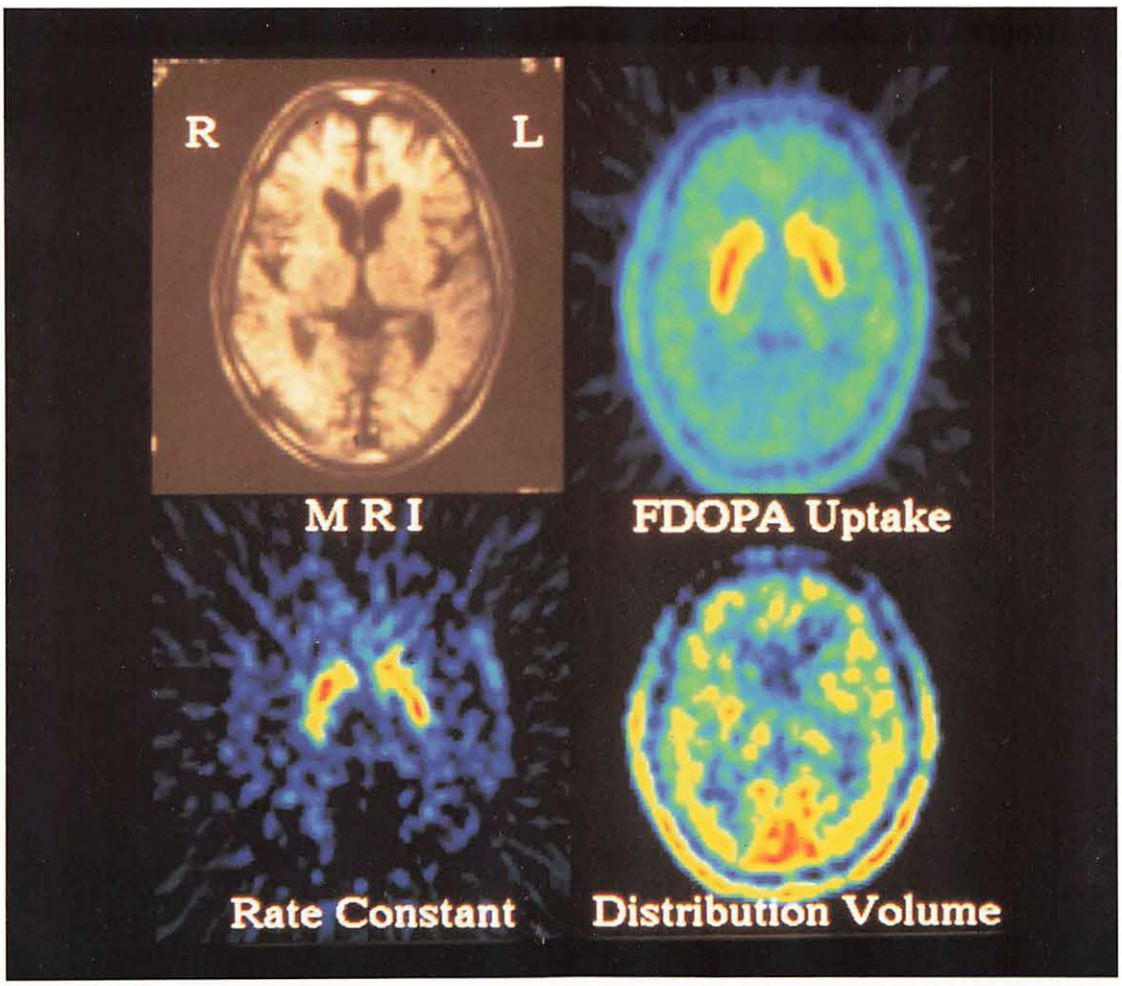

Fig. 1. Representative appearances of brain images at the level of the striatum obtained by magnetic resonance or computed tomographic scan, FDOPA uptake, FDOPA influx rate and distribution volume from a normal control (A) and from the patients with young onset Parkinson's disease (B: case 3, C: case 7, and D: case 9).

(B)

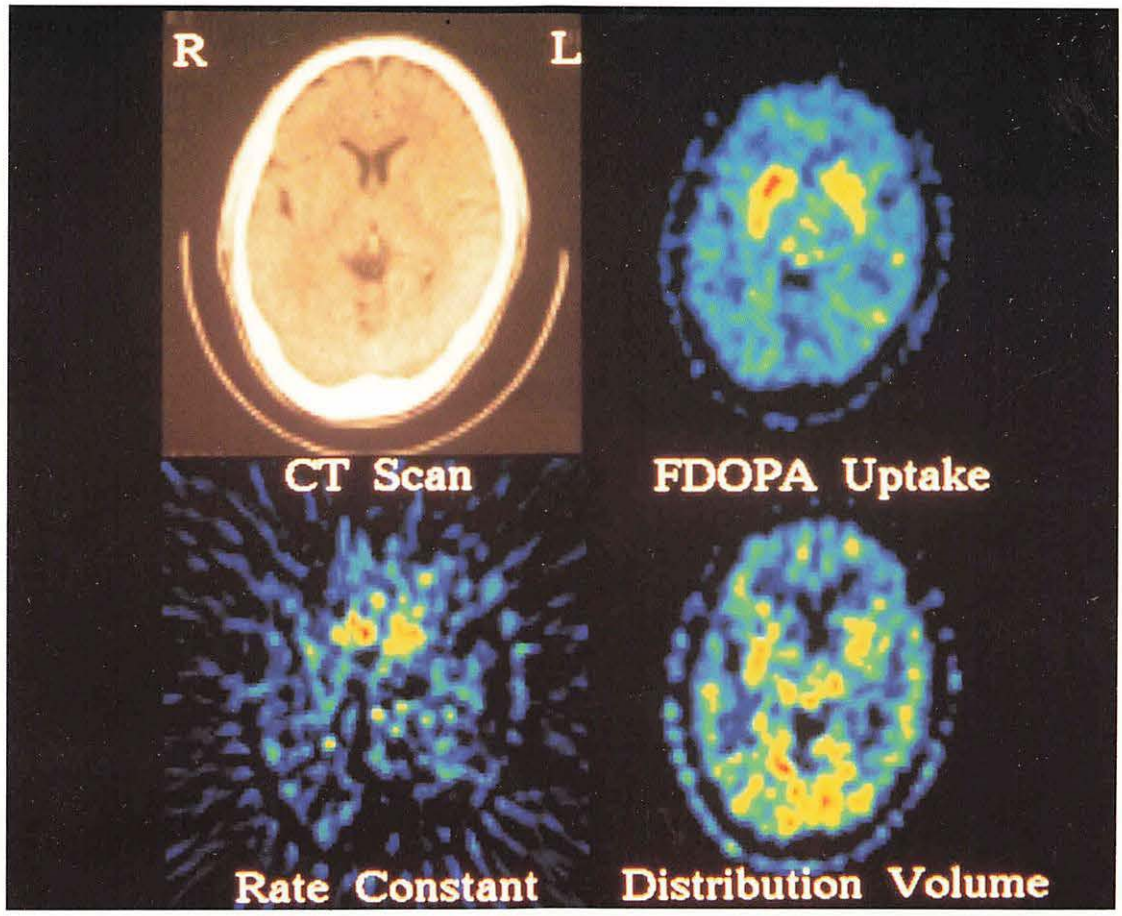
R
L
CT Scan
FDOPA Uptake
Rate Constant
Distribution Volume

(C)

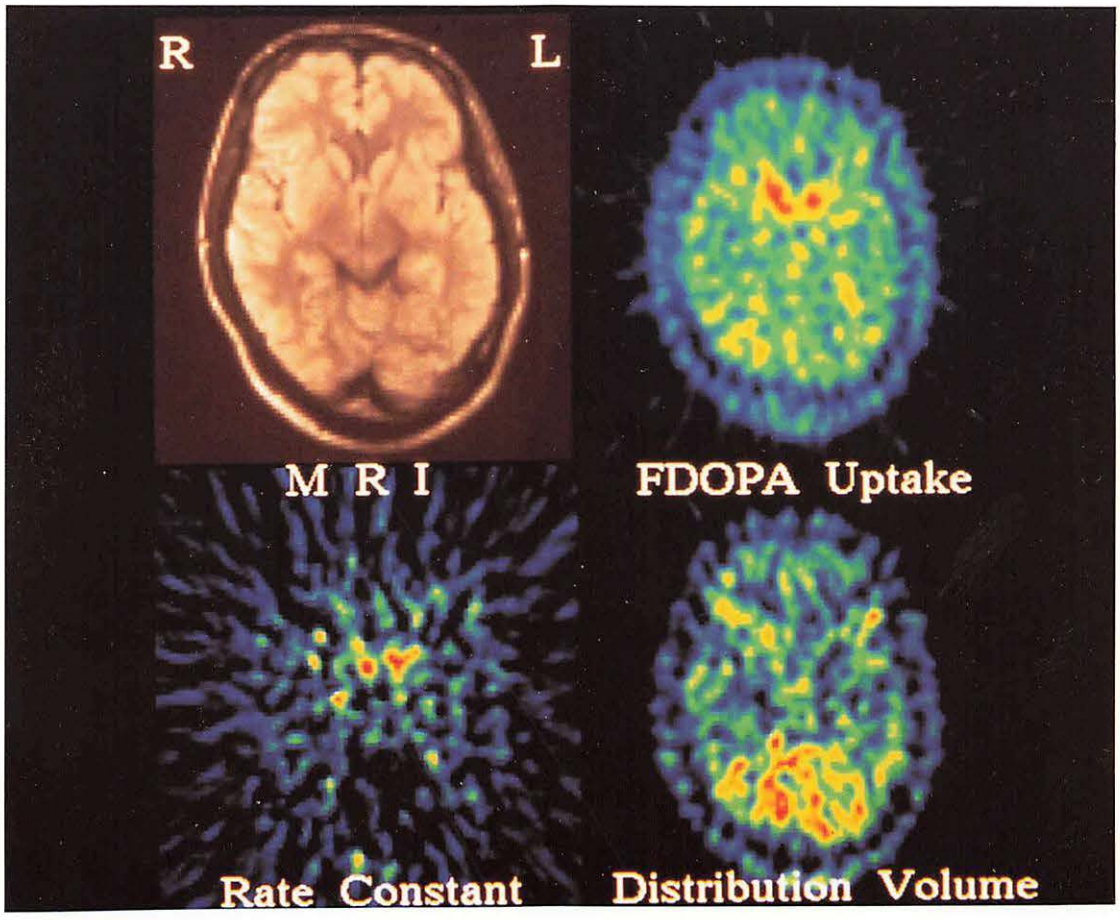
R
L
M R I
FDOPA Uptake
Rate Constant
Distribution Volume

(D)

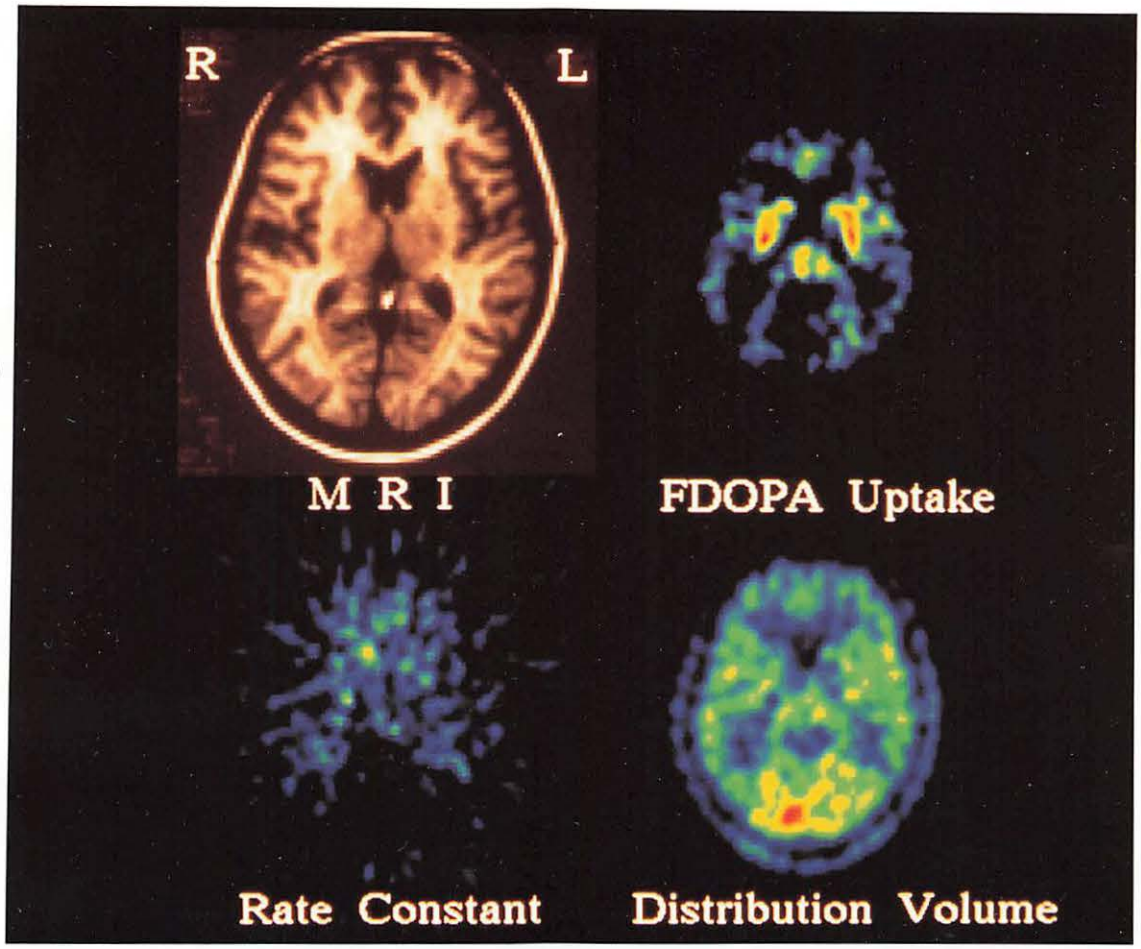

Figure 2 A

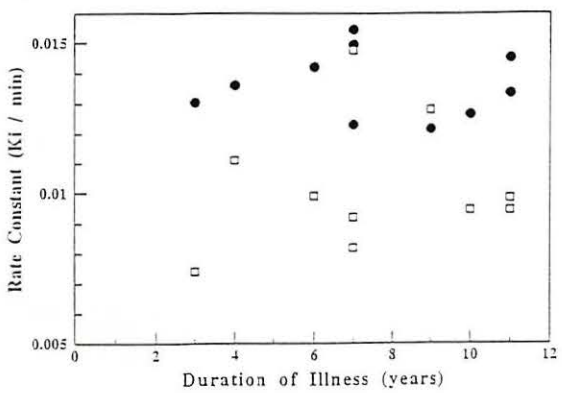

Figure 2 B

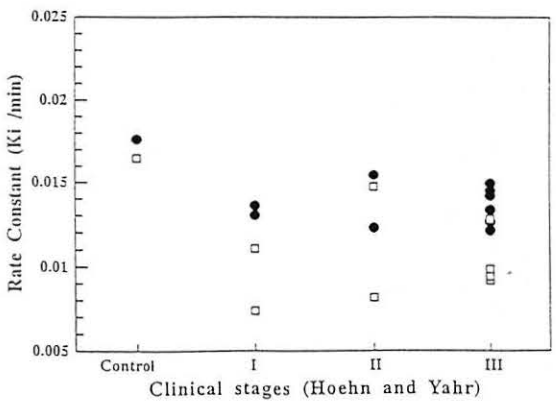

(A) (B)

Fig. 2. Correlations between FDOPA influx rates in the caudate nucleus (●) and the putamen (□) and the duration of disease (A) and clinical stages (B) formulated by Hoehn and Yahr.

Figure 3 A

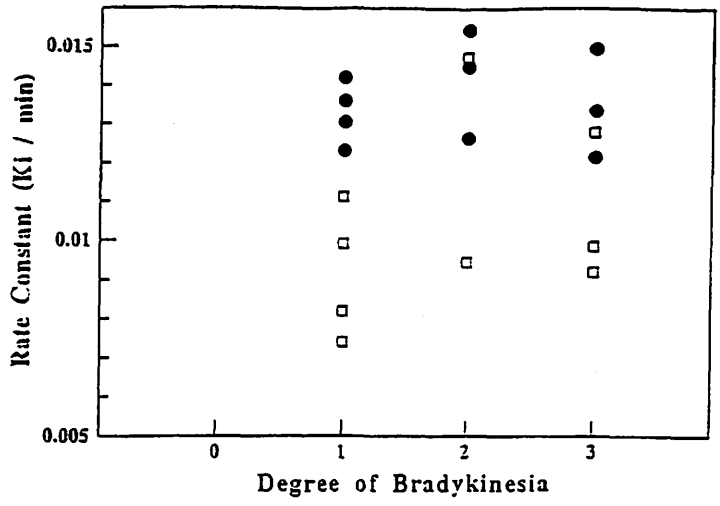

Figure 3 B

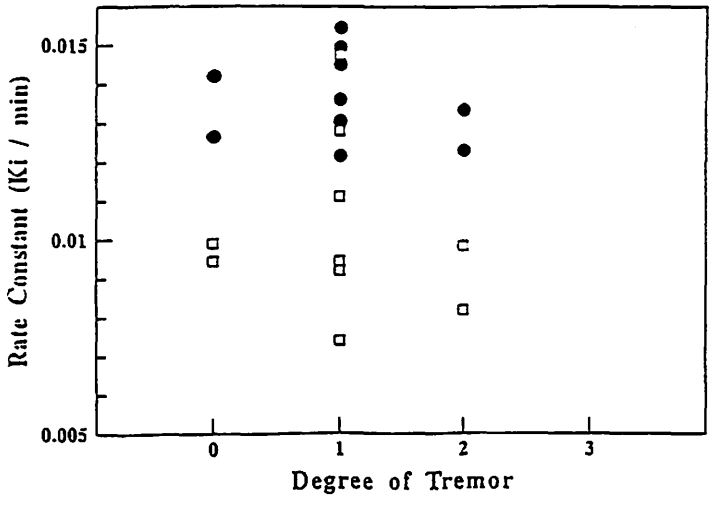

Figure 3 C

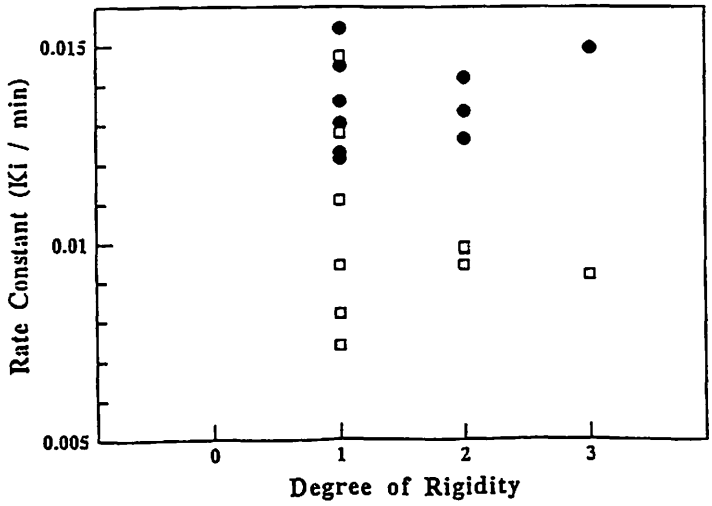

Fig. 3. Correlations between FDOPA influx rates in the caudate nucleus (●) and the putamen (□) and individual clinical symptoms (A: Bradikinesia; B: Tremor; C: Rigidity) of 10 patients with young onset Parkinson's disease.

IV. 9. Multi-Focal Metabolic Disturbances in Human Brain at a Chronic Stage of Stroke Studied with ^{18}FDG and Positron Emission Tomography

Nagasawa H., Tanji H., Itoyama Y.*, Itoh M.** and Ido T.***

Department of Neurology, Miyagi National Hospital,
*Department of Neurology, Tohoku University School of Medichine**
*Cyclotron and Radioisotope Center, Tohoku University***

Introduction

We have reported that postischemic delayed neuronal damage was observed in the remote areas, i.e., the ipsilateral thalamus and the substantia nigra of the rat brain after occlusion of the middle cerebral artery (MCA)[1]. These exo-focal postischemic neuronal damages in the remote areas might be caused by transsynaptic process associated with the infarcted areas and intracellular and transsynaptic signal transduction systems might play important roles in this mechanism[2-4]. To determine if that phenomenon also occurs in humans, we measured cerebral metabolic rates for glucose (CMRGlc) in the remote brain areas at the chronic stage after cortical infarction using 2[^{18}F]-fluoro-2-deoxy-D-glucose (^{18}FDG) and positron emission tomography (PET).

Subjects and Methods

We studied 7 patients, 5 men and 2 women, ranging in age from 41-72 years (mean ±SD, 61.1±8.8), who were affected by unilateral cerebral infarction in the cortex supplied by the MCA. The patients were diagnosed by a neurological examination, neuropsychological evaluation and using magnetic resonance imaging (MRI) and/or computed tomography (CT) scans of the brain. In all patients, the infarcted areas were limited in the cortex and no ischemic lesions were observed in the remote brain areas, such as the thalamus and the cerebellum, using MRI and/or CT scan. PET study was performed at the chronic stage, more than three months after stroke in all patients.

The control group consisted of 6 normal volunteers, 4 men and 2 women with an age range of 49-74 years (63.5±9.0), without a history of recent medical illness, neurological diseases, developmental disorder, or substance abuse. MRI and/or CT scan of the brain, obtained in the control group, were normal. Control subjects underwent a complete neurological examination and neuropsychological evaluation before PET scanning. The project was approved by the Research Ethics Committee of the Tohoku University, School of

Medicine. All subjects gave their written informed consent after a full explanation of the procedure.

Positron emission tomography

PET study was performed with a scanner, PT-931 (CTI Inc, USA), according to the FDG method[5,6] at the Cyclotron and Radioisotope Center, Tohoku University, Sendai, Japan. Before the study, a short 21-gauge cannula was placed in a brachial or a radial artery under local anesthesia for arterial blood sampling. Each subject was then positioned in the scanner, with the orbitomeatal (OM) line parallel to the detector rings according to the brain slices by MRI and/or CT scan. A cross of light was projected onto marks on the subjects' heads from three dimensions and their heads were set at the standard points of 16, 63, and 110 mm above and parallel to the OM line. All studies were conducted in a quiet, semidarkened room with minimal background noise. The subjects had their eyes opened and ears unplugged.

Before the emission scanning, a 20-min transmission scan using a ^{68}Ge-^{68}Ga external ring source was performed. Thirty min after an intravenous bolus injection of 111-183 MBq ^{18}FDG (3-5 mCi), a series of three emission scans, each of 10 min duration, was commenced by using a PT-931 with an 8 mm axial and transaxial resolution at the center of each standard point. Each emission data was simultaneously collected from seven contiguous axial sections. A total of 21 slices parallel to the OM line with a slice thickness of 6 mm comprising virtually the whole brain including the cerebellum were analyzed. Twenty blood samples were colleccording to the following protocol: from injection to 2 minutes, one sample every 20 seconds, then samples at 2.5, 3, 4, 5, 7.5, 10, 15, 20, 25, 30, 40, 50 and 60 min after the intravenous administration of ^{18}FDG. The blood samples were immediately centrifuged, and the arterial plasma radioactivities of ^{18}FDG was measured with the cross-calibrated well counter. The arterial plasma glucose concentrations were measured every 10 min during the study.

In each case, CT scan or MR was examined in detail at the same head position as the PET study. To ascertain the anatomical position of each brain structure, the positions of regions of interest (ROIs) were manually defined on the PET images using MRI or CT images of the same brain slices. Each ROI was positioned in the relevant region, if some ROIs appeared on several slices that overlapped the entire volume of each structure, using neuroanatomical atlases[7,8]. Cerebral metabolic rates for glucose (CMRGlc) were calculated using the operational equation derived by Phelps et al.[5] and Huang et al.[9] from that of Sokoloff et al.[10] The emission data were corrected for attenuation using transmission data. The average values of CMRGlc within each structure were calculated and data of CMRGlc were analyzed using a paired Student's t-test with $p<0.01$ considered to be statistically significant.

Results

Two different pairs of images of two patients, the PET images and the images obtained by CT scan or MR at the same brain slices, are shown in Figures 1 and 2. The values of CMRGlc (mean±S.D.) in each structure of the control subjects and the patients are represented in Table 1. In the patients, regional CMRGlc in the parietal cortex of the infarcted side was markedly decreased as 3.51±1.21 mg/100g/min. The parietal cortex was defined as infarcted area by CT scan or MRI, which was directly affected by ischemic insult. However, significant decreases of CMRGlc were observed as 3.74±1.86 in the ipsilateral thalamus and 4.54±1.70 mg/100g/min in the contralateral cerebellum compared with the value of each corresponding region of the opposite side and normal control values ($p<0.01$). No ischemic lesions had been detected in the thalamus and the cerebellum of the patients by CT scan or MRI (Figure 1 and 2).

Discussion

In the present study, we selected the patients who had suffered from cortical stroke more than three months. In all patients examined by CT scan or MRI, the infarcted areas were limited to the unilateral cerebral cortex with variable involvement of the adjacent centrum semiovale, in which areas had been supplied by the MCA. Our results indicate that focal cortical stroke produces widespread metabolic disturbances in the ipsilateral thalamus and the contralateral cerebellum, regions which are remote from the infarcted areas. Recent studies using experimental animals with MCA occlusion have revealed the delayed neuronal degeneration in the ipsilateral thalamus which had not directly been affected by the original ischemic insult[1,11]. Kataoka et al. reported that the disturbances of the neuronal network occurred in the remote areas in the MCA occlusion model of the rats using Fink-Heimer silver impregnation and succinate dehydrogenase immunohistochemistry[12]. In their study, massive silver staining of degenerated synaptic terminals and decreases in succinate dehydrogenase activity were observed in the ipsilateral thalamus at a chronic stage after the MCA occlusion and they considered that the absence of succinate dehydrogenase staining reflected early changes in retrograde degeneration of thalamic neurons associated with the thalamocortical pathways from the cortex with ischemic insult[12]. We also reported that regional glucose metabolism was decreased in the ipsilateral thalamus one week after the ischemia using the MCA occlusion model in rats[1]. Delayed neuronal damage and decrease of glucose metabolism in the ipsilateral thalamus are considered to explain by retrograde neuronal degeneration due to thalamocortical fiber damage in ischemic cortical regions. The present data suggest that such phenomenon observed in the animal experiments also occur in the ipsilateral thalamus of the patients with cortical infarction. Reduction of CMRGlc in the thalamus may be explained by retrograde neuronal degeneration due to thalamocortical fiber damage after cortical stroke in humans.

In another opinion, reduction of CMRGlc in the ipsilateral thalamus might reflect a significant functional suppression of neuronal activity caused by loss of corticothalamic fibers from the ischemic cortical regions. This could happen without cell death in the thalamus and consequently would not be detected by CT scan and MRI. Furthermore, such hypometabolism due to corticothalamic fiber damage might not be reversible and this would consequently lead to delayed neuronal death in the thalamus during the chronic stage of stroke.

On the other hand, decrease of glucose metabolism in the contralateral cerebellum is not easily explained. In our study, metabolic disturbance observed in the contralateral cerebellum three months and more after the cortical infarction. As shown in Figure 2, metabolic disturbance still observed in the right cerebellum, though a patient who had suffered from left cortical infarction more than 4 years previously. Such a phenomenon may reflect irreversible change of neuronal function and is quite different from the crossed cerebellar diaschisis reported by Baron et al.[13]. There were few reports about the delayed damage in the contralateral cerebellum after cortical injury using experimental animals[14]. Further detailed study is required to clarify the mechanism of decreased glucose metabolism in the contralateral cerebellum at a chronic stage after the cortical infarction. In conclusion, decreases of regional glucose utilization in the exo-focal remote areas indicate that disturbances in brain function after stroke occur not only in the ischemic areas directly affected by the original ischemic insult, but also in the remote areas due to secondary neuronal degeneration. We suggest that these multi-focal metabolic disturbances observed in the postischemic brain may exacerbate clinical symptoms at a chronic stage of stroke.

Acknowledgments

We are grateful to Shinya Seo and Shoichi Watanuki for technical assistance.

References

1) Nagasawa H. and Kogure K., Brain Res. **524** (1990) 196.
2) Kogure K., Tanaka J. and Araki T., Neurochem. Pathol. **9** (1988) 145.
3) Nagasawa H. and Kogure K., J. Neurosci. Res. **31** (1992) 507.
4) Nagasawa H., Araki T. and Kogure K., J. Neurosci. Res. **33** (1992) 485.
5) Phelps M. E. et al., Ann. Neurol. **6** (1979) 371.
6) Reivich M. et al., Circ. Res. **44** (1979) 127.
7) Salamon G. and Huang Y. P., Computed tomography of the brain. Springer, Berlin, Heidelberg, New York, 1980.
8) Talairach J. and Tournoux P., Co-planar stereotaxic atlas of the human brain. 3-dimensional proportional system: an approach to cerebral imaging. Thieme, Stuttgart, 1988.
9) Huang S. C. et al., Am. J. Physiol. **238** (1980) E69.
10) Sokoloff L. et al., J. Neurochem. **28** (1977) 897.
11) Iizuka H., Sakatani K. and Young W., Stroke **21** (1990) 790.
12) Kataoka K. et al., Stroke **21** (1989) 1226.
13) Baron J. C. et al., Trans. Am. Neurol. Assoc. **105** (1980) 459.
14) Andrews R. J., Stroke **22** (1991) 943.

Table 1. Cerebral metabolic rate of glucose in each brain structure of normal control and patients.

Structure	Control (N=6)	Patients (N=7)	
		Infarcted side	Non-infarcted side
Frontal cortex	7.64 ± 1.45	6.37 ± 1.70	7.56 ± 1.81
Parietal cortex	7.87 ± 1.38	3.51 ± 1.21**	7.22 ± 1.46
Occipital cortex	7.74 ± 1.62	7.73 ± 1.76	7.65 ± 1.79
Temporal cortex	7.26 ± 1.64	5.81 ± 1.51	6.92 ± 0.90
Thalamus	7.57 ± 1.97	3.74 ± 1.86**	8.07 ± 1.71
Cerebellum	7.02 ± 1.89	6.77 ± 1.60	4.54 ± 1.70**

Values are given in mean ± S.D. mg/100g/min. N: number of subjects.
**: $p<0.01$, significant difference from the values in the corresponding area of the contralateral side and normal control values.

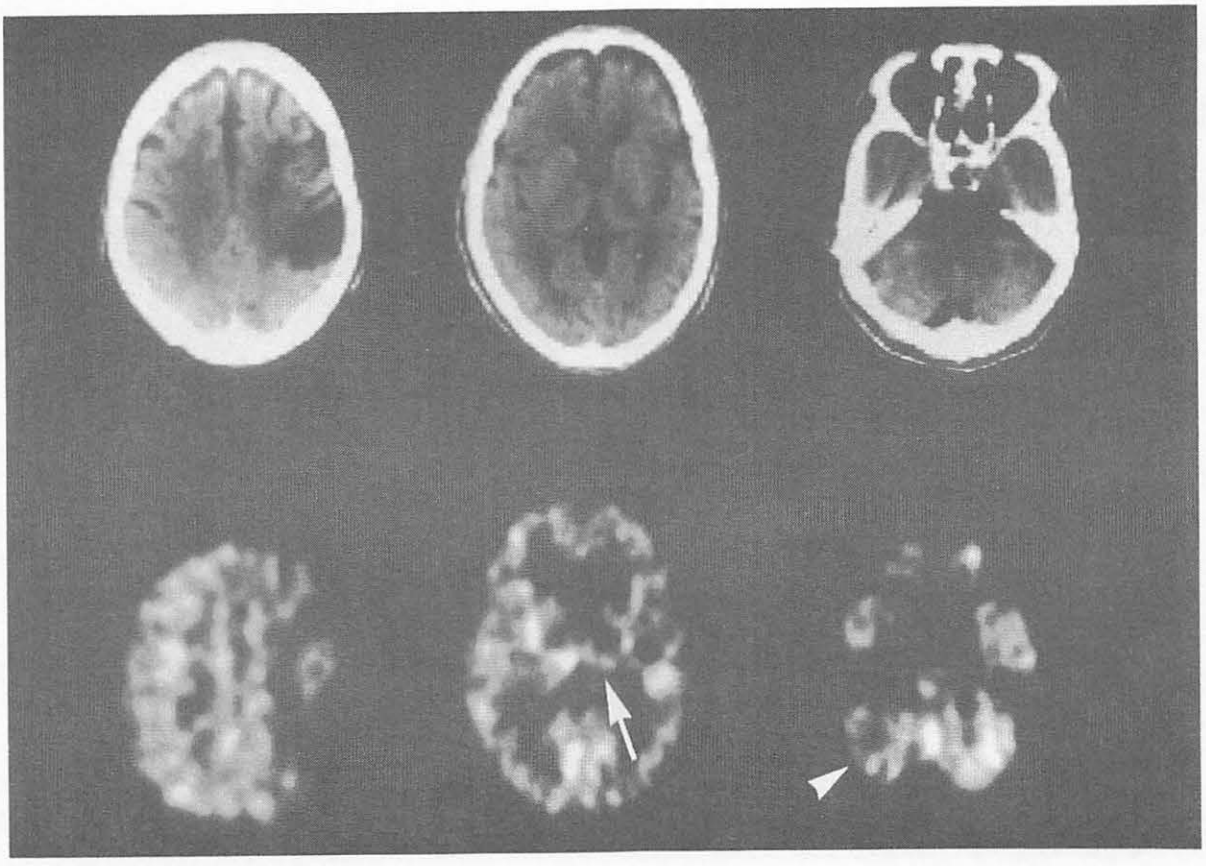

Fig. 1. Representative appearances of CT Scan and PET image data at the same brain slices from a 68-year-old man who had suffered from left cortical infarction 5 months previously. Decreases of CMRGlc were observed in the left thalamus (arrow) and in the right cerebellum (arrowhead).

Table 1. Glucose metabolic rate of glucose in each brain structure of control and [illegible]

Structure	Control (mg/...)	Fasting (mg/...)	
		Intravenous saline	Non-lactacted acid
Frontal cortex	7.04 ± 1.60	6.07 ± 1.79	7.80 ± 1.41
Parietal cortex	7.37 ± 1.34	6.81 ± 1.14	7.32 ± 1.16
Occipital cortex	7.74 ± 1.42	7.75 ± 1.66	7.46 ± 1.73
Temporal cortex	7.24 ± 1.64	6.41 ± 1.81	6.39 ± 0.00
Thalamus	7.81 ± 1.67	6.76 ± 1.86	8.09 ± 1.71
Cerebellum	7.09 ± 1.34	6.71 ± 1.60	6.61 ± 1.74

Values are given in mean ± SD. [illegible] of subjects.
[illegible] significant difference from the values in the corresponding
line [illegible] and normal-control values.

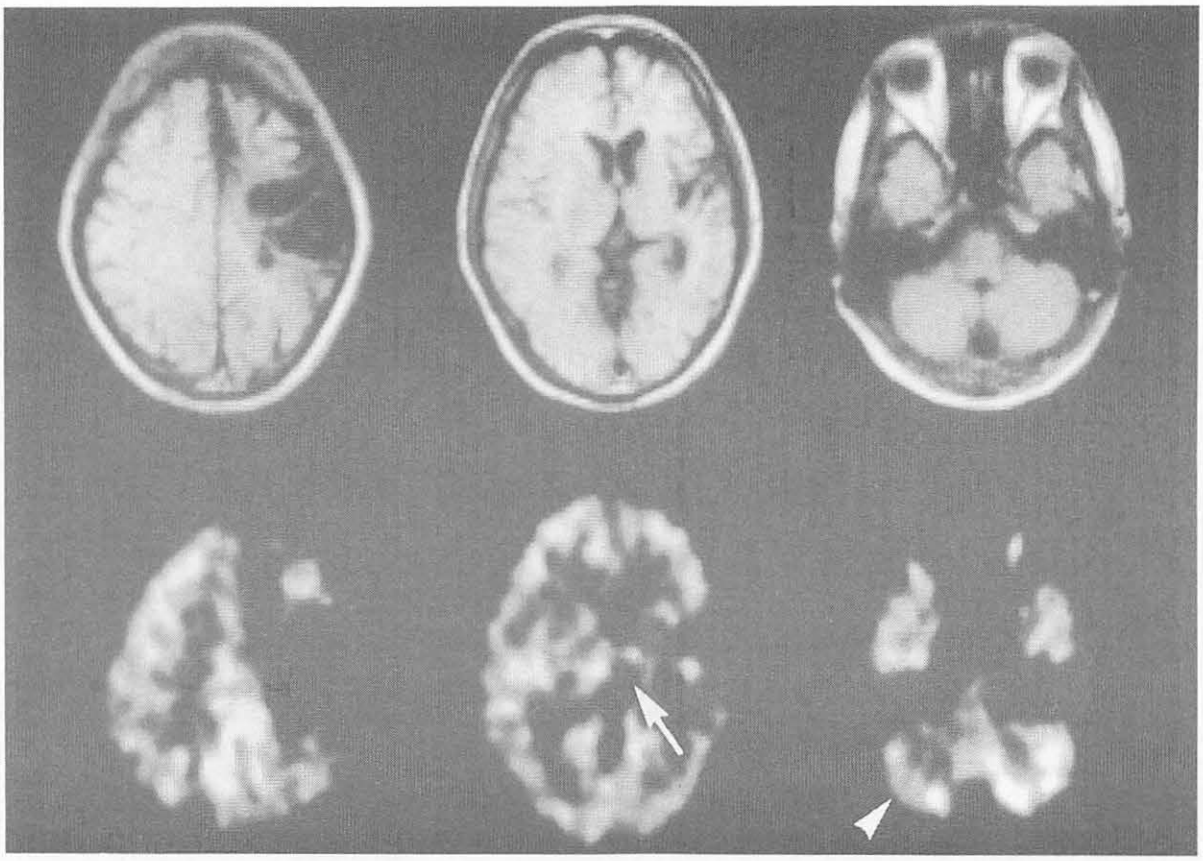

Fig. 2. Representative appearances of MRI and PET image data at the same brain slices from a 41-year-old man who had suffered from left cortical infarction 4 years and 2 months previously. Decreases of CMRGlc were observed in the left thalamus (arrow) and in the right cerebellum (arrowhead).

IV. 10. Oxygen Metabolism Disturbance in the Cerebral Cortex of Infantile Hydrocephalus Detected by Positron Emission Tomographpy

*Shirane R., Takahashi T., Hara Y., Satoh S., Yoshimoto T., and Itoh M.**

Department of Neurosurgery, Tohoku University School of Medicine
*Division of Nuclear Medicine, CYRIC Tohoku University**

Introduction

In infacy, hydrocephalus can present with symptoms of increased intracranial pressure, or more insidiuously with mental retardation, which is a fairly common and serious complication[1]. During infancy, the brain undergoes sequential anatomic, functional and organizational changes necessary to support the complex adaptive behavior of a fully mature normal individual. In earlier communications, we measured the cerebral blood flow and oxygen metabolism in hydrocephalic infants by oxygen-15 gases inhalation method with positron emission tomography (PET) and we demonstrated that there was hypoperfusion and lower metabolism in the frontal, parietal, and visual association corticies[2,3]. These results suggested that enlarged ventricles tended to damage these association corticies, where functional development occurs later than in other regions, and this seemed to cause mental retardation. However, developmental changes should exist in the cerebral circulation and metabolism during the first year of life[4,5]. Therefore, the data obtained from hydrocephalic infants should be compared with those of normal subjects. In the present study, the cerebral blood flow and oxygen metabolism of hydrocephalic infants were measured and compared to infants of the same age with normal development.

Subjects and Methods

Six hydrocephalic infants with symptoms of intracranial hypertension were selected for the PET study. The medical criteria for inclusion in the study were:(1) a diagnosis of hydrocephalus before 12 months of age; and (2) an absence of seizure activity or cortical signs on neurologic examination. The age distribution of these patients was 4 to 12 months (7.3+2.5 months). Hydrocephalus was due to aqueductal stenosis (four cases), and intraventricular hemorrhage (one case), and Dandy-Walker syndrome (one case). The patients' details are given in Table 1. Tomographic images of all cases are shown in Figure 1. Ventriculo-peritoneal shunts were placed in all patients and thereafter, the ventriculomegaly resolved in all cases. Among the patients studied, none had worsoning of

their neurological symptoms following surgery. The patients' pre-operative developmental qualifications (Tsumori-Inage method) were determined before the PET studies.

The control group consisted of six infants. Their ages were from 2 to 12 months (7.3 + 4months) (Table 2). All infants in this group have showed normal development before and at least 2 years after PET examinations. The patients were hospitalized for the following reasons: one probable case of unilateral lambdoid suture, one probable case of craniosynostosis, one case of Chiari malformation, one case of partial closure of unilateral coronal suture, one postoperative patient of unilateral lambdoid suture closure, one postoperative case of unilateral coronal suture closure. None of these infants had neurologic deficits, seizures or intracranial hypertension either before or after the PET studies.

PET Procedure

All PET studies were performed in accordance with the policies of the committee for clinical PET study of Tohoku University. Informed consent was obtained from the patients' parents. We used a PT-931 (CTI, Knoxville, Tennessee)[6]. The spatial resolution of the image was 8 mm full width at half maximum (FWHM), and the slice thickness was 7 mm. Seven slices were obtained simultaneously. All subjects were scanned in the axial tomographic plane from the thalamus to the centrum semiovale. The patients were not allowed to eat or sleep for 3 hours prior to the examination. Venous and arterial catheters were inserted in a hand vein and the brachial artery under local anesthesia.

Thiopental sodium (3 mg/kg) was administered 20 min prior to the emission scan in order to sedate the patient during the examination. If this did not achieve sufficient sedation, an additional dose (2 mg/kg) was administered. All visual, auditory, and other sensory stimuli were minimized during the emission scan to prevent the patient from awakening. Measurements of the regional cerebral blood flow (rCBF), the regional cerebral metabolic rate of oxygen (rCMRO2), and the regional oxygen extraction fraction (rOEF) were carried out with steady state inhalation of O-15 labelled CO_2, O_2 and CO, respectively[7,8]. The radioactivity of the inhaled gases was lowered to 10% of the adult dose, in order to reduce the radiation exposure. Arterial blood was drawn for blood gas analysis and radioactivity. The total amount of blood removed was approximately 7 ml. The brain-blood partition coefficient used in this study was 1.0 ml/g. The region of interest (ROI) was between the axial slices through the thalamus and cetrum semiovale. An estimate was made of the frontal association cortex (FC), sensorimotor cortex (SM), parietal cortex (PC), visual association cortex (VA), visual cortex (VC) and thalamus (TH). Oval regions of interest were located in each structure, which were verified by magnetic resonance imaging. The rCBF, rOEF, and $rCMRO_2$ were detrmined from these regions of interests.

Results

Tables 3 and 4 show the mean values of the rCBF, $rCMRO_2$ and rOEF for the left and right cerebral hemispheres for the hydrocephalic infants and normal subjects. The rCBF and $rCMRO_2$ in the association cortices were lower than in the primary cortex and thalamus in both groups, while relatively uniform values of the rOEF were observed throughtout the brain. Figure 2 compares the mean values of these cerebral functions for both groups. Using the Welch's method of statistical analysis to correct for the presence of multiple comparisons, the hydrocephalus infants had a significantly reduced $rCMRO_2$ in the cerebral cortex except for the parietal cortex compared with the control subjects. The $rCMRO_2$ values in the other cerebral regions of the hydrocephalic infants were also lower than in the controls, but this was not significant at a 5% level. The values of the rOEF of the hydrocephalic infants were slightly lower than the controls, but this was not significant. In addition, the level of the rOEF remained in the normal range. Interestingly, while the hydrocephalic patients had approximately 80% of the $rCMRO_2$ values of the controls, no significant rCBF and rOEF changes were observed. Therefore, so-called "coupled reductions" in the levels of $rCMRO_2$ and rCBF were not found in infants with hydrocephalus.

Discussion

In the normal adult brain, rCBF and rCMRO2 have been shoen to be closely coupled to each other, and so the rOEF is similar throughout the brain[7]. In both groups of infants in the present study, the association cortex had lower values of rCBF and rCMRO2, which is similar to the adult brain. In addition, the rOEF was rather similar in all brain regions evaluated.

Brain tissue has a reserve in its arterial oxygen supply, and if blood flow is compromised, it can raise its rOEF in order to maintain cerebral oxygen metabolism. This phenomenon, raised rOEF with inappropriately low rCBF has been described as the "misery-perfusion syndrome" in patients with cerebral ischemia[9]. If cerebral tissue damage occurs, $rCMRO_2$ falls with the fall of rCBF[10]. Brooks has reported that in adults with the acute onset of hydrocephalus there were significantly reduced levels of $rCMRO_2$ and rCBF with elevated rOEF[11]. Adult patients with a more insidious onset of hydrocephalus due to congenital abnormalities had reduced baseline levels of $rCMRO_2$ and rCBF. Their levels of rOEF, however, were normal, implying that the observed reduction in $rCMRO_2$ and rCBF was a coupled form, reflecting tissue damage produced by long-lasting hydrocephalus.

In the present study, infants with hydrocephalus had significantly reduced levels of cortical $rCMRO_2$ with slightly lower cortical rCBF and rOEF compared to the control subjects. These results indicate that the reduction of cerebral oxygen metabolism in hydrocephalus was not produced by decreased cerebral blood flow. We have reported a characteristic pattern of cerebral circulation and oxygen metabolism in infantile hydrocephalus[2,3]: (1) lower cortical $CMRO_2$, (2) slightly lower CBF, (3) unchanged OEF as

CBF decreased, and (4) postoperative increase in cortical $CMRO_2$. This suggests that an anaerobic change of metabolism might be activated in infantile hydrocephalus.

It should be pointed out that $rCMRO_2$ and rCBF, when assessed by PET, are measured per unit volume. However, rOEF measured by this technique is free from partial volume artifacts, and thus the rOEF reflects the rOEF of the cerebral tissue itself. The reduced $rCMRO_2$ in hydrocephalic infants may reflect to an extent the increased partial volume contribution of the increased extracellular fluid in the ROI, as well as decreased function of the hydrocephalic brain. If partial volume artifacts were considered to be the main reason for the reduction of $rCMRO_2$, it should be coupled with a reduction of rCBF.

In experimental hydrocephalus, the cerebral metabolic rate of glucose, measured by deoxyglucose autoradiography, has been found to be increased independent of a reduction in rCBF[12]. Deoxy-glucose, which is glucose analog, does not enter the tricarboxylic acid cycle and accumulate in the brain cells, and so this method can evaluate the rate of glucose uptake[13], which is equal to the sum of aerobic and anaerobic metabolism[14]. Furthermore, we have previously tried to clarify the ratio of anaerobic to aerobic glucose metabolism in experimental hydrocephalus by comparing the metabolic rates of deoxyglucose and glucose using double-labeled autoradiography[15]. This experiment demonstrated that anaerobic glucose metabolism was responsible for approximately 15% of the cortical metabolism in hydrocephalus[16].

These clinical and experimental studies suggest that an anaerobic change of metabolism is activated in infantile hydrocephalus. Activation of anaerobic metabolism may compensate for the shortage of energy produced by an oxygen metabolism disturbance. This cortical energy metabolism disturbance in hydrocephalus may causes a harmful effect on the developing brain. Finally, tissue damage will develop and a coupled reduction in the rCBF and $rCMRO_2$ will be observed by PET.

The application of PET with O-15 radiopharmaceuticals in infants has received little attention, due to the concern for the risk of radiation exposure. The absorbed radiation dose of this method has been estimated by Powers[17]. The maximum organ dose is 1.6 rads to the lungs with 0.22 rads to the total body. In the present study, the actual radiation exposure was measured using Cs-137 luminescence dosimetry. These doses were lower than those previously reported. One of the technical difficulties of applying this procedure to infants is the stabilization of the infants in the PET scanner. During the examination, an anesthetic should be administered. Thiopental sodium was used in this study. Barbiturates are known to reduce the cerebral metabolism. To reduce the influence on cerebral metabolism, the dose used was the minimal one and all studies were performed with the same protocol. When we measured rCBF, $rCMRO_2$, and rOEF in adult patients usingthe same protocol as for infants, the values were similar to those when awake.

References

1) Dennis M. et al., Arch. Neurol. **38** (1981) 607-615.
2) Shirane R. et al., Child's Nerv. Syst. **8** (1992) 118-123.
3) Shirane R. et al., Cerebral blood flow and oxygen metabolism in children with hydrocephalus, in Matsumoto S, Tamaki N (eds): Hydrocephalus. Springer-Verlag: pp144-152, 1991.
4) Chugani H. T. and Phelps M. E. Science **231** (1986) 840-843.
5) Chugani H. T , Phelps M. E., and Mazzziotta J. C Ann. Neurol. **22** (1987) 487-497.
6) Spinks T. J., Guzzardi R., and Bellina C. R., J. Nucl. Med. **29** (1988) 1833-18411.
7) Frackowiak R. S. et al., J. Comput. Assit. Tomogr. **4** (1980) 727-736.
8) Lammertsma A. A et al., J. Cereb. Blood Flow Metab. **3** (1978) 425-531.
9) Baron J. C. et al., Human hemispheric infarction studied by positron emission tomography and the O-15 continuous inhalation technique. In Caille JM, Salamon G (eds) Computerized Tomography. Berlin, Springer-Verlag, pp 231-237, 1980.
11) Brooks D. J. et al., Brain **109** (1986) 613-628.
10) Frackowiak R. S., et al., Brain, **104** (1981) 753-778.
12) Sato S. et al., Current Treatment for hydrocephalus, **2** (1992) 2-4.
13) Sokoloff L. et al., J. Neurochem. **28** (1977) 897-916.
14) Ackermann R. and Lear J., J. Cereb. Blod Flow Metab. **9** (1989) 238.
15) Lear L. L. and Ackermann R. F., J. Cereb. Blood Flow Metab. **8** (1988) 575-585.
16) Hara Y. et al., Anaerobic changes of glucose metabolism in experimental hydrocephalus rat, in Nagai H, Kamuya K, Ishii S (eds):Intracranial Pressure IX. Tokyo Berlin Heiderberg New York: Springer-Verlag, 1994, pp641-642.
17) Powers W. J. et al., J. Nucl. Med. **29** (1988) 1961-1970.

Table 1. Cases with hydrocephalus.

	age	sex	diagnosis	symptoms	DQ
case 1	5m	male	AC stenosis	elevated ICP	60
case 2	6m	female	IVH	elevated ICP	64
case 3	6m	female	AC stenosis	elevated ICP	106
case 4	7m	female	AC stenosis	elevated ICP	95
case 5	8m	female	D-W	elevated ICP	145
case 6	12m	male	AC stenosis	elevated ICP	80

Table 2. Normal controls.

	age	sex	diagnosis
case 1	2m	male	Chiari malformation
case 2	4m	female	skull deformity
case 3	5m	female	partial coronal closure
case 4	10m	male	skull deformity
case 5	11m	female	post-ope coronal closure
case 6	12m	female	post-ope lambda closure

Table 3. Regional cerebral blood flow of hydrocephalus infants.

(a)

	age	FC	SM	PC	VA	VC	TH
case1	5M	30	40	34	30	57	55
case2	6M	38	54	28	20	56	54
case3	6M	30	39	34	30	44	66
case4	7M	29	43	30	26	50	47
case5	8M	36	39	38	30	50	50
case6	12M	35	44	41	38	61	42
mean		33	43	34	29	53	52
S.D.		3.8	5.7	4.8	5.9	6.1	8.2

(ml/min/100g)

Table 3. Regional cerebral metabolic rate of oxygen of hydrocephalus infants.

(b)

	age	FC	SM	PC	VA	VC	TH
case1	5M	19	28	20	19	40	35
case2	6M	16	22	12	6	25	24
case3	6M	21	23	28	26	21	27
case4	7M	18	29	18	19	28	29
case5	8M	22	27	26	20	30	33
case6	12M	20	26	25	21	34	25
mean		19	26	22	20	30	29
S.D.		2.2	2.8	6.0	4.5	6.7	4.4

(X10 ml/min/100g)

Table 3. Regional oxygen extraction fraction (X100) of hydrocephalus infants.

(c)

	age	FC	SM	PC	VA	VC	TH
case1	5M	50	55	47	49	55	57
case2	6M	47	38	33	39	47	44
case3	6M	41	34	46	50	26	31
case4	7M	50	55	50	47	52	52
case5	8M	43	47	48	44	46	42
case6	12M	39	44	36	38	40	41
mean		45	46	43	45	44	45
S.D.		4.7	8.6	7.0	5.1	10.4	9.1

Table 4. Regional cerebral blood flow of normal controls.

(a)

	age	FC	SM	PC	VA	VC	TH
case1	2M	21	35	28	27	45	36
case2	4M	23	31	31	24	47	36
case3	5M	32	51	38	35	53	45
case4	10M	48	48	39	47	78	65
case5	11M	33	50	37	37	66	56
case6	12M	32	49	34	23	51	35
mean		32	44	35	32	57	46
S.D.		9.6	8.7	4.3	9.3	12.8	12.5

(ml/min/min)

Table 4. Regional cerebral metabolic rate of oxygen of normal controls.

(b)

	age	FC	SM	PC	VA	VC	TH
case1	2M	21	32	23	21	37	30
case2	4M	21	24	21	21	37	24
case3	5M	25	33	24	23	40	31
case4	10M	30	31	26	29	50	41
case5	11M	25	32	27	30	49	33
case6	12M	29	32	28	31	28	34
mean		25	30	25	26	40	32
S.D.		3.8	3.3	2.6	4.7	8.3	3.2

(X10 ml/min 100g)

Table 4. Regionzl oxygen extraction fraction (x100) of normal controls.

(c)

	age	FC	SM	PC	VA	VC	TH
case1	2M	49	49	45	46	49	49
case2	4M	51	52	46	47	53	44
case3	5M	47	43	43	43	46	42
case4	10M	41	38	45	45	42	48
case5	11M	49	41	46	56	48	37
case6	12M	43	41	46	45	44	44
mean		47	44	45	47	47	44
S.D.		3.9	5.3	1.2	4.6	3.9	4.3

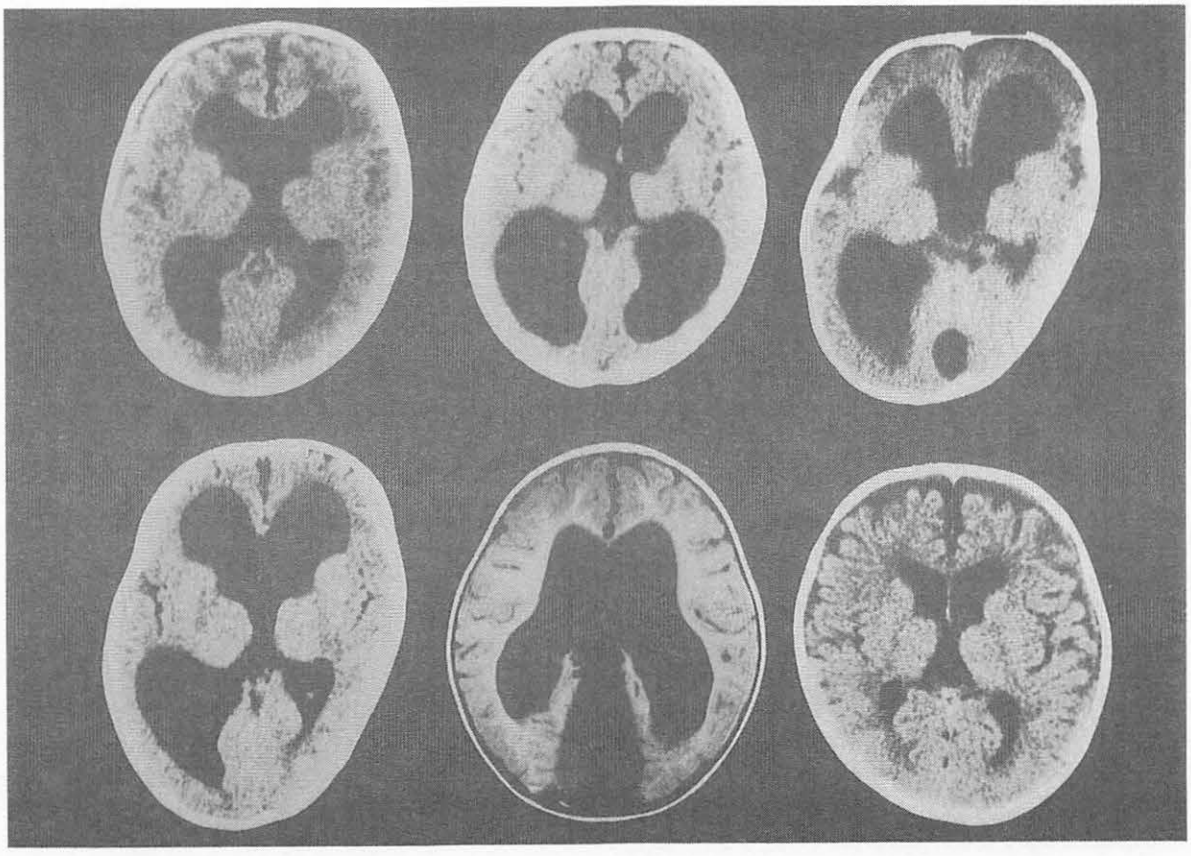

Fig. 1. Tomographic images of six infants with hydrocephalus. Upper: cases 1, 2, 3 Lower: cases4, 5, 6 (from left to right).

(a)

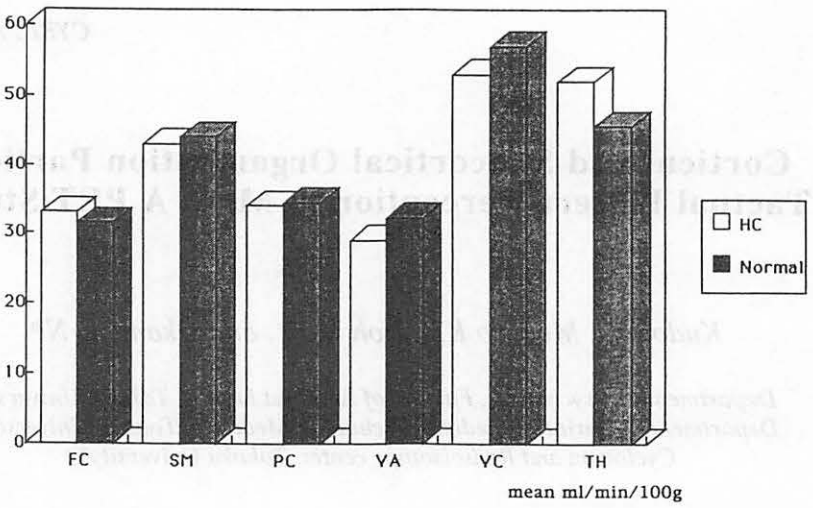

(b)

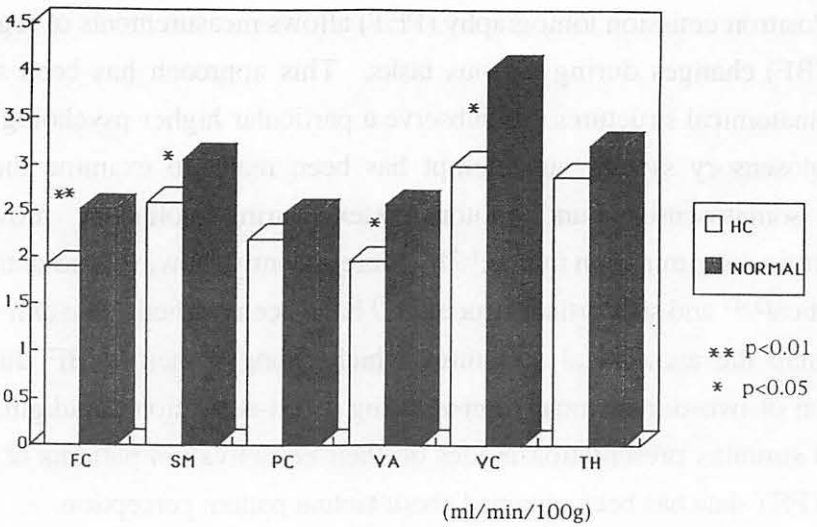

(c)

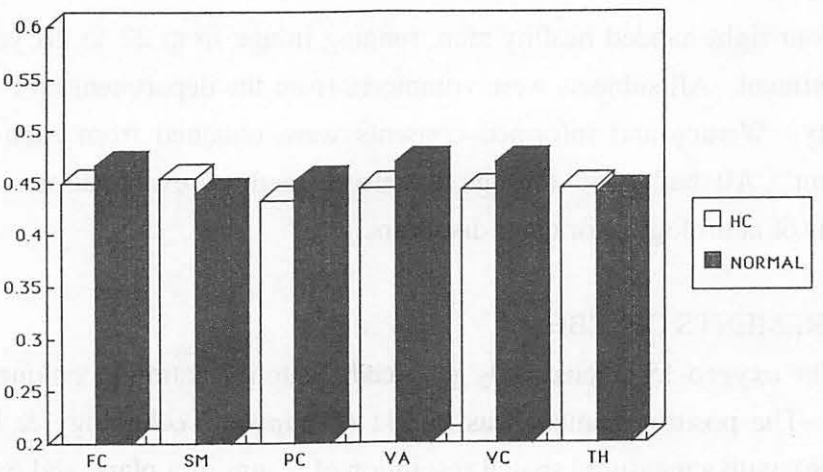

Fig. 2. (A, B, C): Comparison of the mean values of rCBF, rCMRO2, and rOEF in the two groups. FC: frontal association cortex, SM: sensorimotor cortex, PC: parietal cortex, VA: visual association cortex, VC: visual cortex, TH: thalamus.

IV. 11. Cortical and Subcortical Organization Participating in Tactual Pattern Perception in Man: A PET Study

Kudoh N., Meguro K., Itoh M.**, and Okamura N*.*

Department of Psychology, Faculty of Arts and Letters, Tohoku University
*Department of Geriatric Medicine, School of Medicine, Tohoku University**
*Cyclotron and Radioisotope center, Tohoku University***

Introduction

Positron emission tomography (PET) allows measurements of regional cerebral blood flow (rCBF) changes during various tasks. This approach has been successfully used to identify anatomical structures that subserve a particular higher psychological function. As to the somatosensory system, an attempt has been made to examine the activations of the primary somatosensory and motor cortex during voluntary movements, especially stereognostic discrimination in man[1,2]. More recently, however, co-activation patterns with other cortical[3,4] and subcortical structures[5] have been studied. The aim of the present study was to map the anatomical structures which changed their rCBF during tactual pattern perception of two-dimensional figures, using a rest-activation paradigm. We also evaluated effects of stimulus presentation modes on their co-activation patterns of rCBF changes. No available PET data has been obtained about tactual pattern perception.

Methods

SUBJECTS

Four right-handed healthy men, ranging in age from 22 to 28 years, participated in this experiment. All subjects were volunteers from the department of Psychology, Tohoku University. Written and informed consents were obtained from each subject before the experiment. All had gone through extensive medical examinations and none had any symptoms of neurological or other disorders.

MEASUREMENTS OF rCBF

The oxygen-15 labeled CO_2 gas steady-state inhalation technique was used to rCBF changes. The positron camera was PT931 (Computer Technology & Imaging Knoxville, Tennessee), with a measured spatial resolution of 7 mm in a plane and a slice thickness of 7 mm. Count images were used to estimate relative rCBF without arterial sampling. We obtained 2 emission scans of 1.5 min during each tactual mode, and reconstructed a total of

14 PET images of the brain. Emission scans were corrected for individual attenuation characteristics by using transmission scan on the same planes. Furthermore, MRI scanning was performed for each subject with magnetic field of 0.15 telsa and could be used as anatomical templates.

STIMULI AND MODES OF TOUCH

The tactual stimuli were twelve raised-line drawings of familiar objects, produced by the stereo copying system. All drawings were formed by a single continuous line on cards, which defined the outline of the object easily identifiable by sight. An average outline length of 12 drawings was 72.9 cm. The width of the raised lines was 1.5 mm.

The subject explored the drawings with his right index finger in either of 2 modes [2, 3]. In the active mode, the drawings was stationary, and the subject was free to tactually explore one of 12 drawings with any force or velocity. In the tactile mode, the exploring finger remained stationary and the raised drawing was moved, along its outline, beneath his finger tip by the experimenter. Exploration began at the upper part of the raised drawing and proceeded in a clock-wise direction. The same drawing was explored with repetition until the subject made the verbal identification of the drawing.

PROCEDURES

The experiment was conducted at the Cyclotron Radioisotope Center, Tohoku University. The subject lay in the scanning bed on his back, with his head position being carefully set by using light projectors. He had small tubes fixed in his mouth for the inhalation of ^{15}O-CO_2 gas. The right forearm was suspended in a freely moving sling. Thus, exploratory movements in the active mode involved rotations of the elbow and shoulder joints.

Table 1 shows a time schedule used in this experiment. First, a reference of rCBF was determined at a control 1 state. The subject was lying comfortably, with his eyes being closed. He was told not to move and to think of nothing at this state. Then, the subject began to perform each task three or six min prior to rCBF measurements during the tasks in order to facilitate neuronal activities associated with a demand of each task. Prior to the experiment, the subject was instructed to concentrate his fingertip to be stimulated during execution of the task. The presentation order of 12 raised drawings was randomized, and the order of the active and tactile modes was as counterbalanced as possible over 4 subjects.

Results

Serial rCBF images over 4 subjects were accumulated and mean rCBF change images were calculated by pixel-by-pixel (256×256) subtraction of each tactual mode minus control 1. Figure 1 shows the descriptive t-images of mean rCBF changes. Statistically significant increases in rCBF during each mode compared to the control condition (t-test, $p<005$) are

represented in the red zone. As seen in Figure. 1, it is clear that activated areas extended over multiple regions of the whole brain beyond the somatosensory and motor cortex. There also appeared hemispheric asymmetries in the activation patterns: the somatosensory association areas were activated contralaterally to the stimulated hand, whereas there were the bilateral and ipsilateral increases in rCBF in other regions.

The active mode increased rCBF in the contralateral somatosensory cortex, motor cortex, parietal association cortex, cingulate gyrus, ipsilateral midfrontal cortex, midtemporal and inferior temporal cortex, bilateral basal ganglia, and thalamus nuclei. During the tactile mode, rCBF increases were found in the contralateral somatosensory cortex, motor cortex, parietal association cortex, cingulate gyrus, ipsilateral midfrontal and inferior frontal cortex, bilateral basal ganglia, and thalamus nuclei. It appeared that the similar areas were activated during the both modes. However, if the brain organized its activities in a modular way, activities in the somatosensory association areas were strongly co-activated with those in the right temporal cortex in the active mode, and with those in the right frontal cortex in the tactile mode.

Discussion

The main finding in this study was that the tactile mode increased rCBF in about the same regions as the active mode. This finding was parallel to that reported by Roland et al., who demonstrated that tactile learning and tactile recognition of complicated geometrical objects increased rCBF in the same anatomical structures in the cerebral cortex, thalamus, and basal ganglia[5]. The activated areas in this study agreed well with those earlier reported during stereognostic discrimination of three-dimensional objects, except the temporal cortex[1,2,4,6]. The fact that about the same areas could be activated during the both modes suggests that the co-activation patterns of the whole brain are dependent on what is required in the tasks, i.e. identification of tactually perceived figures in this study, rather than on what degree sensory inputs are involved in the tasks. However, a degree of activation or strength of the co-activations seems different between the two modes.

In the psychological experiments, the tactile mode allowed poorest performance at identifying the figures of all the four modes[7,8]. In addition to the active and tactile modes, the passive, where the exploring hand was guided along the raised lines by the experimenter, and proprioceptive modes, where the exploring hand was guided passively along the outline of a figure with no raised lines, were involved in their experiments. With regard to the source of information available to the subject, they indicated that tactile inputs in the absence of proprioceptive ones in the tactile mode were not sufficient to give optimal performance. Therefore, they suggested that proprioceptive information concomitant with movement played a critical role in the tactual pattern recognition. If it is appropriate to apply these findings in this study, a degree of activation during the tactile mode should be smaller than that during the active mode within the peri-rolandic cerebral cortex contralateral to the stimulated hand. As

seen in Figure 1 however, the apparent degree of activation during the active mode was rather less within those areas, despite that a larger amount of information was available to the subject in the active than in the tactile mode. Ginsberg et al.[3] have compared cerebral glucose metabolic rate during active manipulation of mah-jongg tiles with that during passive vibratory stimulation within the somatosensory cortex and found that the mere passive reception of stimuli influenced cortical metabolism less vigorously. They indicated that somatosensory tasks involving active participation and conscious effort could elevate glucose metabolism in the somatosensory cortex. The discrepancy between poorer performance and the larger amount of activation may be explained by conscious effort: that is, the subject may concentrate more attention on his fingertip in the tactile mode because of the limited amount of information.

During the active mode, there were increases in rCBF in the midtemporal and inferior temporal cortex (area TE). It has recently been suggested that a ventral pathway of projections from the striate cortex to the inferior temporal cortex was crucial for the visual identification of objects[9]. Probably, the visual properties of the particular object is coded within area TE, and this area serves as the store for the later recognition. Sampled somatosensory information about the figures might be converted into a visual image, and then, stored visual information might be retrieved from TE for matching, which resulted in the increases in rCBF within these areas during the active mode. On the other hand, greater conscious effort caused rCBF increases within the somatosensory association cortex during the tactile mode, while, because of the limited amount of incoming information, visual images might not be reconstructed in this mode; so that this leads poorer performance than the active mode.

It has been found that the anterior superior prefrontal cortex was strongly activated during tasks in which subjects were required to direct their attention toward a specific sensory modality. Based on these findings, Roland[6] postulated a mechanism of differential turning: there existed two different neural mechanisms during execution of the goal-directed tasks. One participated in the modality-specific information processing such as feature extraction of incoming sensory inputs, perception, and cognition, and the other was selective attention-dependent mechanism independently on stimulus rates and intensities. However, different patterns of co-activation observed in this study support the idea that there exist some separate networks of attention that perform different but interrelated functions[10], rather than the idea that a single neural mechanism acts to control attention. Furthermore, the frontal cortex in the right hemisphere showed localized increases in rCBF during the active and tactile modes, which may indicate that these areas participate in the maintenance of an alert state[10].

In the present study, we could not superimpose PET images on MRI images on the same slice level, so that the anatomical structures participating in tactual pattern perception could not be identified in detail. Further analysis will be necessary in this point.

References

1) Roland, P. E. and Larsen, B., Arch. Neurol. **33** (1976) 551.
2) Roland, P. E. et al., Acta Neurol. Scand. Suppl. **64** (1977) 540.
3) Ginsberg, M. et al., Neurology. **34** (1987) 1301.
4) Roland, P. E., Trends Neurosci. **7** (1984) 430.
5) Roland, et al., Eur. J. Neurosci. **1** (1989) 3.
6) Roland, P. E., J. Neurophysiol. **48** (1982) 1059.
7) Loo, C. K. C. et al., Behav. Brain Res. **7** (1983) 383.
8) Magee, L. E. and Kennedy, J. M., Nature. **283** (1980) 287.
9) Mishkin, M. and Ungerleider, L. G., and Macko K. A., Trends Neurosci. **66** (1983) 414.
10) Posner, M. I. and Petersen, S. E., Annu. Rev. Neurosci. **13** (1990) 25.

Table 1. The time schedule in the experiment.

Time (min)	*Task*	*PET scanning*
20	*rest*	*transmission scanning*
3	*control 1*	*emission scanning 1*
5	*rest*	
6 or 9	*active mode*	*emission scanning 2*
5	*rest*	
6 or 9	*tactile mode*	*emission scanning 3*
5	*rest*	
3	*control 2*	

Note: The presentation order of the active and tactile modes was counterbalanced as possible over 4 subjects.

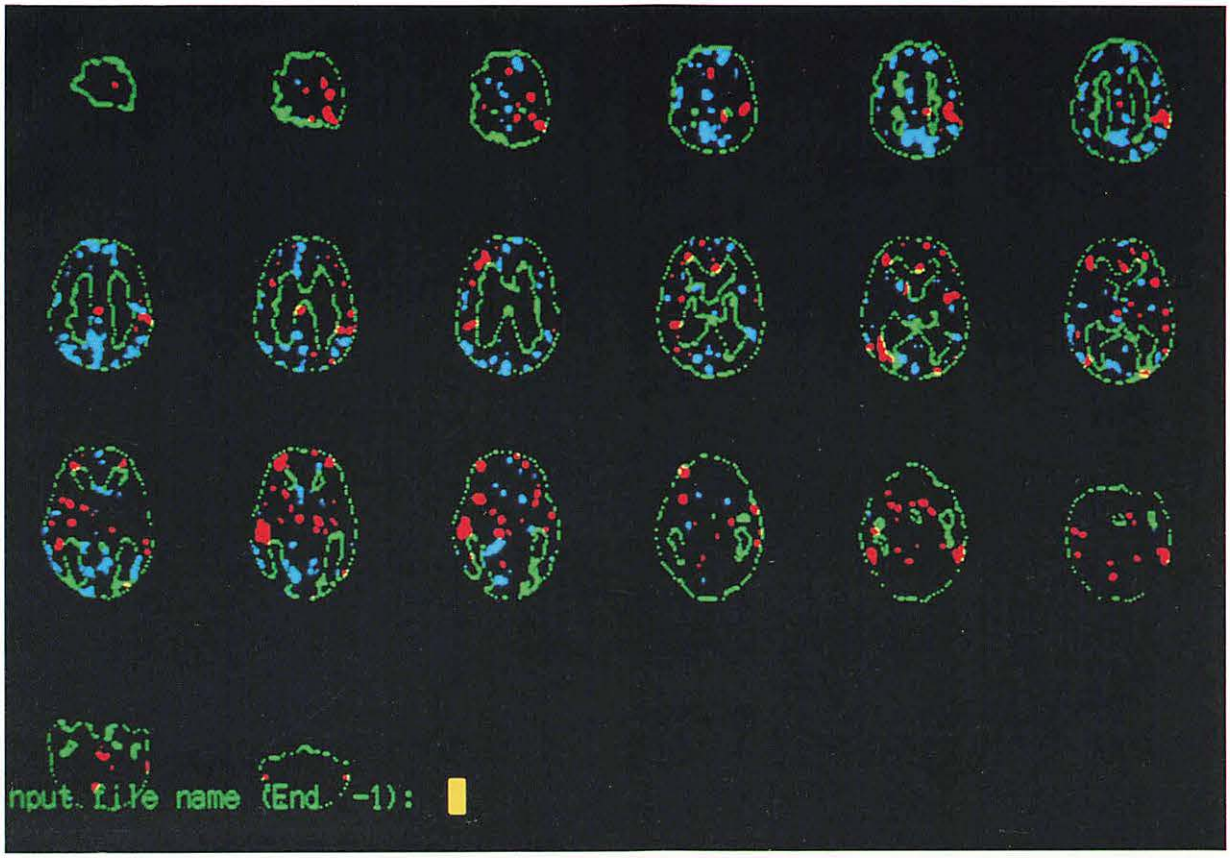

(A)

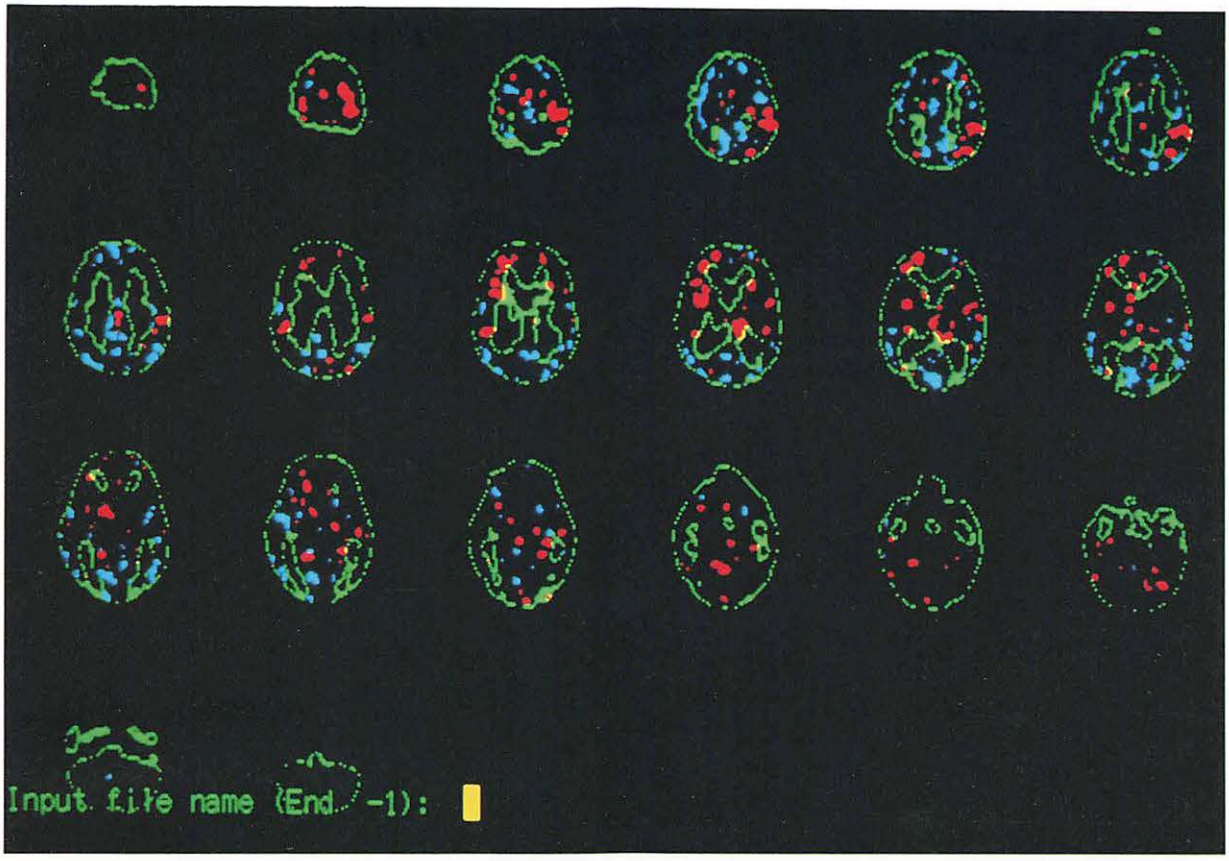

(B)

Fig. 1. Changes in rCBF, induced by the active (upper picture) and tactile (lower picture) modes. Each section of the brain is viewed from below (shown with the right side of the brain to the left). The slices of the brain proceed from the top of the brain to the bottom. During each mode, a marked increase in rCBF compared to the rest condition (t-test; .5% in significance level) is represented in the red zone, and a significant decrease in the blue.

IV. 12. Cerebral Blood Flow and Oxygen Metabolism in Developing Brain

*Takahashi T., Shirane R., Hara Y., Sato S., Yoshimoto T. and Ito M.**

Department of Neurosurgery, Tohoku University School of Medicine
**Division of Nuclear Medicine, CYRIC, Tohoku University*

Introduction

Since glucose and oxygen are the principle substrates for meeting the energy demands of the brain, measurements of the rates at which these substrates are utilized provide an assessment of the level of neuronal function in the brain. Normal values for cerebral blood flow and metabolism in adults are well established[1,2], but not for children except the cerebral metabolic rate for glucose[3,4]. Measurement of the rates of regional substrate utilization in the brain during maturation provide a means whereby local functional activity can be related to various stages of behavioral development. This study measured regional cerebral blood flow (rCBF), regional cerebral metabolic rate for oxygen ($rCMRO_2$), and regional oxygen extraction fraction (rOEF), using positron emission tomography (PET) in children to clarify human brain functional development.

Subjects and Methods

This study included 24 children (11 males, 13 females), aged from 1 month to 16 years old. All subjects had minor neurosurgical problems, but their motor and mental development were normal. None had neurological deficits.

Twenty-six PET studies were performed using a PT-931 scanner (CTI, Knoxville, Tennessee[5]) in accordance with the policies of the Committee for Clinical PET Study of Tohoku University. Informed concent was obtained from the parents. The spartial resolution of the images were 8mm in FWHM and slice thickness was 7mm. Seven or fourteen images were obtained simultaneously. All subjects were scanned at the axial tomographylevel at least from the midbrain to the upper ventricular level. The PET images were reconstructed using attenuation correction. Venous and arterial catheters were inserted in the dorsal venous network of the hand and radial artery, respectively, under local anesthesia. Thiopental sodium was administered (3 mg/kg, intravenous) just prior to the transmission scan to immobilize the patient during the examination. If this did not bring about sufficient sedation, an additional dose (2 mg/kg) was given. All visual, auditory, and other sensory stimuli were

minimized. Measurements of rCBF, and $rCMRO_2$, and OEF were carried out using the steady state inhalation method with $C^{15}O_2$ and $^{15}O_2$, respectively. Arterial blood was drawn for the analysis of blood gases and radioactivity. Head counts in each emission scan were corrected for tissue attenuation using previously performed transmission scan. Oval regions of interest were defined in the primary cerebral cortex, basal ganglia, and association cortex, and verified by magnetic resonance imaging. The absolute values for the children were compared to adult values.

Results

1. rCBF: Infants rCBF values were lower than adults values. rCBF values in the primary cerebral cortex and basal ganglia were higher than those in the cerebral association cortex. rCBF reached the adult level at approximately age 6 months in the primary cortex and basal ganglia, and at age 1 year in the association cortex. Subsequently, gradual increases of rCBF values in all cerebral regions were observed, peaking around age 7 years. Thereafter, the rCBF values fell to the adult level during adolescence (Figure 1 a,b).

2. $rCMRO_2$: Infant $rCMRO_2$ values followed the same trends as rCBF, but the values were somewhat lower than adult values. $rCMRO_2$ gradually increased in all cerebral regions during childhood, reaching the adult level in the primary cerebral cortex and basal ganglia during early childhood, and in the cerebral association cortex after adolescence (Figure 2 a,b).

3. rOEF: rOEF was uniform in all brain regions and showed no remarkable changes during development, but stayed within the adult level. Somewhat lower values were observed in school age subjects (Figure 3 a,b).

Discussion

During development, the brain undergoes the sequential anatomical, functional, and organizational changes necessary to support the complex adaptive behavior of a fully mature normal individual and has good plasticity. One approach to the study of these phenomena has been to measure regional substrate utilization at different stages of cerebral maturation. Since the development of the N_2O method for measuring cerebral blood flow[6], due to progress the non-invasive method for measuring cerebral blood flow and metabolism such as single photon emission computed tomography and positron emission tomography, the measurements of cerebral blood flow and metabolism are useful for not only adults but also children[3,4,7-9], both in normal and pathological individuals[2,10]. But in children, it is difficult to judge the value because of no normal control value including changes during development[9].

The reports for developmental changes of regional cerebral blood flow and metabolism from infant to adult were rare, Chugani et al studied regional cerebral metabolic rates for glucose (rCMRglc) using 2-deoxy-2[^{18}F]fluoro-D-glucose[3,4]. In these studies, the distribution of high values for rCMRGlc corresponded to the well developed cerebral regions

for every childhood. Therefore the changes of the distribution for rCMRGlc were considered to be the change of the brain during development. In our study, in the distribution for rCBF and $rCMRO_2$ the same trend were observed. But the period and course of the changes for rCBF and $rCMRO_2$ were different, furthermore rOEF was uniform during childhood. These results were very interesting to consider the developing brain.

This study will contribute to clarifying not only functional development but also much pathophysiology in child's brain. For example in the report of CBF and oxygen metabolism in infants with hydrocephalus[9], lower rCBF and higher rOEF values were observed, and the regional differences in $rCMRO_2$ were not as evident as those observed in rCBF. Higher rOEF was obviously abnormal, this indicated metabolic deterioration produced by venticulomegaly. On the other hand, maturational raise in $rCMRO_2$ is somewhat later than in rCBF. Just because this phenomenon would be obtained, metabolic deterioration do not always occur. The value should be investigated detailed in accordance with the results of this study.

Conclusion

1. A notable increase in rCBF and $rCMRO_2$ occurred during early childhood. rCBF values were higher than those of adults, peaking around age 7 years, while $rCMRO_2$ showed a gradual increase.

2. rCBF and $rCMRO_2$ values reached the adult level during adolescence.

3. Dynamic changes were observed in rCBF and $rCMRO_2$ in infants and young children, while rOEF was stable during childhood.

References

1) Frackowiak R. S. J., Lenzi G. L., Jones T., J Comput. Assist. Tomogr. **4** (1980) 727.
2) Lammertsma A. A., Wise R. J. S., J Cereb. Blood Flow Metab. **3** (1978)425.
3) Chugani H. T., Phelps M. E., Science **231** (1986) 840.
4) Chugani H. T., Phelps M. E., Mazziotta J. C., Ann. Neurol. **22** (1987) 487.
5) Spinks T. J., Guzzardi R., Bellina C. R., J Nucl. Med. **29** (1983) 1833.
6) Ketty S. S., Schmidt C. F., Am. J Physiol. **143**(1945) 53.
7) Altman D. I., Volpe J. J., Powers W. J., J Cereb. Blood Flow Metab. 9 [suppl1] (1989) S25.
8) Rubinstein M., Denays R., Ham H. R., J Nucl Med **30** (1989) 1982.
9) Shirane R., Sato S., Sato K., Child's Nerv. Syst. **8** (1992) 118.
10) Ogawa A., Kameyama M., Muraishi K., J. Neurosurg **76** (1992) 955.

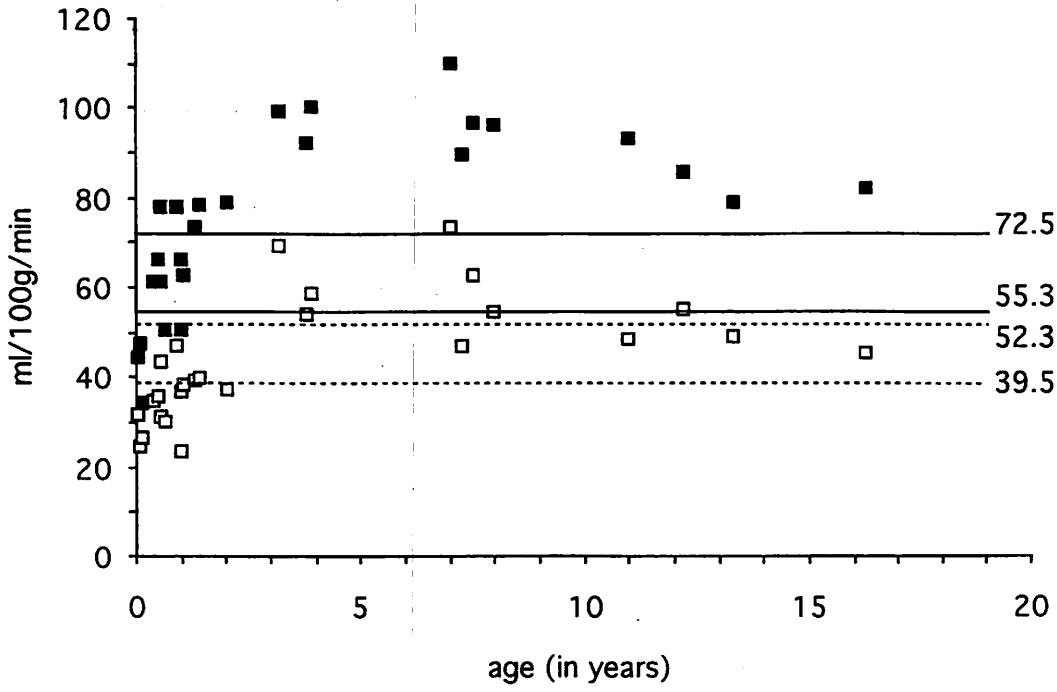

(a)

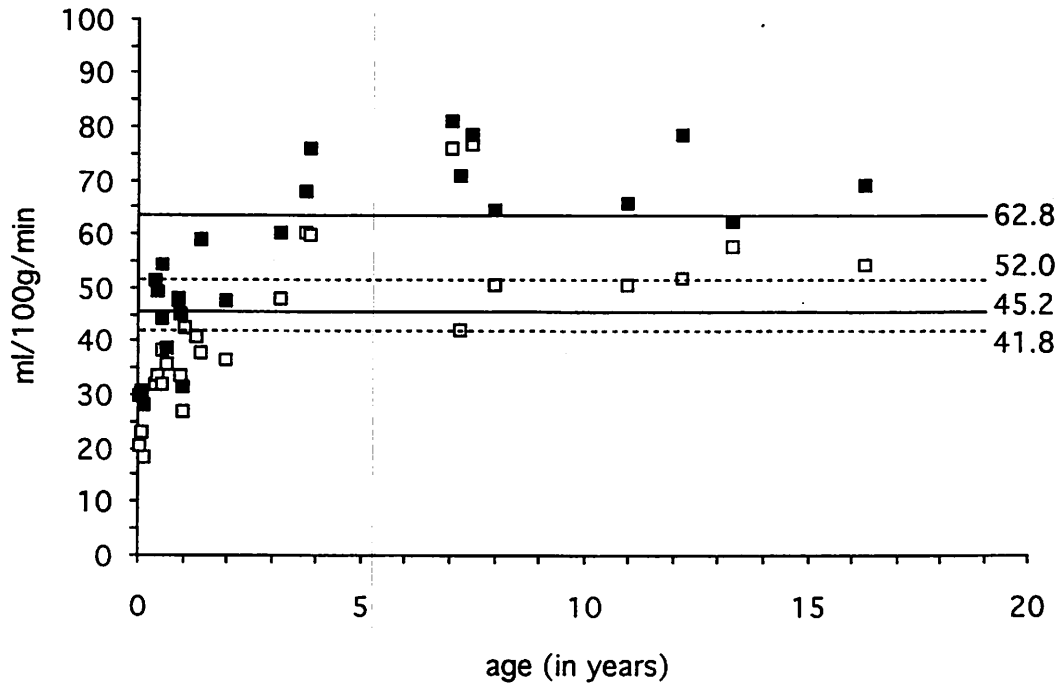

(b)

Fig. 1. Sequential changes of rCBF at visual and visual association cortices (a; : ■ visual, □ : visual association), and at senseorimotor and frontal association cortices (b; ■ :sensorimotor, □ :frontal asocisation). Adult's values are indicated with lines at visual (a), and sensorimotor cortices (b), and with dotted lines at visual association (a), and frontal association (b) cortices.

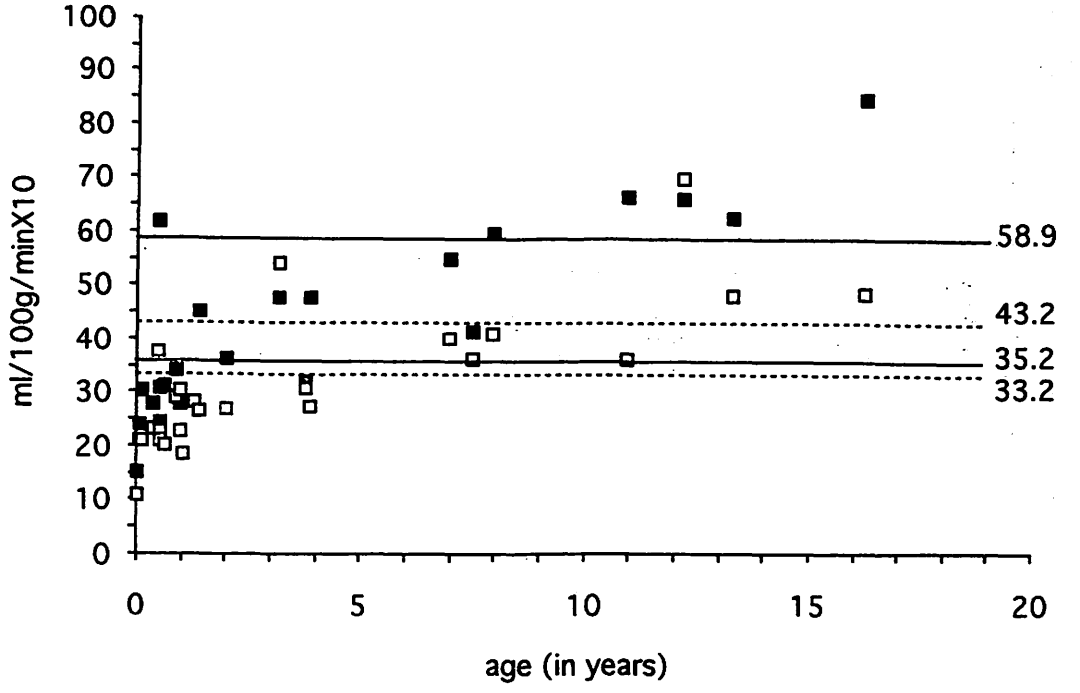

(a)

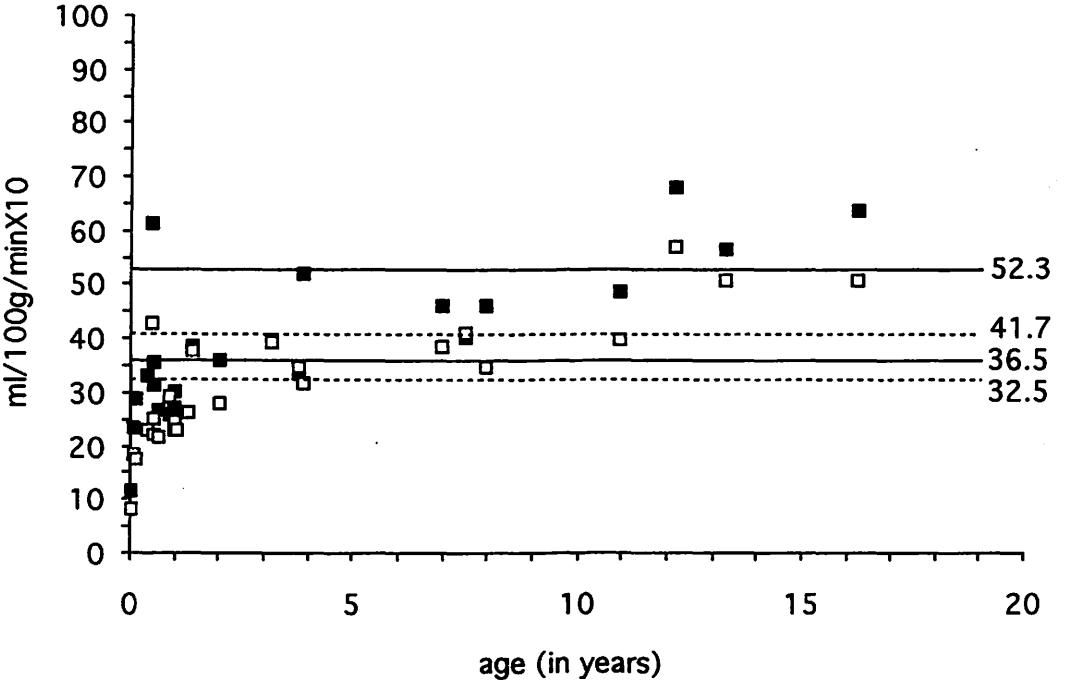

(b)

Fig. 2. Sequential changes of $rCMRO_2$ at visual and visual association cortices (a; ■ : visual, □ : visual association), and at senseorimotor and frontal association cortices (b; ■ : sensorimotor, □ : frontal asocisation). Adult's values are indicated with lines at visual (a), and sensorimotor cortices (b), and with dotted lines at visual association (a), and frontal association (b) cortices.

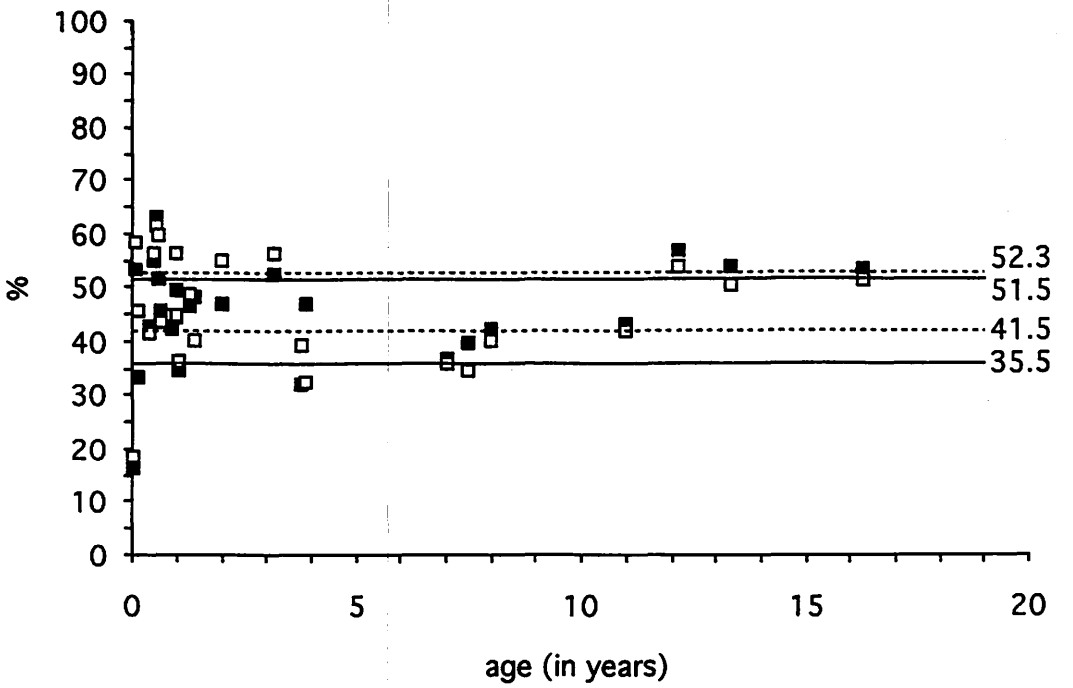

(a)

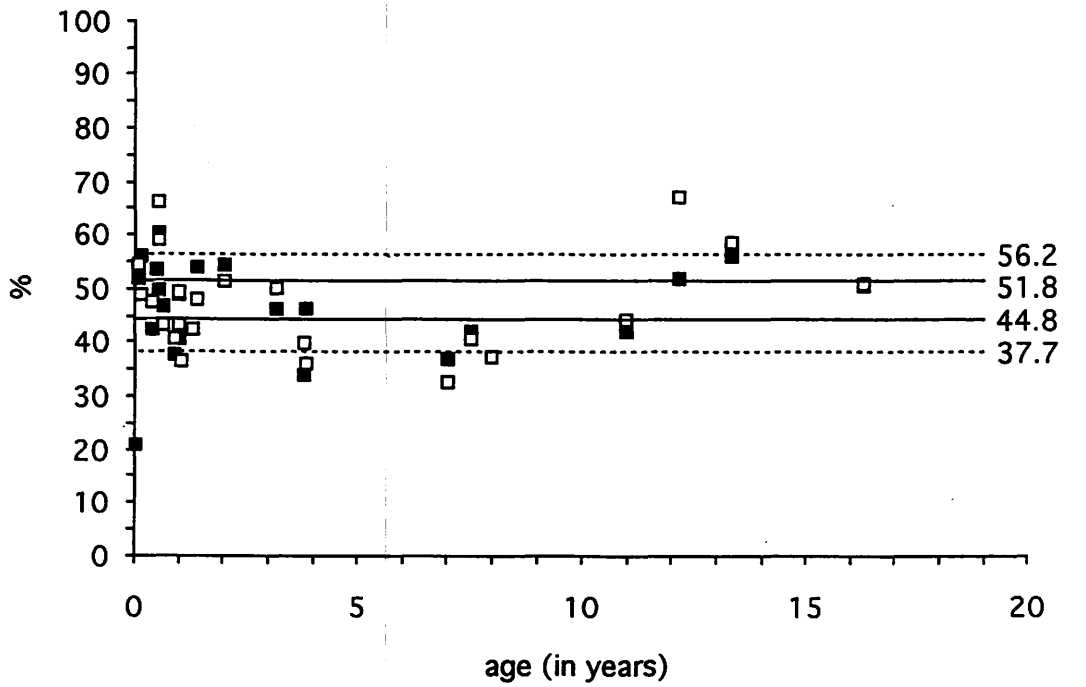

(b)

Fig. 3. Sequential changes of rOEF at visual and visual association cortices (a; ■ : visual, □ : visual association), and at senseorimotor and frontal association cortices (b; ■ :sensorimotor, □ :frontal asocisation). Adult's values are indicated with lines at visual (a), and sensorimotor cortices (b), and with dotted lines at visual association (a), and frontal association (b) cortices.

V. RADIATION PROTECTION AND TRAINING OF SAFEHANDLING

V. 1. An External Approach for Organ Biodistribution and Dose Estimation due to Intake of Radiopharmaceuticals by IP and TLD

Deloar H. M. , Yamadera A., Nakamura T., Fujiwara T., Itoh, M.

Cyclotron and Radioisotope Center, Tohoku University

Introduction

In the nuclear medicine procedure internal dose estimation due to intake of the radioisotope has been established by the MIRD committee of the Society of the Nuclear Medicine[1].

Matsumoto et al. 2, have developed a new method to estimate the cumulated activities in source organs from external measurement with TLD (Thermo-Luminescent Dosimeter) during PET study, by coupling with the mathematical unfolding analysis.

In our present study the same method was applied to a simultaneous external measurement with IP (Imaging Plate) and TLD which were attached on the body surface close to the source organs. In diagnostic radiography the application of IP is increasing as a more sensitive image sensor than the conventional X-ray film. We tried to use IP having much higher sensitivity and larger sensitive zone than TLD for this internal dosimetry. But IP has highly increasing sensitivity with decreasing energy, while TLD has rather flat energy response, then we compared both results obtained by IP and TLD. Using these obtained results, the absorbed doses in the target organs were estimated with the MIRD method.

Material and Methods

IP (BAS-UR, Fuji Photo Film Co. Ltd.) and TLD of BeO (UD-170A, Matsushita Electric Co., Ltd) have been used for the experiment. During the PET study both IP and TLD were placed at nine positions together on the skin surface of the subject as shown in Figure 1. Nine positions were selected to be close to nine organs. 20 mCi of ^{11}C labeled radiopharmaceutical (benzotropin) was injected intravenously for the PET study. During the experiment both IP and TLD were exposed by the internal radiation. In order to get the absorbed dose in mSv from the measured value of IP and TLD, the conversion factor of PSL(Photo-Stimulated Luminescence)/mm^2 to mSv and the TLD reader calibration factor must be known. These factors were obtained with the measurement of a 13mCi ^{18}F point

source and water absorber. Since IP has non-uniform response, differently from TLD, the conversion factor PSL/(mm)^2 per mSv must change with photon energy.

In our present approach we have used the conversion factor of 836 mSv per PSL/mm^2 for 511 KeV gamma rays of ^{18}F, without absorber, as the first approximation.

Dose Calculation

In the dose calculation by the MIRD method, the absorbed dose D_i in i-th target organ is expressed by a sum of contributions from several source organs as follows;

$$D_i = \sum_j S_{ij} A_j, \qquad (1)$$

where A_j is the cumulated activity in the j-th source organ. In this study the target organ is replaced by the IP and TLD position as

$$C_i = \sum_j R_{ij} X_j, \qquad (2)$$

where C_i is the absorbed dose measured at the i-th IP and TLD position, X_j is the integrated activity in the j-th source organ during IP and TLD attachment on the body surface and R_{ij} absorbed dose at the i-th position per unit cumulated activity in j-th source organ. The R value of IP and TLD for each position was calculated by the VADMAP simulation code[3] in which the MIRD mathematical phantom models the geometry of human organs. The cumulated activity of the source organ, X_j was obtained from Eq. 2 using the SAND-II unfolding code[4] based on successive iteration method.

After IP and TLD measurement the contribution of residual cumulated activities was estimated by assuming only a physical decay without a biological clearance, and the cumulated activity of each source organ A_j was finally estimated. The absorbed doses of the target organs only for gamma ray were calculated from Eq. (1) using the IDES code[5].
The effective dose equivalent can be estimated from the following equation

$$H_E = \sum_i w_i H_i = \sum_i w_i D_i \qquad (3)$$

where w_i is the organ weighting factor given by ICRP 60, and H_i is the organ dose equivalent.

Result and Discussion

Figures 2 and 3 show the absorbed dose C obtained at nine positions and the cumulated activities A for eight source organs excluding the remainder of the body, respectively. The figures clearly show that the results obtained by IP are higher than those by TLD, except brain. This difference mainly comes from the conversion factor, PSL/mm^2 per mSv, of IP used in this study. The present value was obtained for 511 KeV gamma rays, but

the exact conversion factor must be a larger value, since the gamma ray energy becomes lower on the body surface after penetration through a body and the IP sensitivity becomes higher for lower energy. The use of the proper conversion factor considering the energy dependence may give better agreement of cumulated activities obtained by IP with those by TLD. Figure 4 shows the absorbed doses of target organs obtained by IP and TLD. Both data give good agreement in general tendency, although the absolute values are larger for IP than for TLD. Pancreas, spleen, heart-wall, kidney and bladder give higher dose in this descending order. The effective dose equivalent estimated by IP is 1.75E-02(mSv/MBq) and by TLD is 1.45E-02(mSv/MBq). Generally speaking, the internal dose values given by IP and TLD indicate good agreement.

References

1) Loevinger R., et al., Soc. Nucl. Med.Inc., New York (1998).
2) Matsumoto M., et al., Med. & Biol. Eng. Comp., **31, 151** (1993).
3) Yamaguchi Y., et al., JAERI **M 87-186** (1987).
4) McElroy W. N. et al., AFWL-TR-67-41, Air Force Weapons Laboratory (1967).
5) Yamaguchi H., NIRS-**M-51** (1984).

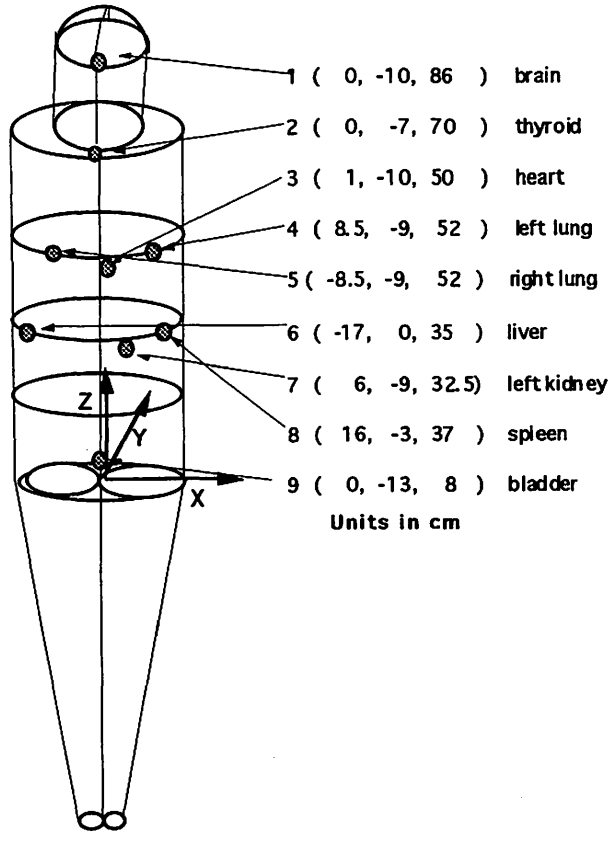

Fig. 1. Schematic diagram of the MIRD mathematical phantom and the positions of IP and TLD attachment on the body surface, together with the Cartesian coordinates.

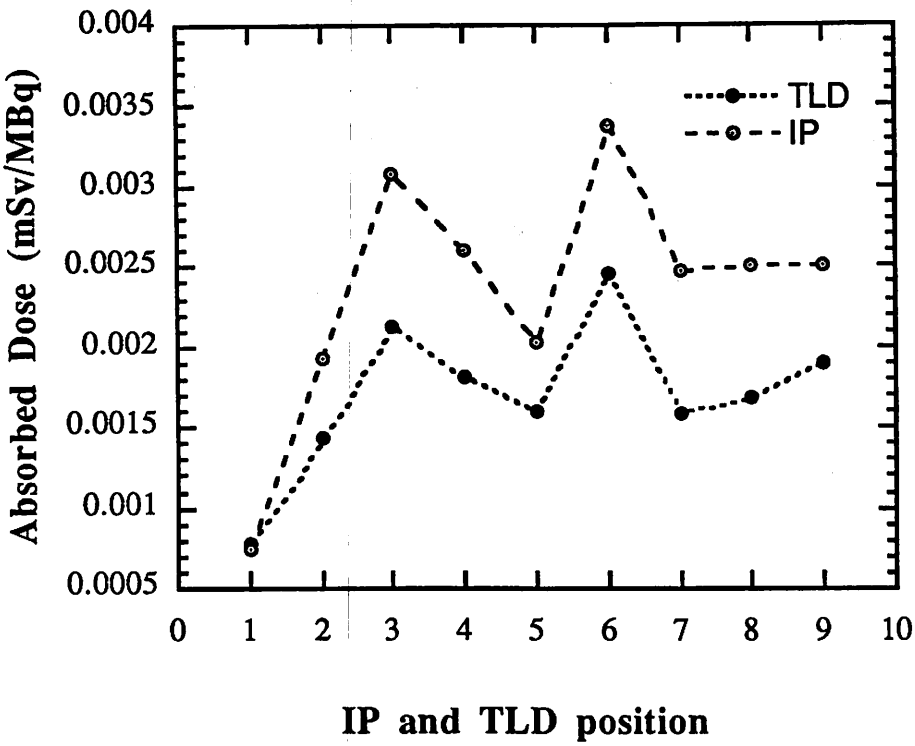

Fig. 2. Absorbed doses at nine positions on the body surface obtained by IP and TLD.

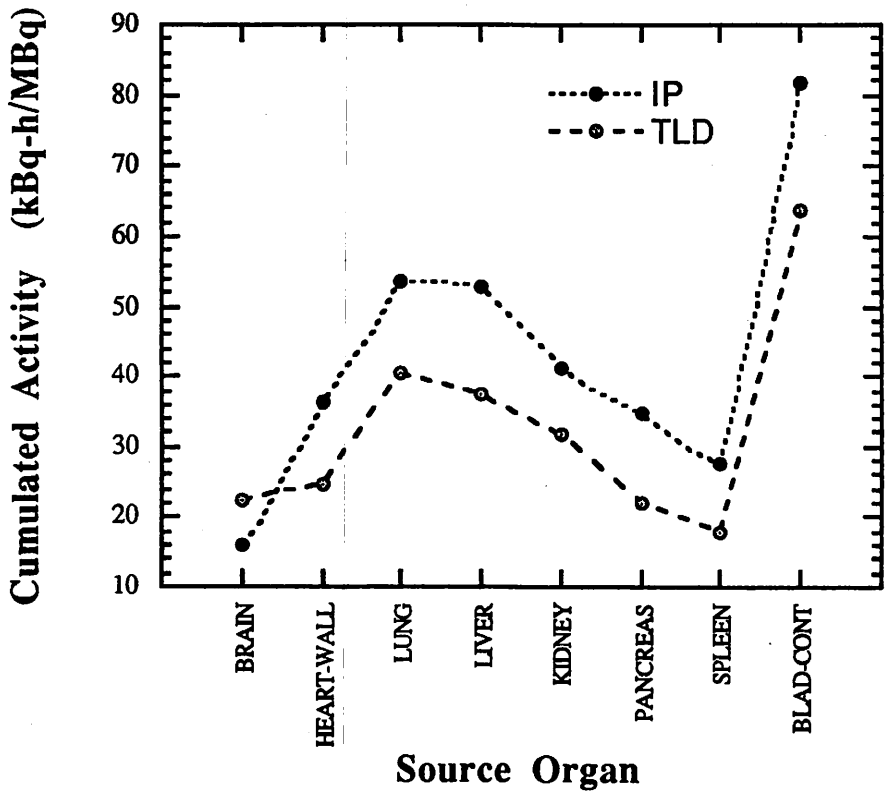

Fig. 3. Cumulated activities of eight source organs estimated by IP and TLD.

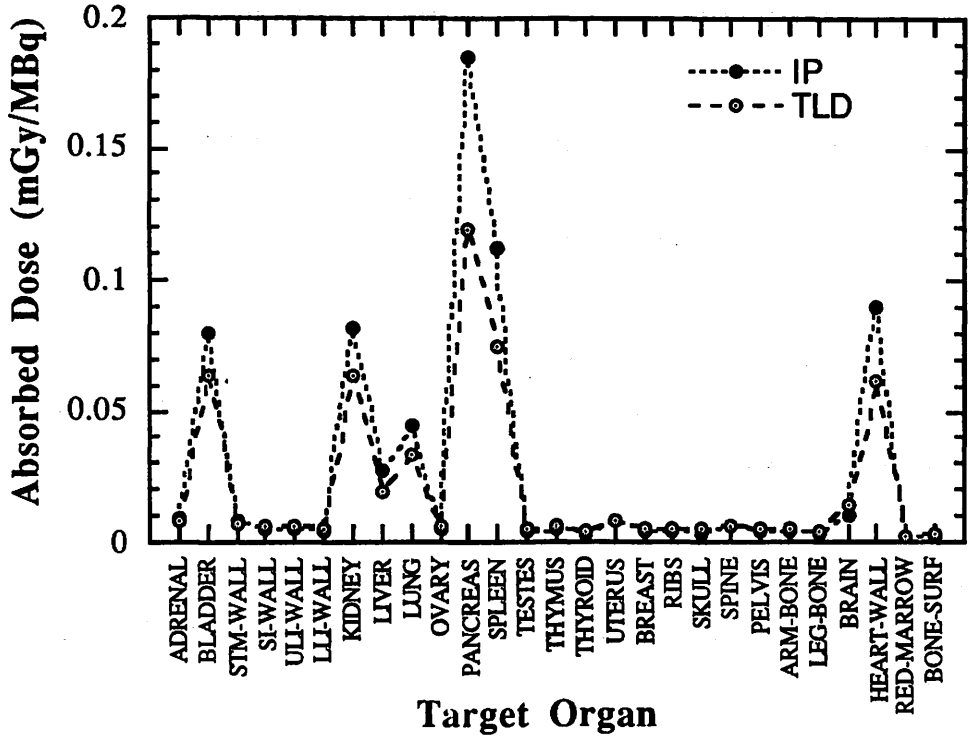

Fig. 4. Absorbed doses for various target organs estimated by IP and TLD.

V. 2. Radiation Protection and Management

Miyata T., Yamadera A., Nakamura T., Satake Y. and Watanabe N.**

Cyclotron and Radioisotope Center, Tohoku University
*Japan Radiation Protection Co., Ltd.**

(1) Unsealed radionuclides used in the center

The kinds and activities of unsealed radionuclides handled in the center in 1994 are shown in Table 1. The table includes the isotopes produced by the cyclotron, purchased from the Japan Isotope Association and took over from another RI institutes.

(2) Individual monitoring

The exposure doses of the workers in the center in 1994 is given in Table 2. They were less than the permissible doses.

(3) Monitoring of the workplace

Radiation dose rates inside and outside of the controlled areas were monitored periodically and as needed. They were below the legal permissible levels. Surface contamination levels of the floors inside the controlled areas were measured by smear method and with survey meters periodically and as needed. They also cleared under the legal regulation levels.

(4) Wastes management

The radioactive wastes delivered to the Japan Radioisotope Association in 1994 are shown in Table 3. The concentration of radioisotopes in the air released after filtration from the stack was monitored with stack gas monitors. The levels were less than the legal regulation levels. The radioactive water was storaged at the tanks at least for 3 days and then released to the sewerage after confirming that the concentration was less than permissible levels.

The treated volume of radioactive waste of organic scintillator was 1773 ℓ by the incinerator made by Fujikogyo Co., Ltd.

Table 1. Unsealed radionuclides used in the center in 1994 .

(a)Cyclotron Building	(kBq)
2. ^{54}Mn	4,000.000
total	4,000.000
3. ^{11}C	532,581,850.000
^{111}In	2,508,718.000
^{28}Mg	2,664.000
^{61}Cu	3,000.000
^{55}Fe	4,000.000
total	535,840,232.000
4. ^{18}F	289,246,800.000
^{51}Cr	7,400.000
total	289,254,200.000
(b) R I Building	(kBq)
1. ^{90}Sr	330.000
total	330.000
2. ^{45}Ca	96,569.388
^{60}Co	126.000
^{68}Ge	84,342.000
^{125}I	553,682.591
^{137}Cs	369.940
^{160}Tb	11,332.200
^{170}Tm	9,028.100
^{65}Zn	4,720.000
total	760,170.219
3. ^{11}C	3,372,100.000
^{123}I	133,200.000
^{131}I	47,028.333
^{140}La	138.210
^{177}Lu	31,037.200
^{28}Mg	1,653.900
^{32}P	2,306,400.062
^{35}S	590,377.600
^{153}Sm	208.860
^{48}V	0.010
^{175}Yb	10,201.500
total	6,492,345.675
4. ^{14}C	149,290.500
^{18}F	188,251,160.629
^{3}H	37,870,268.514
total	226,270,719.643
(c)Research Building	(kBq)
3. ^{11}C	5,718,350.000
total	5,718,350.000
4. ^{18}F	3,744,400.000
total	3,744,400.000

Table 2. Occupational radiation exposures at the center in 1994.

Dose range (mSv)	Number of individuals
No measurable exposure	30
Measurable exposure less than 1.0	7
1.0 to 2.5	2
2.5 to 5.0	2
5.0 to 10.0	0
10.0 to 15.0	0
Total persons monitored	41

Table 3. Radioactive wastes delivered to the Japan Radioisotope Association in 1994.

Wastes	Container	Number
solids		
combustibles	50 ℓ drum	41
incombustibles	50 ℓ drum	22
dried animals	50 ℓ drum	4
liquids		
inorganic substances	25 ℓ PE bottle	7

V. 3. Training for Safehandling of Radiation and Radioisotopes and X-Ray Machines for Beginners in Tohoku University

Nakamura T., Yamadera A. and Miyata T.

Cyclotron and Radioisotope Center, Tohoku University

Training for safehandling of radiation and radioisotopes for beginners has been conducted twice a year from 1977 in Tohoku University. The contents of lectures and practices are shown in Table 1. In 1994 the training was performed for 477 persons. The departments to which they belong are given in Table 2.

Training for safehandling of X-ray machines and electron microscopes began from the end of 1983. The training is scheduled to be held twice a year at the same time as the safehandling of radiation and radioisotopes. Only lectures are given and not practices. The contents of the lectures and the distributions of trainees are shown in Tables 3 and 4, respectively.

Table 1. Contents of lectures and practices for safehandling of radiation and radioisotopes in 1994.

Lectures (one day)	
Radiation physics and measurements	1.5 (hours)
Chemistry of radioisotopes	1.0
Radiological protection ordinance	1.0
Effects of radiation on man	1.0
Safehandling of radioisotopes	1.5
VTR for safehandling of radiation and radioisotopes	2.0

Practices (one day)	
Treatment of unsealed radioactive solution (hours)	4.0
Measurements of surface contamination and decontamination	1.0
Measurements of gamma rays and beta rays	2.0

Table 2. Distribution of trainees for safehandling of radiation and radioisotopes in 1994.

Department	Staff	Student	Total
Faculties			
Medicine	21	112	133
Dentistry	1	5	6
Pharmacy	0	40	40
Science	7	103	110
Engineering	5	33	38
Agriculture	1	70	71
Research Institutes	10	69	79
Total	45	432	477

Table 3. Contents of lectures for safehandling of X-ray machines and electron microscopes in 1994.

Safehandling of X-ray machines	1.5 (hours)
Radiological protection ordinance	1.0
VTR for safehandling of radiation and radioisotopes	1.0

Table 4. Distribution of trainees for safehandling of X-ray machines and electron microscopes in 1994.

Department	Staff	Student	Total
Faculties			
Medicine	2	13	15
Science	1	19	20
Engineering	9	66	75
Agriculture	0	0	0
Research Institutes	25	84	109
Total	37	182	219

VI. PUBLICATIONS

VI. Publications

(January 1994 ~ December 1994)

A

1. Gamow-Teller strengths near the ground states in A = 110 - 120 nuclei studied by (p, n) reaction.
Orihara H., Zhong G. C. Hosaka M., Ishimaru H., Itoh K., Miyamoto S., Terakawa T., Ishii K., Narita A., Yujii Y., Nakagawa T., Miura K., and Ohnuma H.
Nuclear Physics **A577**(1994)9-12.

2. Measurement of Gamma-Ray Production Cross Sections of Iron for Incident Neutron Energies between 6 and 33 MeV.
Tanabe E., Shin K., and Nakamura T.
Journal of Nuclear Science and Technology **31-11**(1994)1133-1142.

3. Residual Long-Lived Radioactivity Distribution in the Inner Concrete Wall of a Cyclotron Vault.
Kimura K-I., Ishikawa T., Kinno M., Yamadera A., and Nakamura T.
Health Physics **67-6**(1994)621-631.

4. Assessment of dopamine metabolism in brain of patients with dementia by means of ^{18}F-fluorodopa and PET.
Itoh M., Meguro K., Fujiwara T., Hatazawa J., Iwata R., Ishiwata K., Takahashi T., Ido T., and Sasaki H.
Annals of Nuclear Medicine **8-4**(1994)245-251

5. Detection Limit for a very Thin Backing Film.
Ishii K., Orihara H., Iwata Y., and Bessho K.
International Journal of PIXE **4-1**(1994)1-7.

6. Neutron Penetration Through Iron and Concrete Shields with the Use of 22.0- and 32.5-MeV Quasi-Monoenergetic Sources
Ishikawa T., Miyama y., and Nakamura T.
Nuclear Science and Engineering **116**(1994)278-290.

B

7. Nuclear g-factors of the 1229 and 2911 keV isomers in ^{143}Nd.
Kawamura N., Higashino I., Kimura M., Fujioka M., and Hayashibe S.
Zeitschrift für Physik **A348**(1994)173-176.

8. Characteristics of a single-wire proportional counter with very thin rectangular cross section.
Kageyama K., Hayashibe S., Kanazawa M., Watanabe H., and Fujioka M.
Nucl. Instr. Methods in Physics Research **A342**(1994)509-515.

9. Spectrum of proton-induced mutagenesis of the Escherichia coli crp gene
Takimoto K., Yamamoto K., Sagara T., and Ishizaki K.
Mutation Res., DNA Repair **314**(1994)1-9.

10. Microautoradiographic Study for the Differentiation of Intratumoral Macrophages, Granulation Tissues and Cancer Cells by the Dynamics of Fluorine-18-Fluorodeoxyglucose Uptake.
Kubota R., Kubota K., Yamada S., Tada M., Ido T., and Tamahashi N.
The Journal of Nuclear Medicine **35-1**(1994)104-112.

11. Alteration of muscarinic acetylcholine binding sites in the postischemic brain areas of the rat using in vitro autoradiography.
Nagasawa H., Araki T., and Kogure K.
Journal of the Neurological Science **121**(1994)27-31.

12. Accumulation of 2-Deoxy-2[^{18}F]Fluoro-D-Glucose in Human Cancers Heterotransplanted in Nude Mice: Comparison Between Histology and Glycolytic Status.
Yoshioka T., Takahashi H., Oikawa H., Maeda S., Wakui A., Watanabe T., Tezuka F., Takahashi T., Ido T., and Nakamura R.
*Journal of Nuclear Medicine***35-1**(1994)97-103.

13. Technetium(VII) extraction by a primary amine and technetium(VII) coprecipitationwith ammonium diuranate in hydrofluoric acid solution.
Itoh K., and Akai-Imoto Y.
Journal of Radioanal. and Nuclear Chemistry, Articles **178-1**(1994)41-53.

14. Multi-focal metabolic disturbances in human brain after cerebral infarction studied with ^{18}FDG and positron emission tomography
Nagasawa H., Kogure K., Itoh M., and Ido T.
NeuroReport **5**(1994)961-964.

15. Heterogeneous distributions of histamine H3, dopamine D1 and D2 receptors in rat brain.
Hoon Ryu J., Kogure K., Itoh M., and Ido T.
NeuroReport **5**(1994)621-624.

16. Active and Passive Mechanisms of [Fluorine-18] Fluorodeoxyglucose Uptake by Proliferating and Prenecrotic Cancer Cells In Vivo: A Microautoradiographic Study.
Kubota R., Kobota K., Yamada S., Tada M., Ido T., and Tamahashi M.
Journal of Nuclear Medicine **35-6**(1994)1067-1075.

17. Binding Characteristics of a Histamine H_3-Receptor Antagonist, [^{3}H]*S*-Methylthioperamide: Comparison with [^{3}H](*R*)α-Methylhistamine Binding to Rat Tissues.
Yanai K., Hoon Ryu J., Sakai N., Takahashi T., Iwata R., Ido T., Murakami K., and Watanabe T.
Jpn. J. Pharmacol. **65**(1994)107-112.

18. An Efficient Synthesis of N^{ω}-[^{18}F]Fluoroacetylserotonin (N^{ω}-[^{18}F]Fluoroacetyl-5-hydroxytryptamine)
Tada m., Iwata R., Sugiyama H., Sato k., Fukuda h., Kubota K., Kubota R., Takahashi H., Wakui A., and Ido T.
Journal of Labelled Compounds and Radiopharmaceuticals **34-4**(1994)741-746.

19. Delayed damage of striatal interneurons after cerebral ischemia in the gerbil.
Araki T., Kato H., Liu X-H., Itoyama Y., Kogure K., and Kato K.
Neuroscience Letters **176**(1994)17-20.

20. Alteration of adenosine A_1 receptor binding in the post-ischaemic rat brain.
Nagasawa H., Araki T., and Kogure K.
NeuroReport **5**(1994)1453-1456.

21. Cerebral circulatory and metabolic changes following EC/IC bypass surgery in cerebral occlusive diseases.
Muraishi K., Kameyama M., Sato K., Sirane R., Ogawa A., Yoshimoto T., Hatazawa J., and Ito M.
Neurological Research **15**(1993)97-103.

22. Effect of pentobarbital on postischemic MK-801, muscimol, and naloxone bindings in the gerbil brain.
Kanai Y., Araki T., Kato H., and Kogure K.
Brain Research **657**(1994)51-58.

23. Functional anatomy of taste perception in the human brain studied with positron emission tomography.
Kinomura S., Kawashima R., Yamada K., Ono S., Itoh M., Yoshida S., Yamaguchi T., Matsui H., Miyazawa H.
Brain Research **659**(1994)263-266.

24. Metabolic disturbances in exo-focal brain areas after cortical stroke studied by positron emission tomography.
Nagasawa H., Kogure K., Fujiwara T., Itoh M., and Ido T.
Journal of the Neurological Sciences **123**(1994)147-153.

25. Effects of Vinconate and Pentobarbital against Postischemic Alterations in Spirodecanone Binding Sites in the Gerbil Brain.
Murakami F., Araki T., Kanai Y., Kato H., Fujiwara T., Kogure K.
Pharmacology **49**(1994)286-295.

26. Autoradiographic distribution of neurotransmitter and second messenger system receptors in animal brains.
Kanai Y., Araki T., Kato H., Kogure K.
Behavioural Brain Research **65**(1994)67-73.

27. Age-dependent changes in second messenger and rolipram receptor systems in the gerbil brain.
Araki T, Kato H., Kanai Y., Kogure K.
Journal of Neural Transmission, [Gen Sect] **97**(1994)135-147.

28. Autoradiographic Analysis of Second-Messenger and Neurotransmitter Receptor Systems in the Exo-Focal Remote Areas of Postischemic Rat Brain.
Nagasawa H., Araki T., and Kogure K.
Brain Research Bulletin **35-4**(1994)347-352.

29. An Immunohistochemical Study of Parvalbumin Containing Interneurons in the Gerbil Hippocampus After Cerebral Ischemia.
Araki T., Kato H., Liu X-H. Kato K., and Itoyama Y.
Metabolic Brain Disease **9-3**(1994)225-234.

30. Effects of diluted sewage on biochemical parameters of carp, *Cyprinus carpio.*
Kakuta I., Ishii K., and Murachi S.
*Comp. Biochem. Physiol.***107C-2**(1994)289-294.

VII. MEMBERS OF COMITTEES

VII. Members of Committees (as of Jan. 1, 1995)

General

(Chairman)	Hikonojo	Orihara	(CYRIC)
	Tsutomu	Tohei	(Faculty of Science)
	Yoshiaki	Fujii	(Faculty of Science)
	Takashi	Yoshimoto	(School of Medicine)
	Tadashi	Yamada	(School of Dentistry)
	Yasuo	Suzuki	(Faculty of Pharmaceutical Sciences)
	Katsunori	Abe	(Faculty of Engineering)
	Shichiro	Sugawara	(Faculty of Agriculture)
	Reimon	Hanada	(Institute for Materials Research)
	Ken-ichi	Akiba	(Research Institute for Mineral Dressing and Metallurgy)
	Takeo	Fujino	(Research Institute for Mineral Dressing and Metallurgy)
	Hiroshi	Fukuda	(Institute for Development, Aging and Cancer)
	Kiyohiko	Sakamoto	(School of Medicine)
	Yasushi	Inoue	(Faculty of Engineering)
	Masumi	Sugawara	(Faculty of Science)
	Manabu	Fujioka	(CYRIC)
	Tatsuo	Ido	(CYRIC)
	Takashi	Nakamura	(CYRIC)
	Masatoshi	Itoh	(CYRIC)
	Keizo	Ishii	(CYRIC)
	Akira	Yamadera	(CYRIC)
	Ren	Iwata	(CYRIC)

Research Program

(Chairman)	Takashi	Nakamura	(CYRIC)
	Takemi	Nakagawa	(Faculty of Science)
	Takashi	Yamaya	(Faculty of Science)

	Tutomu	Sekine	(Faculty of Science)
	Kazuyoshi	Masumoto	(Faculty of Science)
	Mieko	Kawamura	(Faculty of Agriculture)
	Takashi	Yoshimoto	(School of Medicine)
	Hidetada	Sasaki	(School of Medicine)
	Katsunori	Abe	(Faculty of Engineering)
	Reimon	Hanada	(Institute for Materials Research)
	Hiroshi	Fukuda	(Institute for Development, Aging and Cancer)
	Masao	Tada	(Institute for Development, Aging and Cancer)
	Manabu	Fujioka	(CYRIC)
	Tatsuo	Ido	(CYRIC)
	Masatoshi	Itoh	(CYRIC)
	Keizo	Ishii	(CYRIC)

Cyclotron

(Chairman)	Manabu	Fujioka	(CYRIC)
	Tsutomu	Tohei	(Faculty of Science)
	Satoru	Kunii	(Faculty of Science)
	Tutomu	Sekine	(Faculty of Science)
	Takashi	Yamaya	(Faculty of Science)
	Akira	Hasegawa	(Faculty of Engineering)
	Kyuya	Kodajima	(Faculty of Engineering)
	Ken	Abe	(Faculty of Engineering)
	Reimon	Hanada	(Institute for Materials Research)
	Kenichi	Akiba	(Research Institute for Mineral Dressing and Metallurgy)
	Tatsuo	Ido	(CYRIC)
	Takashi	Nakamura	(CYRIC)
	Keizo	Ishii	(CYRIC)
	Masatoshi	Itoh	(CYRIC)
	Ren	Iwata	(CYRIC)
	Tsutomu	Shinozuka	(CYRIC)
	Atuki	Terakawa	(CYRIC)

Radiation Protection and Training of Safe Handling

(Chairman)	Yasushi	Inoue	(Faculty of Engineering)

	Yoshiaki	Fujii	(Faculty of Science)
	Satoshi	Tukahara	(Faculty of Science)
	Tetsuya	Ono	(School of Medicine)
	Kiyohiko	Sakamoto	(Schol of Medicine)
	Tadashi	Yamada	(School of Dentistry)
	Kazuo	Ouchi	(Faculty of Pharmaceutical Sciences)
	Toshiyasu	Yamaguchi	(Faculty of Agriculture)
	Masayuki	Hasegawa	(Institute for Materials Research)
	Hiroshi	Fukuda	(Institute for Development, Aging and Cancer)
	Manabu	Fujioka	(CYRIC)
	Takashi	Nakamura	(CYRIC)
	Akira	Yamadera	(CYRIC)

Life Science

(Chairman)	Tatsuo	Ido	(CYRIC)
	Kazuo	Yamamoto	(Faculty of Science)
	Kiyohiko	Sakamoto	(School of Medicine)
	Yasuhito	Itoyama	(School of Medicine)
	Motonobu	Kameyama	(School of Medicine)
	Masahiko	Yamamoto	(School of Medicine)
	Kazuie	Iinuma	(School of Medicine)
	Michinao	Mizugaki	(University Hospital)
	Shin	Maruoka	(University Hospital)
	Kazuo	Ouchi	(Faculty of Pharmaceutical Sciences)
	Mieko	Kawamura	(Faculty of Agriculture)
	Hiroshi	Fukuda	(Institute for Development, Aging and Cancer)
	Masao	Tada	(Institute for Development, Aging and Cancer)
	Kazuo	Kubota	(Institute for Development, Aging and Cancer)
	Manabu	Fujioka	(CYRIC)
	Takashi	Nakamura	(CYRIC)
	Masatoshi	Itoh	(CYRIC)
	Keizo	Ishii	(CYRIC)
	Takehiko	Fujiwara	(CYRIC)
	Yoshihito	Funaki	(CYRIC)

	Takehiko	Fujiwara	(CYRIC)
	Yoshihito	Funaki	(CYRIC)

Prevention of Radiation Hazards

(Chairman)	Takashi	Nakamura	(CYRIC)
	Takemi	Nakagawa	(Faculty of Science)
	Satoshi	Tukahara	(Faculty of Science)
	Ken	Abe	(Faculty of Engineering)
	Manabu	Fujioka	(CYRIC)
	Tatsuo	Ido	(CYRIC)
	Akira	Yamadera	(CYRIC)
	Takehiko	Fujiwara	(CYRIC)
	Muneo	Aoyama	(CYRIC)
	Takamoto	Miyata	(CYRIC)

VIII. PERSONNEL

VIII. Personnel (as of Jan. 1, 1995)

Director Hikonojo Orihara

Division of Accelerator

Manabu	Fujioka
Shogo	Hayashibe[1)]
Takashi	Yamaya[1)]
Tsutomu	Shinozuka
Toshihiro	Honma
Shizuo	Kan[3)]
Ki-ichi	Ishiwata[3)]
Shizuo	Chiba[3)]
Naoto	Takahashi[3)]

Division of Instrumentations

Hikonojo	Orihara
Tsutomu	Tohei[2)]
Keizo	Ishii
Atuki	Terakawa
Sho-ichi	Watanuki
Tsutomu	Ichikawa

Division of Radiopharmaceutical Chemistry

Tatsuo	Ido
Masao	Tada[4)]
Ren	Iwata
Yoshihito	Funaki
Hideo	Takahashi
Yo-ichi	Ishikawa[5)]
Yutaka	Naitoh[5)]

Division of Cyclotron Nuclear Medicine

Masatoshi	Itoh
Takehiko	Fujiwara
Kazuhiko	Yanai[6]
Shinya	Seo

Division of Radiation Protection and Safety Control

Takashi	Nakamura
Akira	Yamadera
Takamoto	Miyata
Noboru	Watanabe[5]
Yasuhiro	Satake[5]

Graduate Student and Researcher

Masahiro	Fujita (Graduate School, Division of Science)
Yoshihiro	Kimura (Graduate School, Division of Science)
Ai	Watanabe (Graduate School, Division of Science)
Yasumori	Kanai (Graduate School, Division of Science)
Guan	Zhong (Graduate School, Division of Science)
Kazuya	Itoh (Graduate School, Division of Science)
Yohiko	Teramoto (Graduate School, Division of Science)
Asaki	Yamamoto (Graduate School, Division of Science)
Susumu	Sasaki (Graduate School, Division of Faculty of Pharmaceutical Sciences)
Kouji	Yamaguchi (Graduate School, Division of Pharmaceutical Sciences)
Naoto	Nakagawa (Graduate School, Division of Pharmaceutical Sciences)
Masanobu	Mukoyoshi (Graduate School, Division of Pharmaceutical Sciences)
Tsuyoshi	Yamaguchi (Graduate School, Division of Pharmaceutical Sciences)
Masato	Higuchi (Graduate School, Division of Medicine)
Marko	Mejia (Graduate School, Division of Medicine)

Hiroshi	Watabe (Graduate School, Division of Engineering)
Noriaki	Nakao (Graduate School, Division of Engineering)
Masashi	Takada (Graduate School, Division of Engineering)
Yu-ichiro	Narita (Graduate School, Division of Engineering)
Atuko	Konno (Graduate School, Division of Engineering)
Masayasu	Miyake (Graduate School, Division of Engineering)
Kim Eun Ju	(Graduate School, Division of Engineering)
Hiroyuki	Ooguchi (Researcher)
Osamu	Satoh (Researcher)

Office Staff

Muneo	Aoyama
Ichiro	Fukuda
Hashime	Wako
Urara	Saso
Kyoko	Fujisawa
Satoshi	Kawamura
Fumiko	Mayama
Mitsuko	Endo
Yu-ko	Yamashita
Noriko	Tanno
Rie	Yoshida
Yoshie	Suzuki
Yuri	Okumura
Toshiyuki	Watanabe[5)]

1) Faculty of Science
2) Institute for Materials Research
3) SUMI-JU Accelerator Service Ltd.
4) Institute for Development, Aging and Cancer)
5) Japan Radiation Protection Co., Ltd.
6) School of Medecine